

INFORMATION TO USERS

This material was produced from a microfilm copy of the original document. While the most advanced technological means to photograph and reproduce this document have been used, the quality is heavily dependent upon the quality of the original submitted.

The following explanation of techniques is provided to help you understand markings or patterns which may appear on this reproduction.

1. The sign or "target" for pages apparently lacking from the document photographed is "Missing Page(s)". If it was possible to obtain the missing page(s) or section, they are spliced into the film along with adjacent pages. This may have necessitated cutting thru an image and duplicating adjacent pages to insure you complete continuity.
2. When an image on the film is obliterated with a large round black mark, it is an indication that the photographer suspected that the copy may have moved during exposure and thus cause a blurred image. You will find a good image of the page in the adjacent frame.
3. When a map, drawing or chart, etc., was part of the material being photographed the photographer followed a definite method in "sectioning" the material. It is customary to begin photoing at the upper left hand corner of a large sheet and to continue photoing from left to right in equal sections with a small overlap. If necessary, sectioning is continued again – beginning below the first row and continuing on until complete.
4. The majority of users indicate that the textual content is of greatest value, however, a somewhat higher quality reproduction could be made from "photographs" if essential to the understanding of the dissertation. Silver prints of "photographs" may be ordered at additional charge by writing the Order Department, giving the catalog number, title, author and specific pages you wish reproduced.
5. PLEASE NOTE: Some pages may have indistinct print. Filmed as received.

Xerox University Microfilms

300 North Zeeb Road
Ann Arbor, Michigan 48106

76-13,526

FORTINO, Andres Guillermo, 1947-
NUMERICAL METHODS FOR
MULTIDIMENSIONAL MODELING OF
MIS DEVICES.

The City University of New York
Ph.D., 1976
Engineering, electronics, and electrical

Xerox University Microfilms, Ann Arbor, Michigan 48106

© 1976

ANDRES GUILLERMO FORTINO

ALL RIGHTS RESERVED

NUMERICAL METHODS FOR
MULTIDIMENSIONAL MODELING
OF MIS DEVICES

by

ANDRES G. FORTINO

A dissertation submitted to the
Graduate Faculty in Engineering
in partial fulfillment of the
requirements for the degree of
Doctor of Philosophy, The City
University of New York

1976

This manuscript has been read and accepted for the Graduate Faculty in Engineering in satisfaction of the dissertation requirements for the degree of Doctor of Philosophy.

Jan 26, 1976
Date
1/26/76
Date

Joseph J. Nadan
Chairman of Examining Committee
Jacques E. Benveniste
Executive Officer

Professor Morris Ettenberg

Professor Paul Karmel

Professor Donald Goldfarb

Professor Joseph Nadan
Chairman

The City University of New York

ABSTRACT

NUMERICAL METHODS FOR MULTIDIMENSIONAL MODELING OF MIS DEVICES

by

Andres G. Fortino

Advisor: Joseph S. Nadan

The DC and small signal AC operation of MIS devices under equilibrium conditions in one and two spatial dimensions is investigated. A variant of Gummel's algorithm is implemented for the one dimensional DC study of MIS capacitors. A one-step iterative method, SOR-Newton, is applied with success to the semiconductor nonlinear Poisson equation in two dimensions. The method of complementary functions, with reconditioning, is applied to the analysis of MOS capacitors. The admittance of inhomogeneously doped MOS capacitors is presented. Favorable comparisons are made to classical analysis of the small signal problem in one dimension. The method of complementary functions is extended to two spatial dimensions to study the small signal AC problem. A two dimensional structure, the three terminal varactor is studied and reported.

To

Kathleen...

ACKNOWLEDGEMENTS

To the City College of New York for their financial support, in particular to C.U.N.Y. for their award FRAP No. 10598...

To IBM for their technical assistance in the reproduction of this dissertation...

To my colleagues at City College, Michael Cascione, Raymond Camisa, Larry Kurowski, Jack Mandelman, Colman Wong, and others...

To Dr. Thomas Gerson for many years of generous collaboration...

To Professors Jacques Benveniste, Morris Ettenberg, Donald Goldfarb and Paul Karmel for their intellectual support and encouragement...

To Dr. William Rosenberg for assistance in all matters: financial, intellectual and emotional...

To my friend, advisor and mentor, Professor Joseph S. Nadan, for believing in me and providing the leadership for this work...

To my family for the many years of understanding, especially Marie Grimm for her help freely given...

To my parents for their love and encouragement...

Finally, to Kathleen, my friend, for whom this work was a labor of love...

I offer my sincere thanks.

TABLE OF CONTENTS

Chapter	Page
1. INTRODUCTION	
1.1 Organization	1
1.2 Historical Background and Motivation	3
1.3 Characterization of the Electronic Operation of Semiconductive and Insulating Media	5
2. THE DC MODELS IN ONE AND TWO SPATIAL DIMENSIONS	
2.1 Introduction	13
2.2 The DC Model in One Dimension	15
2.3 The DC Model in Two Dimensions	32
2.4 Results of Studies with the One Dimensional DC Models	60
2.5 Results of Studies with the Two Dimensional DC Algorithm	81
3. THE SMALL SIGNAL AC MODEL IN ONE SPATIAL DIMENSION	
3.1 Introduction	100
3.2 The Structure and Small Signal AC Equations in One Spatial Dimension	102
3.3 The Numerical Method of Solution- The Method of Complementary Functions and Reconditioning Operations	115
3.4 The Calculation of the Small Signal AC Admittance in One Spatial Dimension	133
3.5 The Total Solution	167
3.6 Studies of the Gram-Schmidt Results and Other Observations on the Algorithm	185
4. THE SMALL SIGNAL AC MODEL IN TWO SPATIAL DIMENSIONS	

4.1	Introduction	192
4.2	The Structure and Small Signal AC Equations in Two Spatial Dimensions	194
4.3	The Theory of the Method of Complementary Functions for Elliptic Partial Differential Equations	206
4.4	The Small Signal AC Equations in Two Dimension-Numerical Method of Solution and Implementation of the Algorithm	219
4.5	The Three Terminal Varactor-Small Signal AC Analysis in Two Dimensions	230
5.	SUMMARY	247
Appendices		
A.	High Frequency Model of the Generation-Recombination Mechanism	250
B.	Stability Analysis of the Numerical Method Used in the Solution of the Nonlinear Poisson Equation	254
C.	Analysis of Measured MIS Capacitance-Voltage Curves	263
D.	Verification of the Lateral Boundary Approximation in the Two Dimensional Problem	274
E.	Algorithm Listings	279
	References	336
	Autobiographical Statement	342

LIST OF TABLES

1.1	Pertinent constants employed in device analysis.	12
2.1	Grid data for numerical experiments 2 and 3.	69
3.1	One dimensional solution of the small signal AC problem--A comparison of classical and shooting methods.	190

LIST OF ILLUSTRATIONS

Figure		Page
1.1	Energy band diagram showing definition of the potential $V(x)$.	7
2.1a	One dimensional MIS structure and pertinent DC equations.	16
b	One dimensional MIS structure showing boundary conditions and typical solution.	
2.2a	Discretization of the x axis and solution with a grid.	21
b	Uniform one dimensional grid.	
c	Nonuniform one dimensional grid.	
2.3	Matrix system for the one dimensional discretized potential.	28
2.4	Computational flowchart of subroutine VDC1D used to solve for the one dimensional potential.	29
2.5a	General two dimensional structure considered.	33
b	Finite boundaries on the two dimensional device.	36
c	Simple example to study boundary approximation.	
2.6	Typical uniform grid structure.	36
2.7	Typical nonuniform grid structure.	37
2.8a	Five point uniform discretization grid employed in discretizing the Laplacian.	39
b	Nonuniform five point discretization grid.	
c	Discretization grid at the insulator-semiconductor interface employed in discretizing Gauss' Law.	
2.9	Matrix system for two dimensional discretized potential.	42
2.10	Accelerated Newton's method.	44

2.11	Graphical example of taking the first part of a SOR-Newton step.	47
2.12	Completing the SOR-Newton step.	48
2.13	Decomposition of the two dimensional structure into one dimensional strips for the generation of an initial guess.	52
2.14	Error criteria versus relaxation parameter obtained experimentally for the three terminal varactor structure.	55
2.15	Error criteria versus number of iterations for varying relaxation parameter.	56
2.16	Computational flowchart of MAIN to solve for the DC potential in two dimensions.	58
2.17	Computational flowchart of subroutine VDC2D.	59
2.18	One dimensional potential solution as a function of distance for varying gate biases.	61
2.19	Gate charge as a function of surface potential.	62
2.20	Gate charge as a function of gate voltage showing definition of C_{DC} .	66
2.21	Results of numerical experiment 3.	70
2.22	Results of numerical experiment 2.	71
2.23	Cost factor versus accuracy criteria for the generation of a particular C_{DC} -V curve.	73
2.24	Accuracy criteria versus number of iterations showing breakpoint.	74
2.25	Ideal linearly graded junction doping profile of an MOS-PN junction.	76
2.26	Incremental capacitance-voltage curves for the MOS-PN junction.	77

2.27	Potential profiles of an MOS-PN junction showing sweeping out of the epitaxial region.	78
2.28	Potential profile showing no sweeping out of the epitaxial region due to high epitaxial doping.	79
2.29	Three terminal MOS varactor structure studied.	82
2.30	Grid structure employed in the two dimensional analysis of the three terminal varactor.	84
2.31a	Ideal potential distribution for an infinitesimal gap.	86
b	The discretized potential at an exterior point.	
c	Discretization grid for exterior region employed in the potential calculation.	
2.32	Surface potential of the three terminal varactor ($V_2=0v$).	89
2.33	Surface potential of the three terminal varactor ($V_2=-1v$).	90
2.34	Surface potential of the three terminal varactor ($V_2=2v$).	91
2.35	Surface potential of the three terminal varactor ($V_2=2v$).	92
2.36	Surface potential of the three terminal varactor ($V_2=2v$).	93
2.37	Comparison of surface potential for various gap sizes and biases of the three terminal varactor.	95
2.38	Surface carrier concentration for various gap sizes of the three terminal varactor.	96
2.39	Potential along the air-insulator interface as a function of position for varying applied voltages.	97
2.40	Potential along the air-insulator interface for a $.6\mu m$ gap varactor.	98

2.41	Potential along the air-insulator interface for a 1.0 μ m gap varactor.	99
3.1	The "one dimensional" MIS structure studied with appropriate parameters.	103
3.2	The matrix system of the small signal AC problem in one dimension as a set of first order differential equations.	110
3.3	The one dimensional MIS structure with boundary conditions, grid and x axis assignments.	112
3.4	Computational flowchart of the algorithm VDC1D.	128
3.5	Computational flowchart of the integration subroutine STEP.	132
3.6	Capacitance-voltage curves for varying oxide thicknesses.	137
3.7	Capacitance-voltage curves for varying doping densities.	138
3.8	Comparison of the calculated incremental, "high" and "low" frequency capacitance.	141
3.9	Calculated frequency dependence of the inversion capacitance of an MOS capacitor.	142
3.10	Detail of Fig. 3.9.	143
3.11	Experimental and modeled capacitance of an MOS capacitor.	145
3.12	General gaussian complementary doped profile.	148
3.13	Capacitance-voltage curves of an inhomogeneously doped MOS capacitor for varying junction depths.	150
3.14	Energy band diagram and equivalent circuit of an inhomogeneously doped MOS Capacitor.	152
3.15	Capacitance-voltage curves for inhomogeneously doped MOS capacitance of varying surface doping.	153

3.16	Doping profiles of the Hswe, et.al. capacitor.	156
3.17	Experimental and modeled capacitance-voltage curves of ion-implanted MOS capacitors.	157
3.18	Two-level MOS capacitor and resulting C-V curve (at high frequency).	159
3.19	Capacitance-voltage curve of three level MOS capacitor (model and experiment).	160
3.20	Capacitance-voltage curve of a three level MOS capacitor (model and experiment).	161
3.21	Capacitance-voltage curves of a three level MOS capacitor (model and experiment).	162
3.22a	Two three-level MOS capacitors.	163
b	Detail of three-level MOS capacitor.	
3.23	Typical high frequency conductance-voltage curve of an MOS capacitor.	165
3.24	Conductance versus voltage of the ion-implanted (Hswe, et.al.) MOS capacitors.	166
3.25	Computational flowchart of VACSTUDY, employed to calculate the total solution.	172
3.26	Small signal AC current densities in an MOS capacitor in inversion (high frequency).	175
3.27	Small signal AC current densities in an MOS capacitor in inversion (low frequency).	176
3.28	Small signal AC current densities in an MOS capacitor in flat-band (low frequency).	177
3.29	Small signal AC current densities in an MOS capacitor in flat-band (high frequency).	178

3.30	Small signal AC current densities in an MOS capacitor in depletion (low frequency).	179
3.31	Small signal AC current densities in an MOS capacitor in depletion (high frequency).	180
3.32	Small signal AC current densities in an MOS capacitor in accumulation (low frequency).	181
3.33	Small signal AC current densities in an MOS capacitor in accumulation (high frequency).	182
3.34	Effect of reconditioning criteria on the calculated small signal capacitance.	186
3.35	Effect of reconditioning on the calculated small signal conductance.	187
4.1	Structure, equations and boundary conditions for two dimensional small signal MIS device simulation.	203
4.2a	The general two dimensional problem used in developing the shooting method.	207
b	The region above discretized with a grid and shooting direction assigned.	
4.3	Scheme of computation using the shooting method.	211
4.4	Example of the application of the shooting method to Laplace's equation.	214
4.5	Scheme of computation for the two dimensional small signal AC problem by application of the shooting method.	220
4.6	Arbitrary starting vectors as columns of $\underline{V}(2)$, employed in the small signal AC simulation.	225
4.7	Application of boundary conditions (at $J=M$ for V_1 and at $J=J_0$ for J_{py} and J_{ny}) in the small signal AC problem.	228

4.8	Computation flowchart of VAC2D.	229
4.9	Structure and biasing of the three terminal varactor.	231
4.10a	Distributed capacitive circuit showing definitions of pertinent capacitances in the three terminal varactor studied.	233
	b Grid and variables employed in the small signal AC capacitance calculation.	
4.11	Three terminal varactor capacitance-voltage curve (.2 μ m gap, $V_2=-1$ v.).	235
4.12	Three terminal varactor capacitance-voltage curve (.2 μ m gap, $V_2=0$ v.).	236
4.13	Three terminal varactor capacitance-voltage curve (.2 μ m gap, $V_2=+1$ v.).	237
4.14	Three terminal varactor capacitance-voltage curve (.6 μ m gap, $V_2=-1$ v.).	238
4.15	Three terminal varactor capacitance-voltage curve (.6 μ m gap, $V_2=0$ v.).	239
4.16	Three terminal varactor capacitance-voltage curve (.6 μ m gap, $V_2=+1$ v.).	240
4.17a	Inversion under lead 1, showing lateral spread of inversion region.	242
	b Reduction of lateral inversion region under lead 1 by accumulation under lead 2.	
	c Increase in lateral inversion by the inversion under lead 2.	
4.18a	The influence of a nearby accumulation region on the capacitance of a short gap device.	244
	b Reduction of the influence of the accumulation region by the increase in gap width.	
C.1	Definition of terms in the modeling of the capacitance of an MIS capacitor.	264
C.2	Measured and calculated capacitance-voltage curve.	268

C.3a	Structure of a three level MOS capacitor.	273
b	Definition of terms in the example of a three level MOS varactor.	
D.1	Structure and decomposition of the problem.	275
D.2	Redefinition of the boundary conditions.	276
D.3	Further redefinition of the boundary conditions.	276

INTRODUCTION

1.1 Organization

In this thesis improved numerical methods for the characterization of semiconductor devices in two dimensions are presented. In particular, Metal-Insulator Semiconductor (MIS) and Metal-Oxide Silicon (MOS) structures are studied.

The thesis is organized into five chapters and five appendices: Chapter 1 presents the historical background and organization. The general device equations are derived in Chapter 1 and general semiconductor device parameters discussed.

In Chapter 2 the one and two dimensional DC numerical models are developed, discussed and typical results of studies with each given. Whereas the one dimensional DC algorithm is a standard one, the two dimensional one successfully employs a nonlinear method.

Chapter 3 deals with the one dimensional AC model of the MIS capacitor. Whereas this has been quite thoroughly studied, the model is developed with as few assumptions as possible yielding an algorithm which accepts nonuniform doping concentrations, varying positive interface charge densities and other parameter variations. The model employs the method of complementary

functions which is very powerful in correcting the recognized "ill-conditioning" of the problem. Experimental evidence is compared to the model and found to be in close agreement. In Chapter 4, the two dimensional AC operation of the three terminal varactor structure is modeled. Use is made of the other three algorithms in this analysis. The method of complementary functions is extended and used in two dimensions; the development of this technique is presented with some numerical examples.

In Chapter 5, obtained results are summarized and suggested further work is described. The appendices deal with the derivation of a recombination-generation term, stability analysis of the DC scheme, capacitance-voltage measurements and analysis, a study of an approximation made in the text and finally, a listing of computer codes, in that order.

The following notation convention is employed: a variable underlined with a (\sim) represents a vector in either Cartesian space or an N-dimensional vector space, its particular application made as unambiguous as possible. A (\sim) over a variable designates it as a complex number, usually when representing phasors. An underlining (-) indicates a variable is a matrix.

1.2 Historical Background and Motivation

Three concurrent developments at the City College have given impetus to the modeling work described in the previous section. First, the ongoing interest in high frequency (microwave) devices, an active area of study, provided the necessary background and generated the problems to be studied. Second, the natural continuation of previous work by R. Camisa⁽¹⁾ in the analysis and application of microwave MIS varactors. Lastly, the three terminal varactor, a device found by J. Nadan⁽²⁾, provided a two dimensional structure to be studied.

A search of past and current work in the modeling of semiconductor devices shows that numerical techniques are preferable to analytic ones. Further, one-dimensional models abound, the classical example being the work of⁽³⁾ H. K. Gummel. Two dimensional models have only recently received attention, as may be gleaned from the survey of A. H. Agajanian⁽⁴⁾.

Basically all device modeling work may be separated into the following categories:

1. DC operation, in which a current exists; such as in MOSFET's (Metal Oxide Semiconductor Field Effect Transistors); or the zero current case, such as MIS capacitance structures,
2. Small signal AC operation about the DC operating point for any bias condition and device conformation, and
3. Transient analysis or Large Signal AC operation.

For all three cases, one may study models for devices described in one or two spatial dimensions. Decidedly, the DC problem with non-zero current is more difficult to solve because there are more equations to be solved. The small signal problem presents certain challenges which are discussed herein. The transient problem is the most difficult, in this author's opinion, since it involves all the problems of the above conditions and severe numerical technique constraints. One dimensional transient operation of MIS capacitors have been studied successfully by T. Collins⁽⁵⁾. There are few two dimensional models for small signal AC device operation reported as of this date⁽⁶⁾. The developments at City College, outlined earlier, together with this apparent void in the analysis techniques described, provided the motivation for this thesis.

1.3 Characterization of the Electronic Operation of Semiconductive and Insulating Media

The analysis of semiconductor devices requires a set of equations that relate the proper dependent variables to each other. For semiconductive media these variables are the hole and electron charge densities, p , n , the hole and electron currents, \vec{J}_p , \vec{J}_n , and the potential, V .

The Semiconductor

Taking moments of the Boltzman equation of the phase space distribution of carriers in the material one may obtain the continuity and current density equations for holes and electrons⁽⁷⁾. The zeroth moment of the Boltzman equation is the law of conservation of mass in the media which becomes the continuity of charge equation for each carrier species

$$q \cdot \frac{\partial p}{\partial t} = -q \cdot R_p - \nabla \cdot \vec{J}_p \quad (1.3.1)$$

$$q \cdot \frac{\partial n}{\partial t} = -q \cdot R_n + \nabla \cdot \vec{J}_n \quad (1.3.2)$$

where q is the electronic charge and R_p and R_n are very general thermal recombination terms for holes and electrons which is considered in more detail. The first moment of the Boltzman equation is the law of conservation of carrier momentum. We shall assume here that we

have collision dominance and constant temperature throughout the media. This results in the electron and hole current density equations

$$\vec{J}_p = -qD_p \nabla \cdot p - q\mu_p p \nabla V \quad (1.3.3)$$

$$\vec{J}_n = +qD_n \nabla \cdot n - q\mu_n n \nabla V \quad (1.3.4)$$

where D_S and μ_S are the diffusion constants and mobilities of the S^{th} type carrier respectively. The assumption of constant temperature made above in deriving Eqs. 1.3.3 and 1.3.4 is a very realistic one since no appreciable self-heating of the device is expected and it is maintained at a constant ambient temperature. This assumption is necessary to terminate moment taking at this point and not introduce energy terms into Eqs. 1.3.3 or 1.3.4.

The last equation which must be added to the ones above to obtain a complete independent set is Poisson's equation

$$\nabla^2 V = - \frac{q}{\kappa_S \epsilon_0} (p - n + N_D - N_A) \quad (1.3.5)$$

The charge density term in the right hand side is composed of holes and electrons as shown and the background doping density. Henceforth, this background doping shall be considered one term, the algebraic sum

of the donor and acceptor ion concentration: $N_{DOP} = N_D - N_A$. Furthermore, the Boltzman relation for carriers as a function of potential may be assumed, yielding

$$p = n_i \exp\left(\frac{E_i - E_F}{kT}\right) \quad (1.3.6)$$

$$n = n_i \exp\left(\frac{E_F - E_i}{kT}\right) \quad (1.3.7)$$

This is valid for $|E_F - E_C| < k_B T$ or $|E_F - E_V| < k_B T$. The potential V is defined as

$$V = -\left(\frac{E_i - E_F}{q}\right) \quad (1.3.8)$$

and the Fermi energy level in the bulk is used as the reference datum for potential.

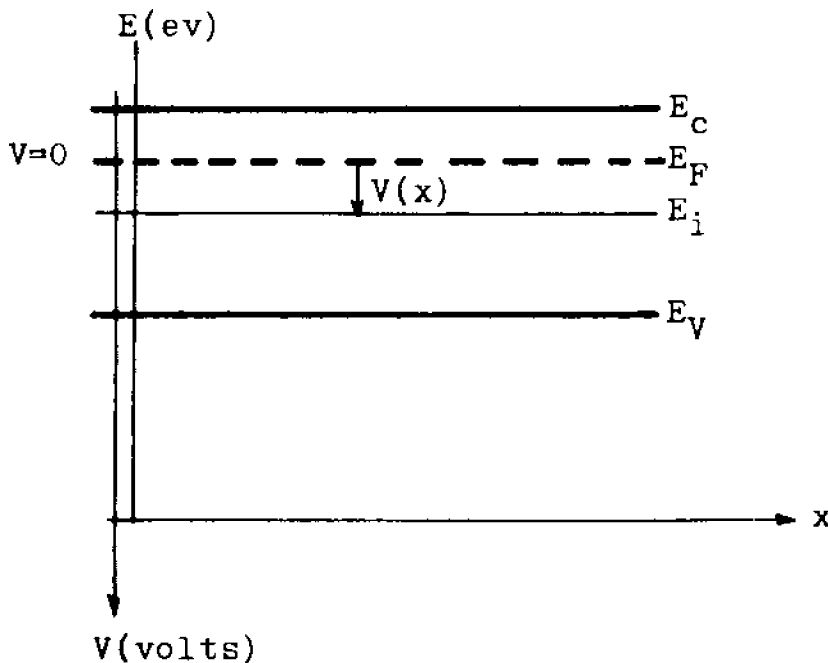


Figure 1.1 Energy band diagram showing definition of the potential $V(x)$.

The Fermi potential is, by definition above, $V_F = -\frac{E_F - E_i}{q}$. Defining a thermal voltage V_T as $V_T = \frac{kT}{q}$ then Eqs. 1.3.6 and 1.3.7 become

$$p = n_i \exp\left(-\frac{V}{V_T}\right) \quad (1.3.9)$$

$$n = n_i \exp\left(\frac{V}{V_T}\right) \quad (1.3.10)$$

Using this in Poisson's equation, one obtains

$$\nabla^2 V = \frac{2qn_i}{K_S \epsilon_0} \left(\sinh \frac{V}{V_T} - \frac{N_{DOP}}{2n_i} \right) \quad (1.3.11)$$

For applied biases which bring the intrinsic level into either the conduction band or the valance band, or whenever $E_i - E_F = E_g/2$, full Fermi statistics must be employed⁽⁸⁾. For most applications considered in this work, the use of these statistics has not been found necessary although their implementation is not prohibitive. Satisfactory results, as shown in Chapter 3, have been achieved with Boltzman statistics thus they are used throughout.

The complete describing set of equations in semiconductor media may then be expressed as⁽⁹⁾

$$q \frac{\partial p}{\partial t} = -q \cdot R_p - \nabla \cdot \underline{J}_p \quad (1.3.12)$$

$$q \frac{\partial n}{\partial t} = -q \cdot R_n + \nabla \cdot \underline{J}_n \quad (1.3.13)$$

$$\underline{J}_p = -qD_p \nabla \cdot p - q\mu_p p \nabla V \quad (1.3.14)$$

$$\underline{J}_n = +qD_n \nabla \cdot n - q\mu_n n \nabla V \quad (1.3.15)$$

$$\nabla^2 V = - \frac{q}{K_S \epsilon_o} (p - n + N_{DOP}) \quad (1.3.16)$$

Two other dependent variables of interest, which may be defined using the above, are the electric field \underline{E} and the total current density \underline{J}_{TOT}

$$\underline{E} = - \nabla \cdot V \quad (1.3.17)$$

and

$$\underline{J}_{TOT} = \underline{J}_p + \underline{J}_n + K_S \epsilon_o \frac{\partial \underline{E}}{\partial t} \quad (1.3.18)$$

Throughout this work, the temperature of operation of the devices modeled is implicitly assumed to be room temperature ($T=300^\circ K$). The intrinsic carrier concentration is then a constant and its value is shown in Table 1.1, together with other constants used. The thermal recombination-generation terms which appear in Eqs. 1.3.14 and 1.3.15 are derived and discussed in Appendix A. The mobilities μ_p and μ_n are functions of doping density and electric field, this relationship is discussed by Caughey and Thomas⁽¹⁰⁾. As a function of doping densities, the following functions are used

$$\mu_p = \frac{495. - 47.7}{1 + (N_{DOP}/6.3 \times 10^{16}) \cdot 72} + 47.7 \frac{\text{cm}^2}{\text{v} \cdot \text{sec}} \quad (1.3.19)$$

and

$$\mu_n = \frac{1330 - 65}{1 + (N_{DOP}/8.5 \times 10^{16}) \cdot 76} + 65 \frac{\text{cm}^2}{\text{v} \cdot \text{sec}} \quad (1.3.20)$$

for silicon. For electric fields much greater than 2×10^4 v/cm in silicon, corrective factors must multiply the above expressions to take into account the field dependence of mobility,

$$c_n = \frac{1}{1 + (|E|/8000)^2} \quad (1.3.21)$$

$$c_p = \frac{1}{1 + |E|/1.95 \times 10^4} \quad (1.3.22)$$

Since all of the practical application work has been done in silicon, the above formulas suffice. This, of course, does not detract from the general applicability of the methods herein derived to other semiconductor materials.

The Insulator

It should be assumed that the insulator, whatever its composition (e.g. SiO_2 , SiNO_3 , etc.), is a perfect insulator and that no carrier current exists within it. Satisfactory results are obtained by this simple assumption. Therefore only Laplace's equation need be

solved in the insulator

$$\nabla^2 v = 0 \quad (1.3.23)$$

If the electric field is defined as in the semiconductor, i.e. using Eq. 1.3.17, the current density, which is totally a displacement current density, is

$$\vec{J}_I = \kappa_I \epsilon_0 \frac{\partial \mathbf{E}}{\partial t} \quad (1.3.24)$$

The value of the relative permittivity of various insulators of interest is shown in Table 1.1.

The Metal

Whereas all metals exhibit a finite conductivity, the assumption of infinite conductivity is applied here. The algorithms used to solve the equations have been programmed for zero work function difference between metal and semiconductor. Most of the experimental devices have been fabricated with aluminum gates and thus care must be exercised in interpreting the results to accommodate nonzero work function differences.

Subsequent chapters develop these equations further as they apply to varying bias conditions and various multidimensional MIS device geometries.

NAME	VALUE	UNITS	DESCRIPTION
q	1.69×10^{-19}	coulombs	electric charge
V_T	.0259	volts	thermal voltage = $\frac{k_B T}{q}$ for $T=300^\circ\text{K}$
n_i	1.45×10^{10}	$1/\text{cm}^3$	intrinsic carrier concentration for Silicon at $T=300^\circ\text{K}$
ϵ_0	8.86×10^{-14}	f/cm	free space dielectric constant
K_{SiO_2}	3.9	—	relative permittivity of thermal Silicon Dioxide
K_{Si}	11.7	—	relative permittivity of silicon
$K_{\text{Si}_3\text{N}_4}$	5.0	—	relative permittivity of deposited Si_3N_4

Table 1.1 Pertinent Constants Employed in Device Analysis

CHAPTER 2

THE DC MODELS IN ONE AND TWO
SPATIAL DIMENSIONS2.1 Introduction

In this chapter the development of DC models for MIS capacitors with a corresponding output of physical parameters such as the potential, charge densities and electric field is described.

In Sections 2.2 and 2.3 the describing equations for one and two dimensional DC operation are derived from the general set given in Chapter 1. The numerical algorithms necessary for their solution are also developed and explained. The classical Gummel algorithm is implemented for the one dimensional DC problem. The SOR-Newton method of solution of semiconductor device modeling, is used for the two dimensional case. These algorithms are investigated for accuracy, stability, speed, and limits of operation.

In Section 2.4 the developed codes are applied to calculate the incremental capacitance of MOS capacitors. Results are shown for inhomogeneously doped devices. In Section 2.5 the DC operation of the three terminal varactor is investigated. The effect of lead separation is studied.

The algorithms in this chapter are an integral part of the small signal AC models of Chapters 3 and 4, and are developed to satisfy their requirements as well.

2.2 The DC Model in One Dimension

Structure and Equations

The structure under investigation in this section, shown in Fig. 2.1, is the MIS capacitor. The variables of interest and the equations interrelating them are first presented.

The insulator is assumed to be ideal and zero DC current exists in this region. For the semiconductor in equilibrium Boltzman statistics for the charge densities as functions of the potential are used. The only variable to be found is the DC potential everywhere as a function of x . From this calculation one may find the charge densities and electric field directly.

The self-consistent set of equations in this case are: Poisson's equation in the semiconductor

$$\frac{d^2V(x)}{dx^2} = -\frac{q}{K_s\epsilon_0} \left\{ n_i \exp\left(\frac{-V(x)}{V_T}\right) - n_i \exp\left(\frac{V(x)}{V_T}\right) - N_A(x) + N_D(x) \right\} \quad (2.2.1)$$

Laplace's equation in the insulator

$$\frac{d^2V(x)}{dx^2} = 0 \quad (2.2.2)$$

Equation 2.2.1 may be rewritten by expressing the two exponential terms as a combined hyperbolic sine term resulting in

$$\frac{d^2V(x)}{dx^2} = \frac{2qn_i}{K_s\epsilon_0} \left\{ \sinh\left(\frac{V(x)}{V_T}\right) - \frac{N_{DOP}(x)}{2n_i} \right\} \quad (2.2.3)$$

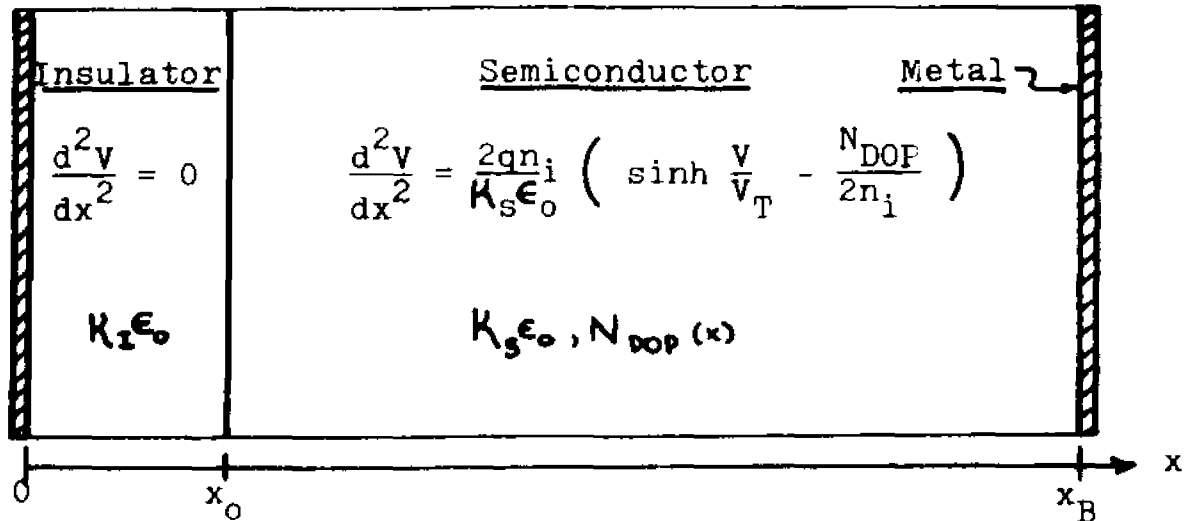


Figure 21a. One dimensional MIS structure and pertinent DC equations.

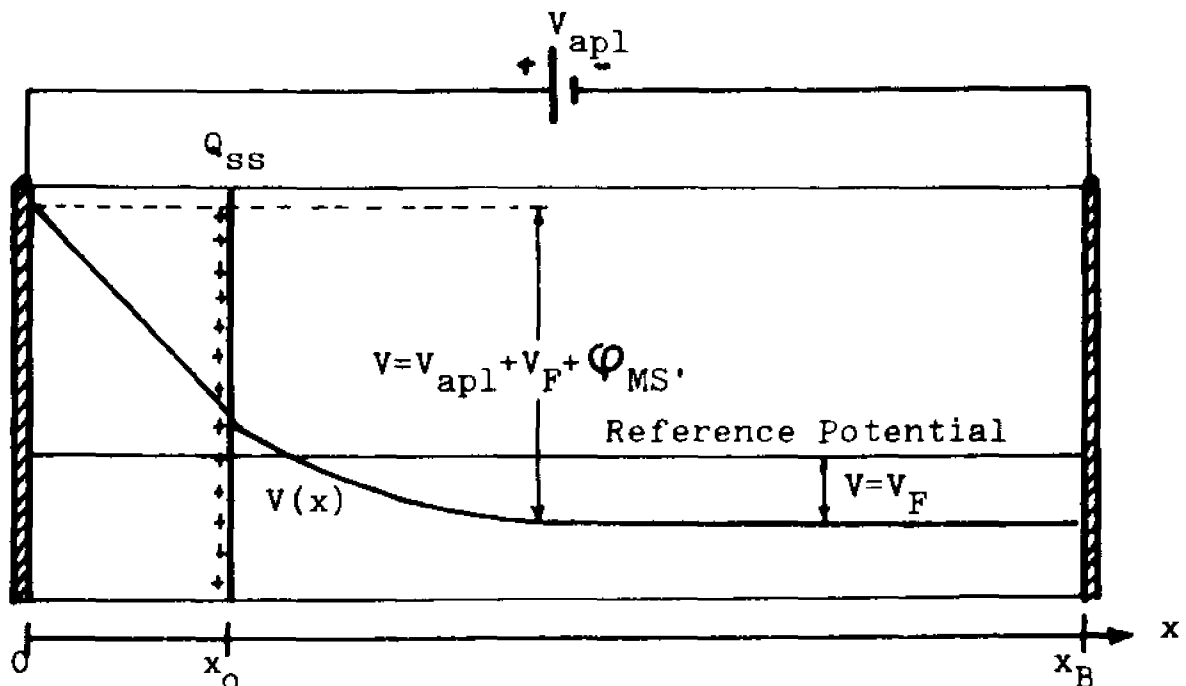


Figure 21b. One dimensional MIS structure showing boundary conditions and typical solution.

The solution to these two second order ordinary differential equations for the potential is made unique and self-consistent by determining a complete set of boundary conditions. It is the boundary data which determines whether a differential equation represents a boundary value problem or an initial value problem⁽¹¹⁾. In this case the DC potential at the metal-semiconductor boundary is taken as our reference potential, in other words, this boundary is to be considered the reference datum. Furthermore, this contact shall be assumed to be ohmic, that is, a free flow of electrons may occur in either direction without charge buildup at this interface. A potential drop across this boundary is then not expected and the bulk of the semiconductor is considered to be at a potential equal to the Fermi potential for that bulk type material. This boundary value derives from the way DC potential difference is defined in Chapter 1.

Consequently, at the metal-insulator boundary, the potential in the insulator will be the applied potential plus the bulk Fermi potential. The ideal case for a metal-insulator semiconductor system is that of zero work function difference between any of the materials. To investigate the correlation between experiment and theory, work function differences in the system shall be taken into account as an additive term to the left hand boundary data. This work function difference is

the algebraic sum of the metal-insulator and insulator-semiconductor difference. Essentially, this is the difference between the metal-semiconductor work functions. Discussion of this system and of typical values for material of interest are given in Wolf ⁽¹²⁾. An example of how it comes into the calculation of modeled parameters of interest, such as capacitance-voltage curves, is shown in Appendix C.

At the insulator-semiconductor boundary, one obtains two boundary data: a) the potential must be continuous, and b) application of Gauss' Law at this interface for the electric field. This last condition may be expressed as

$$K_S \epsilon_0 \left(\frac{-dV(x_{0+})}{dx} \right) - K_I \epsilon_0 \left(\frac{-dV(x_{0-})}{dx} \right) = Q_{SS} \quad (2.2.4)$$

where the electric field density has been defined in Eq. 1.3.16; Q_{SS} is the net positive interface surface charge density. Summarizing the boundary data,

$$V(x_{B-}) = V_F \quad (2.2.5)$$

$$V(x_{0+}) = V(x_{0-}) \quad (2.2.6)$$

$$-K_s \frac{dV(x_{o+})}{dx} + K_I \frac{dV(x_{o-})}{dx} = \frac{Q_{ss}}{\epsilon_0} \quad (2.2.7)$$

$$V(0^+) = V_{apl} + V_F \quad (2.2.8)$$

Equations 2.2.2 and 2.2.3 together with the boundary data shown in Eqs. 2.2.5 through 2.2.8 constitute a boundary value problem and equilibrium type solutions are sought. Figure 2.1b shows a typical solution, together with externally applied DC potential difference and appropriate boundary conditions.

Discretization Scheme

The Poisson equation of the preceding section (see Eq. 2.2.3) is a nonlinear equation and analytic solutions are not known for all excitations. Rather than search for a closed form type of solution of this equation, a numerical technique is investigated and implemented. Much success with numerical methods applied to this equation has been obtained and accurate solutions are commonplace. The standard reference in this area is Gummel's algorithm⁽³⁾ and it is used widely to study MIS structures. In the present work an algorithm, which may be shown equivalent to Gummel's is implemented

and studied.

To solve ordinary differential equations numerically, one takes the independent variable, in this case x , and discretizes it. Then the dependent function, in this case the potential $V(x)$, which is a continuous function of x , is defined only at those discrete intervals of x . This yields $V^*(x_i)$, as shown in Fig. 2.2a. The o.d.e. is discretized by obtaining a Taylor series expansion of the derivatives and retaining as many terms as necessary to obtain the order of truncation desired⁽¹³⁾. In this case the second derivatives are discretized with the standard three point formula which has an $O\{h^2\}$ truncation error for uniform grid steps

$$\frac{d^2u}{dx^2} \cong \frac{u_{i+1}^* + u_{i-1}^* - 2u_i^*}{h^2} \quad (2.2.9)$$

Where u^* are the discrete analogues of $u(x)$ at the grid points and h is the grid size (see Fig. 2.2.b). At grid points where the grid sizes are different on either side, a three point formula may still be used but its truncation error is then of $O\{h\}$ where the largest grid size is the dominant term

$$\frac{d^2u}{dx^2} \cong \frac{h_{i-1}u_{i+1}^* + h_i u_{i-1}^* - (h_i + h_{i-1})u_i^*}{(h_i + h_{i-1})h_i h_{i-1}/2} \quad (2.2.10)$$

The form of Eq. 2.2.10 is the more general of the two and it may be seen that when $h_i = h_{i-1}$, (a uniform grid) is

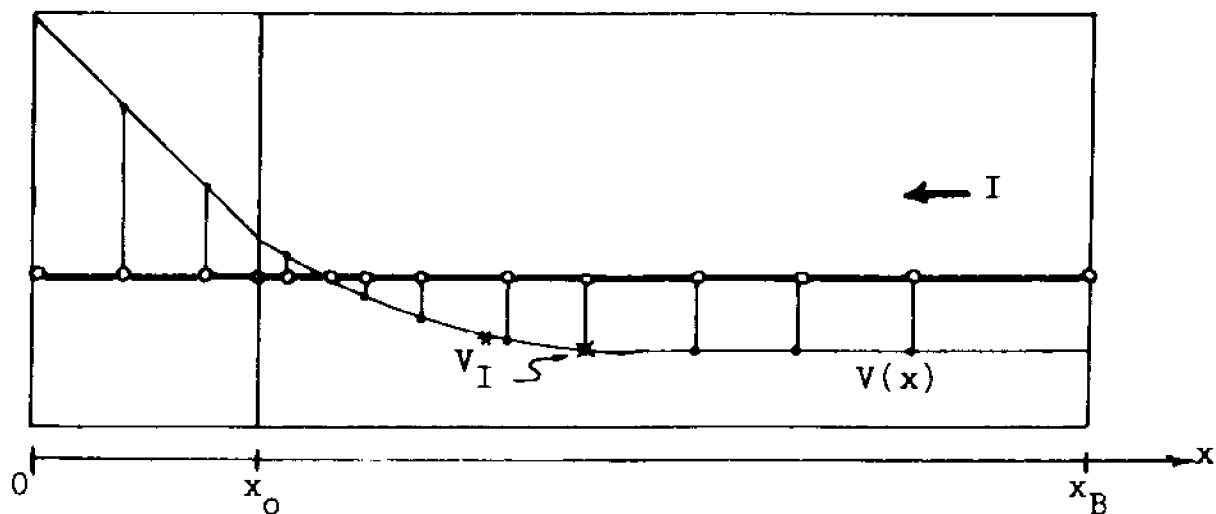


Figure 2.2a. Discretization of the x axis and solution with a grid.

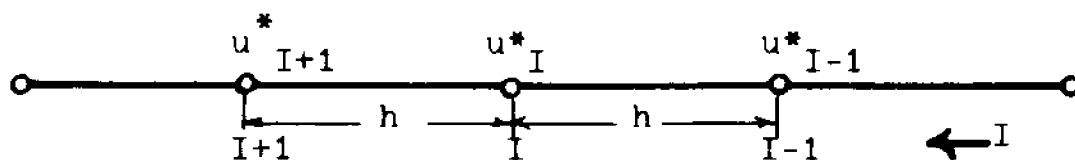


Figure 2.2b. Uniform one dimensional grid.

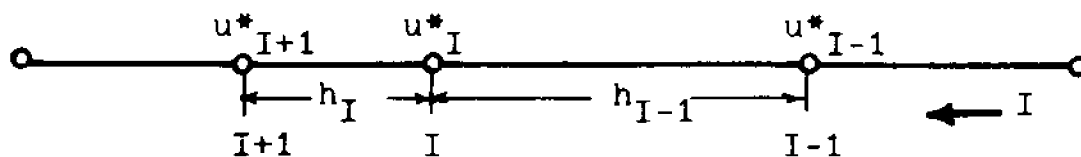


Figure 2.2c. Nonuniform one dimensional grid.

used, it reduces to Eq. 2.2.9. It is appropriate at this point to discuss which of the discretization schemes should be used. The scheme of Eq. 2.2.9 is the more accurate of the two due to a lower truncation error. On the other hand, Eq. 2.2.10 allows one to handle nonuniform grids, useful in locally increasing the solution accuracy. This is investigated and discussed in Section 2.4. Equation 2.2.10 is used to cross from regions of one grid size to another. It is easier to implement Eq. 2.2.10 at all steps since it is equivalent to Eq. 2.2.9 when grid steps are uniform and can take care of nonuniformities automatically. This involves the calculation of certain quantities such as the denominator of Eq. 2.2.10 which is totally unnecessary for uniform grids and adds on to computation time needlessly. It has been found advantageous to implement Eq. 2.2.9 in regions of uniformity and Eq. 2.2.10 to cross from one region of a certain step size to another contiguous region of another step size. Thus the semiconductor is divided into a specified number of regions of uniform step sizes with discretization schemes used in the appropriate places. When three regions are used, the boundaries are located at grid points $I=N_1$ and N_2 , at the semiconductor-insulator interface $I=N_3$, at the bottom contact located at $I=1$ and at the top contact at $I=N_4$.

Discretizing Eq. 2.2.3 with a uniform grid

$$\frac{V_{I+1}^* + V_{I-1}^* - 2V_I^*}{h^2} = \frac{2qn_1}{K_S \epsilon_0} \left\{ \sinh \frac{V_I^*}{V_T} - \frac{N_{DOP_I}}{2n_i} \right\} \quad (2.2.11)$$

and with a nonuniform grid

$$\frac{h_{I-1} V_{I+1}^* + h_I V_{I-1}^* - (h_I + h_{I-1}) V_I^*}{(h_{I-1} + h_I) h_I h_{I-1} / 2} = \frac{2qn_1}{K_S \epsilon_0} \left\{ \sinh \frac{V_I^*}{V_T} - \frac{N_{DOP_I}}{2n_i} \right\} \quad (2.2.12)$$

In the insulator Laplace's equation is discretized with a uniform grid

$$V_{I+1}^* + V_{I-1}^* - 2V_I^* = 0 \quad (2.2.13)$$

The boundary conditions for this discrete set are $V^*(1) = V_F$ and $V^*(N4) = V_{apl} + V_F$. The first derivatives in Gauss' Law are discretized with a forward difference formula for the electric field in the insulator and a backward difference formula in the semiconductor resulting in

$$K_S \left\{ \frac{V_{N3}^* - V_{N3-1}^*}{h_{N3-1}} \right\} - K_I \left\{ \frac{V_{N3+1}^* - V_{N3}^*}{h_{N3}} \right\} = - \frac{Q_{ss}}{\epsilon_0} \quad (2.2.14)$$

If an equation in the form of 2.2.11 or 2.2.12 is written for every interior node in the semiconductor, Eq. 2.2.14 is written for the interface node and Eq. 2.2.13 for every interior node in the insulator, then a set of $(N4-3)$ equations relating $(N4-3)$ unknowns results. The

set of equations is

$$\frac{V_{I+1}^* + V_{I-1}^* - 2V_I^*}{h^2} = \frac{2qn_i}{K_s \epsilon_0} \left\{ \sinh \frac{V_I^*}{V_T} - \frac{N_{DOP I}}{2n_i} \right\} \quad (2.2.15)$$

$$(2 \leq I \leq N3-1)$$

$$\frac{h_{N1-1} V_{N1+1}^* + h_{N1} V_{N1-1}^* - (h_{N1} + h_{N2-1}) V_{N1}^*}{(h_{N1} + h_{N1-1}) h_{N1} h_{N1-1}} = \frac{2qn_i}{K_s \epsilon_0} \left\{ \sinh \frac{V_I^*}{V_T} - \frac{N_{DOP I}}{2n_i} \right\}$$

$$(I = N1)$$

$$(2.2.16)$$

$$\frac{h_{N2-1} V_{N2+1}^* + h_{N2} V_{N2-1}^* - (h_{N2} + h_{N2-1}) V_{N2}^*}{(h_{N2} + h_{N2-1}) h_{N2} h_{N2-1}} = \frac{2qn_i}{K_s \epsilon_0} \left\{ \sinh \frac{V_I^*}{V_T} - \frac{N_{DOP I}}{2n_i} \right\}$$

$$(I = N2)$$

$$(2.2.17)$$

$$K_s \epsilon_0 \left\{ \frac{V_{N3}^* - V_{N3-1}^*}{h_{N3-1}} \right\} - K_s \epsilon_0 \left\{ \frac{V_{N3+1}^* - V_{N3}^*}{h_{N3}} \right\} = Q_{SS} \quad (2.2.18)$$

$$(I = N3)$$

$$V_{I+1}^* + V_{I-1}^* - 2V_I^* = 0 \quad (2.2.19)$$

$$(N3+1 \leq I \leq N4-1)$$

Method of Solution

Due to the hyperbolic sine function of the potential in the above set of equations, it is clearly evident that one is dealing with a nonlinear set of equations. An iterative procedure, shown by Ames ⁽¹⁴⁾, is used to provide a solution. Essentially the method has two steps:

1. Linearize the equations about some guess solution.
2. Solve the resulting linear set of equations for the new values of the unknowns, which it is hoped are close to the actual solution.

The method proposed and implemented is a Newton second order method and may be described as follows. Consider a linear difference operator \underline{L} operating on the dependent variable vector \underline{u} and the resultant being a function of \underline{u}

$$\underline{L}(\underline{u}) = \underline{f}(\underline{u}) \quad (2.2.20)$$

Consider further two consecutive resultant vectors from the iteration described above, i.e. $\{\underline{u}^k, \underline{u}^{k+1}\}$,

ideally as $k \rightarrow \infty$, $\underline{u}^k \rightarrow \underline{u}_e$ the exact solution vector.

Using \underline{u}^k as the closest vector to \underline{u}_e available, then

Eq. 2.2.20 may be linearized about, and solved for, \underline{u}^{k+1}

$$\underline{L}\underline{u}^{k+1} - \underline{f}'(\underline{u}^k) \cdot \underline{u}^{k+1} = \underline{f}(\underline{u}^k) - \underline{u}^k \cdot \underline{f}'(\underline{u}^k) \quad (2.2.21)$$

with a Newton step. This may be solved for \underline{u}^{k+1} in terms of \underline{u}^k as follows

$$\{\underline{L} - \underline{I} \cdot \underline{f}'\} \cdot \underline{u}^{k+1} = \underline{f}(\underline{u}^k) - \underline{u}^k \underline{f}'(\underline{u}^k) \quad (2.2.22)$$

where the prime denotes differentiation of \underline{f} with respect to its corresponding vector component.

For the problem under consideration, the linear operation is the Laplace operator in discrete form (Δ^2) and the forcing function is the hyperbolic sine,

$$\Delta^2 v^* = \frac{2qn_i}{\kappa_s \epsilon_0} \left\{ \sinh \frac{v^*}{V_T} - \frac{N_{DOP}}{2n_i} \right\} \quad (2.2.23)$$

since

$$f(v^*) = \frac{2qn_i}{\kappa_s \epsilon_0} \left\{ \sinh \frac{v^*}{V_T} - \frac{N_{DOP}}{2n_i} \right\}$$

then

$$f'(v^*) = \frac{2qn_i}{V_T \epsilon_0} \left(\cosh \frac{v^*}{V_T} \right)$$

The linearized step is, (let $C1 = 2qn_i / \kappa_s \epsilon_0$)

$$\Delta^2 v^{*k+1} \left\{ C1 \cosh \frac{v^{*k}}{V_T} \right\} v^{*k+1} = C1 \left(\sinh \frac{v^{*k}}{V_T} - \frac{N_{DOP}}{2n_i} \right) - \left(\frac{C1}{V_T} \cosh \frac{v^{*k}}{V_T} \right) v^{*k} \quad (2.2.24)$$

Considering the potential at every interior node of the device as a component of a vector which is ($N4-2$) long defined as:

$$\underline{v}^{*k} = \left\{ v_2^*, v_3^*, \dots, v_{N4-1}^* \right\}^T$$

and applying Eq. 2.2.24 to the set of Eqs. 2.2.15 through

2.2.19, one obtains a matrix equation for v^{*k+1}

$$\underline{A}(v^{*k}) \cdot v^{*k+1} = \underline{U}(v^{*k}) \quad (2.2.25)$$

It may be seen from Fig. 2.3, which shows matrix \underline{A} and the forcing vector \underline{U} , that \underline{A} is tridiagonal, as expected from the use of centered difference discretization formulas for the Laplacian.

The matrix \underline{A} can therefore be inverted with relatively little effort by efficient direct tridiagonal inversion algorithm⁽¹⁵⁾. The computational flowchart for the full algorithm is shown in Fig. 2.4.

Two questions remain to be discussed concerning the results and the nature of the algorithm:

1. Since this is an iterative process, the starting vector is of great importance for rapid convergence.
2. What is a reasonable measure of such convergence.

It has been shown⁽¹⁶⁾ that application of the Newton step to this nonlinear set of equations is stable and will produce a solution if the starting vector is close enough to the desired solution. This is very hard to insure and the full analysis of the stability of the scheme for any starting vector is very difficult⁽¹⁷⁾. In this work, success has been found in most cases by using a starting vector which assumes that the applied voltage is linearly dropped across the oxide. When the applied DC bias is varied, e.g. to generate a C-V curve, a more efficient

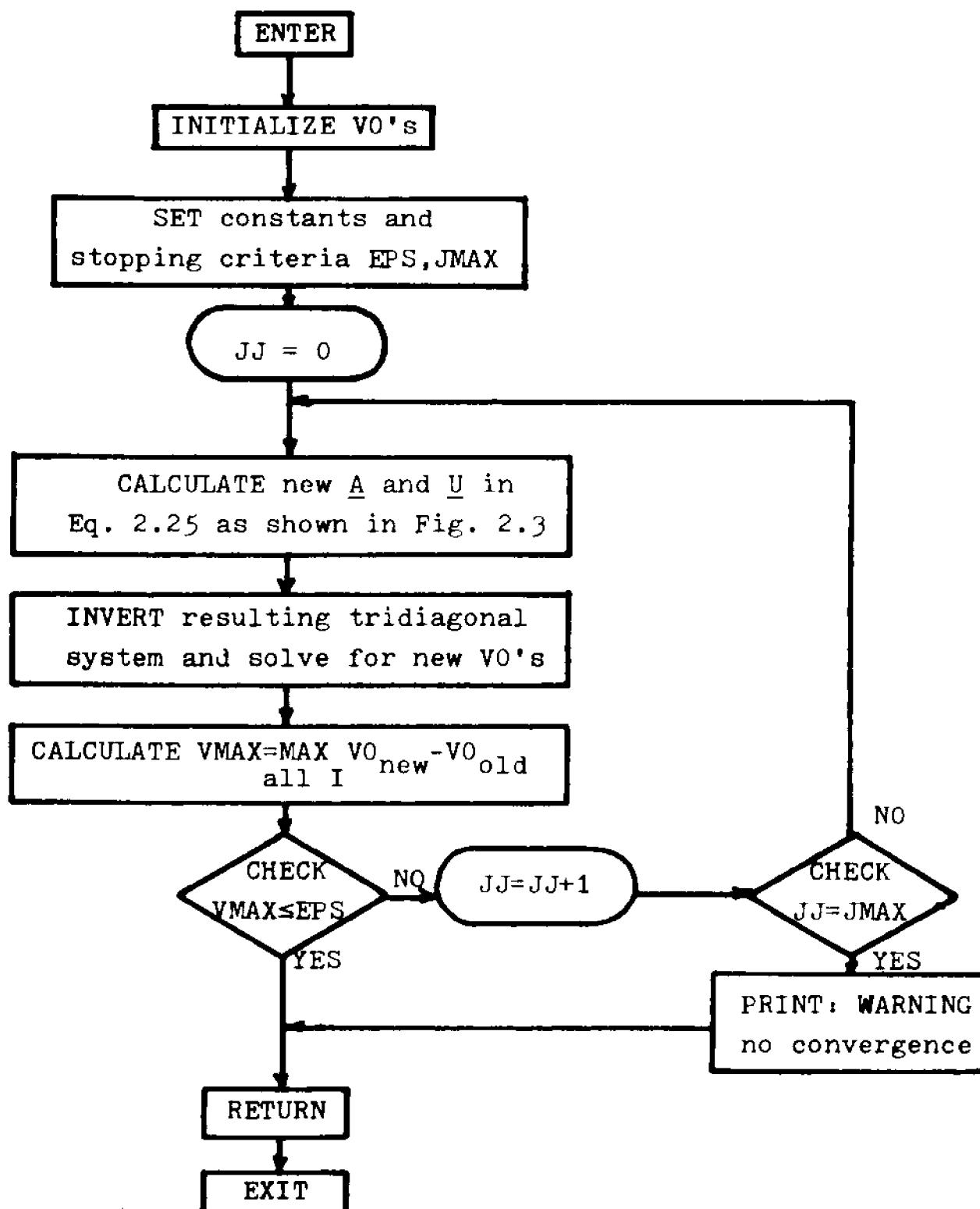


Figure 2.4 Computational Flowchart of Subroutine VDC1D
Used to Solve For the One Dimensional Potential.

method may be used. At the first starting vector use the linearly dropped voltage at one of the extreme bias points, and then sweep using the solution for the previous case as the initial guess for the next case. If small enough steps in applied bias are used, the solutions do not radically differ and an extremely good starting guess is obtained.

As the iteration progresses, a check should be made on how the last iteration solution vector compares to the exact solution. The exact solution is not available, thus alternate methods need to be used. One method is to compute some norm of $\| \underline{u}^{k+1} - \underline{u}^k \|$. As the iterative process converges, the norm becomes small, e.g. smaller than the expected order of truncation of the discretization scheme. One may then say that the last vector iterate is a very good approximation to the solution vector. The L^∞ norm⁽¹⁸⁾ is easily computed during the iteration and is used to check the last iterate. Application of this norm requires that

$$\max_I \| u_I^{k+1} - u_I^k \| \leq \epsilon \quad (2.2.26)$$

where ϵ is some prescribed value. Since in this case, the value of u is the potential in volts and it varies less than 50% in the semiconductor where Eq. 2.2.26 is checked it is not very useful to normalize the norm by the absolute value of the potential at the i^{th} point

The value of ϵ is chosen so as to be smaller than the smallest truncation error of the discretization formulas used (a typical value of ϵ used for double precision arithmetic is $\epsilon = 10^{-14}$). This is because not much effort should be expended in obtaining the solution to the difference equations to an order of accuracy greater than the truncation error since ultimately the difference solution is itself an approximation to the differential equation.

2.3 The DC Model in Two Dimensions

Structure and Equations

If the structure shown in Fig. 2.1 is extended in a second orthogonal spatial direction, one obtains the structure shown in Fig. 2.5a: the general structure of the two dimensional devices considered. As in Section 2.2, there are two equations to be solved In the semiconductor

$$\nabla^2 V(x,y) = \frac{2qn_i}{K_S \epsilon_0} \left(\sinh \left(\frac{V(x,y)}{V_T} \right) - \frac{N_{DOP}(x,y)}{2n_i} \right) \quad (2.3.1)$$

In the insulator

$$\nabla^2 V(x,y) = 0 \quad (2.3.2)$$

The same assumptions hold here as those discussed for the one dimensional case. An important difference exists, however; the Laplacian is now a partial and not an ordinary differential operator. Essentially, since no DC current is allowed to exist, the above equations, with the proper boundary conditions, completely specify the DC operation of the two dimensional structure.

Those boundary conditions are developed in a manner similar to Section 2.2 using the same assumptions. The conditions are

$$V(x,y) = V_F(x) \quad (2.3.3)$$

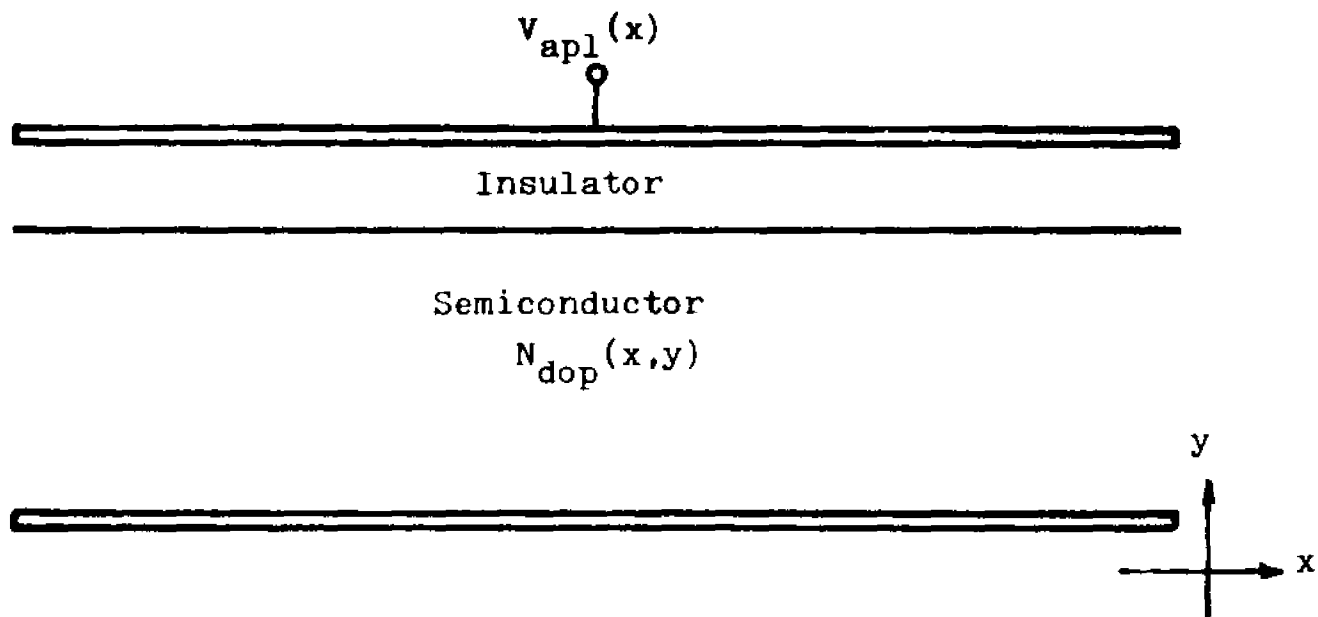


Figure 2.5a. General two dimensional structure considered.

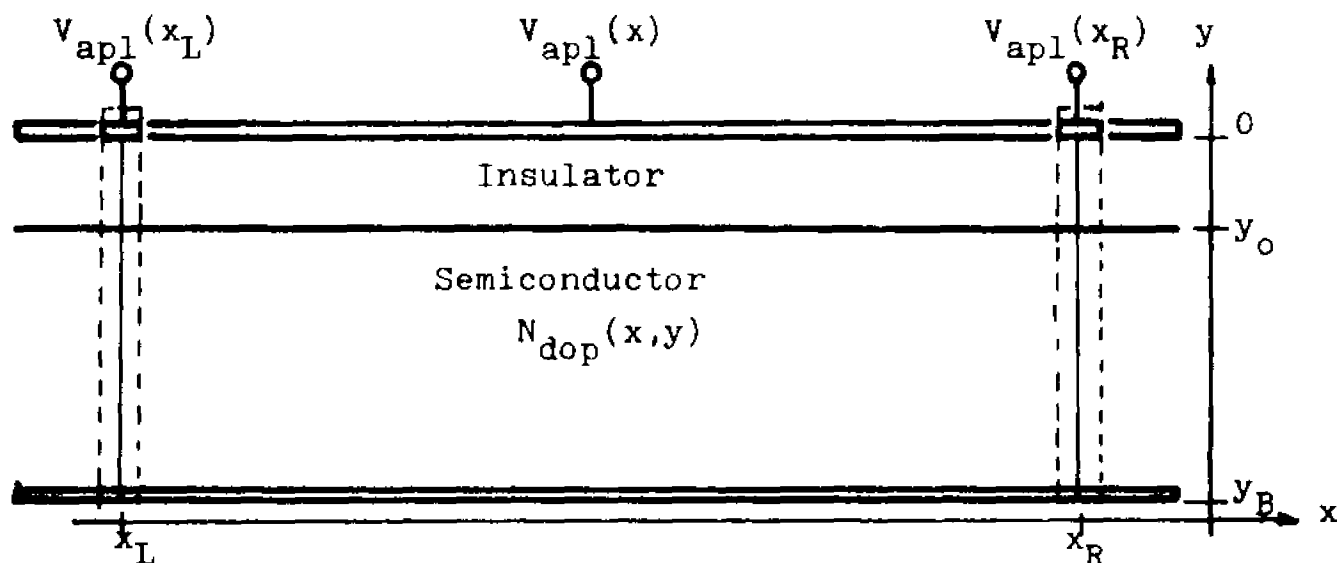


Figure 2.5b. Finite boundaries on the two dimensional device.

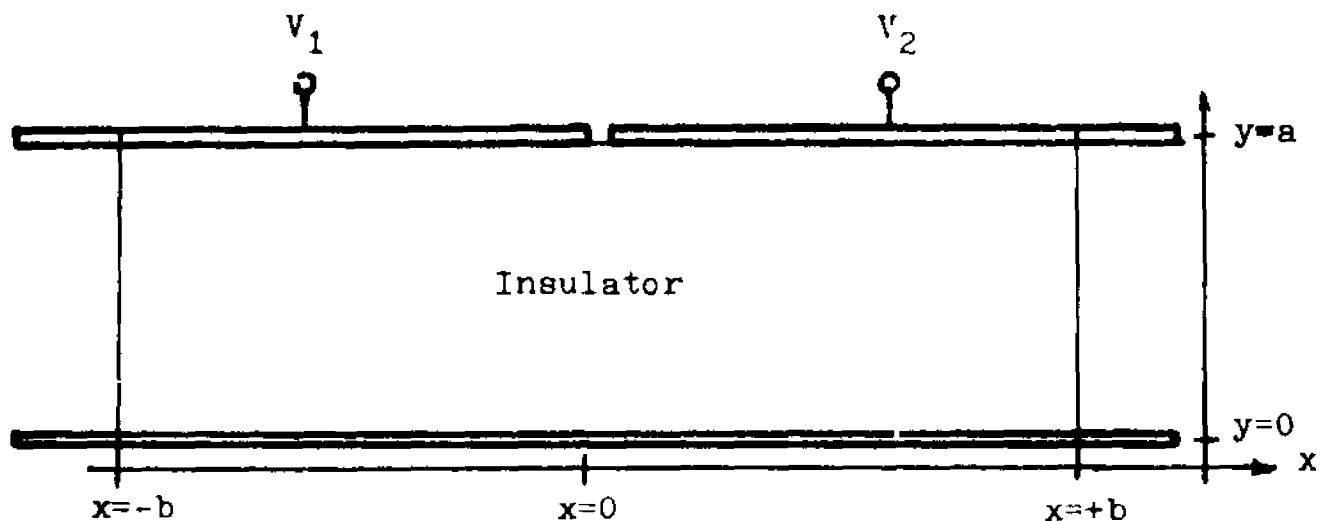


Figure 2.5c. Simple example to study boundary approximation.

$$V(x, y_{0+}) = V(x, y_{0-}) \quad (2.3.4)$$

$$-K_S \epsilon_0 \frac{\partial V(x, y_{0-})}{\partial y} + K_I \epsilon_0 \frac{\partial V(x, y_{0+})}{\partial y} = Q_{SS}(x) \quad (2.3.5)$$

and

$$V(x, 0) = V_{apl}(x) + V_F(x_L, y_B) \quad (2.3.6)$$

For a complete set of boundary conditions one must also consider the lateral boundaries. Since Eqs. 2.3.1 and 2.3.2 are elliptic p.d.e.'s the proper⁽¹⁹⁾ boundary is a closed one, either the potential (Dirichlet type b.c.) or its derivative normal to the boundary (Neumann type b.c.) or a linear combination of the variable and its derivative at the boundary (mixed type) must be specified. In this case it is assumed that the dimension of the device in the x direction is several times that in the y direction. Further, the doping past the lateral boundaries shown in Fig. 2.5b is assumed to be constant in the x direction and the potential applied for $x > x_R$ is that applied at x_R ; and for $x < x_L$ is that at x_L . A one dimensional model is used to model the boundary; the potential is found using the algorithm of Section 2.2 and this potential is used at the boundary condition at the lateral boundaries. This method converts it

into a Dirichlet type. As some justification for using this approximation, consider the linear problem shown in Fig. 2.5c. In this case, similar to a particular structure studied (see Chapter 4), one may obtain an analytic solution. For the transverse dimensions several times the vertical dimension, the magnitude of the first harmonic is at least two orders of magnitude below the fundamental justifying the approximation being used. The exact details of the potential calculation in this simple example are given in Appendix D. Thus the lateral boundaries will be selected to insure that the doping density is uniform and also that the applied potential is constant in the transverse direction. This leads to the use of a one dimensional solution as the boundary conditions for Eq. 2.3.1 and 2.3.2.

Discretization Scheme

As in one dimension, a numerical solution of the discretized equations is implemented. For this purpose the region in the x-y space over which the equations hold is discretized with a grid. Figure 2.6 shows a typical uniform grid, and Fig. 2.7 shows a typical non-uniform grid each yielding different accuracies.

The Laplacian operator is expanded by a double Taylor series about the $(i^{\text{th}}, j^{\text{th}})$ point and approximated by its first order terms. For the uniform grid the approximation is

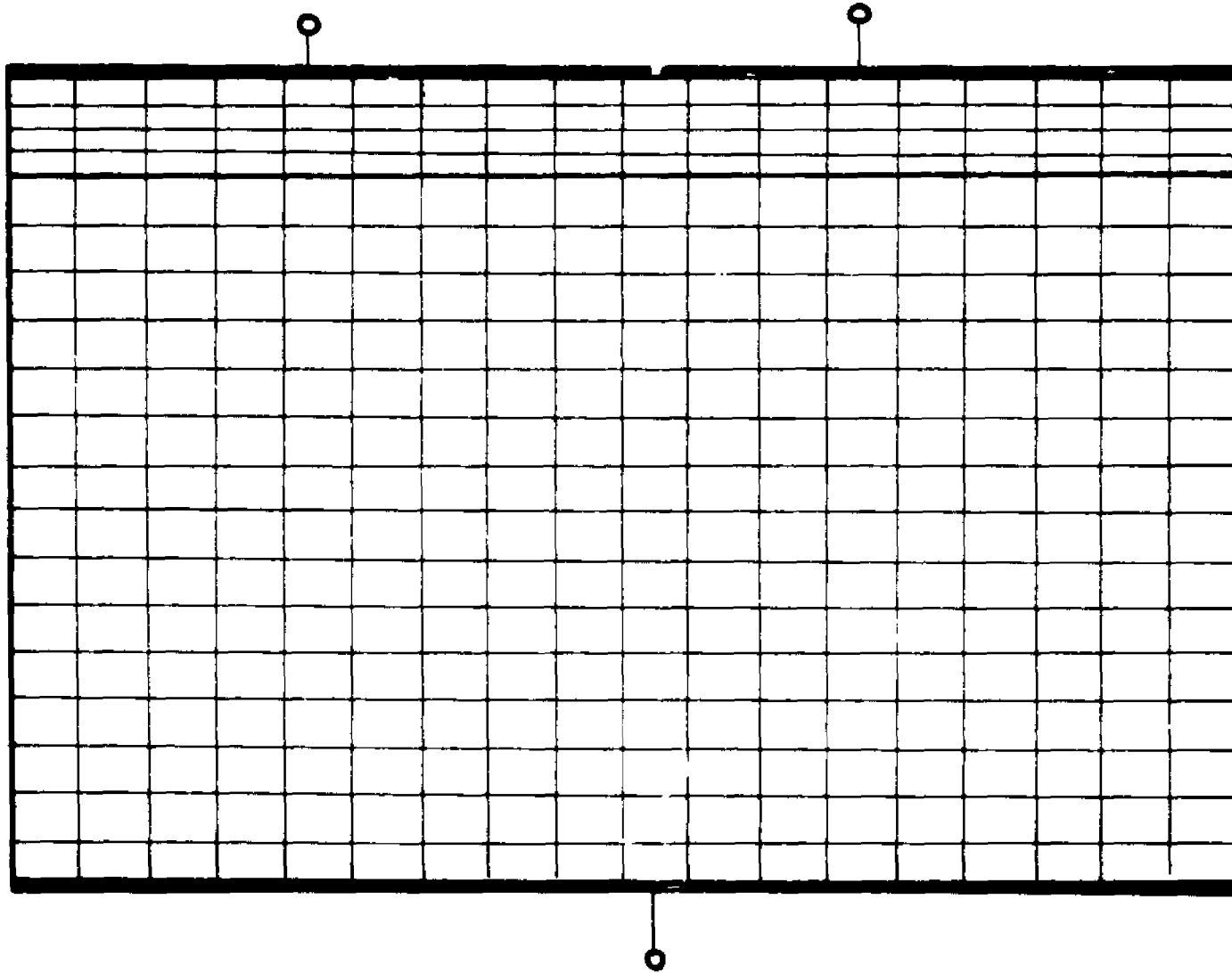


Figure 2.6. Typical uniform grid structure.

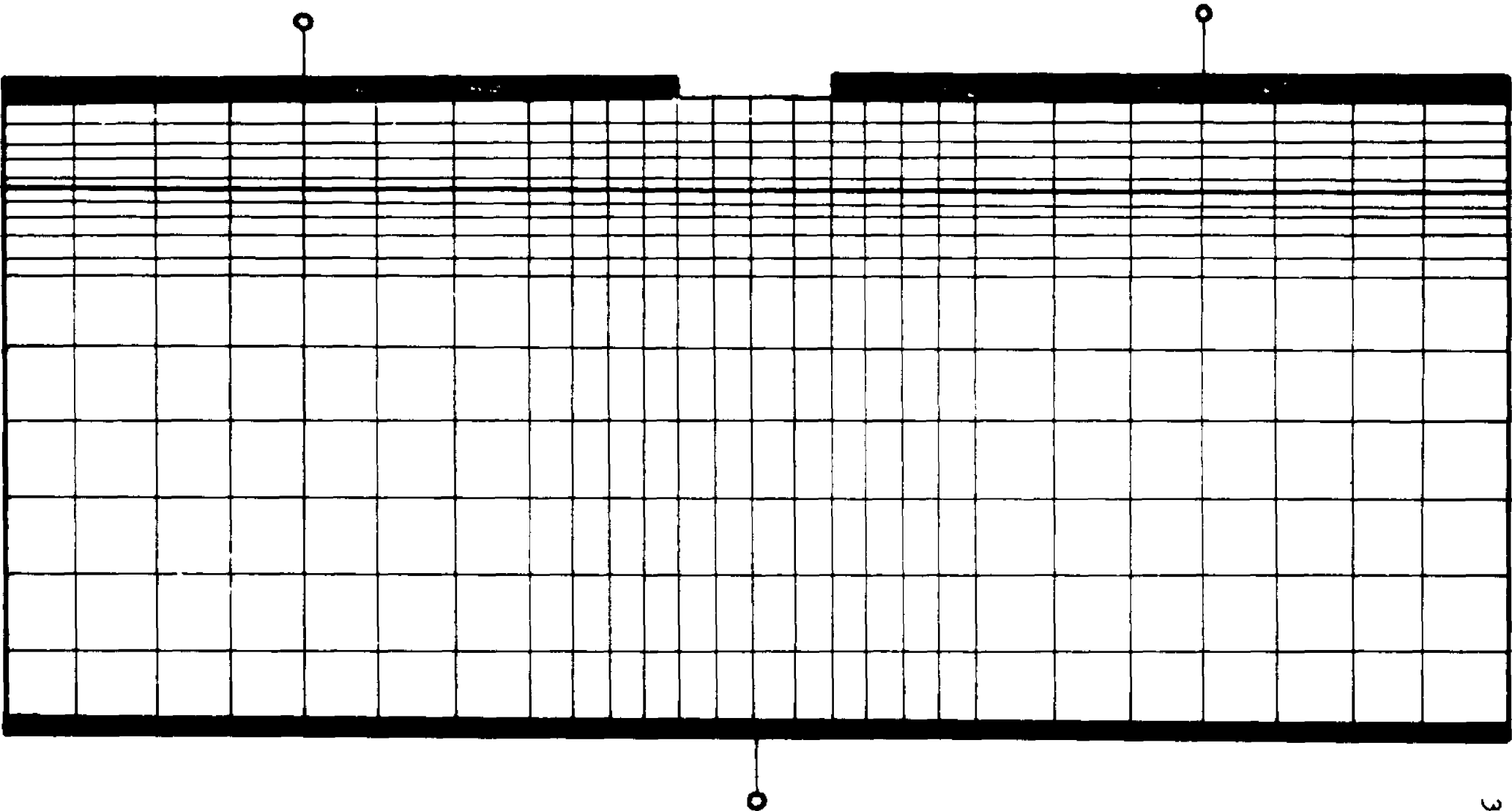


Figure 2.7. Typical nonuniform grid structure.

$$\nabla^2 u \cong \frac{u_{I,J-1}^* + u_{I,J+1}^* + u_{I-1,J}^* + u_{I+1,J}^* - 4u_{I,J}^*}{h^2} \quad (2.3.7)$$

In the case of a totally nonuniform grid where all four neighboring nodes are at different distances from the central node (see Fig. 2.8b), the Laplacian is

$$\nabla^2 u \cong \frac{\frac{u_{I,J+1}^* - u_{I,J}^*}{k_J} - \frac{u_{I,J}^* - u_{I,J-1}^*}{k_{J-1}}}{(k_J + k_{J-1})/2} + \frac{\frac{u_{I+1,J}^* - u_{I,J}^*}{h_I} - \frac{u_{I,J}^* - u_{I-1,J}^*}{h_{I-1}}}{(h_{I-1} + h_I)/2} \quad (2.3.8)$$

For the case where $h_j = h_{j-1} = k_i = k_{i-1}$, Eq. 2.3.8 reduces to Eq. 2.3.7. As the grid spacing goes to zero, the order of truncation goes to zero and the discrete analogues are self consistent with the p.d.e. (20).

No loss of generality is incurred in continuing the discussion of a solution of the equations in question assuming a uniform grid. The complexity is lessened so as to make conceptualization easier yet the principles involved still apply to the nonuniform case.

Discretizing Eqs. 2.3.1 and 2.3.2 one obtains in the semiconductor

$$V_{I+1,J} + V_{I-1,J} + V_{I,J+1} + V_{I,J-1} - 4V_{I,J} = \frac{2qn_i h^2}{K_s \epsilon_0} \left(\sinh \frac{V_{I,J}}{V_T} - \frac{N_{DOP I,J}}{2n_i} \right) \quad (2.3.9)$$

and in the insulator

$$V_{I+1,J} + V_{I-1,J} + V_{I,J+1} + V_{I,J-1} - 4V_{I,J} = 0 \quad (2.3.10)$$

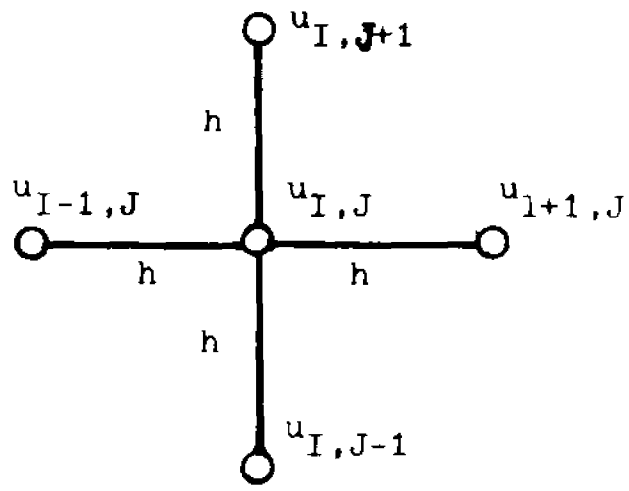


Figure 2.8a. Five point uniform discretization grid employed in discretizing the Laplacian.

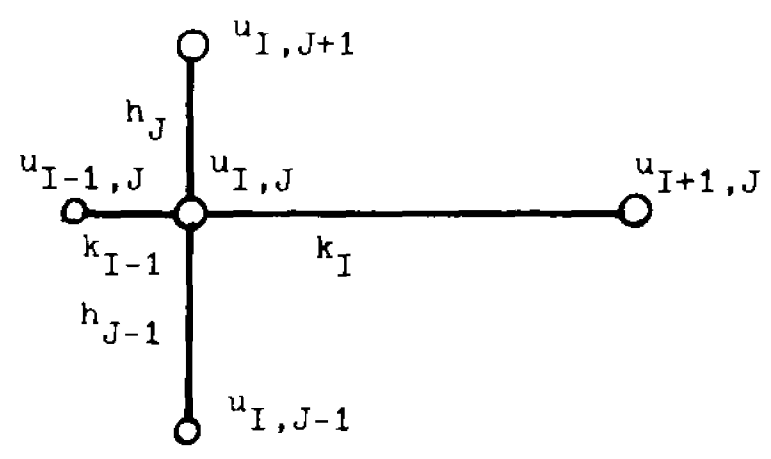


Figure 2.8b. Nonuniform five point discretization grid.

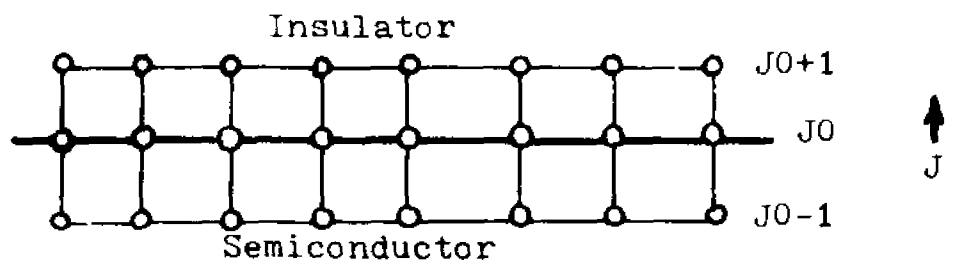


Figure 2.8c. Discretization grid at the insulator semiconductor employed in discretizing Gauss' Law.

Labelling the grid points at the insulator-semiconductor interface $\{J=J_0, VI\}$ and discretizing Gauss' Law yields

$$-K_S \epsilon_0 \left(\frac{V_{I,J_0+1} - V_{I,J_0}}{h_{J_0}} \right) + K_I \epsilon_0 \left(\frac{V_{I,J_0} - V_{I,J_0-1}}{h_{J_0-1}} \right) = Q_{SS_I} \quad (2.3.11)$$

This is a natural point where a change in grid step size in the y direction may be made without too much complexity or extra calculation. The rest of the boundary conditions are used in Eqs. 2.3.9 and 2.3.10 in the appropriate places. One then obtains a set of $(M-2) \times (N-2)$ linearly independent algebraic equations for the discretized potential in the interior nodes of the grid. (M and N are the number of grid points in the x and y directions respectively). The set may be expressed as follows

$$\frac{V_{I+1,J} + V_{I,J-1} + V_{I+1,J} + V_{I-1,J} - 4V_{I,J}}{h_{SEM}^2} = \frac{2qn_i}{K_S \epsilon_0} \left(\sinh \frac{V_{I,J}}{V_T} - \frac{N_{DOP_{I,J}}}{2n_i} \right) \quad (2.3.12)$$

$$(2 \leq I \leq M-1, 2 \leq J \leq J_0-1)$$

$$-K_S \epsilon_0 \left(\frac{V_{I,J_0+1} - V_{I,J_0}}{h_{SEM}} \right) + K_S \epsilon_0 \left(\frac{V_{I,J_0} - V_{I,J_0-1}}{h_{INS}} \right) = Q_{SS_I} \quad (2.3.13)$$

$$(2 \leq I \leq M-1, J = J_0)$$

$$V_{I,J+1} + V_{I,J} + V_{I+1,J} + V_{I-1,J} - 4V_{I,J} = 0 \quad (2.3.14)$$

$$(2 \leq I \leq M-1, J_0+1 \leq J \leq N-1)$$

Method of Solution

Writing the above set of algebraic equations in matrix form $\underline{AV} = \underline{g}(V)$ with the potential at every interior node as the components of a solution vector \underline{V} , two things are evident:

1. The set of equations is nonlinear due to the presence of the hyperbolic sine of the potential term in $\underline{g}(V)$.

2. The matrix \underline{A} is banded, with diagonals, two of them $M-2$ away from the main diagonal (see Fig. 2.9)

There are at present several methods which have been successfully applied to solving the matrix system shown in Fig. 2.9⁽²¹⁾. Most make use of a linearization of the equation about some guess, called the outer iteration, and some efficient matrix solver for the linearized equation, called the inner iteration. Due to the large bandwidth of the \underline{A} matrix involved, usually an iterative inner scheme iteration is used such as SOR or ADI (see for example⁽²²⁾). The question which most often arises in this case is how much computational effort should be spent on calculating the next guess iteratively if it is only to be a next guess and need not be very accurate. On the other hand it is clear that a direct matrix inverter is not very efficient, in this case due to the large bandwidth of \underline{A} . Therefore an iterative method is more advantageous. To try to minimize the number of calculations an iterative method which iterates on

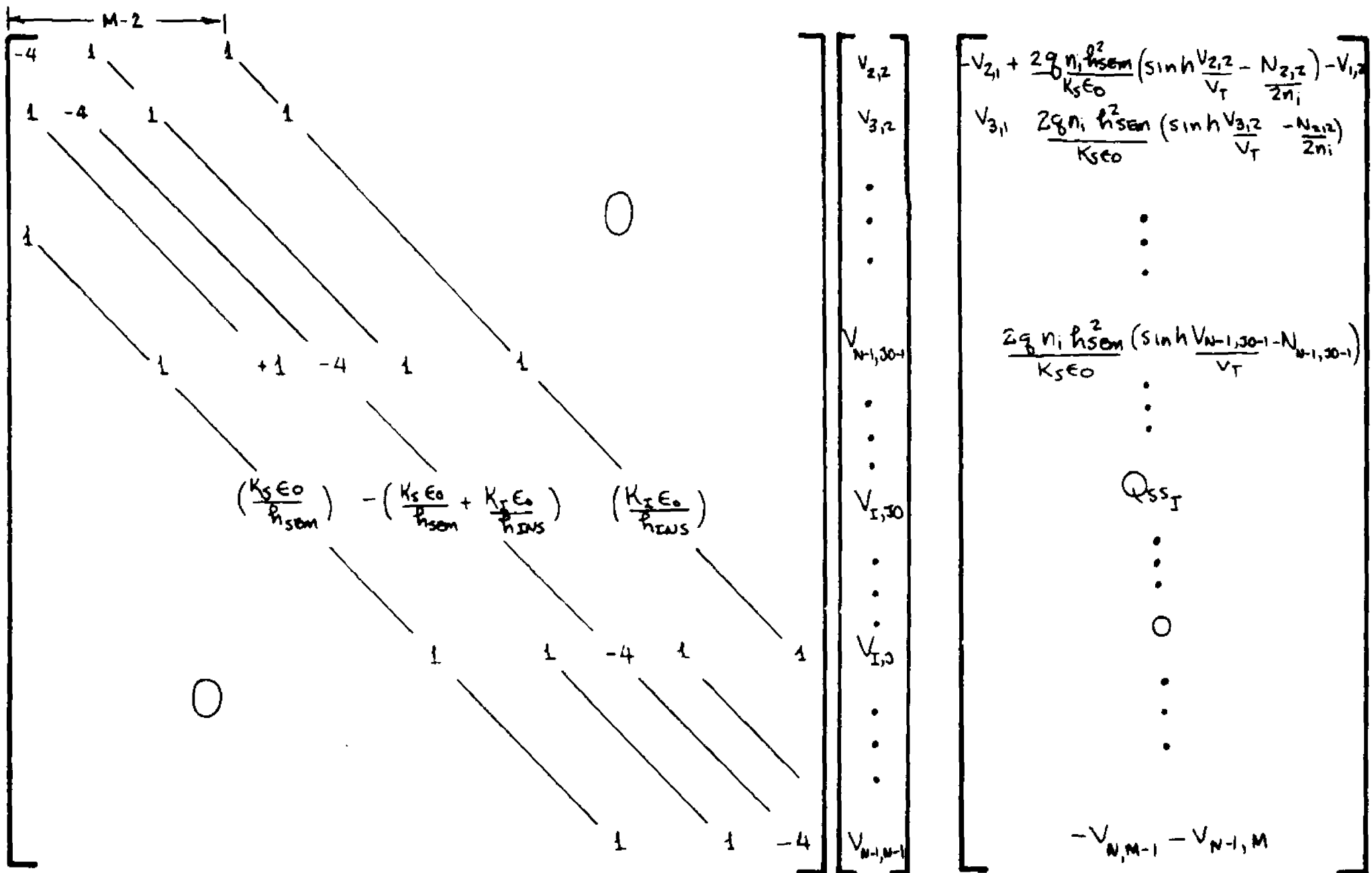


Figure 2.9. Matrix system for two dimensional discretized potential.

both problems at once is developed.

Greenspan⁽²³⁾ has discussed the application of a method he calls nonlinear overrelaxation as applied to elliptic p.d.e.'s, particularly nonlinear ones. Ortega and Rheinboldt more aptly name this method SOR-Newton⁽²⁴⁾. It is properly termed a SOR-Newton since there is an element of overrelaxation successively applied with a Newton linearization of the nonlinearity.

A preliminary review of Newton's method⁽²⁵⁾ is helpful in understanding the SOR-Newton method. Consider the following general nonlinear algebraic equation:
 $f(x)=0$. To find a solution, use the iterative scheme

$$x^{n+1} = x^n - w \frac{f(x^n)}{f'(x^n)} \quad (2.3.15)$$

which is a variation on the usual Newton method in that a relaxation parameter is employed to accelerate convergence to a solution. Figure 2.10 shows a typical iteration with $w=1$ and $w > 1$. The process is as follows:

1. From the point $\{ f(x^n), x^n \}$ draw the slope $f'(x^n)$
2. Where the slope intersects the x axis, call this the next iterate x^{n+1} ,
3. Repeat 1 and 2 until one is within a δ of the solution.

Using this method with $0 < w \leq 1$ one converges to the solution without passing it if the function is concave in the interval $\{x_0, x'\}$ where x_0 is the initial guess

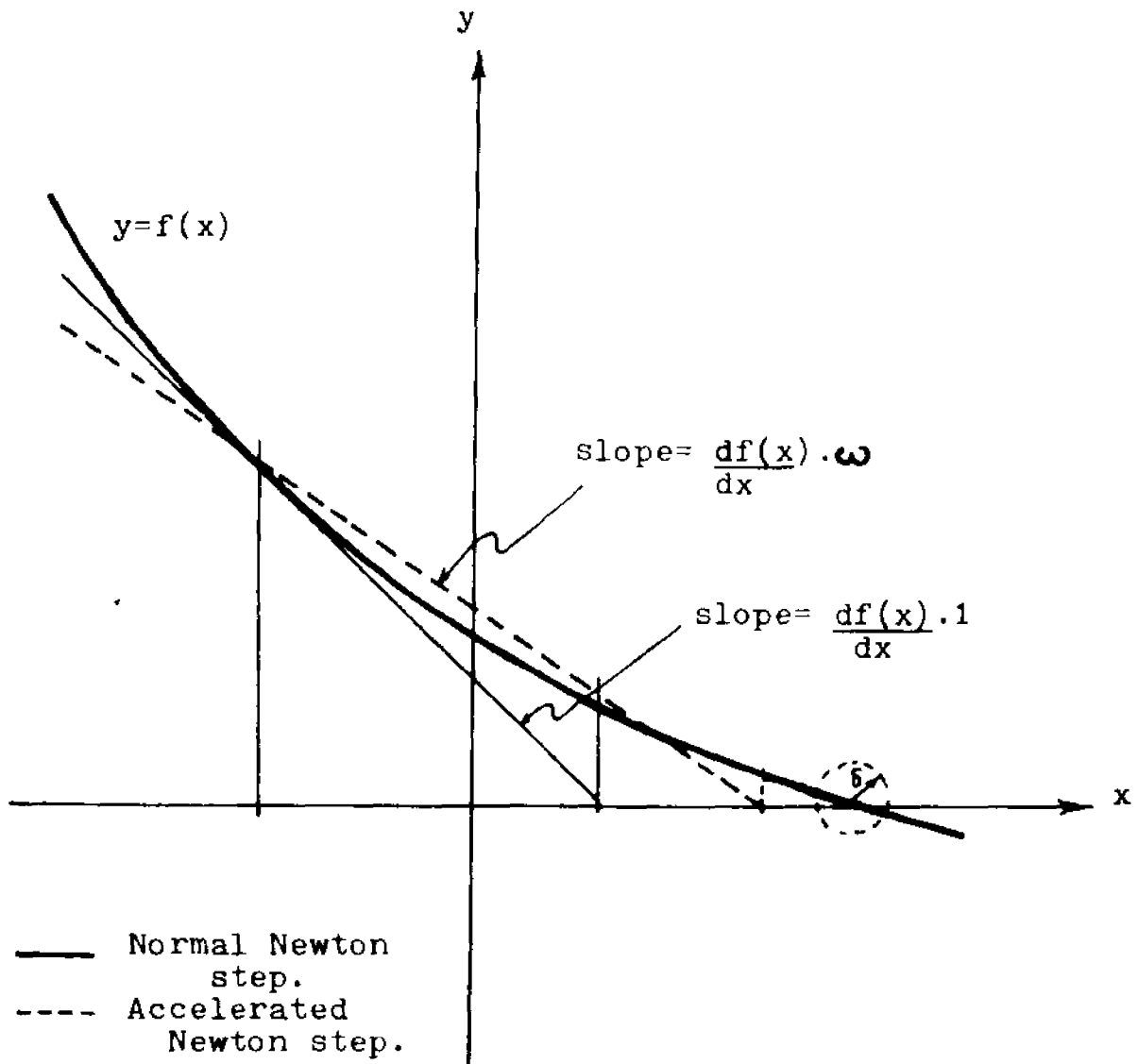


Figure 2.10. Accelerated Newton's method.

and x' is the solution. The danger of using an accelerating factor greater than 1 is that the solution may be overshoot.

Consider now a system of nonlinear algebraic equations $f(x)=0$ and apply the following iterative scheme to it

$$\begin{aligned}
 x_1^{n+1} &= x_1^n - w_1 \frac{f_1(x_1^n, x_2^n, x_3^n, \dots, x_N^n)}{\frac{\partial}{\partial x_1} f_1(x_1^n, x_2^n, x_3^n, \dots, x_N^n)} \\
 x_2^{n+1} &= x_2^n - w_2 \frac{f_2(x_1^{n+1}, x_2^n, x_3^n, \dots, x_N^n)}{\frac{\partial}{\partial x_2} f_2(x_1^{n+1}, x_2^n, x_3^n, \dots, x_N^n)} \\
 &\vdots \\
 x_N^{n+1} &= x_N^n - w_3 \frac{f_N(x_1^{n+1}, x_2^{n+1}, x_3^{n+1}, \dots, x_N^n)}{\frac{\partial}{\partial x_N} f_N(x_1^{n+1}, x_2^{n+1}, x_3^{n+1}, \dots, x_N^n)}
 \end{aligned}
 \tag{2.3.16}$$

As an example consider two equations in this system; $f_1(x_1, x_2)$ and $f_2(x_1, x_2)$. Applying Eqs. 2.3.16 yields the scheme

$$x_1^{n+1} = x_1^n - w_1 \frac{f_1(x_1^n, x_2^n)}{\frac{\partial f_1}{\partial x_1}(x_1^n, x_2^n)}
 \tag{2.3.17}$$

$$x_2^{n+1} = x_2^n - w_2 \frac{f_2(x_1^{n+1}, x_2^n)}{\frac{\partial f_2}{\partial x_2}(x_1^{n+1}, x_2^n)}$$

applied in the following algorithm:

1. Start at $\{x_1^n, x_2^n\}$ and holding x_2 constant, perform a Newton step on $f_1(x_1, x_2^n)$ as shown in Fig. 2.11 (for $w=1$). One ends up at $\{x_1^{n+1}, x_2^n\}$.
2. From $\{x_1^{n+1}, x_2^n\}$ and holding x_1 constant, perform a Newton step on $f_2(x_1, x_2)$ as shown in Fig. 2.12 (for $w=1$). One ends up at $\{x_1^{n+1}, x_2^{n+1}\}$.
3. Repeat 1 and 2 until the last iterate values are as close to the solution as desired.

Hopefully after one iteration, steps 1 and 2, one is closer to the final solution $\{x_1', x_2'\}$, i.e. the error $\epsilon^{n+1} < \epsilon^n$, where $\epsilon^n = \|\underline{x}^n - \underline{x}'\|$.

There are several noticeable points which should be brought out about the proposed algorithm:

1. If the set of equations (such as the ones in the example) are linear, then the surfaces $Z=f_i(\underline{x}^n)$ are planes and Newton's process is stable for any initial vector. This method becomes SOR for $1 < w \leq 2$.
2. Each equation in the iteration scheme of Eq. 2.3.16 may have a different relaxation parameter for

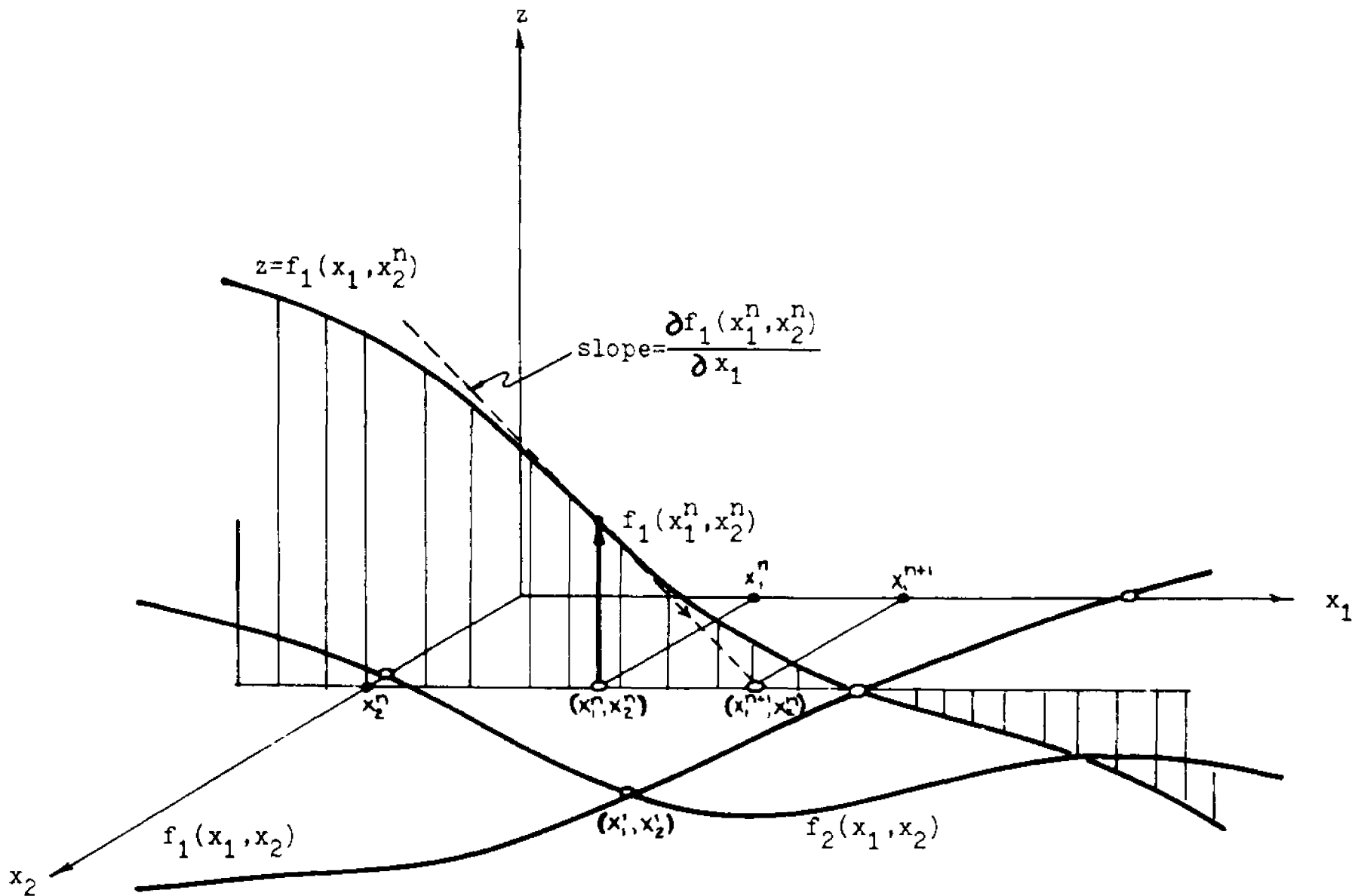


Figure 2.11. Graphical example of taking the first part of a SOR-Newton step.

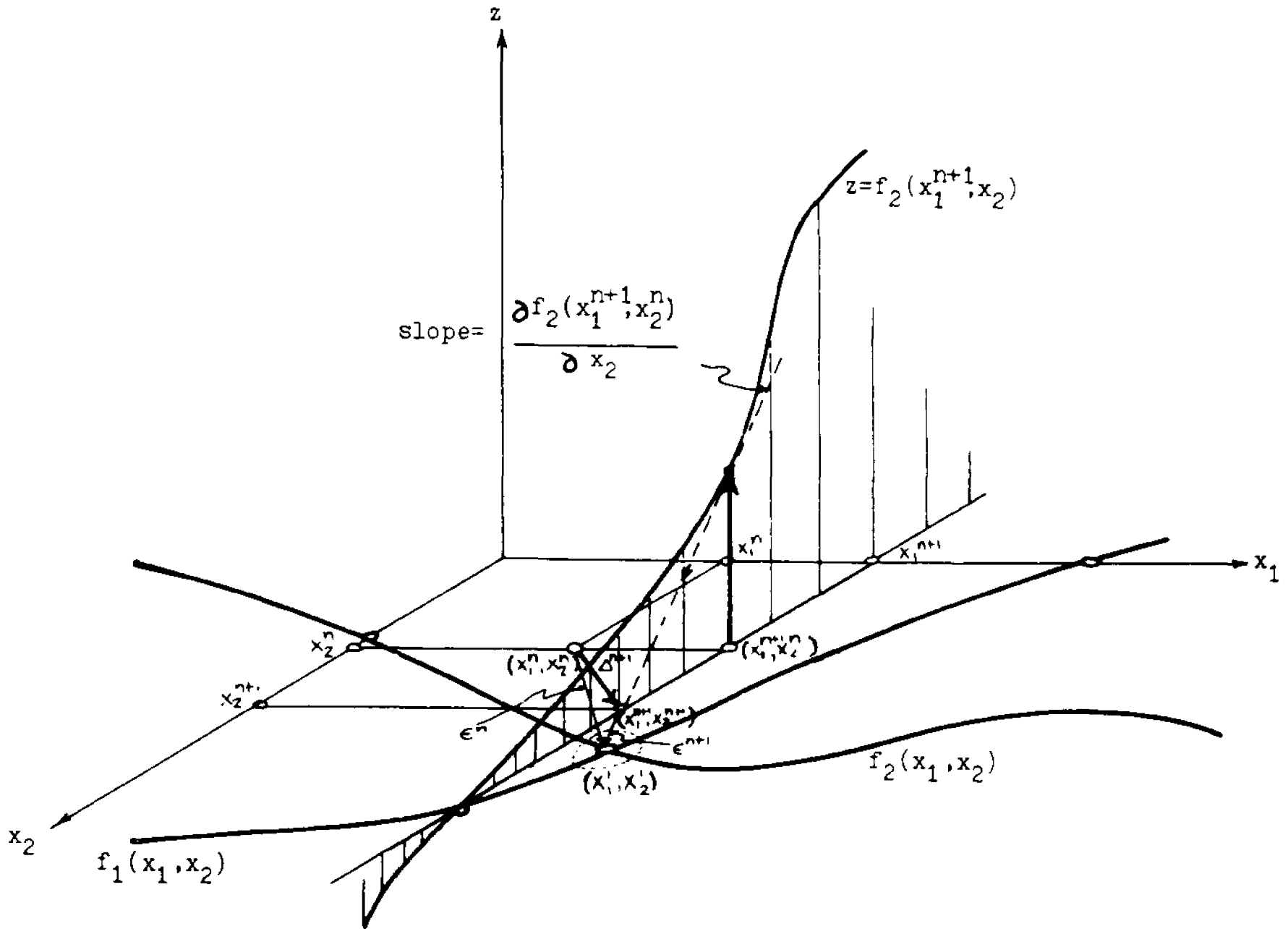


Figure 2.12. Completing the SOR-Newton step.

optimum convergence. This is exposed in depth when the p.d.e. in question is being considered (see later in this Section and Appendix B).

In general, for $f(x)$ nonlinear, there are regions in x space where for an initial vector x_0 , the process will diverge and others where it will converge to the desired solution.

3. Since a solution to the system of equations is usually not known beforehand, applying an error criteria $\epsilon^{n+1} < \epsilon^n$ is not possible. One may look at another criteria imposed on the past and present iterates and stop the iteration when $\Delta^{n+1} < \epsilon_0$, where $\Delta^{n+1} \triangleq \|x^{n+1} - x^n\|$ and ϵ_0 some specified small number. Care must be exercised in applying this criteria since the distance between vector iterates may turn out to be very small, yet one may be far away from a solution.

For a linear system, it is known (see Forsythe and Wasow⁽²⁶⁾) that for a discretization of a linear p.d.e. which is consistent with the p.d.e., stability of the discrete process implies convergence and vice versa. For a nonlinear system, this is not necessarily the case. The full stability analysis of this method applied to nonlinear equations is a very difficult problem and has not been undertaken to date⁽²⁷⁾.

Implementation of the Method

The discrete equations for the potential involving the Laplacian (Eqs. 2.3.11 and 2.3.12) may be rewritten such that they are of the form $f(\underline{v})=0$. The first $(M-2) \times (J_0-2)$ equations being nonlinear

$$\Delta^2 v_{I,J} - \frac{2qn_i h^2}{\kappa_s \epsilon_0} \left(\sinh \frac{v_{I,J}}{V_T} - \frac{N_{DOP_{I,J}}}{2n_i} \right) = 0 \quad (2.3.18)$$

$$(2 \leq I \leq M-1, 1 \leq J \leq J_0-1)$$

where (Δ^2) is used to represent the discrete Laplacian operator. Equation 2.3.13 is used to step across from the semiconductor to the insulator by solving for the interface points explicitly with the last available iterate values. Then the method is applied to Eq. 2.3.12 in which case it is simply successive relaxation. In the semiconductor, $\frac{\partial f_{I,J}}{\partial v_{I,J}}(v)$ is

$$\frac{\partial f_{I,J}}{\partial v_{I,J}}(v) = -4 \frac{2qn_i h^2}{\kappa_s \epsilon_0 V_T} \left(\cosh \frac{v_{I,J}}{V_T} \right) \quad (2.3.19)$$

and in the insulator

$$\frac{\partial f_{I,J}(v)}{\partial v_{I,J}} = -4 \quad (2.3.20)$$

Thus the method applied to the problem becomes

$$v_{I,J}^{n+1} = v_{I,J}^n - w_s \left\{ \frac{\Delta^2 v_{I,J}^n - \frac{2qn_i h^2}{\kappa_s \epsilon_0} \left(\sinh \frac{v_{I,J}^n}{V_T} - \frac{N_{DOP_{I,J}}}{2n_i} \right)}{-4 - \frac{2qn_i h^2}{\kappa_s \epsilon_0 V_T} \left(\cosh \frac{v_{I,J}^n}{V_T} \right)} \right\} \quad (2.3.21)$$

$$(2 \leq I \leq M-1, 1 \leq J \leq J_0-1)$$

$$v_{I,J}^{n+1} = \left(\frac{1}{K_S + K_I} \right) (K_S v_{I,J-1}^{n+1} + K_I v_{I,J+1}^n) - Q_{SS_I} \quad (2.3.22)$$

$$v_{I,J}^{n+1} = v_{I,J}^n - w_{IN} \left\{ \frac{\Delta^2 v_{I,J}^n}{-4} \right\} \quad (2 \leq I \leq M-1, J+1 \leq I \leq N-1) \quad (2.3.23)$$

with the new iterate immediately replacing the old one as it becomes available. The relaxation parameters are w_S for the semiconductor region and w_{IN} for the insulator region.

Several questions which must be answered to successfully implement this method are:

1. What starting vector shall be used?
2. What relaxation parameters are required?
3. What stopping criteria shall be exercised?

The first question is an important one for convergence of the scheme. Barring a full stability analysis of the scheme, it is mostly a matter of experience: whichever starting vector seems to work is the one to be used.

In the problems undertaken, a suitable scheme for generation of the starting vector is as follows:

1. Divide the two dimensional region into a set of strips parallel to the y direction, each strip containing a grid line in the y direction (see Fig. 2.13).
2. Solve for the potential at each grid point with

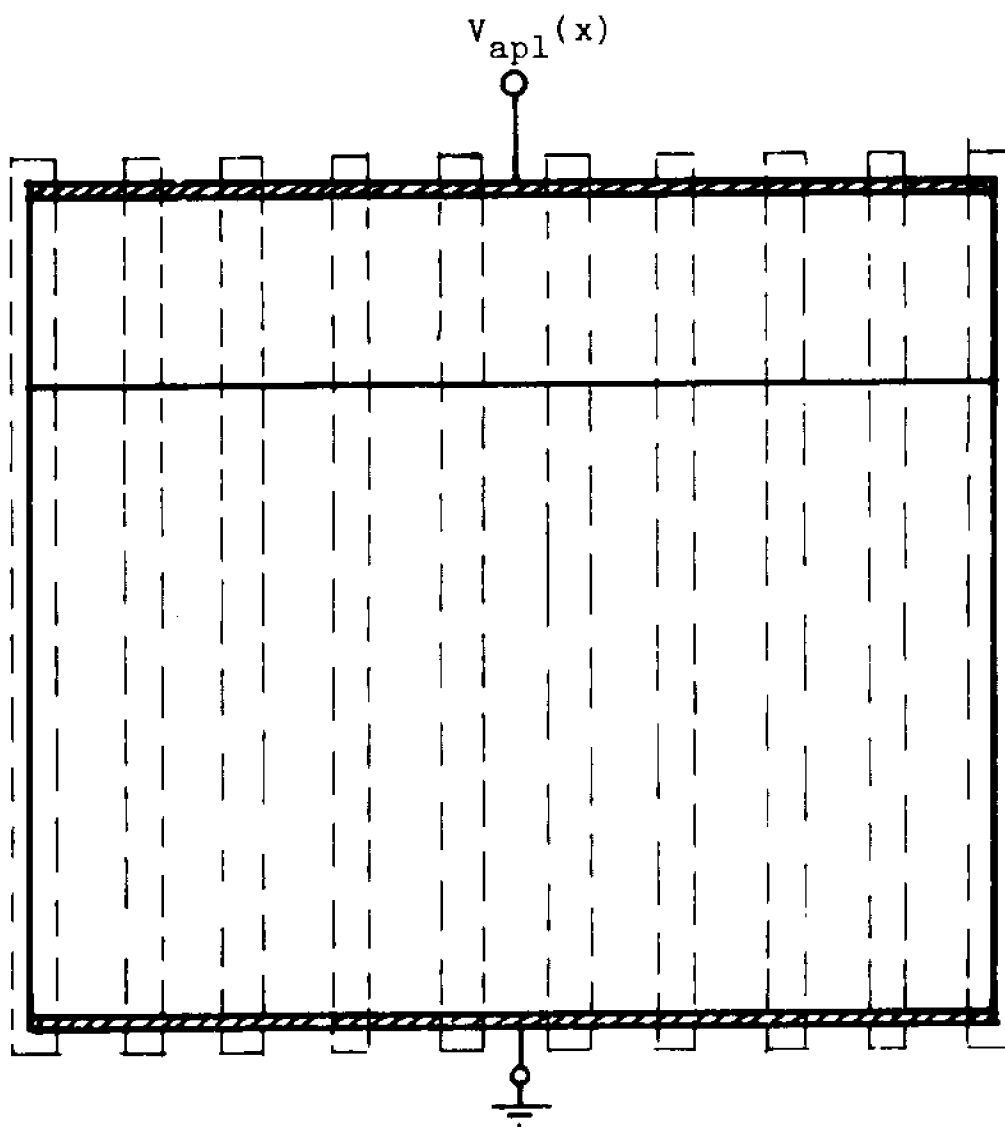


Figure 2.13. Decomposition of the two dimensional structure into one dimensional strips for the generation of an initial guess.

the one dimensional method (see Section 2.2) considering the strip to be a one dimensional device.

3. Load in, strip by strip, the potential found in 2 as the starting value for the two dimensional iteration.

On the matter of the relaxation parameter there are several points which must be considered:

1. for $0 < w \leq 1$ the method is called underrelaxation and is found to be stable; however, a solution is reached slowly.
2. for $1 < w \leq 2$ the method is called overrelaxation which may cause divergence. However, there may be a w in this range which will accelerate convergence optimally.

In Appendix B, an analysis is made of this situation and it is found that a w should be picked for each iterate as the iteration progresses. This, though assuring optimal convergence and stability, is very cumbersome to implement and quite costly in computation time. In practice it has been found that using a relaxation parameter of the linear system (i.e., as if the semiconductor were a perfect insulator), rather than searching for the optimum w results in good convergence. The practical parameter used is that given by Young⁽²⁸⁾ for overrelaxation applied to the Laplacian in a rectangle

$$w_{\text{opt}} = \frac{2}{1 + \sqrt{1 - \lambda_{\text{opt}}^2}} \quad (2.3.24)$$

where

$$\lambda_{\text{opt}}^2 = \cos\left(\frac{\pi}{R}\right) + \cos\left(\frac{\pi}{S}\right) \quad (2.3.25)$$

and R and S are the number of interior grid points in the two spatial dimensions.

Greenspan⁽²⁹⁾ suggests that before the start of each problem an optimum relaxation parameter may be found experimentally by trying a specified number of iterations with different w 's and observing for which w the error criteria is most closely satisfied. This was tried for the three terminal varactor structure where $V_{\text{apl}}(x) = V_1$ for $x_L \leq x \leq 0$ and $V_{\text{apl}}(x) = V_2$ for $0 \leq x \leq x_R$. The results are shown in Fig. 2.14, where the error criteria used is the sum of the absolute value of the change from V^n to V^{n+1} . The trajectory for each value of w as the iteration number increases as shown in Fig. 2.15. One notices in Fig. 2.14 that the w for the linear system is less than the optimum w , and that for values of $w \geq w_{\text{opt}}$ in this case, there is divergence in many cases. Divergence for $w = 2$ is clearly seen in Fig. 2.15 and for $w = 1.9$ some oscillation is observed. In general, the relaxation parameter given in Eq. 2.3.25 shall be used

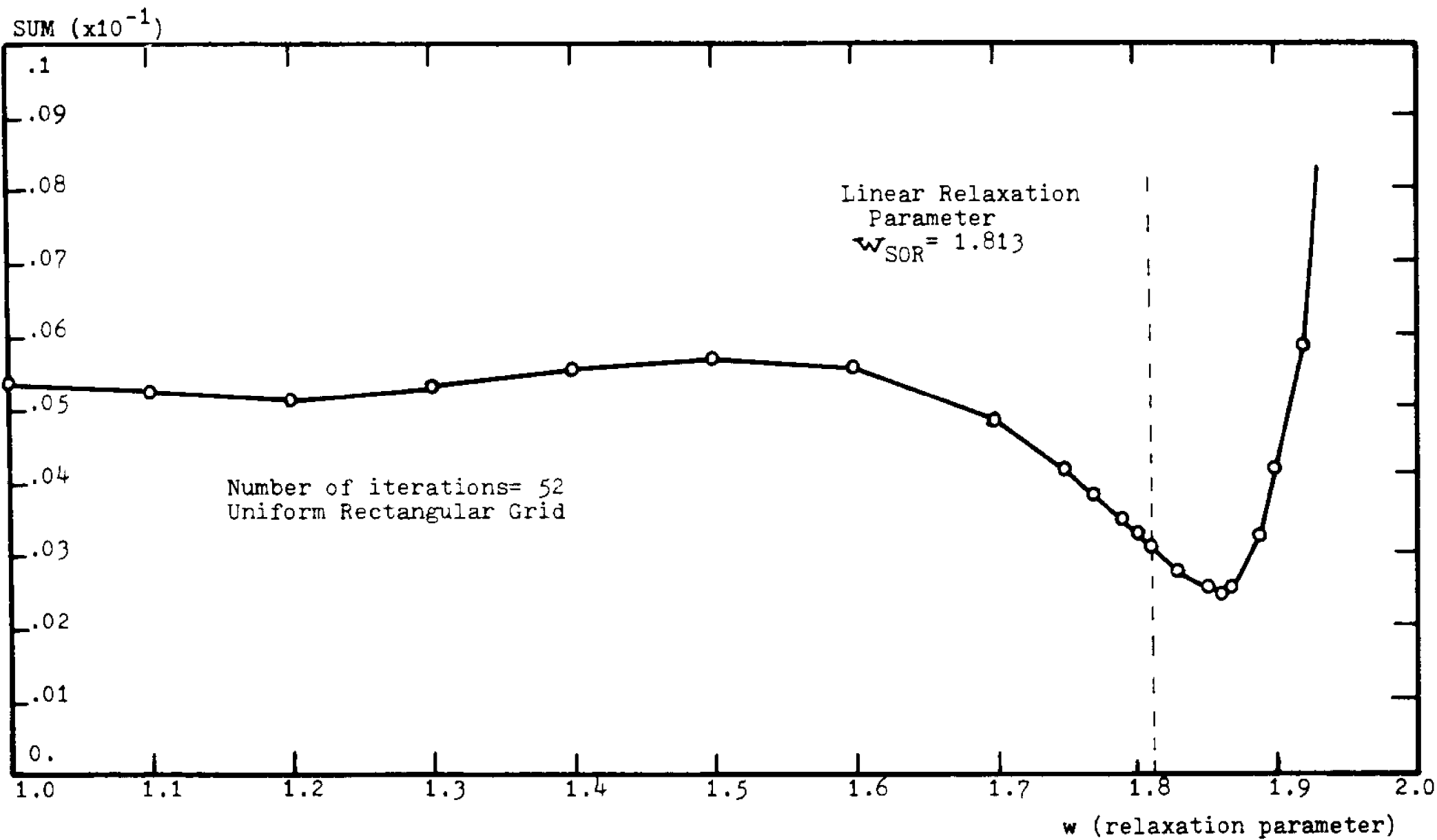


Figure 2.14. Error criteria versus relaxation parameter obtained experimentally for the three terminal varactor structure.

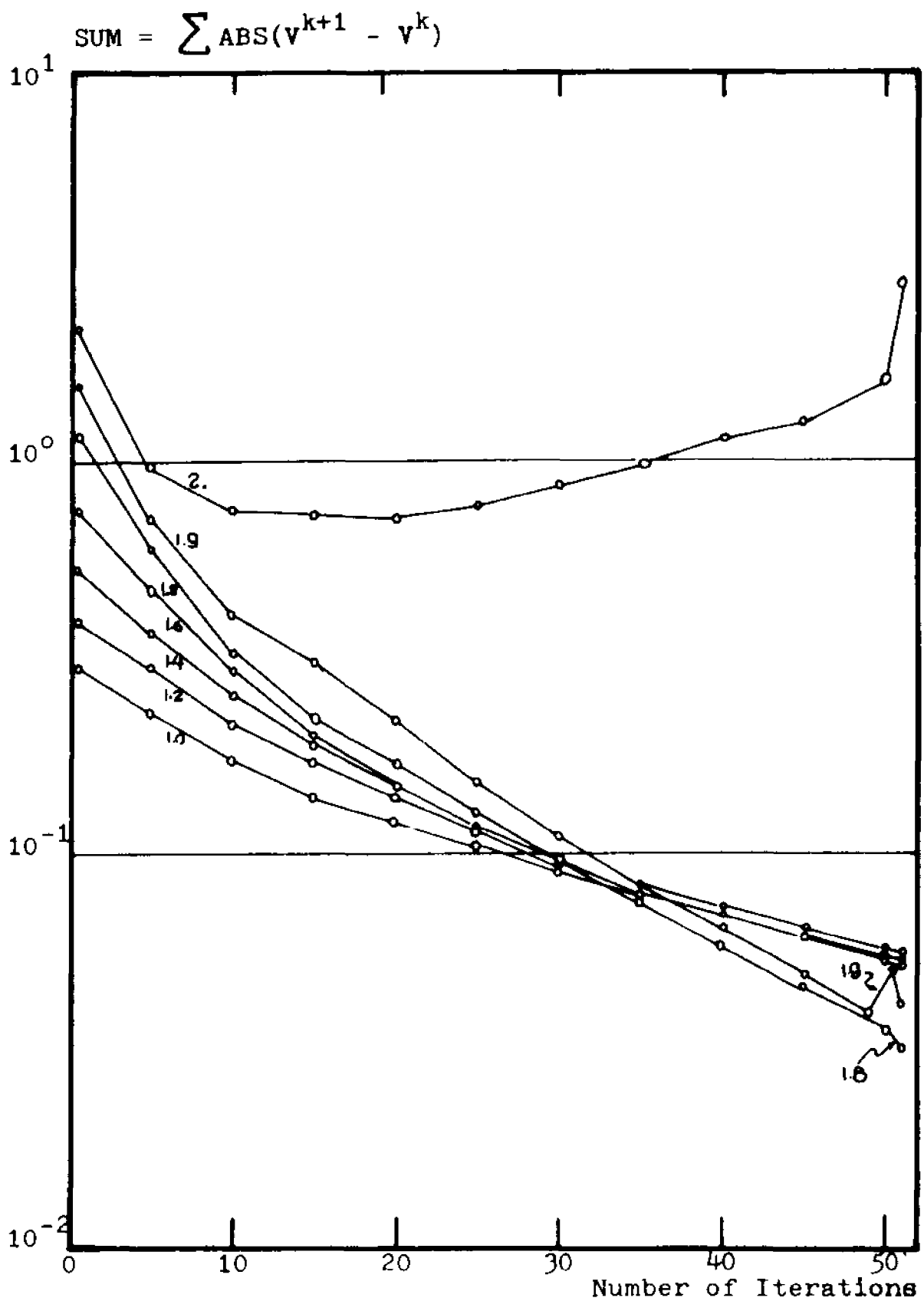


Figure 2.15. Error criteria versus number of iterations for varying relaxation parameter.

in the semiconductor region since it meets both the stability and ease of computation requirements.

A parameter which may be monitored is $\Delta^{n+1} = \|v^{n+1} - v^n\|$. Although there are several norms which may be used, it was chosen to implement the norm defined as

$$S^{n+1} = \sum_{I,J} \text{ABS}(V_{I,J}^{n+1} - V_{I,J}^n) \quad (2.3.26)$$

This norm was used in the investigation of the optimum relaxation parameter and in general has been found to provide successful results.

Finally, the algorithm is organized into a MAIN program which sets up the necessary constants and spatial variables (e.g. background doping grid densities, etc.) which calls on two subroutines:

1. VLC1D, the one dimensional algorithm to initialize the solution,
2. VDC2D, the implementation of the SOR-Newton discussed in this Section to the MIS structure in question.

The MAIN program flow chart is shown in Fig. 2.16 and that of VDC2D is shown in Fig. 2.17.

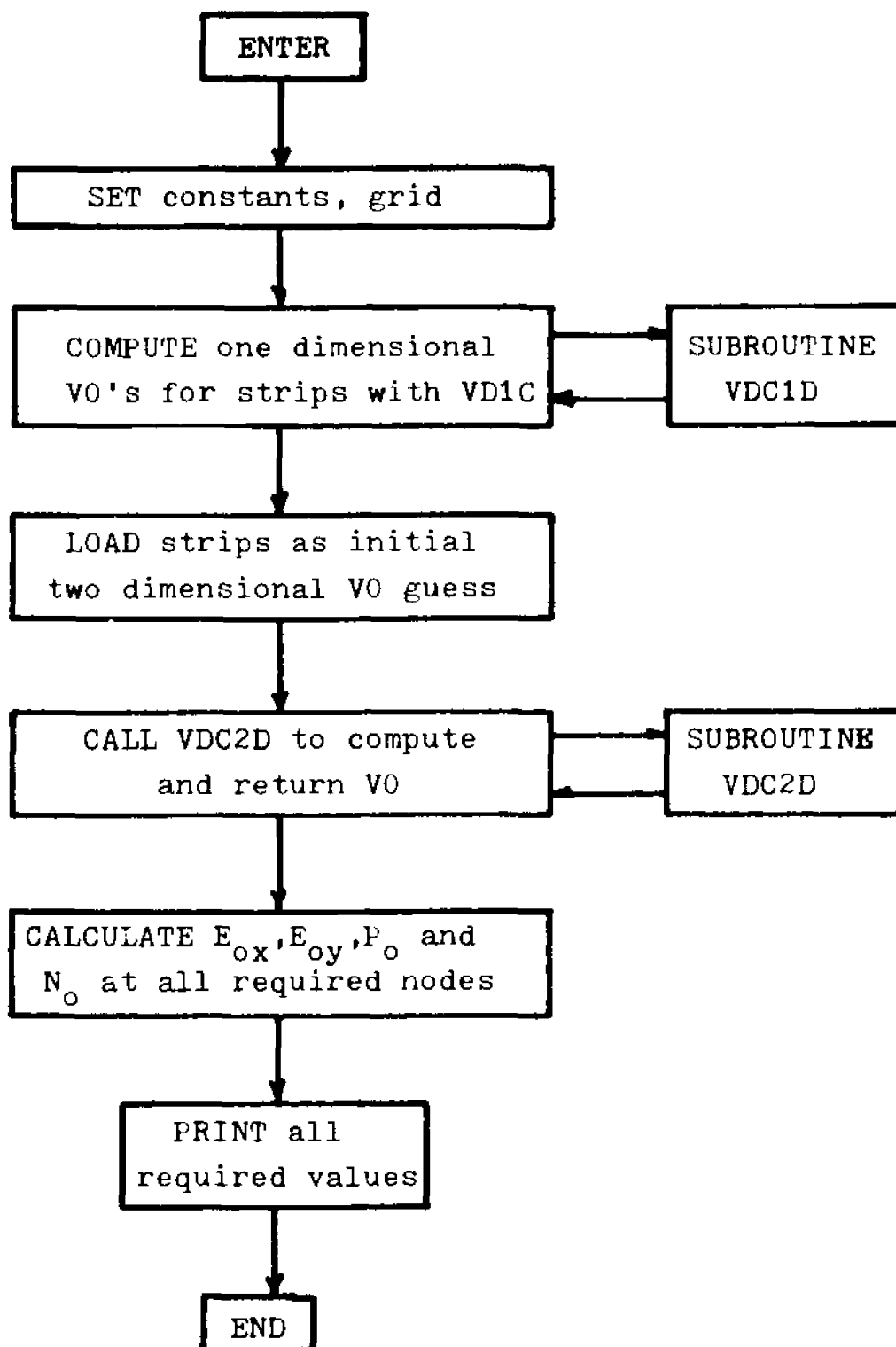


Figure 2.16 Computational Flowchart of MAIN to Solve for the DC Potential in Two Dimensions.

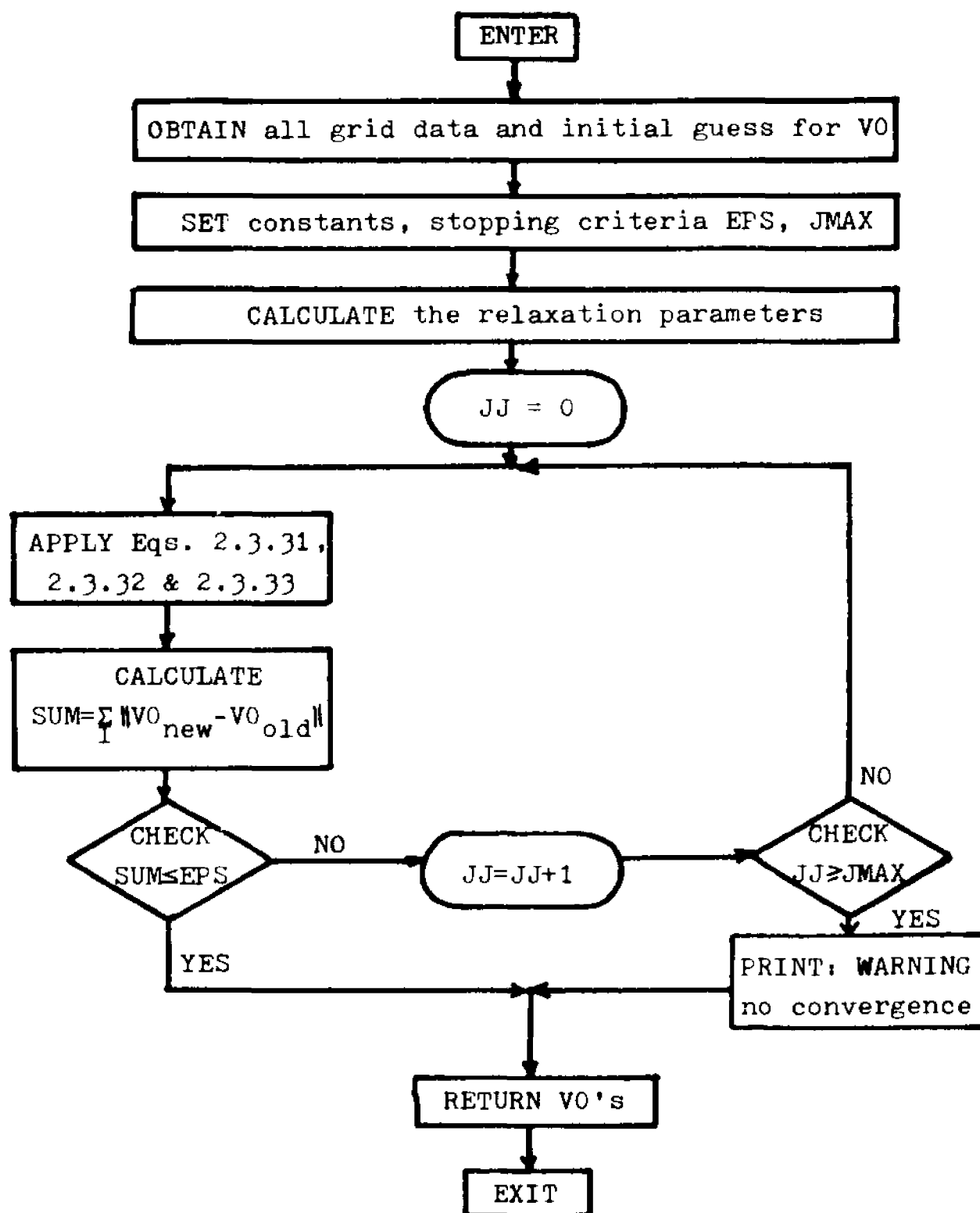


Figure 2.17 Computational Flowchart of Subroutine VDC2D.

2.4 Results of Studies With the One Dimensional DC Models Numerical Investigations With the One Dimensional Algorithm

The basic parameter of interest in the one dimensional case is the DC potential. All other parameters are derived from this variable. These are:

1. DC carrier charge densities, which using the Boltzman approximation are

$$p_o(x) = n_i \exp\left(\frac{-V(x)}{V_T}\right) \quad (1.3.9)$$

$$n_o(x) = n_i \exp\left(\frac{+V(x)}{V_T}\right) \quad (1.3.10)$$

2. The DC electric field

$$\underline{E}_o(x) = \frac{-dV(x)}{dx} \hat{a}_x \quad (2.4.1)$$

3. The charge on the metal plate per unit area may be found as

$$Q_G = \kappa_I \epsilon_o (\underline{E}_o(0^+) \cdot \hat{a}_x) \quad (2.4.2)$$

As an example, the potential for an MIS structure where the insulator is SiO_2 and the semiconductor is silicon (Si) is shown in Fig. 2.18. The charge density per unit area, Q_G , versus surface potential V_S (the potential at the insulator-semiconductor boundary) is shown in Fig. 2.19. This last graph, which agrees well with that

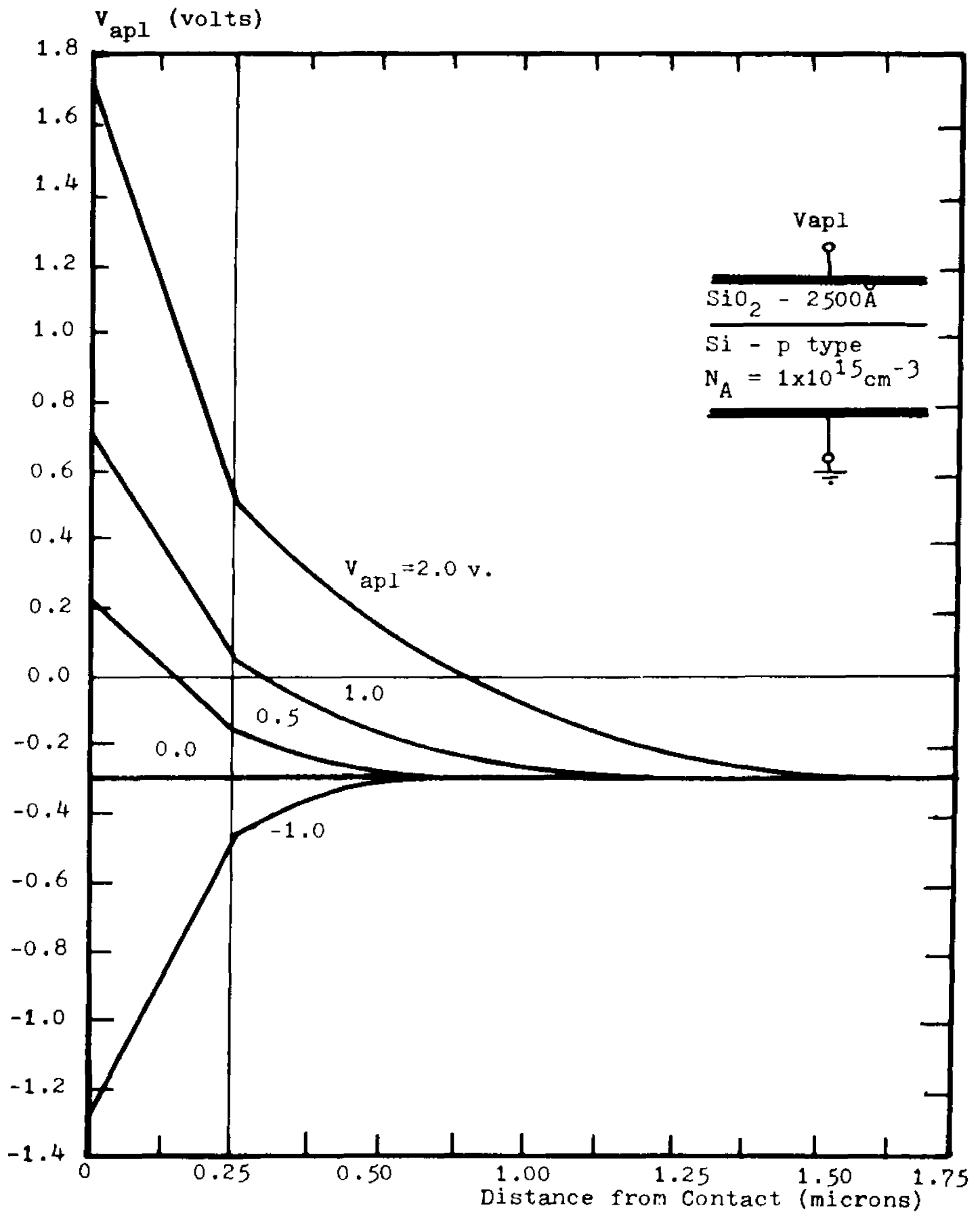


Figure 2.18. One dimensional potential solution as a function of distance for varying gate biases.

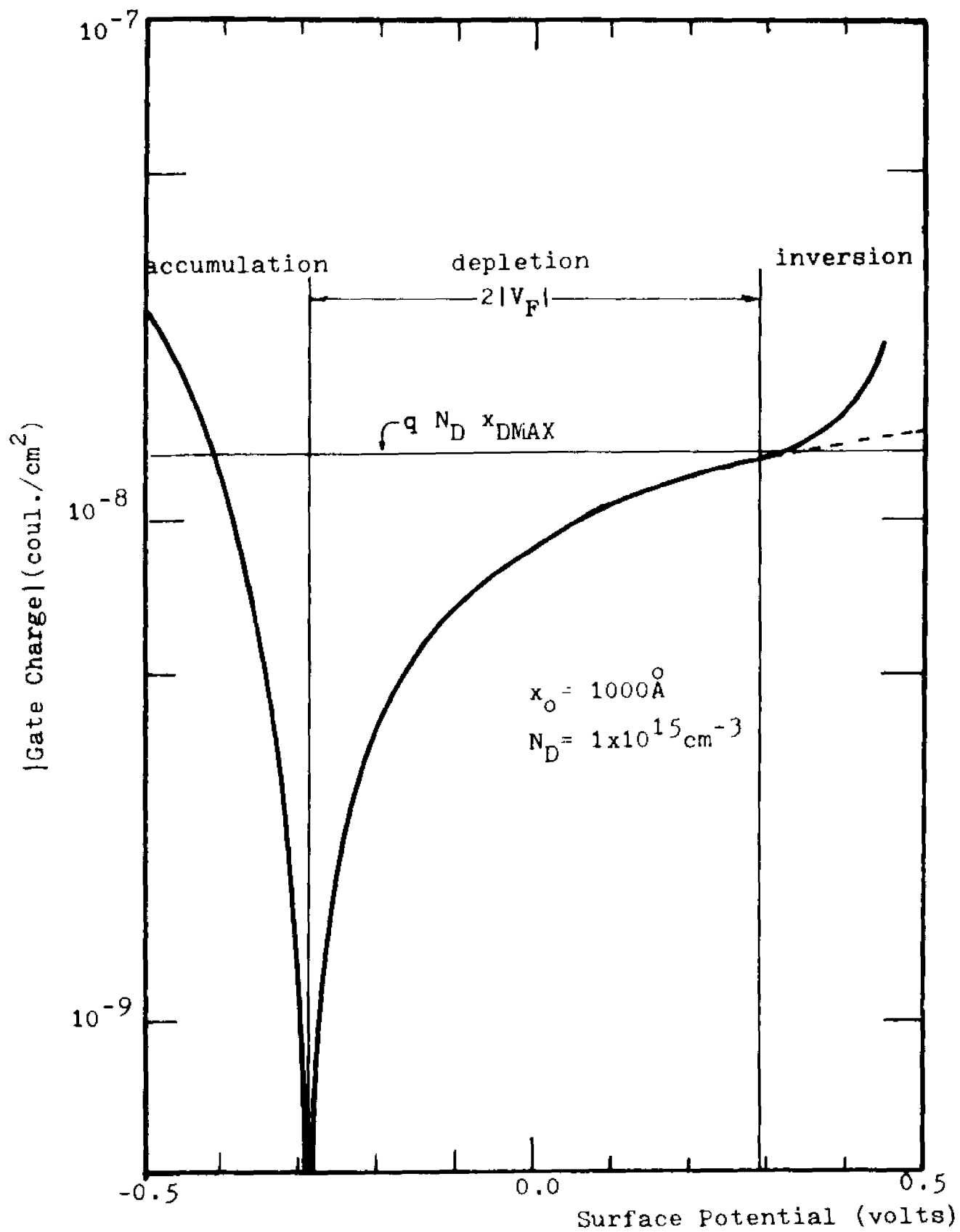


Figure 2.19. Gate charge as a function of surface potential.

shown by Sze⁽³⁰⁾, clearly shows the onset of strong inversion and the physical argument for the common assumption that strong inversion occurs when the surface potential is equal and opposite in sign from the bulk potential (V_F). The gate charge is mirrored by the total charge in the semiconductor

$$\frac{Q_G}{q} = \int_{x_0}^{x_B} (-n_i \exp \frac{-V(x)}{V_T} + n_i \exp \frac{+V(x)}{V_T} + N_{DOP}(x)) dx \quad (2.4.3)$$

There are three distinct regions in the curve shown in Fig. 2.19:

1. Accumulation: where potential is such that the majority carriers dominate the charge term in Eq. 2.4.3.
2. Depletion: for very small potentials the exponential terms are not significant compared to $N_{DOP}(x)$ and so it dominates the charge term. As the potential increases, the minority carrier term becomes the same order of magnitude as the background doping concentration. When the minority carrier concentration at the surface equals the background doping concentration the depletion of majority carriers at the depletion region edge slows down and practically ceases. Any further increase in bias increases the minority carrier concentration exponentially, whereas the depletion of majority carriers increases quadratically; the former mechanism begins to dominate. This is the physical mechanism for what is normally considered the onset of strong inversion.

Figure 2.19 clearly shows that this occurs at $|V_S| = 2|V_F|$.

3. Inversion: for large inversion biases the minority carrier concentration dominates the charge term in Eq. 2.4.3 and thus the gate charge is an exponential function of the applied bias. The increase in depletion of majority carriers practically ceases and thus an approximate value for a "maximum depletion width" may be found by using the "onset of strong inversion" approximation above in Eq. 2.4.3.

The effect of interface charge density (Q_{SS}) is discussed in the next section on the incremental DC capacitance.

Incremental DC Capacitance From the One Dimensional DC Model

Due to the nonlinear relationship of the potential to the mobile charge densities in the semiconductor, the charge on the gate of an MOS capacitor is a nonlinear function of the applied bias. For this reason the capacitance of such a device is not constant for all possible bias voltages and cannot have the simple form of a capacitor with linear dielectric. A definition of capacitance, in the present case, is found in Stern⁽³¹⁾, where incremental capacitance of a nonlinear capacitor is defined

$$C(V_G) = \left. \frac{\partial q(t)}{\partial v(t)} \right|_{V_G} \quad (2.4.4)$$

where the voltage $v(t)$ is applied to the gate of the capacitor with respect to the substrate. If one plots the gate charge as a function of the gate voltage, as done in Fig. 2.20, the value of the slope at any bias point is the capacitance defined in Eq. 2.4.4. The assumption here is that a sufficient time has elapsed and equilibrium established when a change in the bias point occurs. Since an analytic expression for the gate charge versus gate voltage does not exist, a numerical approximation to the slope at any bias point is approximated by the slope of the secant through two neighboring points

$$C_{DC}(Q_G, V_G) = \frac{\Delta Q_G}{\Delta V_G} = \frac{Q_{G1} - Q_{G2}}{V_{G1} - V_{G2}} \quad (2.4.5)$$

The accuracy of this formula in approximating the slope at $\{Q_G, V_G\}$ depends on how close together the two neighboring bias points are taken. Practically, for all incremental capacitance curves calculated, an incremental change in gate voltage of .01 volts was used with $V_{G1} = V_G - .005V$ and $V_{G2} = V_G + .005V$. The calculation of the charge on the gate is done using Eq. 2.4.2 for any given gate voltage and the application of the one dimensional DC algorithm to calculate the potential in the device.

Normally capacitance versus gate voltage of MIS capacitors are shown normalized with respect to the insula-

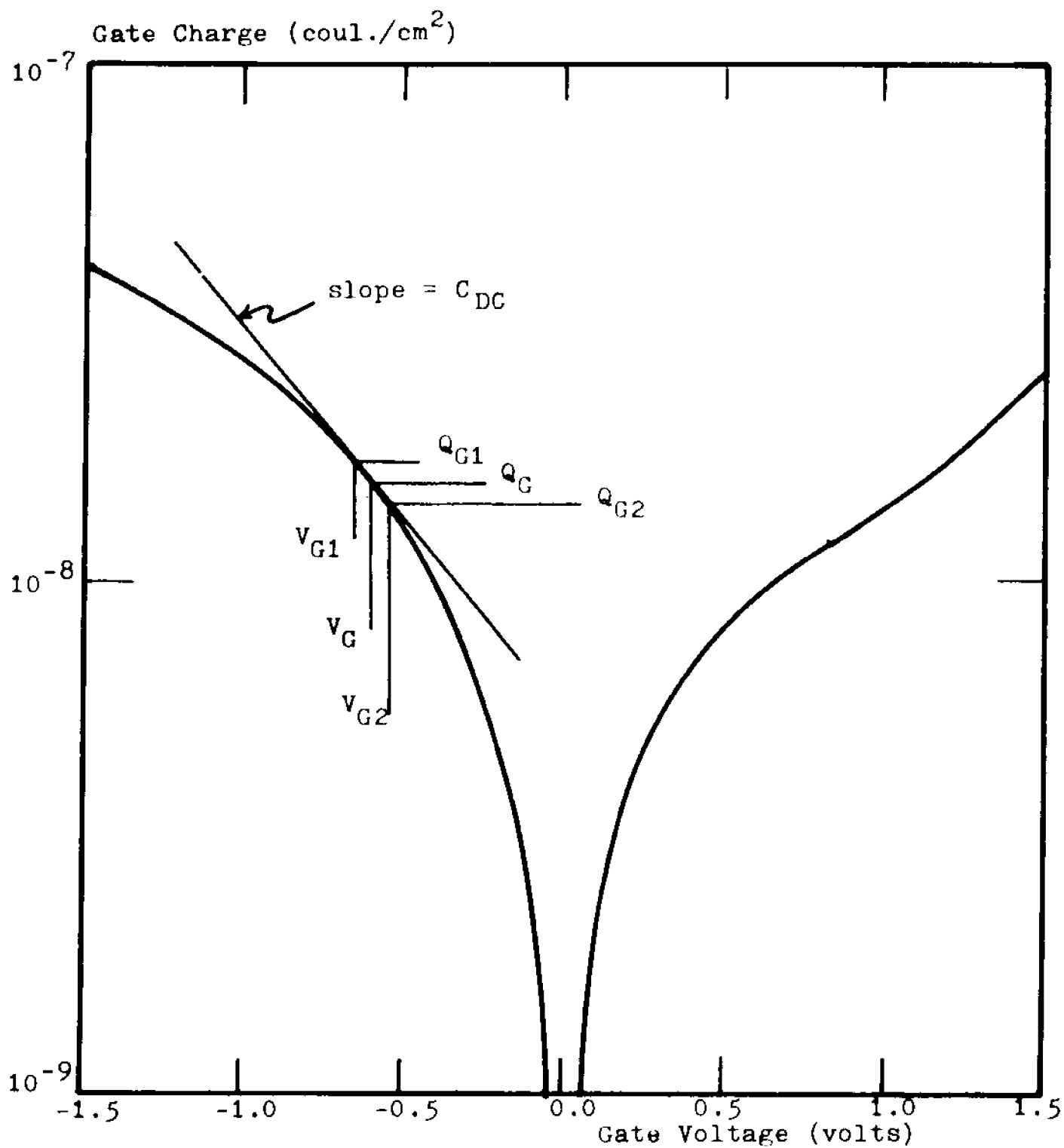


Figure 2.20. Gate charge as a function of gate voltage showing definition of C_{DC} .

tor capacitance (the capacitance of a parallel plate capacitor of thickness equal to the insulator thickness, x_0 where A is the cross sectional area):

$$C_0 = \frac{K_I \epsilon_0 A}{x_0} \quad (2.4.6)$$

Note that since Eq. 2.4.2 gives the gate charge as a charge per unit area, C_{DC} as calculated by Eq. 2.4.5 is a capacitance per unit area. There are several sources of error in the calculation of the incremental capacitance and a study of these errors helps in understanding the accuracy of the algorithm. Besides the expected truncation and discretization errors due to the finite machine arithmetic, there are the following sources of error:

1. Truncation error of the discretization scheme for the second derivative in Poisson's equation (Eq. 2.2.3).
2. Truncation error of the discretization scheme for Gauss' Law (Eq. 2.2.7).
3. Use of the slope of the secant as the approximation to the slope at a bias point.

Numerical experiments were performed to check the effect of 1 and 2 above. Both experiments require the calculation of the incremental capacitance of an MOS capacitor 5 microns in thickness with a 1000Å oxide and zero Q_{SS} . In numerical experiment 2, the number of

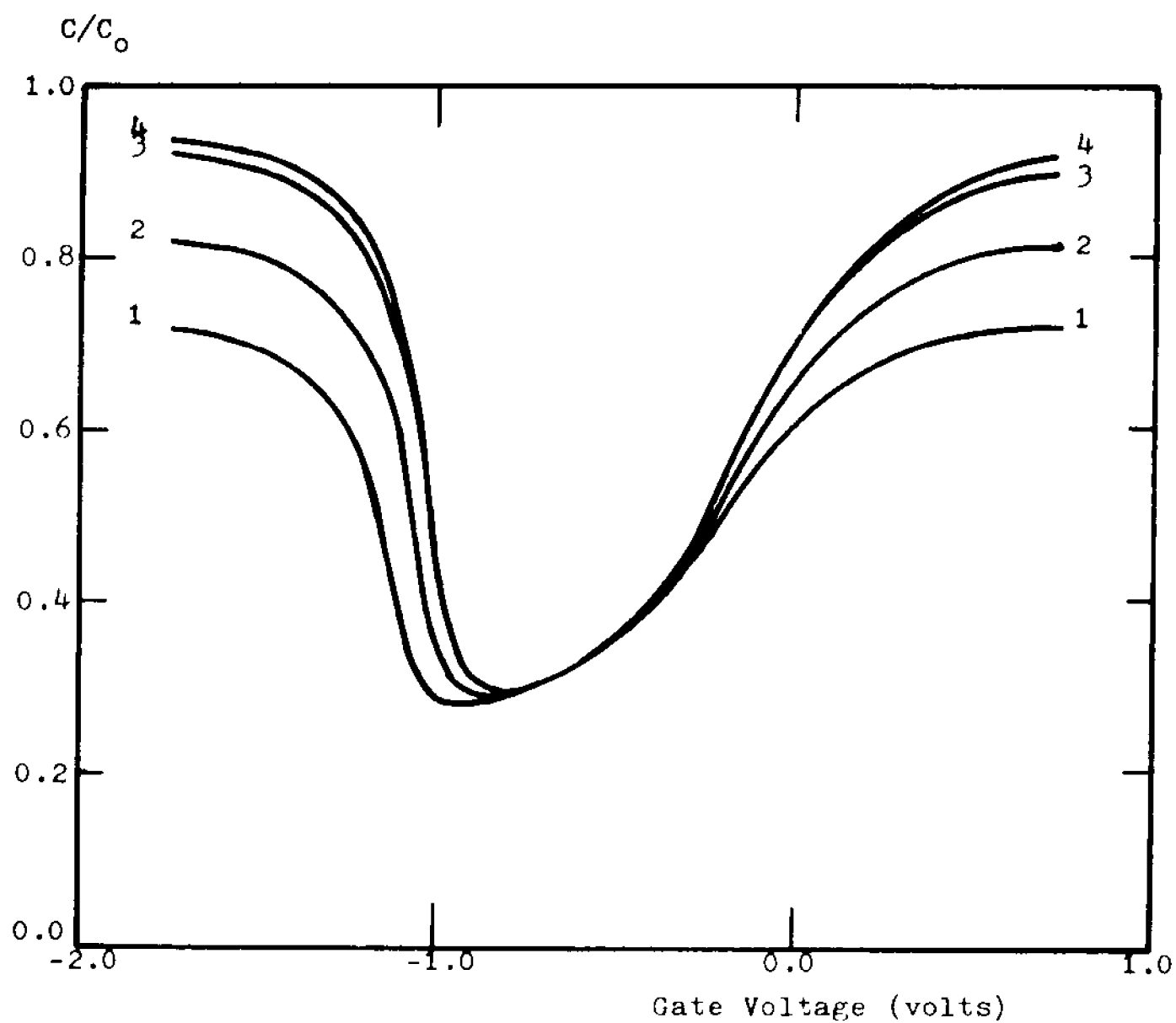
grid points remained fixed but the grid structure changed. In numerical experiment 3, a uniform grid structure was used but a change was made on the number of grid points. Table 2.1 summarizes the conditions of each run.

The resulting C-V curves are shown in Figs. 2.21 and 2.22. A useful measure of the accuracy of a C-V curve at low frequencies is how close does the normalized capacitance in strong inversion and accumulation approach unity. From these results one may observe that for a uniform grid size, the grid with the highest density is the most accurate. As the grid length decreases, the truncation error of the discretizing scheme is decreased. Figure 2.22 indicates that it is advantageous to have a nonuniform grid with several different regions of varying grid lengths than a uniform grid for the same number of grid points. Concentrating the grid points at the surface helps define the charge densities more accurately. Being exponential functions of the potential, they are most in error in the region where the potential is greatest. For uniformly doped devices one may conclude that a nonuniform grid, with very short grid sizes where the charge densities are expected to vary greatly is a reasonable grid structure. For the present work a maximum of three regions are used.

An investigation was also undertaken to determine computational cost versus accuracy for the one dimensional DC algorithm. The measure of the accuracy used is

NUMERICAL EXPERIMENT	TOTAL NUMBER OF GRID POINTS	NUMBER OF REGIONS	NUMBER OF GRID POINTS IN EACH REGION AND GRID SIZES
2a	500	1	1-500-.01 μ m
2b	500	2	1-50-.05 μ m (bulk) 2-450-.0055 μ m (surface)
2c	500	3	1-50-.05 μ m (bulk) 2-150-.013 μ m (depletion) 3-300-.0016 μ m (surface)
3a	50	1	1-50-.1 μ m
3b	100	1	1-100-.05 μ m
3c	500	1	1-500-.01 μ m
3d	1000	1	1-1000-.005 μ m

Table 2.1. Grid data for numerical experiments 2 and 3.



Curve	Number of grid points	Grid size in μm
1	50	.100
2	100	.050
3	500	.010
4	1000	.005

Figure 2.21. Results of numerical experiment 3.

Curve	Number of grid points	Grid sizes in μm
1	500	.01
2	450+50	.0055/.05
3	300+150+50	.0016/.013/.05

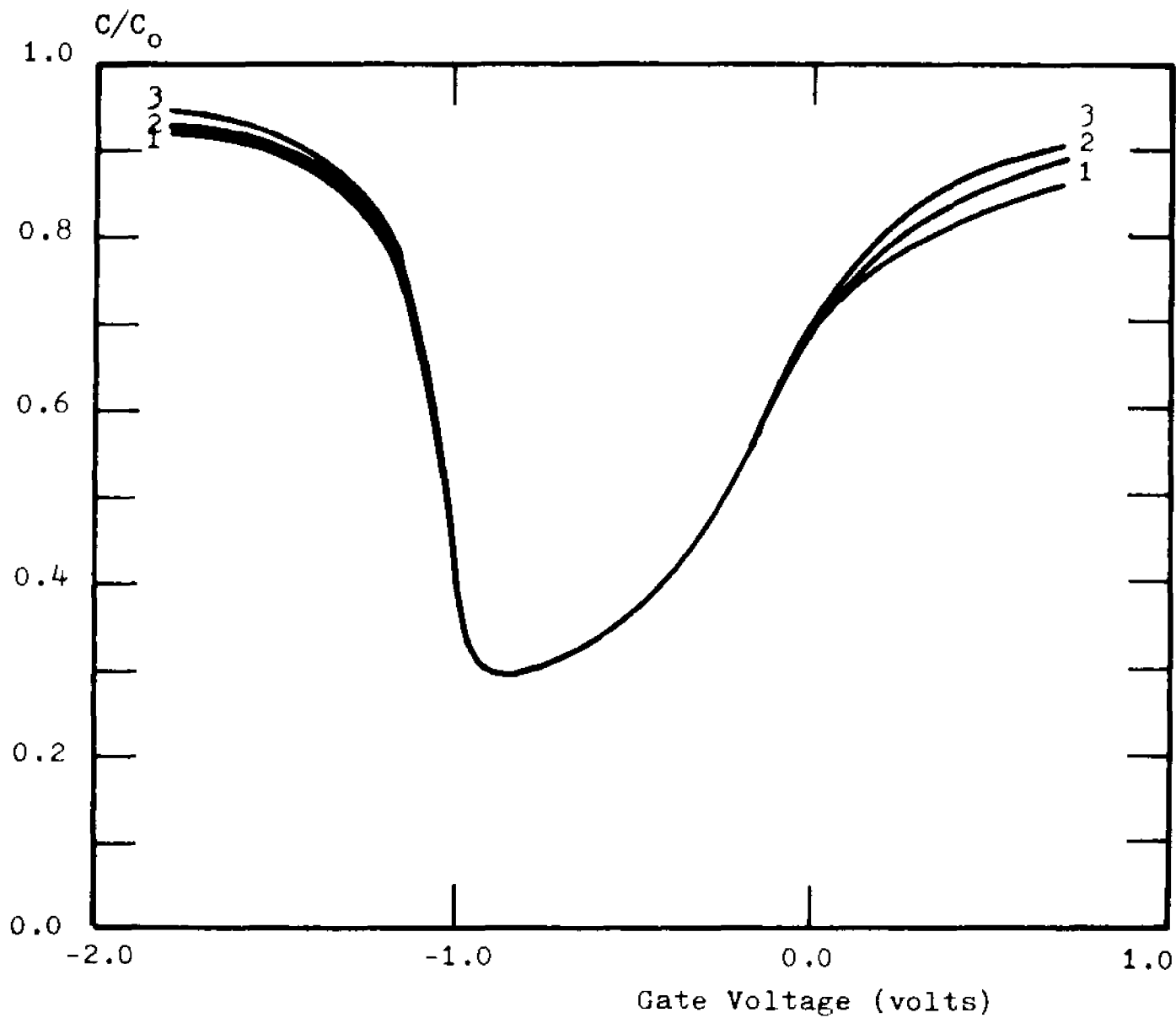


Figure 2.22. Results of numerical experiment 2.

how close the normalized capacitance in strong inversion comes to unity. The structure has n type silicon with a uniform doping of 10^{15} ions/cm³ and an oxide thickness of 1000Å. Strong inversion was considered to occur when the surface potential $|V_S| > 2 |V_F|$. A gate voltage of -2.0V was sufficient to obtain this condition. Each run was made for a fixed number of grid points with a uniform grid for a fixed number of iterations. The product of the number of grid points times the number of iterations is a measure of the cost of producing a particular capacitance-voltage point on a C-V curve, or obtaining the DC potential in the device for a given gate bias. This cost factor is plotted versus an accuracy factor $(1 - \frac{C}{C_0})$ and shown in Fig. 2.23 as a function of the number of grid points. From the results one observes the following:

1. To three significant figures, the capacitance does not change after a certain number of iterations.
2. It is usually disastrous to stop iterating too soon since there is a sharply defined iteration range for a given number of grid points at which the accuracy increases rapidly.
3. Generally, the greater the number of grid points the more accurate the solution but there is a cost trade-off involved.

If the number of iterations is plotted versus the accuracy factor, as shown in Fig. 2.24, one

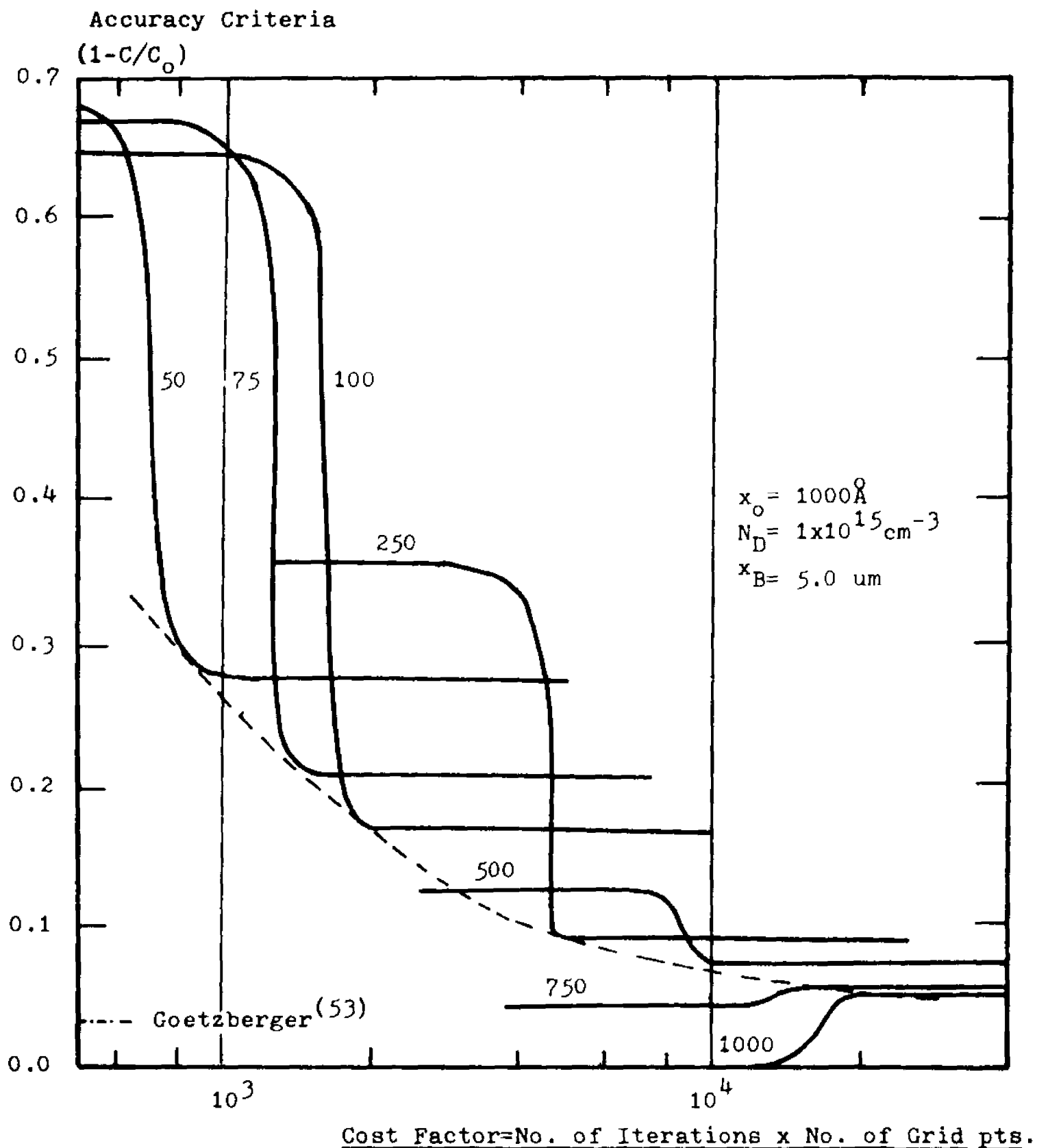


Figure 2.23. Cost factor versus accuracy criteria for the generation of a particular C_{DC} -V curve.

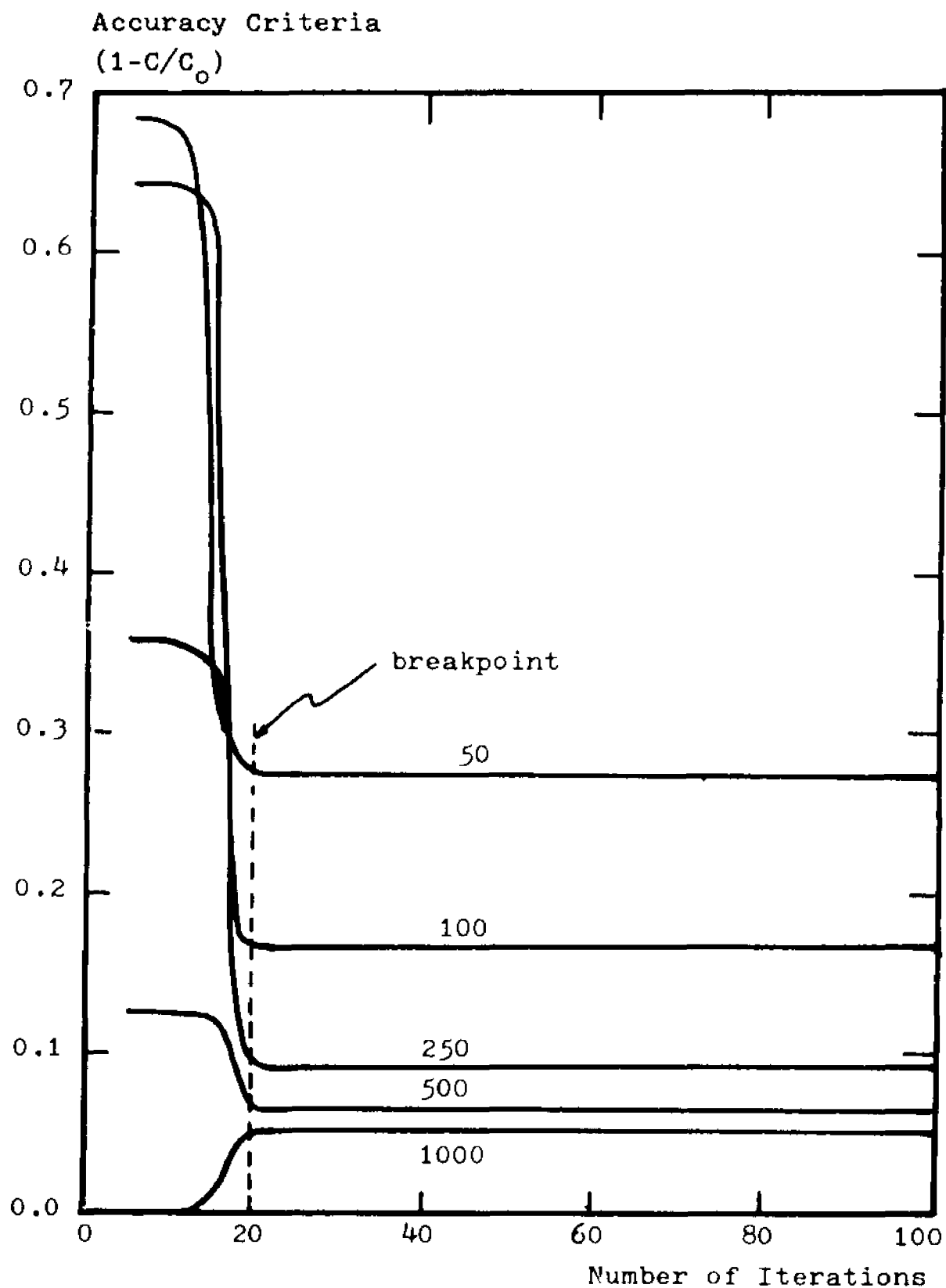


Figure 2.24. Accuracy criteria versus number of iterations showing breakpoint.

observes that there is a certain number of iterations at which there is a considerable drop in $(1 - \frac{C}{C_0})$ for all curves.

DC Studies of Inhomogenous Profiles - The MOS-PN Junction

Certain inhomogeneously doped MOS capacitors have been studied numerically and experimentally. In particular, an investigation was carried out of the inhomogeneous profile shown in Fig. 2.25. The incremental capacitance versus voltage curves calculated for varying x_e (the thickness of the p layer) are shown in Fig. 2.26. It is seen that for p layers which are thin enough to be swept out (depleted of mobile charge carriers) with the applied bias, a flattening of the C-V characteristic occurs. For layers which are too thick ($x_e > x_{DMAX}$) the opposite type C-V curve is obtained (see $x_e = 1.5 \mu m$ for example). Figure 2.27 shows the potential in the semiconductor for various gate biases. As is evident, the p region is swept out. On the other hand, if the layer is too thick compared to the maximum depletion width, then the voltage is dropped at the semiconductor surface and the junction will be relatively undisturbed. A similar effect may be obtained by maintaining the layer thickness constant and increasing the doping concentration. This essentially decreases x_{DMAX} thus shielding the rest of the p layer and the junction from the surface field. This effect is shown in Fig. 2.28. The variable x_{DMAX} is defined⁽³²⁾

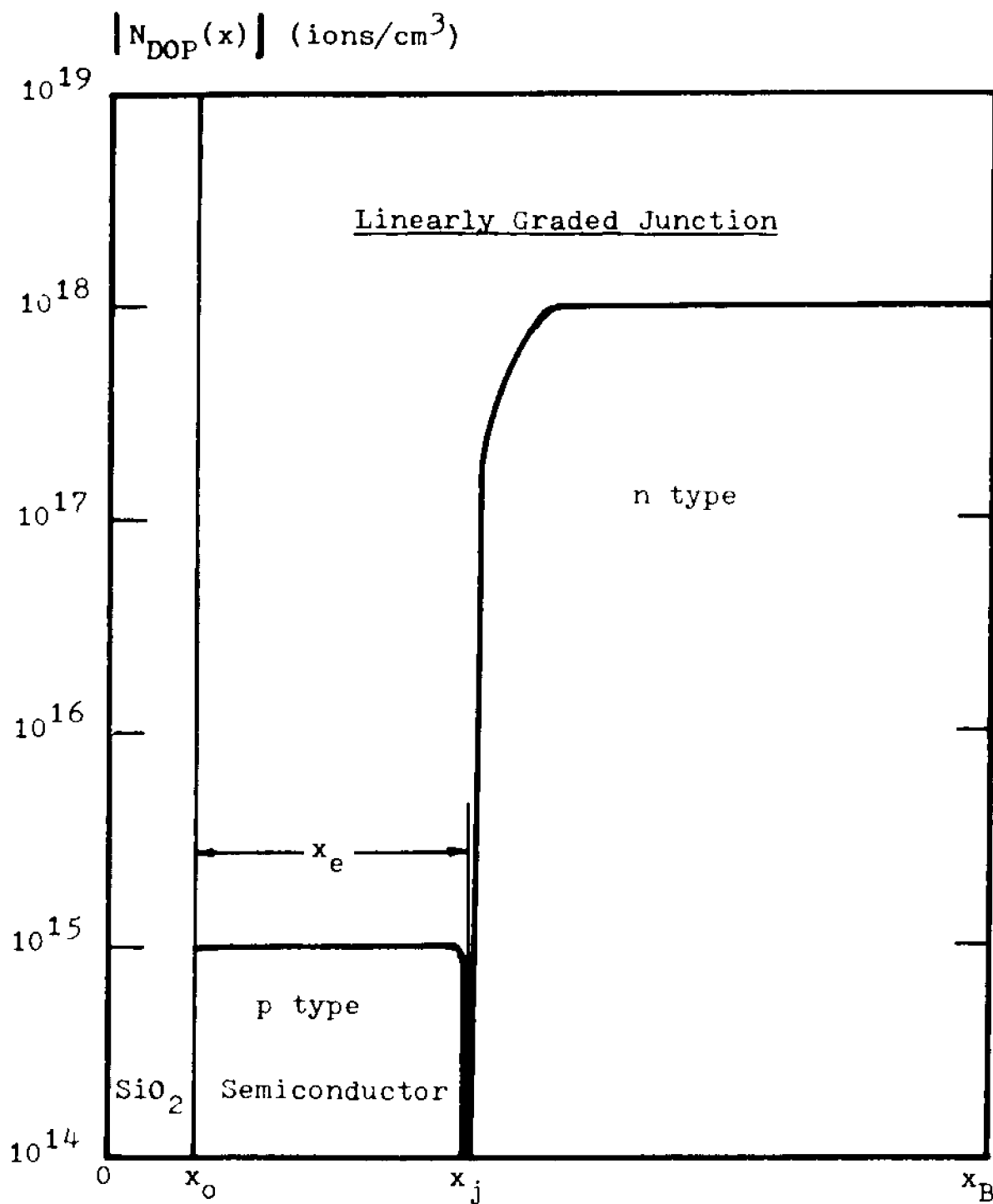


Figure 2.25. Ideal linearly graded junction doping profile of an MOS-PN junction.

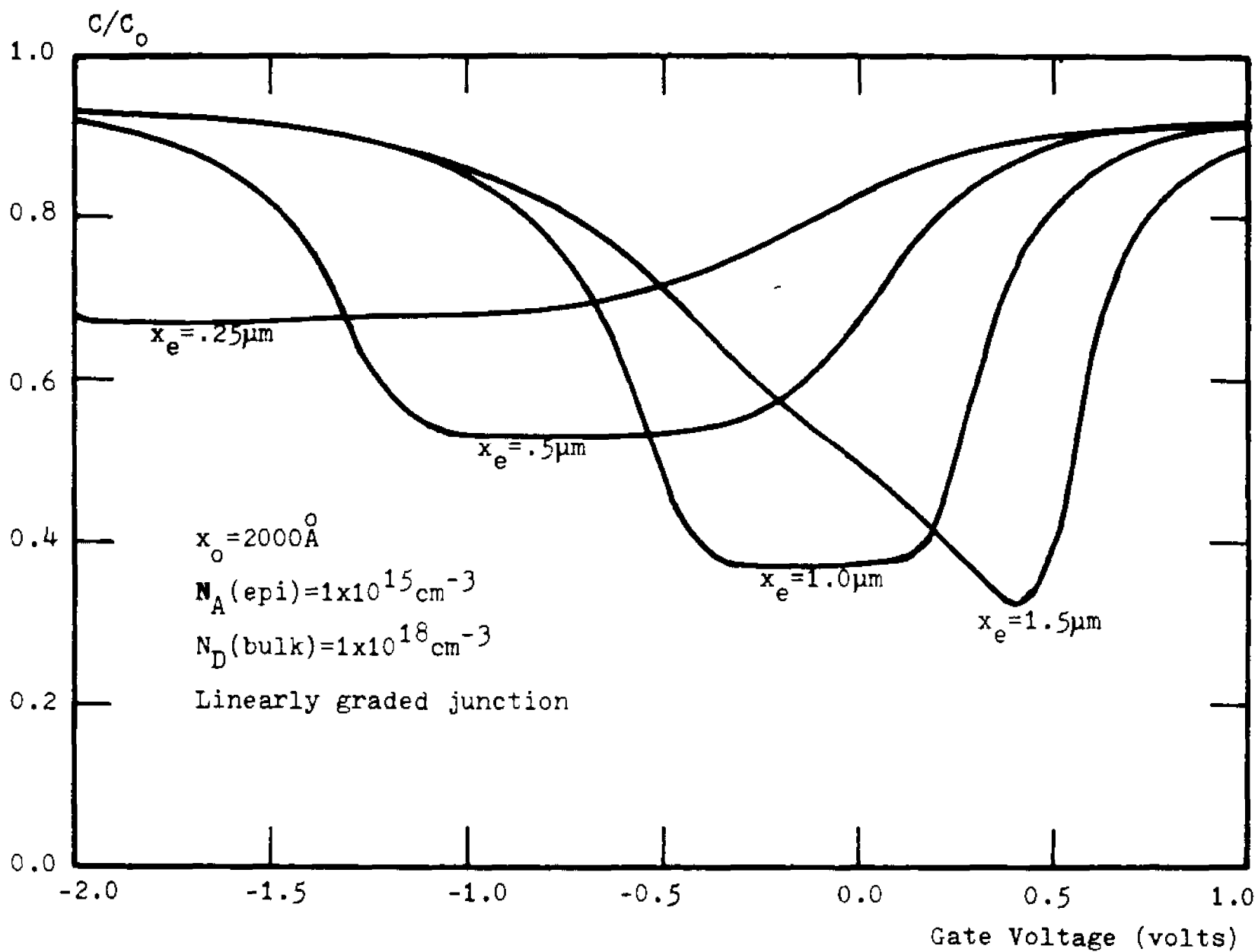


Figure 2.26. Incremental capacitance-voltage curves for the MOS-PN junction.

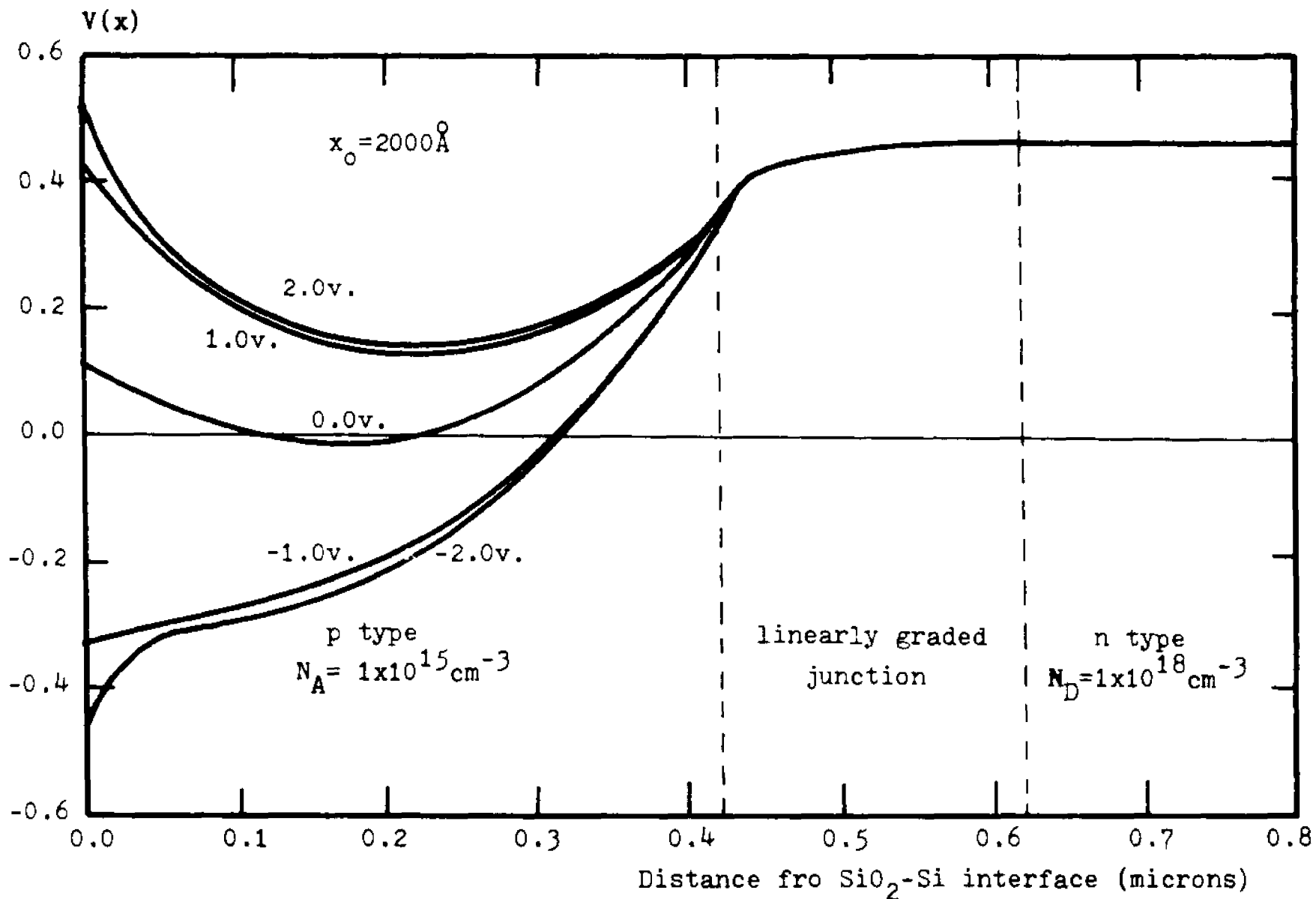


Figure 2.27. Potential profiles of an MOS-PN junction showing sweeping out of the epitaxial region.

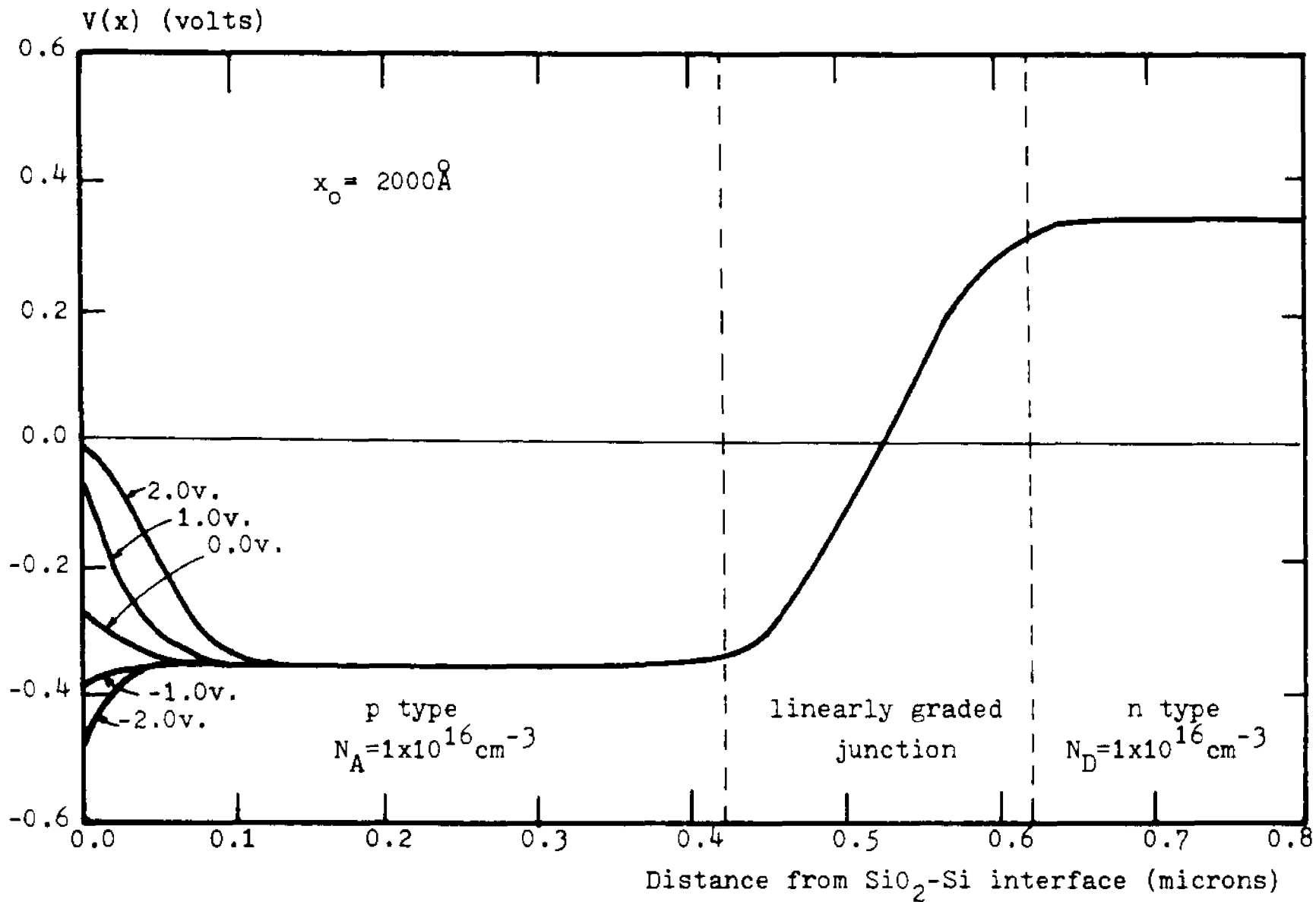


Figure 2.28. Potential profile showing no sweeping out of the epitaxial region due to high epitaxial doping.

$$x_{D\text{MAX}} = \sqrt{\frac{4K_S \epsilon_d V_H}{q \cdot N_{DOP}}}$$

(2.4.7)

2.5 Results of Studies With the Two Dimensional DC

Algorithm

The simplest two dimensional device being considered is the three terminal MOS Varactor; the cross-sectional view Fig. 2.29. The term "three terminal varactor" stems from research into a device such as the one shown, in which the small signal admittance of one of the top leads may be controlled by varying the DC bias on the other lead. Experimentally such devices have been shown to work ⁽²⁾; there is considerable interest in such a device ⁽³³⁾⁽³⁴⁾. To calculate the admittance of a lead on the device, a small signal AC analysis is necessary in two spatial dimensions (Chapter 4). The task here is to use the method outlined in Section 3 of this chapter to produce the DC potential, charge densities and electric field needed as the quiescent operating point for the AC analysis. Also, this device shall constitute the test structure for the two dimensional DC program.

The design parameters of interest are: the plate separation x_d , the oxide thickness y_o , the semiconductor thickness $y_b - y_o$, and the background doping profile. The analysis parameters of interest are the grid points in each direction and applied biases. The actual structure modeled has silicon dioxide as an insulator and silicon as the semiconductor.

A uniform grid in both the x and y directions is superimposed on the structure with 50 grid points in the

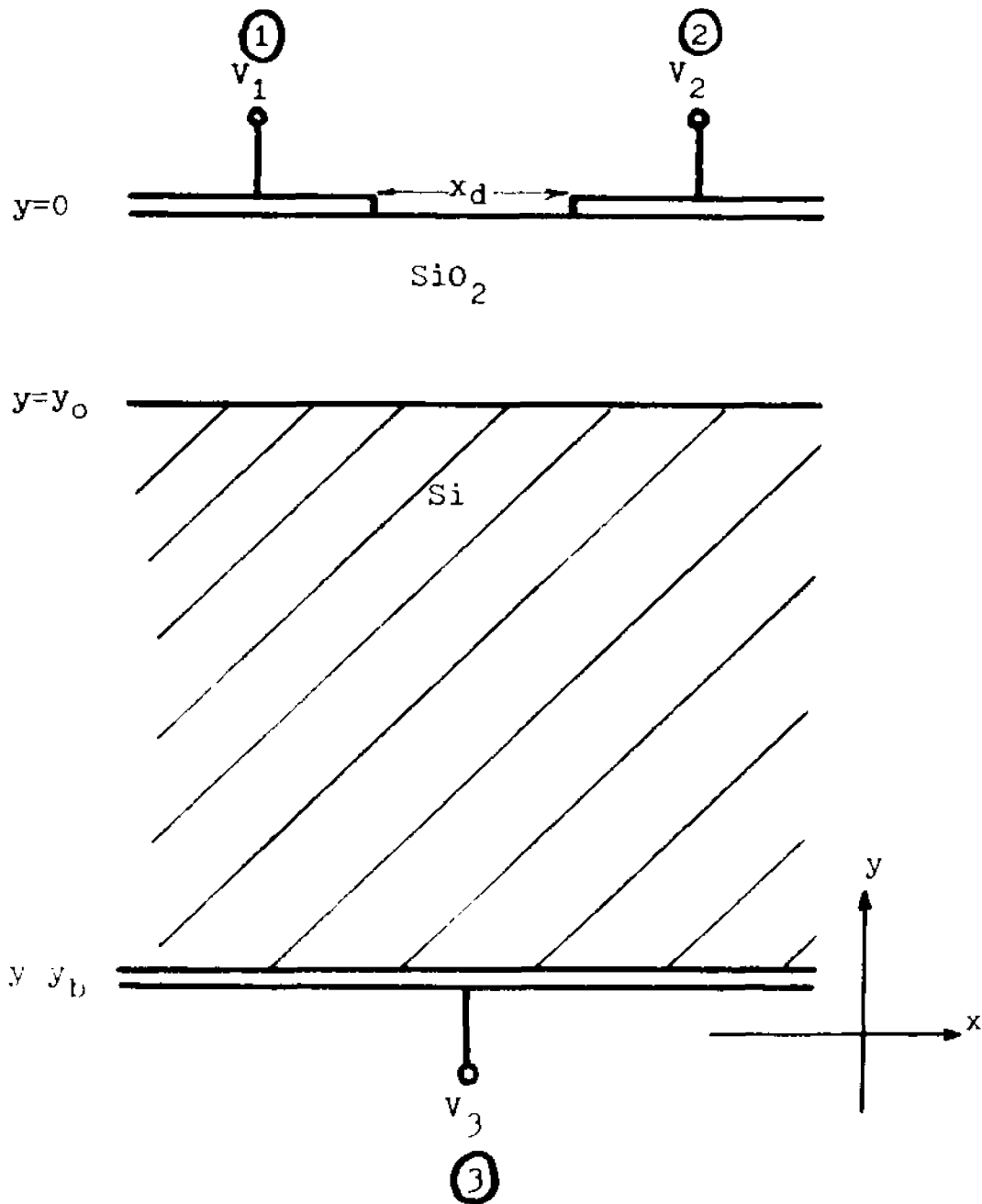


Figure 2.29. Three terminal MOS varactor structure studied.

semiconductor and 10 in the insulator by 25 points across. Whereas the grid may be variable, this particular grid was chosen for testing purposes. Since a finite gap (as different from an infinitesimal one) should be used to model practical devices and the effect of lead separation is to be studied, it was found necessary to include the air space above the gap in the calculation. This is a relatively simple matter in that either an assumption is made on how the voltage drops across the gap from electrode 1 to electrode 2, or calculation must be extended past this interface. For air gaps which are much smaller than the oxide thickness, the voltage from electrode to electrode drops in approximately a linear fashion but such gaps are of no practical interest presently. Most devices of interest fall within the other condition where the gap size is larger than the oxide thickness. In that case, considering the voltage in the air-insulator interface to be unknown and obeying Gauss' Law at that interface, a solution outside may be sought. Figure 2.30 shows the complete structure and grid including the region outside.

The boundary conditions are described in Section 2.3 and are Dirichlet for the lateral boundaries and the metal contacts. It would be advantageous from a computational viewpoint if Dirichlet boundary conditions were available for the outside region. For this purpose the assumption may be made that the voltage far from the gap

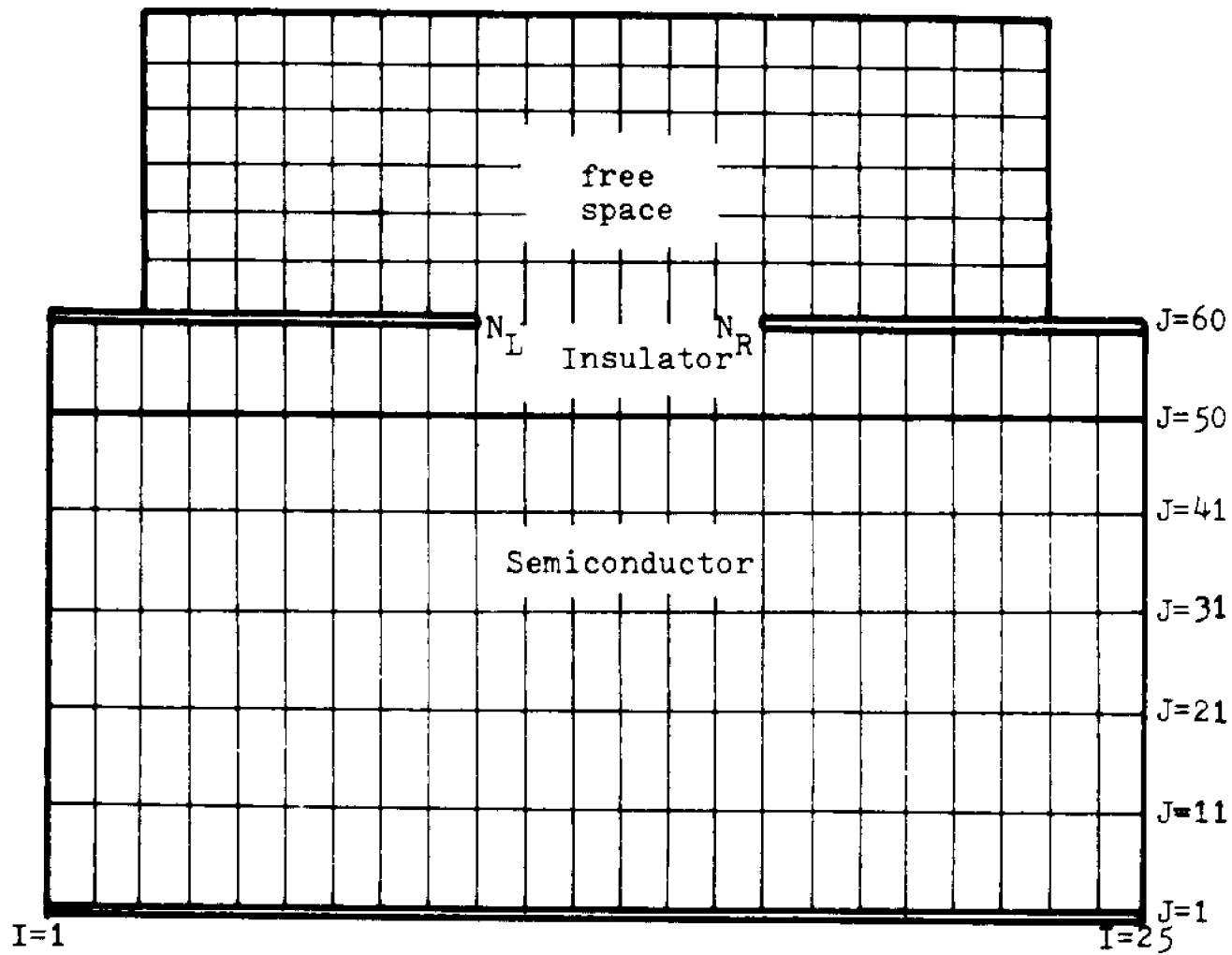


Figure 2.30. Grid structure employed in the two dimensional analysis of the three terminal varactor.

drops uniformly along a circle. This is the voltage that two metal strips at those potentials, an infinitesimal distance apart on the surface of a dielectric, would develop in the air space immediately above them. Figure 2.31a shows the structure which illustrates the assumption and Fig. 2.31b shows how it applies to the problem at hand. The voltage at a given location (I,J) shall be approximated by that of the ideal situation, which as shown is a function only of the angle and the two plate voltages

$$V(I,J) \cong \frac{V_1 - V_2}{\pi} \text{ATAN} \left(\frac{y_j}{x_i} \right) + V_2 \quad (2.5.1)$$

The region modeled was chosen to be rectangular since it is much easier for algorithmic bookkeeping than a semicircular one. The assumption then reduces to equating the far border points to the equivalent voltage given by Eq. 2.5.1 and assuming these borders are far away from the gap for the approximation to be a reasonable one. For 25 points across in the x direction in the device, 21 of them matched points outside. There were 10 rows above the level of the plates, making a total of 210 extra grid points including borders. The solution inside these borders and outside the gap was left free to satisfy Laplace's equation in two dimensions and solved for iteratively by the same method as is used in the rest of the algorithm. The relaxation

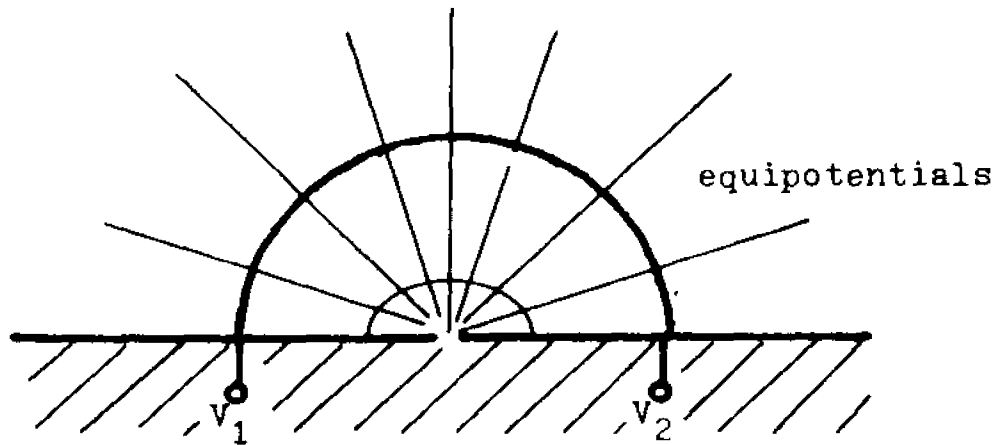


Figure 2.31a. Ideal potential distribution for an infinitesimal gap.

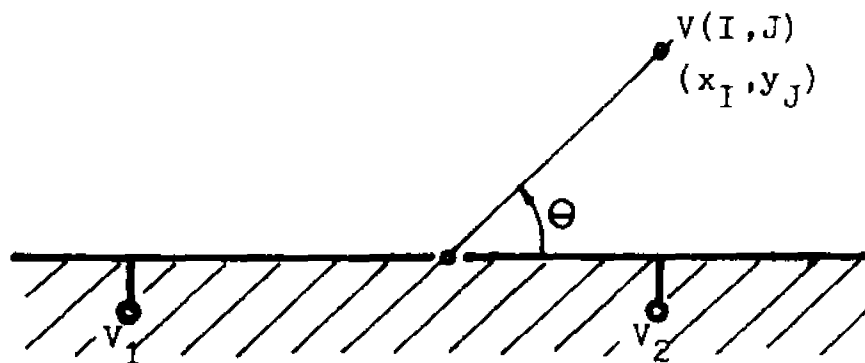


Figure 2.31b. The discretized potential at an exterior point.

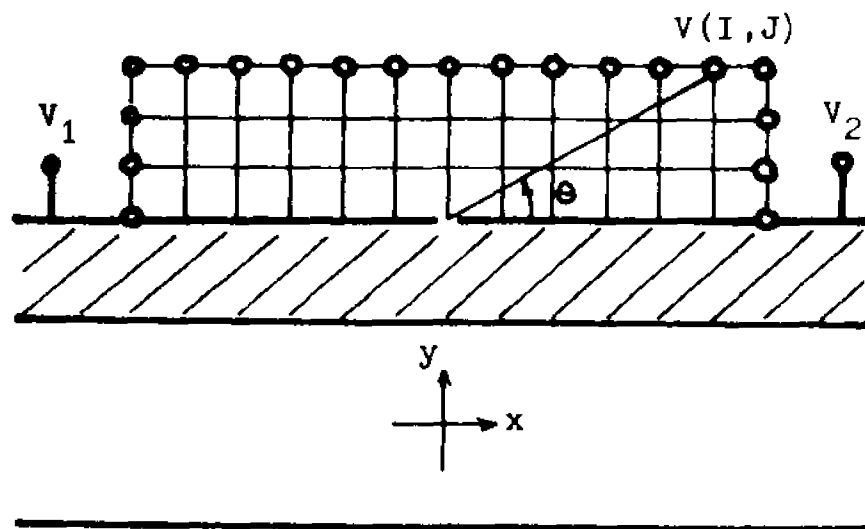


Figure 2.31c. Discretization grid for exterior region employed in the potential calculation.

parameter is that of the linear theory for the corresponding size outside region.

The following studies have been made with this algorithm:

1. The effect of varying lead biases on surface potential and charge densities.
2. The effect on surface potential and surface charge densities of varying lead separation.
3. The potential drop across the gap for varying biases.

A note should be made at this point on the use of surface parameters such as potential and charge densities. Since one is dealing with a uniformly doped structure, looking at the potential or charge densities along the semiconductor-insulator interface is a very good indicator of the electrical conditions immediately below and extending into the bulk for that particular y coordinate.

Whereas two dimensional plots would be esthetically more presentable, there is less clutter and more useful information simply given by displaying just these parameters. The structure under question, with the proper biases, is shown with each graph with an indication for which row of data the graph is plotted. All grid steps in the x direction are $0.1\mu\text{m}$ unless stated otherwise in the diagram, and the grid steps in the y direction are $0.25\mu\text{m}$ in the silicon, $0.01\mu\text{m}$ in the oxide and $0.1\mu\text{m}$ in the outside.

The silicon is p type of 10^{15} ions/cm³ uniform doping with a silicon dioxide insulator of 1000Å thickness.

The first three graphs, Figs. 2.32, 2.33 and 2.34 show the surface potential for various applied biases in a device with a very small gap: 0.2 μm. It may be observed that at this proximity, the presence of a nearby lead with a potential impressed on it will electrically alter the surface conditions under the lead in the area immediately contiguous to it. This alteration takes place by field effect and is a very short range phenomena.

Increasing the lead separation to 0.6 μm creates a virtual electrical isolation of the surface under each electrode as is seen in Fig. 2.35. Even though the bias on each electrode is sufficient to invert the surfaces under them, the region in between is depleted or at flatband which creates a field barrier to charge carriers. This effect contributes to incomplete charge transfer in structures such as charge coupled devices which has been widely and extensively reported. These results are quite expected and in good agreement with those of other workers⁽³⁵⁾.

This effect is much more pronounced for a gap width of 1.0 μm, as shown in Fig. 2.36. The main cause of such a strong barrier is the fact that the bulk is grounded and in regions where neither top electrode has much influence, the semiconductor will come close to

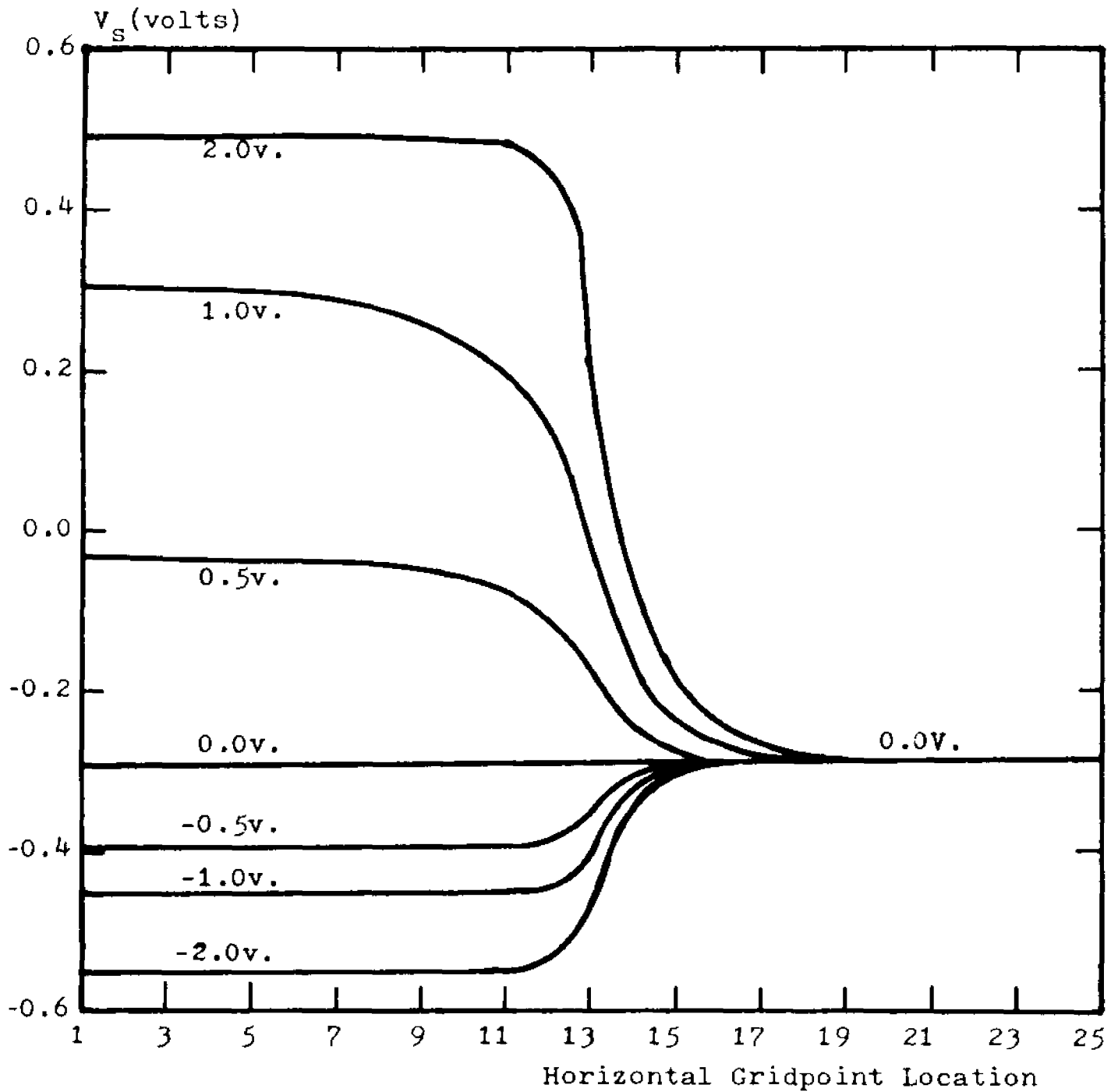
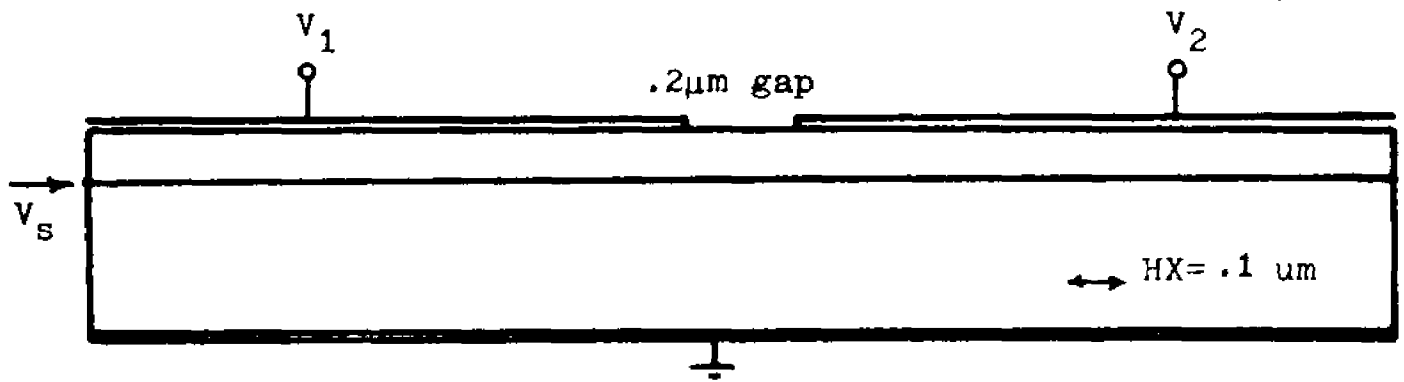


Figure 2.32. Surface potential of the three terminal varactor ($V_2=0V$).

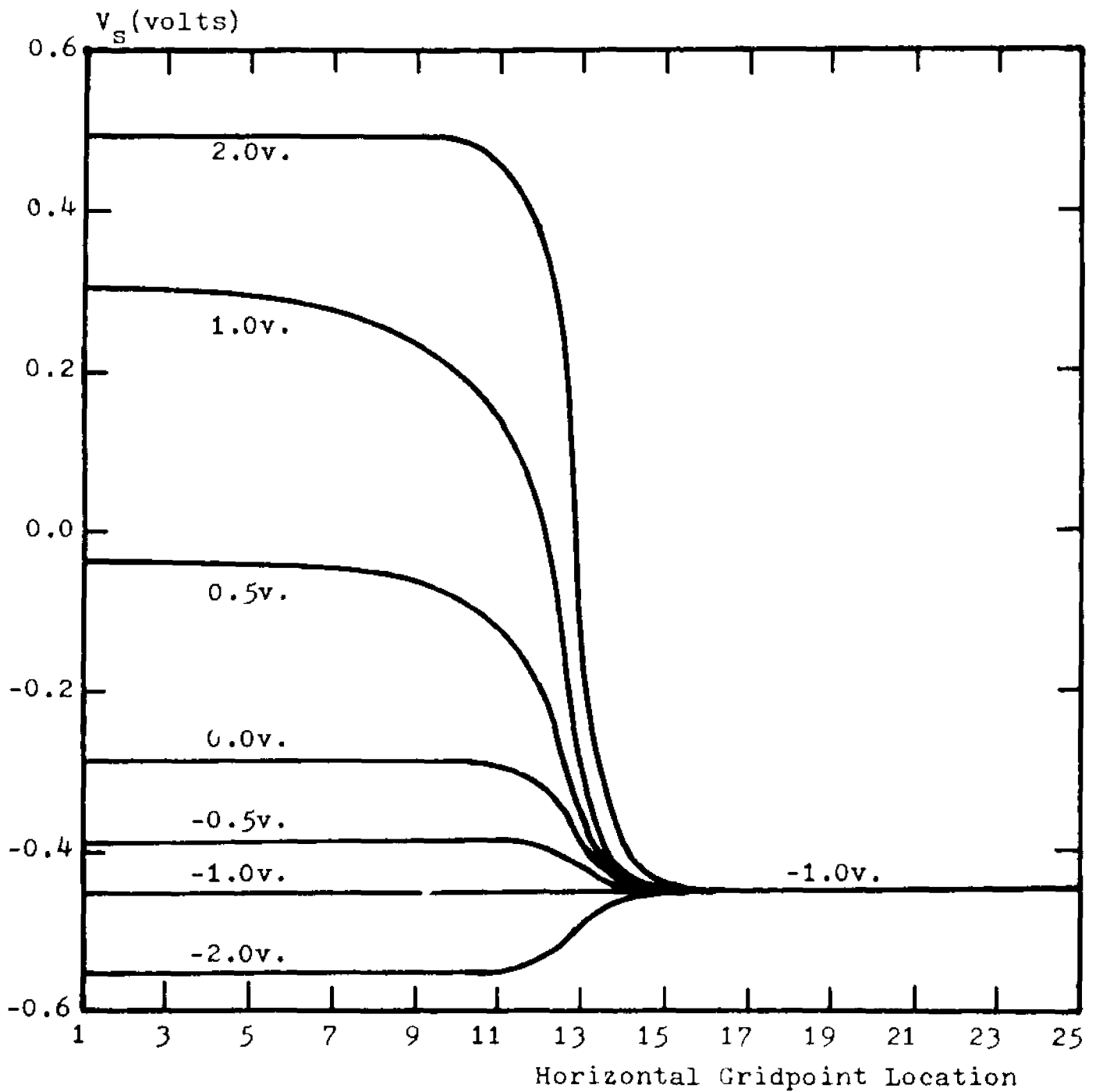
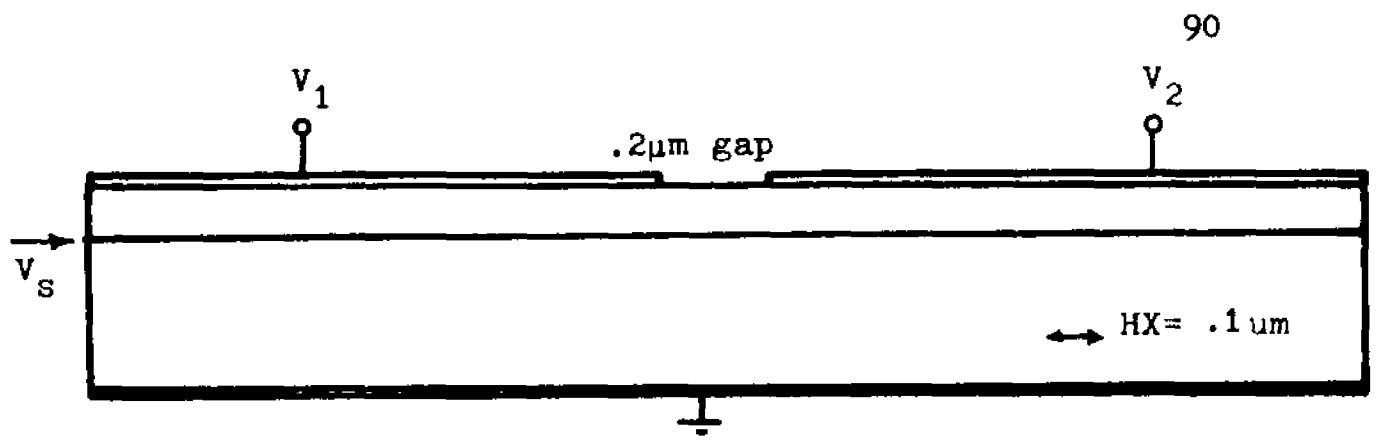


Figure 2.33. Surface potential of the three terminal varactor ($V_2 = -1v$).

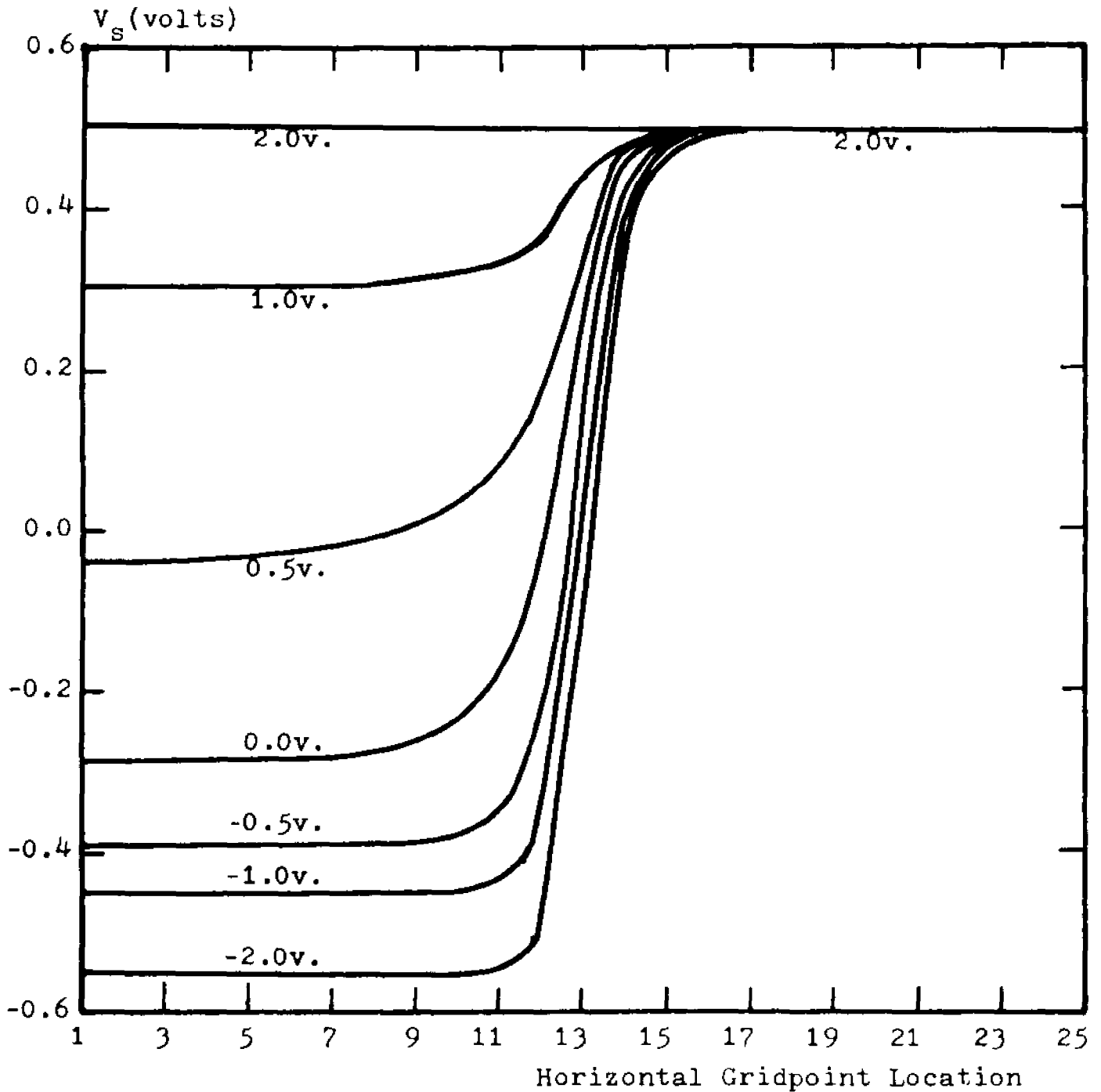
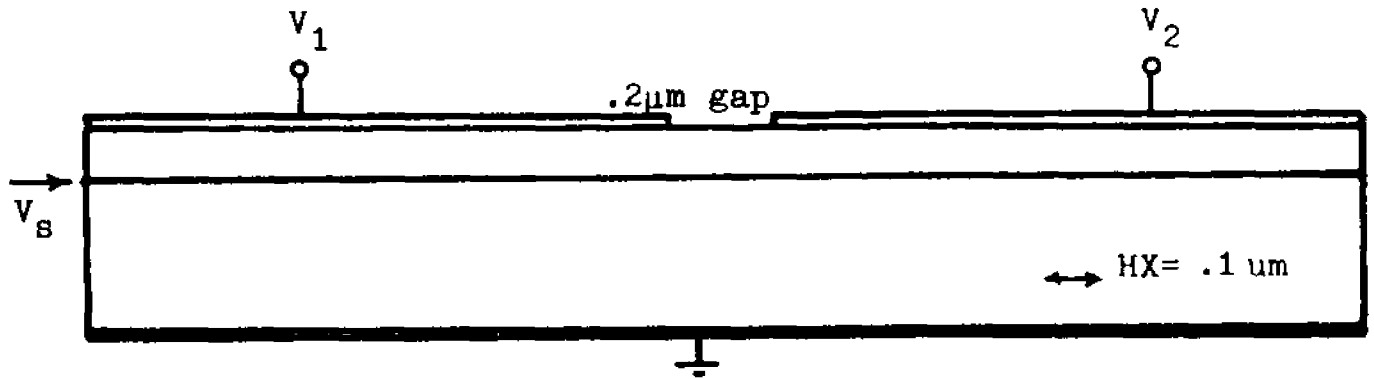


Figure 2.34. Surface potential of the three terminal varactor ($V_2=2\text{v}$).

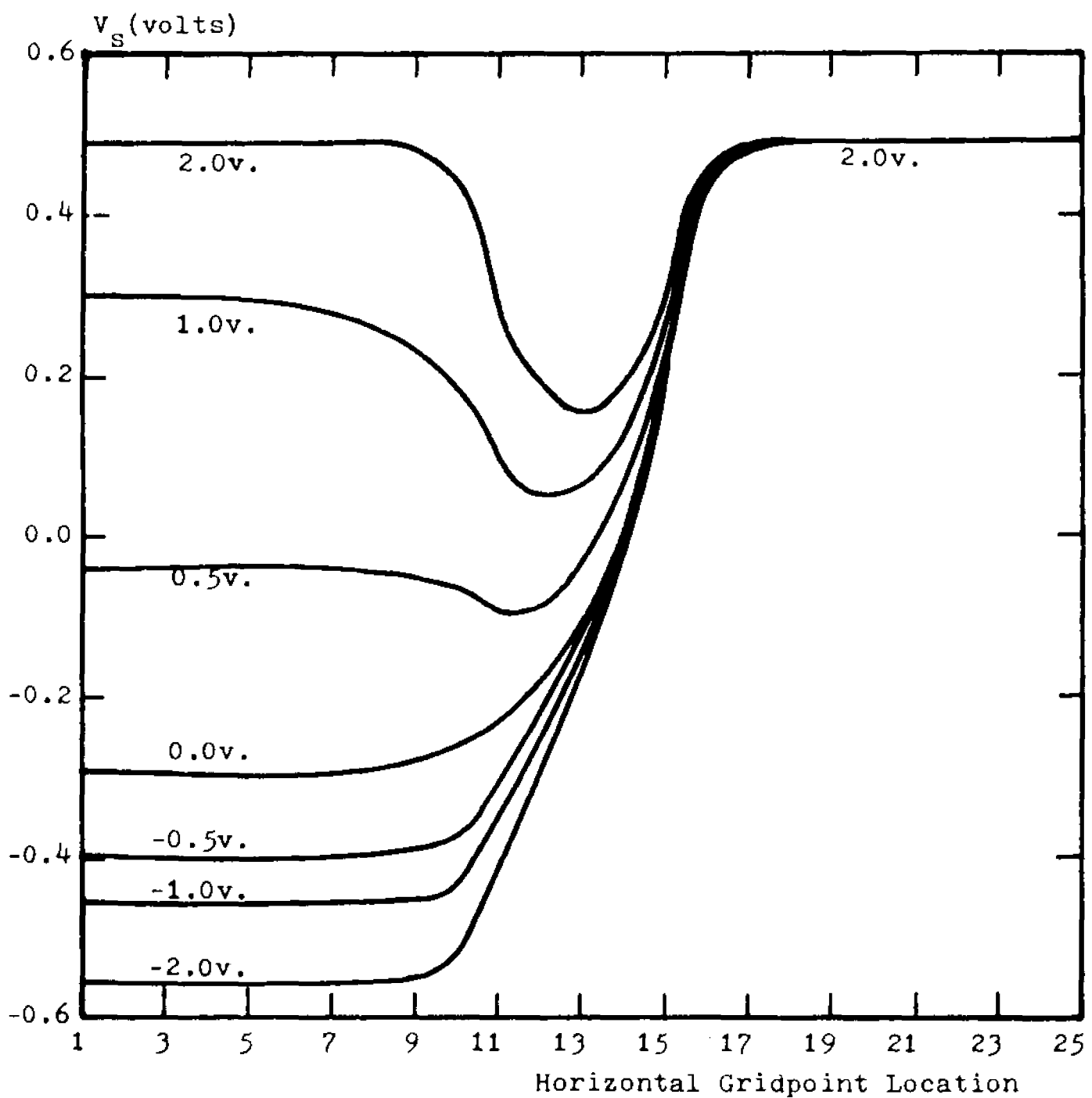
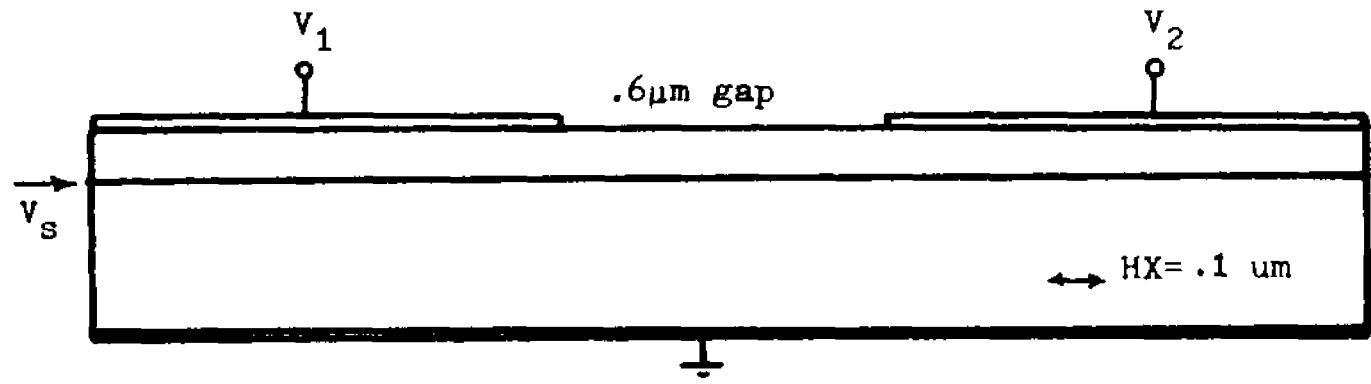


Figure 2.35. Surface potential of the three terminal varactor ($V_2=2\text{v}$).

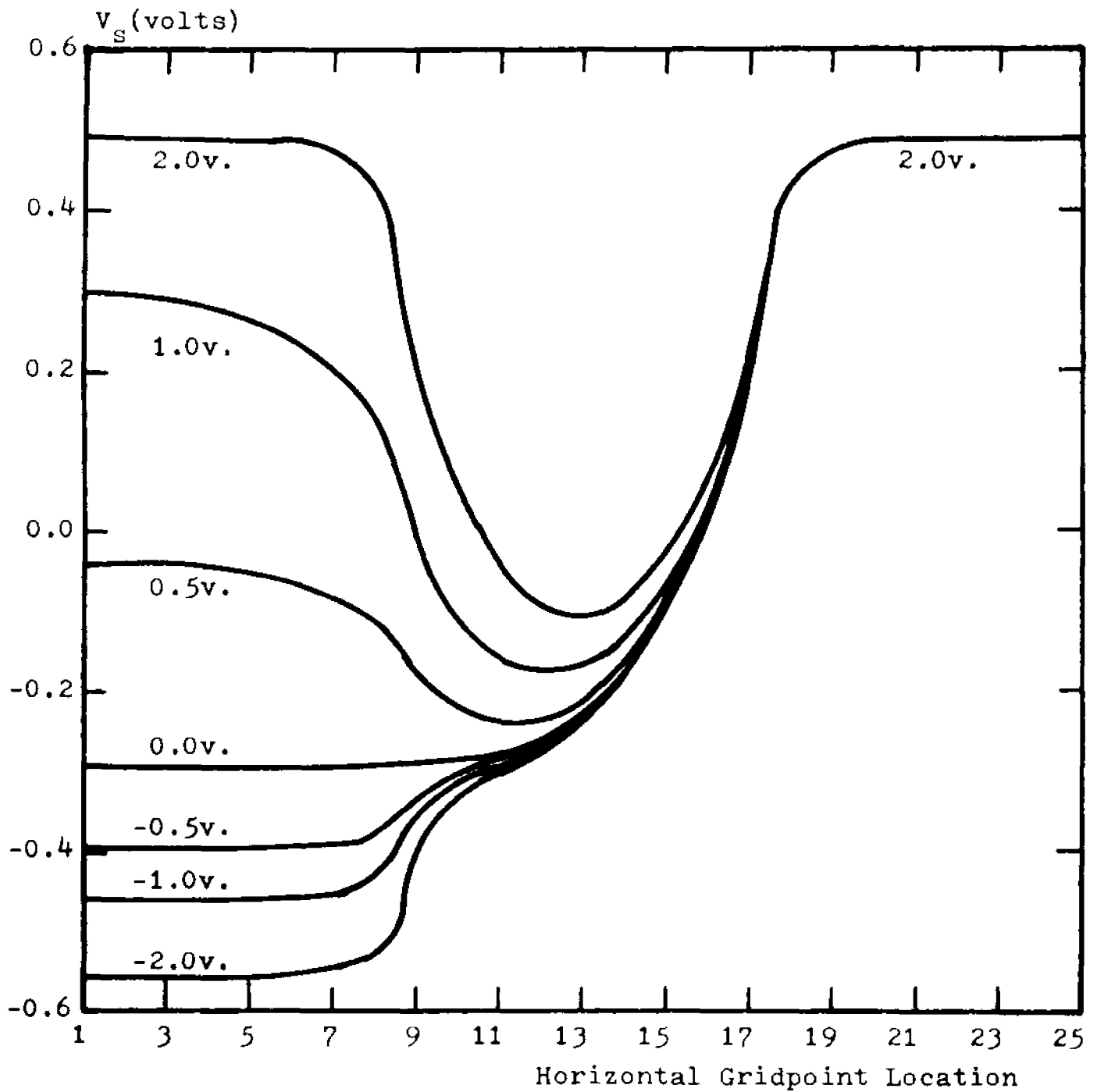
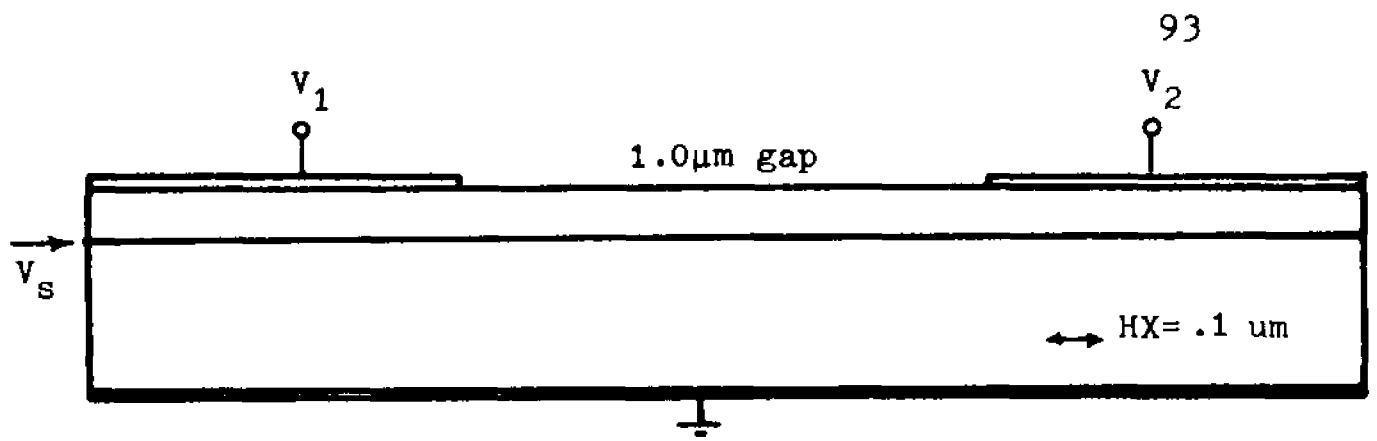


Figure 2.36. Surface potential of the three terminal varactor ($V_2 = 2\text{v}$).

the bulk potential. Such is the case for the region between the plates at the silicon-silicon-dioxide interface. For the sake of clarity and reinforcement of this idea, the surface potential for the various gap widths are plotted in Fig. 2.37 for inversion and accumulation biases. The concentration of mobile charges is shown in Fig. 2.38 for the gap width and biasing of Fig. 2.37.

A study of the potential drop across the gap along the air-insulator interface shows it to be a nonlinear function of the biases. This effect may be observed in Fig. 2.39 where for +2.0 volts on lead 1, the decay along the surface is much slower than for -2.0 volts. The inadequacy of a simple linear approximation is pointed out by the results in Figs. 2.40 and 2.41 for wide gaps. For narrower gaps, these approximations provide a better fit.

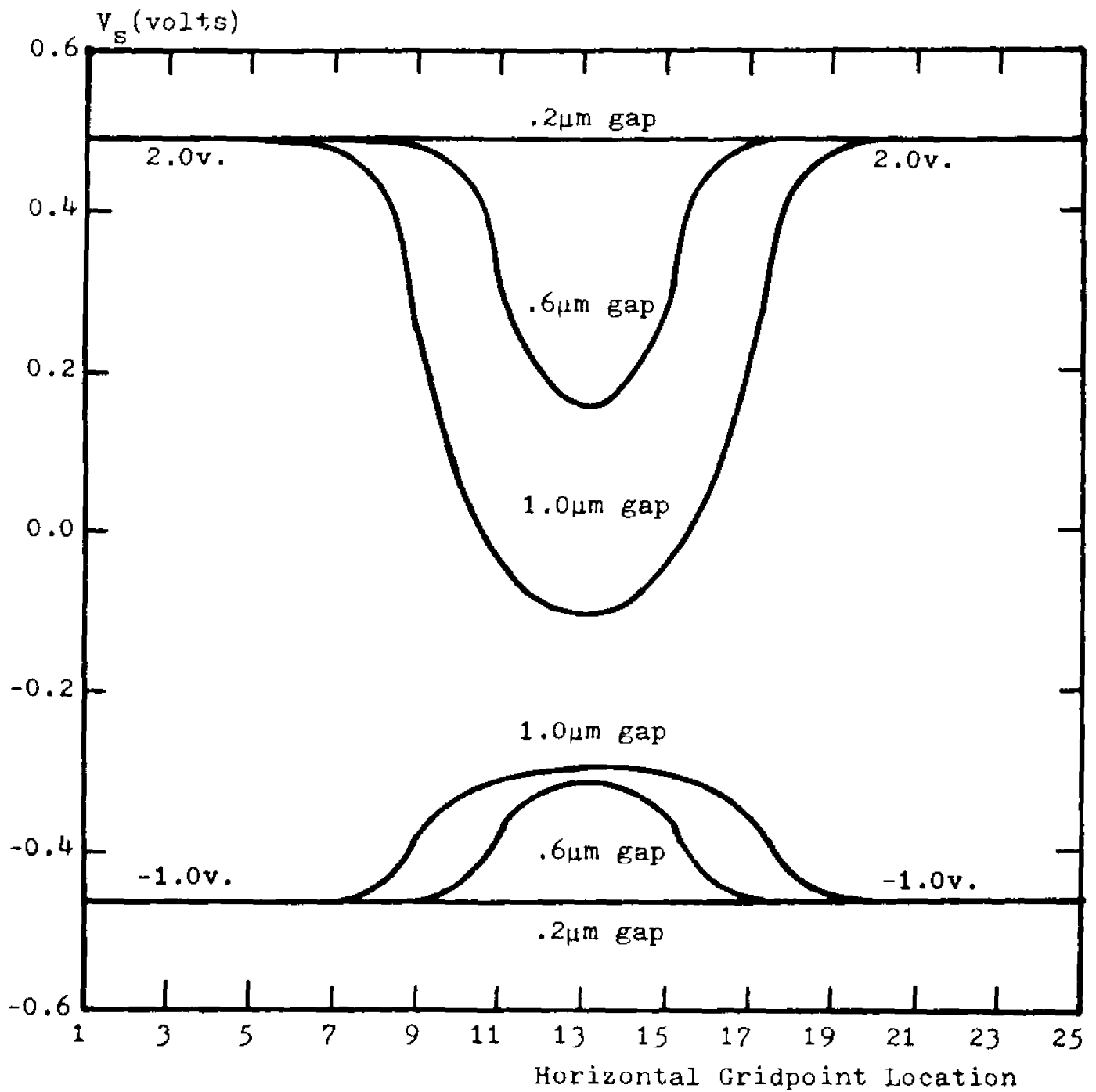
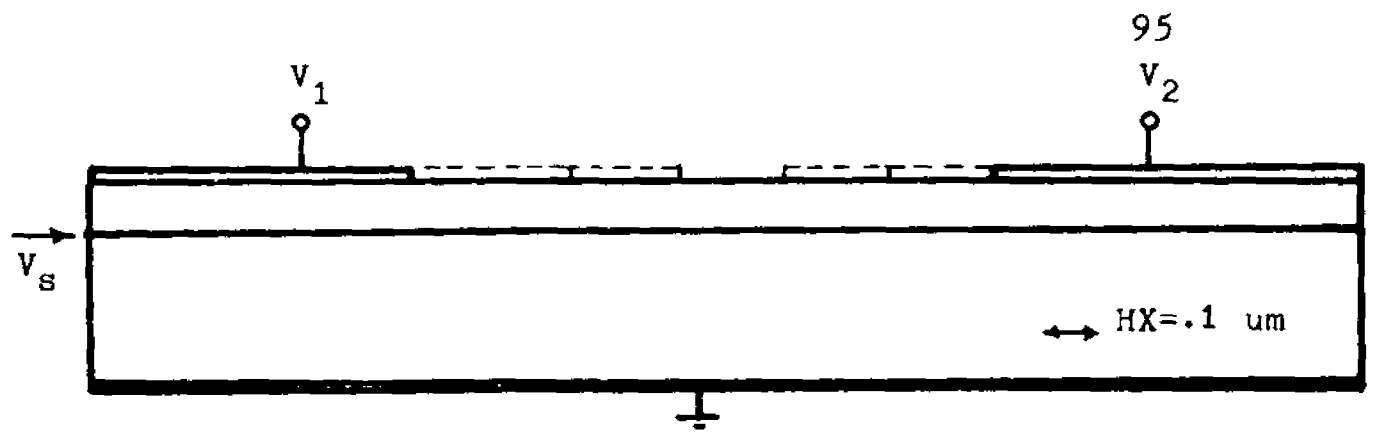


Figure 2.37. Comparison of surface potential for various gap sizes and biases of the three terminal varactor.

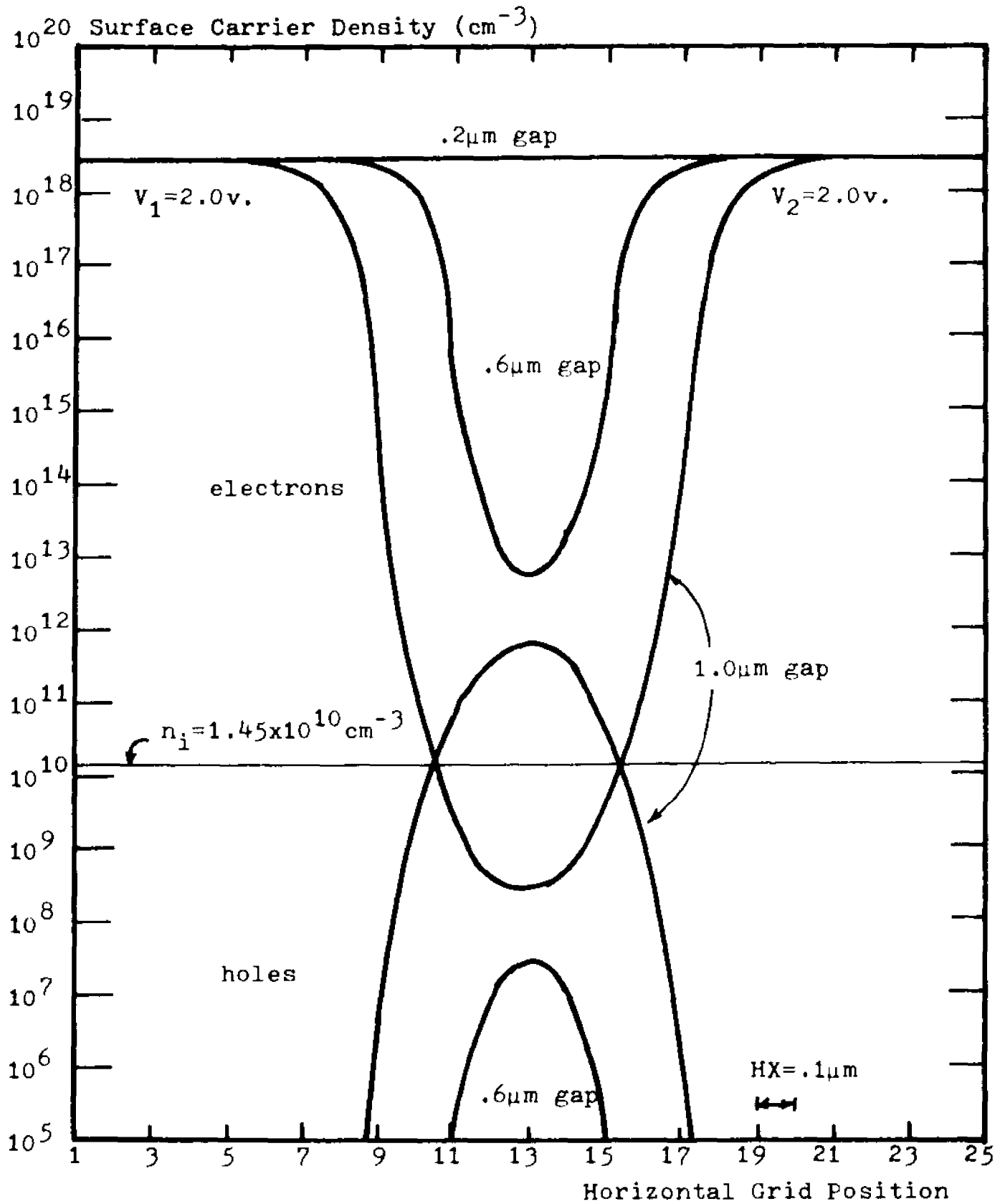


Figure 2.38. Surface carrier concentration for various gap sizes of the three terminal varactor.

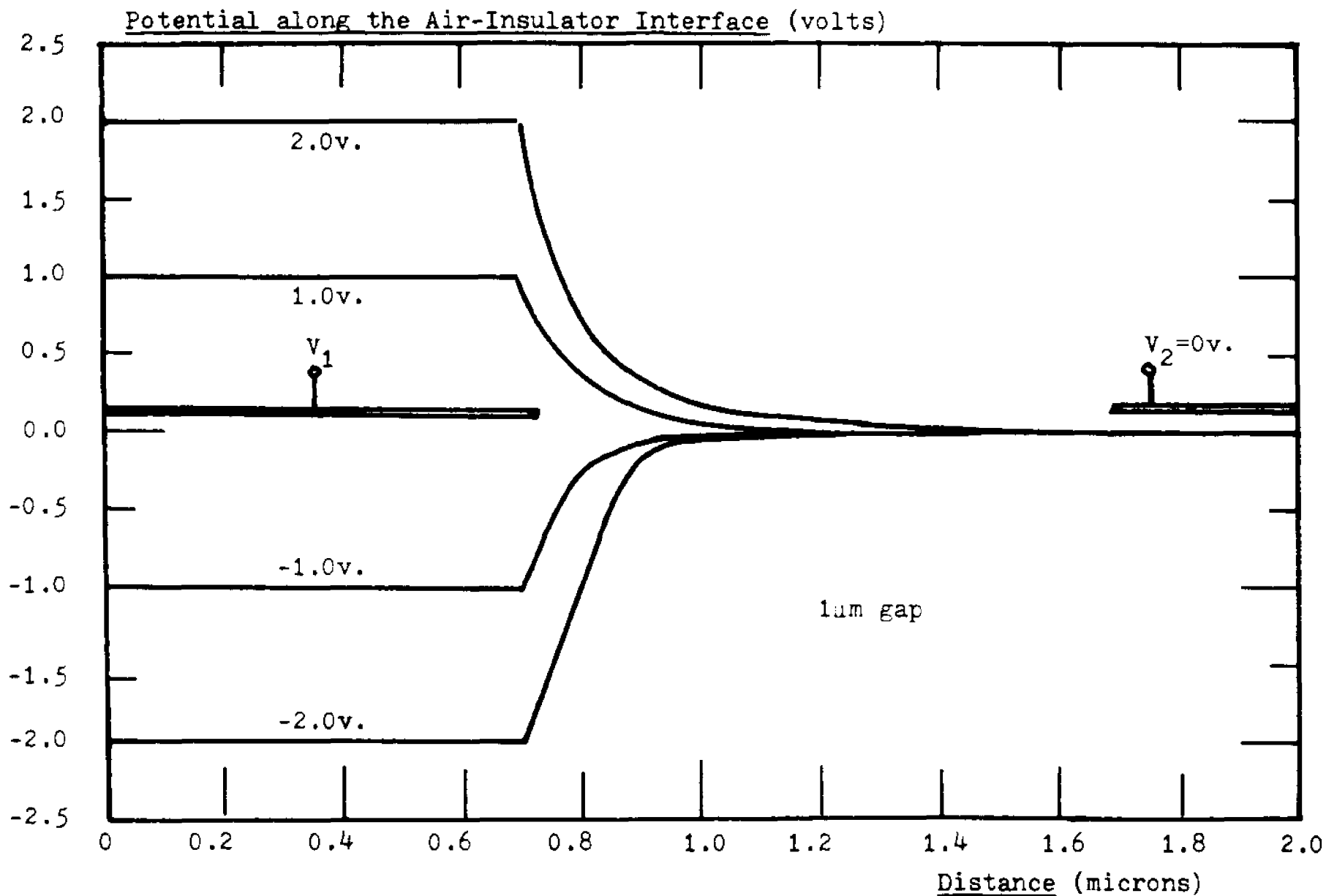


Figure 2.39. Potential along the air-insulator interface as a function of position for varying applied voltages.

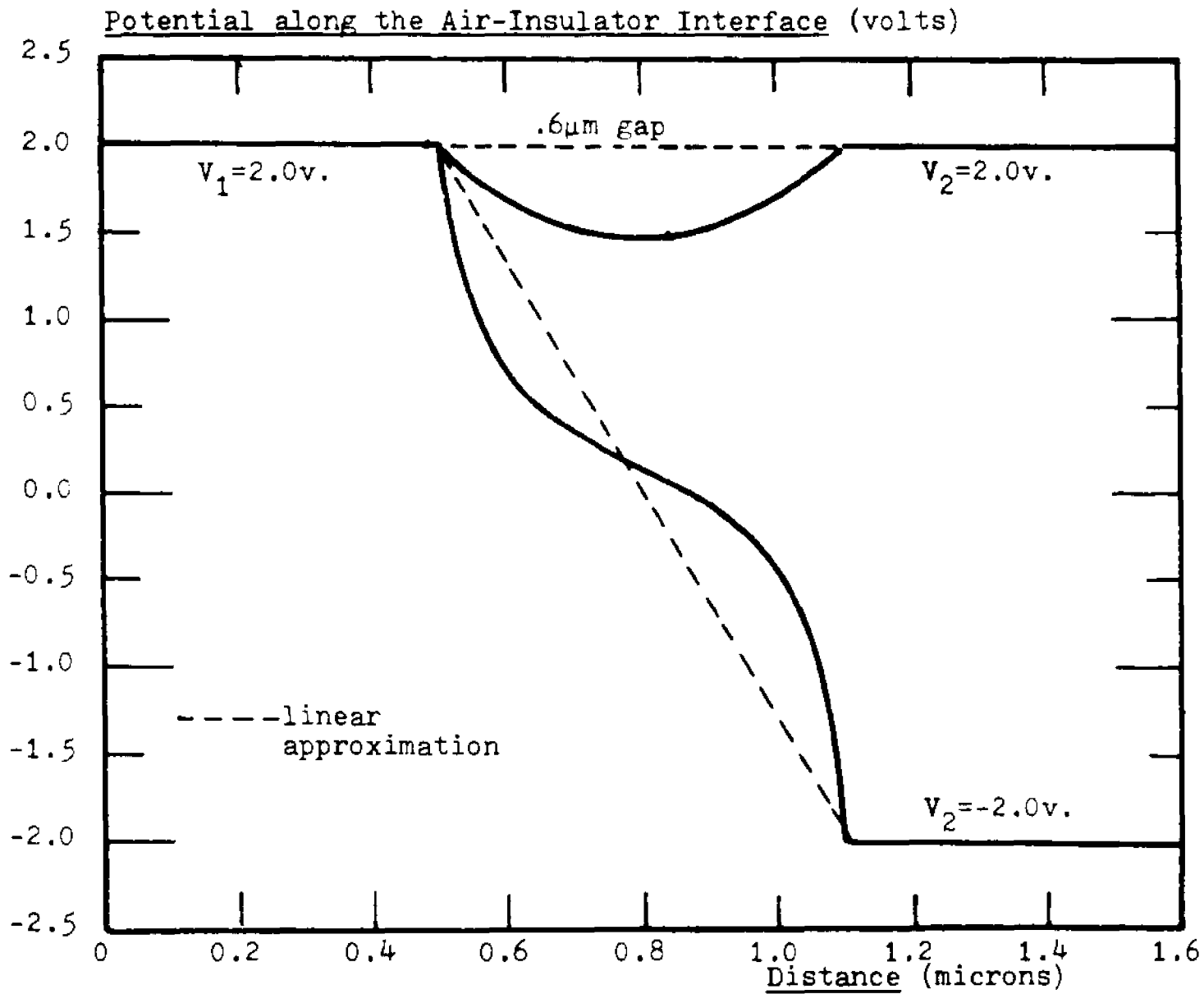


Figure 2.40. Potential along the air-insulator interface for a .6μm gap varactor.

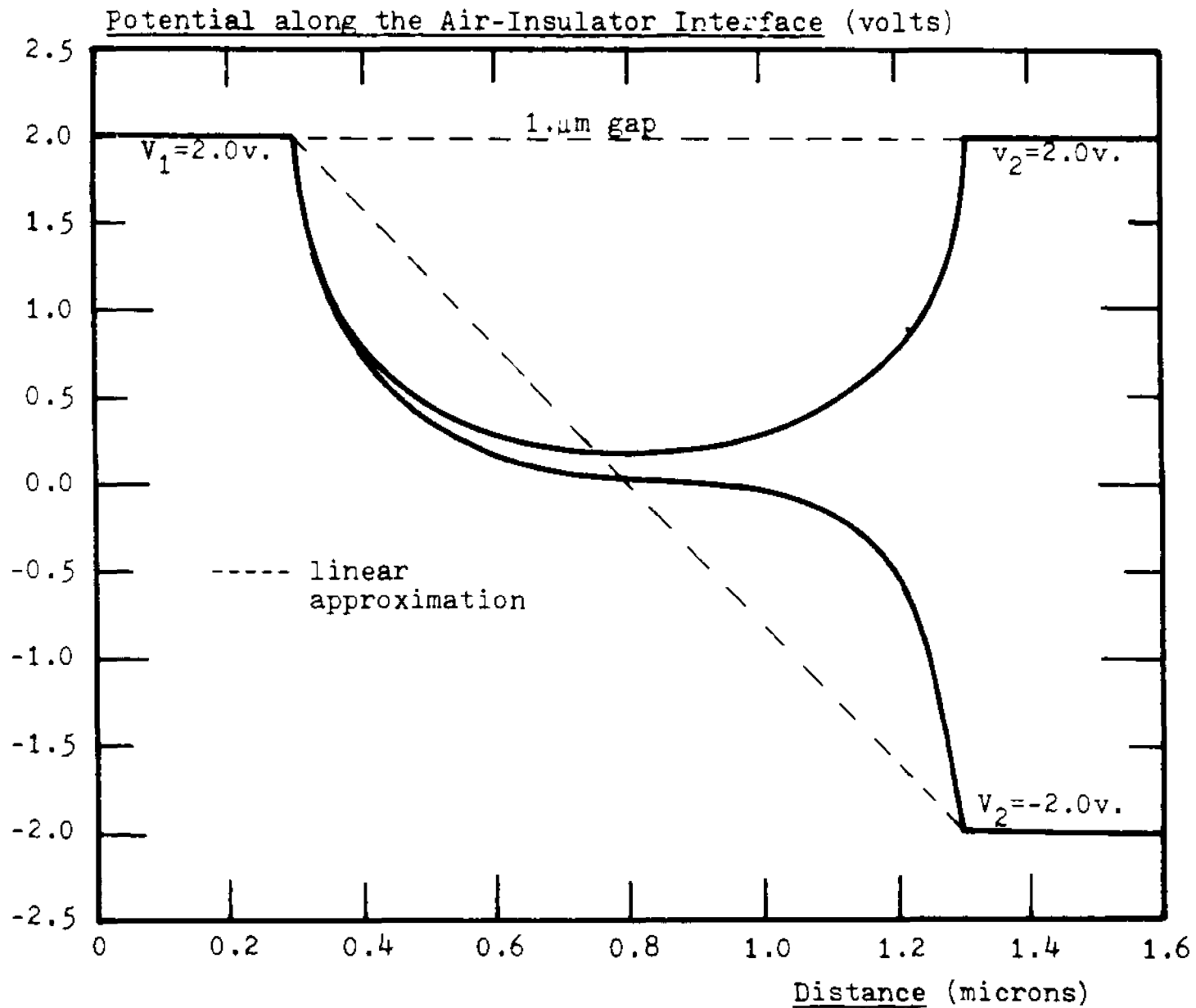


Figure 2.41. Potential along the air-insulator interface for a 1.0 μm gap varactor.

CHAPTER 3

THE SMALL SIGNAL AC MODEL
IN ONE SPATIAL DIMENSION3.1 Introduction

This chapter deals with the solution of the pertinent device equations necessary to model the operation of MIS devices under small signal AC conditions in one spatial dimension. Two particular results are sought and described: the calculation of the small signal admittance of MIS capacitors and the total solution (solution at every interior node) which is employed in Chapter 4.

In Section 3.2 the structure studied is described and the proper equations with associated boundary conditions are developed. The method of complementary functions is applied to the equations to obtain a solution. This is discussed in Section 3.3. The calculation of the small signal admittance using the method described is performed in Section 3.4 where correlation between theory and experiment is pointed out. The small signal AC admittance of several structures are studied: homogeneously doped MIS capacitor, the ion-implanted MIS capacitor and the multilevel MIS capacitor. Correlation between theory and experiment

is demonstrated and a theoretical study of the effect of the implant parameters on the admittance is described.

The solution at every interior point in the device is not necessary to calculate the admittance using the method of complementary functions. This is an enormous advantage of this method over others in the above case. When the total solution is necessary, this method is still able to produce it but at the expense of some computation time. The necessary algorithm is implemented in Section 3.5, where it is labeled the total solution. It is shown that some physical insight into the operation of MIS capacitors may be obtained from knowledge of the total solution. The last section, Section 3.6, contains a comparison of various methods and a study of the reconditioning operation.

3.2 The Structure and Small Signal AC Equations in One Spatial Dimension

Consider the MOS structure of Section 2.2, and superimpose on the DC bias voltage an AC voltage. (see Fig. 3.1). To obtain the two-terminal admittance of the device one must calculate the alternating current excited by the applied AC voltage. The equations describing this relationship are those of Chapter 1, in which the spatial derivatives are ordinary and not partial for this case:

The continuity equations:

$$\frac{\partial p}{\partial t} = -R_p - \frac{1}{q} \frac{dJ_p}{dx} \quad (3.2.1)$$

$$\frac{\partial n}{\partial t} = -R_n + \frac{1}{q} \frac{dJ_n}{dx} \quad (3.2.2)$$

The current density equations:

$$J_p = -qD_p \frac{dp}{dx} - q\mu_p p \frac{dV}{dx} \quad (3.2.3)$$

$$J_n = +qD_n \frac{dn}{dx} - q\mu_n n \frac{dV}{dx} \quad (3.2.4)$$

which are scalar equations for the magnitudes of the current densities, given that their directions are in the positive x direction (see Fig. 3.3)

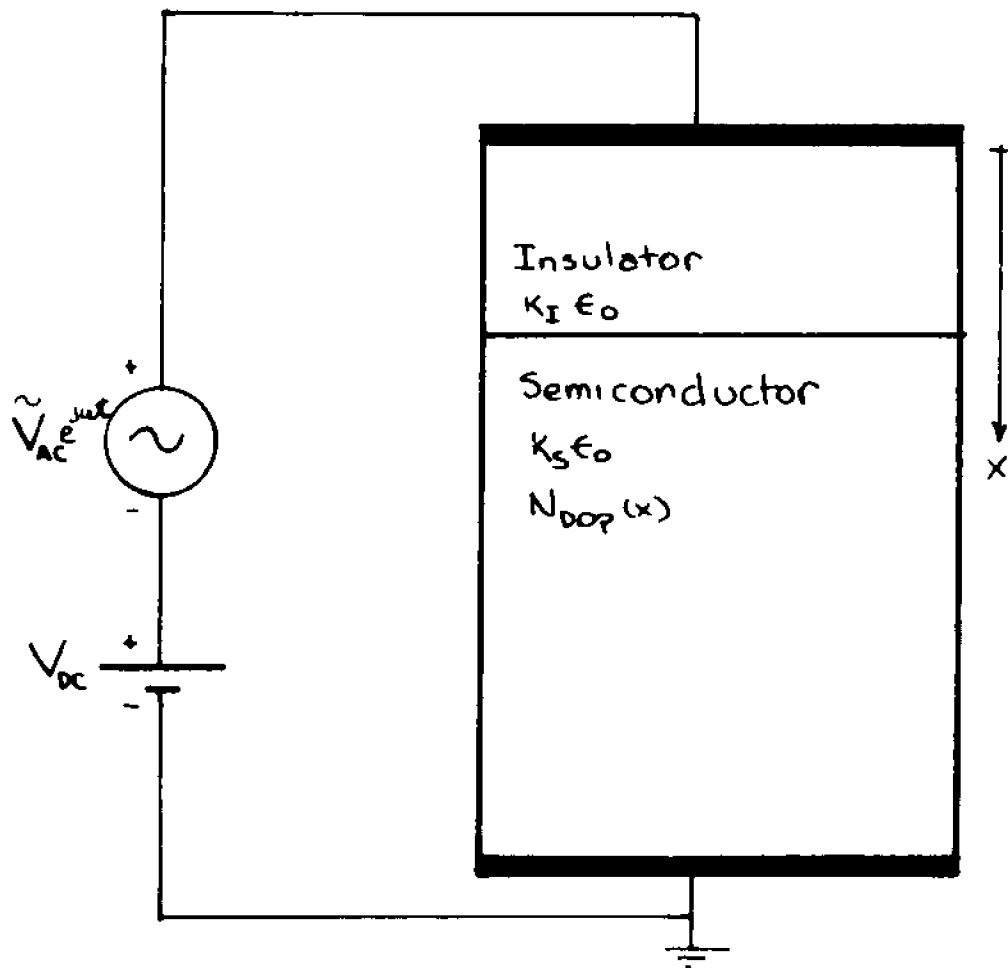


Figure 3.1. The "one dimensional" MIS structure studied with appropriate parameters.

Poisson's equation:

$$\frac{d^2V}{dx^2} = \frac{-q}{\kappa_s \epsilon_0} \cdot (p-n+N_{DOP}) \quad (3.2.5)$$

The above equations are solved in the semiconductor and Laplace's equation in the insulator

$$\frac{d^2V}{dx^2} = 0 \quad (3.2.6)$$

Making the usual small signal approximation, the dependent variables above may be written as

$A = A_0 + \tilde{A}_1 \exp j\omega t$, where A_0 denotes the DC (time invariant) component, \tilde{A}_1 is the AC component, a phasor, ω is the frequency of the input signal with $|\tilde{A}_1| \ll |A_0|$.

The variables may be written as:

$$p = p_0 + \tilde{p}_1 \exp j\omega t \quad ; \quad n_1 = n_0 + \tilde{n}_1 \exp j\omega t$$

$$J_p = J_{p0} + \tilde{J}_{p1} \exp j\omega t \quad ; \quad J_n = J_{n0} + \tilde{J}_{n1} \exp j\omega t$$

$$\text{and } V = V_0 + \tilde{V}_1 \exp j\omega t.$$

Substituting these relationships into Eqs 3.2.1 through 3.2.6 one obtains

$$j\omega \tilde{p}_1 \exp j\omega t = -\tilde{R}_p \exp j\omega t - \frac{1}{q} \left[\frac{dJ_{p0}}{dx} + \frac{d\tilde{J}_{p1}}{dx} \exp j\omega t \right] \quad (3.2.7)$$

$$j\omega \tilde{n}_1 \exp j\omega t = \tilde{R}_n \exp j\omega t + \frac{1}{q} \left[\frac{dJ_{n0}}{dx} + \frac{d\tilde{J}_{n1}}{dx} \exp j\omega t \right] \quad (3.2.8)$$

$$J_{p0} + \tilde{J}_{p1} \exp j\omega t = -qD_p \left[\frac{dp_0}{dx} + \frac{d\tilde{p}_1}{dx} \exp j\omega t \right] - q \mu_p (p_0 + \tilde{p}_1 \exp j\omega t) \left[\frac{dV_0}{dx} + \frac{d\tilde{V}_1}{dx} \exp j\omega t \right] \quad (3.2.9)$$

$$J_{n0} + \tilde{J}_{n1} \exp j\omega t = +qD_n \left[\frac{dn_0}{dx} + \frac{d\tilde{n}_1}{dx} \exp j\omega t \right] - q \mu_n (n_0 + \tilde{n}_1 \exp j\omega t) \left[\frac{dV_0}{dx} + \frac{d\tilde{V}_1}{dx} \exp j\omega t \right] \quad (3.2.10)$$

$$\frac{d^2V_0}{dx^2} + \frac{d^2\tilde{V}_1}{dx^2} \exp j\omega t = \frac{-q}{\kappa_s \epsilon_0} (p_0 + \tilde{p}_1 \exp j\omega t - n_0 - \tilde{n}_1 \exp j\omega t + N_{DOP}) \quad (3.2.11)$$

in the semiconductor, and in the oxide

$$\frac{d^2V_0}{dx^2} + \frac{d^2\tilde{V}_1}{dx^2} \exp j\omega t = 0 \quad (3.2.12)$$

In Chapter 2 it was shown that in this structure, under normal bias conditions, no direct current exists, thus one may set $J_{p0} = J_{n0} = 0$ throughout the semiconductor. Taking advantage of the small signal approximation Eqs. 3.2.7 through 3.2.11 are linearized by setting all second order product terms to zero (a linear relationship for \tilde{R}_p and \tilde{R}_n in terms of \tilde{n}_1 and \tilde{p}_1 is derived in Appendix A). Using these facts and collecting all AC terms, the linearized AC equations become

$$j\omega \tilde{p}_1 = -\tilde{R}_p - \frac{1}{q} \frac{d\tilde{J}_{p1}}{dx} \quad (3.2.13)$$

$$j\omega\tilde{n}_1 = -\tilde{R}_n + \frac{1}{q} \frac{d\tilde{J}_{n1}}{dx} \quad (3.2.14)$$

$$\tilde{J}_{p1} = -qD_p \frac{d\tilde{p}_1}{dx} - q\mu_p \tilde{p}_1 \frac{dV_o}{dx} - q\mu_p p_o \frac{d\tilde{V}_1}{dx} \quad (3.2.15)$$

$$\tilde{J}_{n1} = +qD_n \frac{d\tilde{n}_1}{dx} - q\mu_n \tilde{n}_1 \frac{dV_o}{dx} - q\mu_n n_o \frac{d\tilde{V}_1}{dx} \quad (3.2.16)$$

$$\frac{d^2\tilde{V}_1}{dx^2} = \frac{-q}{\kappa_s \epsilon_o} (\tilde{p}_1 - \tilde{n}_1) \quad (3.2.17)$$

in the semiconductor and in the insulator

$$\frac{d^2\tilde{V}_1}{dx^2} = 0 \quad (3.2.18)$$

The DC quantities appearing in the current density equations (and implicitly in the G-R terms) are p_o , n_o and V_o which satisfy the DC equations and are found from the DC bias, using the algorithm of Chapter 2.

The method of solution of these equations, which shall be described herein necessitates their formulation as a first order set. This is accomplished by the definition of an electric field and assuming its direction to be in the positive x direction. Maintaining the spirit of the small signal approximation, the electric field E may also be thought of as $E = E_o + \tilde{E}_1 \exp j\omega t$ where $E_o = -\frac{dV_o}{dx}$ and $\tilde{E}_1 = -\frac{d\tilde{V}_1}{dx}$. Using these expressions in the above set

of equations yields

$$j\omega\tilde{p}_1 = -\tilde{R}_p - \frac{1}{q} \frac{d\tilde{J}_{p1}}{dx} \quad (3.2.19)$$

$$j\omega\tilde{n}_1 = -\tilde{R}_n + \frac{1}{q} \frac{d\tilde{J}_{n1}}{dx} \quad (3.2.20)$$

$$\tilde{J}_{p1} = -qD_p \frac{d\tilde{p}_1}{dx} + q\mu_p \tilde{p}_1 E_0 + q\mu_p p_0 \tilde{E}_1 \quad (3.2.21)$$

$$\tilde{J}_{n1} = +qD_n \frac{d\tilde{n}_1}{dx} + q\mu_n \tilde{n}_1 E_0 + q\mu_n n_0 \tilde{E}_1 \quad (3.2.22)$$

$$\frac{d\tilde{E}_1}{dx} = \frac{q}{\kappa_s \epsilon_0} (\tilde{p}_1 - \tilde{n}_1) \quad (3.2.23)$$

$$\frac{d\tilde{V}_1}{dx} = -\tilde{E}_1 \quad (3.2.24)$$

Solving for the derivative term in each equation and making use of the assumption that the Einstein relation, $\mu_s = D_s/V_T$, holds, one obtains

$$\frac{d\tilde{J}_{p1}}{dx} = -jq\omega\tilde{p}_1 - q\tilde{R}_p \quad (3.2.25)$$

$$\frac{d\tilde{J}_{n1}}{dx} = +jq\omega\tilde{n}_1 + q\tilde{R}_n \quad (3.2.26)$$

$$\frac{d\tilde{p}_1}{dx} = \frac{-\tilde{J}_{p1}}{q\mu_p V_T} + \tilde{p}_1 \frac{E_o}{V_T} + \frac{p_o}{V_T} \tilde{E}_1 \quad (3.2.27)$$

$$\frac{d\tilde{n}_1}{dx} = \frac{+\tilde{J}_{n1}}{q\mu_n V_T} - \tilde{n}_1 \frac{E_o}{V_T} - n_o \frac{\tilde{E}_1}{V_T} \quad (3.2.28)$$

$$\frac{d\tilde{E}_1}{dx} = \frac{q}{\kappa_s \epsilon_o} (\tilde{p}_1 - \tilde{n}_1) \quad (3.2.29)$$

$$\frac{d\tilde{V}_1}{dx} = -\tilde{E}_1 \quad (3.2.30)$$

in the semiconductor; Laplace's equation is used in the insulator.

Operating the device in the frequency range where the expression for \tilde{R}_p and \tilde{R}_n derived in Appendix A holds, and setting $\tilde{R}_p = \tilde{R}_n = \tilde{R}$ one may replace the G-R term in Eqs. 3.2.25 and 3.2.26 by

$$\tilde{R} = \frac{n_o \tilde{p}_1 + p_o \tilde{n}_1}{\tau_p (n_o + n_i) + \tau_n (p_o + n_i)} \quad (A.8)$$

Equations 3.2.25 through 3.2.30 may be written in more compact form as

$$\dot{\underline{y}} = \underline{A}(x)\underline{y} \quad (3.2.31)$$

where \underline{y} is a vector which is a function of x and $\underline{A}(x)$ a matrix, also a function of x , and the $(\dot{\cdot})$ represents differentiation with respect to x . Figure 3.2 shows the components of \underline{y} and \underline{A} .

Boundary Conditions

Before continuing with the development of a numerical algorithm to solve the set in Fig. 3.2, one must ascertain what type of boundary data is available which in large measure determines the appropriate method of solution.

In the semiconductor there are six variables; the appropriate boundary conditions for each are derived. As seen in Fig. 3.1, the bottom contact of the structure has been made both AC and DC ground (more rigorously, this point in the circuit is considered the reference node). Assuming that the metal-semiconductor junction is ohmic, as was discussed in Chapter 2, the semiconductor bulk may be considered to be at AC ground, i.e. $\tilde{V}_1 = 0$ at $x = x_B$.

The assumed ohmic contact at the metal-semiconductor bulk also implies that no excess carrier concentration exists at that interface; the AC mobile charge carrier concentration may be set equal to zero, i.e. $\tilde{n}_1 = 0$ and $\tilde{p}_1 = 0$ at $x = x_B$.

$$\begin{bmatrix} \dot{j}_{p1} & \dot{p}_1 & \dot{E}_1 & \dot{V}_1 & \dot{N}_1 & \dot{j}_{n1} \end{bmatrix} = \begin{bmatrix} 0 & -j\omega q \frac{n_o q}{A^*} & 0 & 0 & 0 & 0 \\ \frac{-1}{q\mu_p V_T} & \frac{E_o}{V_T} & \frac{E_o}{V_T} & \frac{P_o}{V_T} & 0 & 0 \\ 0 & \frac{q}{K_S \epsilon_o} & \frac{q}{K_S \epsilon_o} & 0 & 0 & 0 \\ 0 & 0 & 0 & -1 & 0 & 0 \\ 0 & 0 & 0 & -\frac{N_o}{V_T} & -\frac{N_o}{V_T} & \frac{-1}{q\mu_n V_T} \\ 0 & \frac{n_o q}{A^*} & 0 & 0 & 0 & 0 \\ 0 & \frac{p_o q}{A^*} & 0 & 0 & 0 & 0 \end{bmatrix} \begin{bmatrix} j_{p1} & p_1 & E_1 & V_1 & N_1 & j_{n1} \end{bmatrix}$$

NOTE: $A^* = \mathcal{Z}_p(n_o + n_i) + \mathcal{Z}_n(p_o + n_i)$

Figure 3.2. The matrix system of the small signal AC problem in one dimension as a set of first order differential equations.

This is all the information that may be obtained at this boundary, leaving the AC currents \tilde{J}_{p_1} and \tilde{J}_{n_1} and the AC electric field \tilde{E}_1 as unknown. At the semiconductor-oxide interface, on the other hand, certain physical models may be used to describe these variables

The mechanism of surface recombination at the insulator-semiconductor surface gives one equation which applies in this case. According to the theory of surface recombination⁽³⁶⁾, the AC current and carrier charge concentration are related by a "surface recombination velocity"

$$\tilde{J}_{p_1} = s_{p_1} \cdot \tilde{p}_1 \quad (3.2.32)$$

for holes, and for electrons

$$\tilde{J}_{n_1} = s_{n_1} \cdot \tilde{n}_1 \quad (3.2.33)$$

It is assumed that the surface recombination velocity is zero giving $\tilde{J}_{p_1} = 0$ and $\tilde{J}_{n_1} = 0$ at $x = x_0$. One may use nonzero values for s_{p_1} and s_{n_1} as given by several authors⁽³⁶⁾⁽³⁷⁾. The effect of using nonzero surface recombination velocity is not investigated in this work.

Applying Gauss' Law at the insulator-semiconductor interface ($x=x_0$) yields an equation relating the remaining variables. Before this is accomplished though, it is worthwhile to explore the nature of the solution in the insulator. There Laplace's equation for the AC potential is to be solved. Designating the potential difference at $x = x_{0-}$ (on the insulator side of the interface, see Fig. 3.3) with respect to the reference

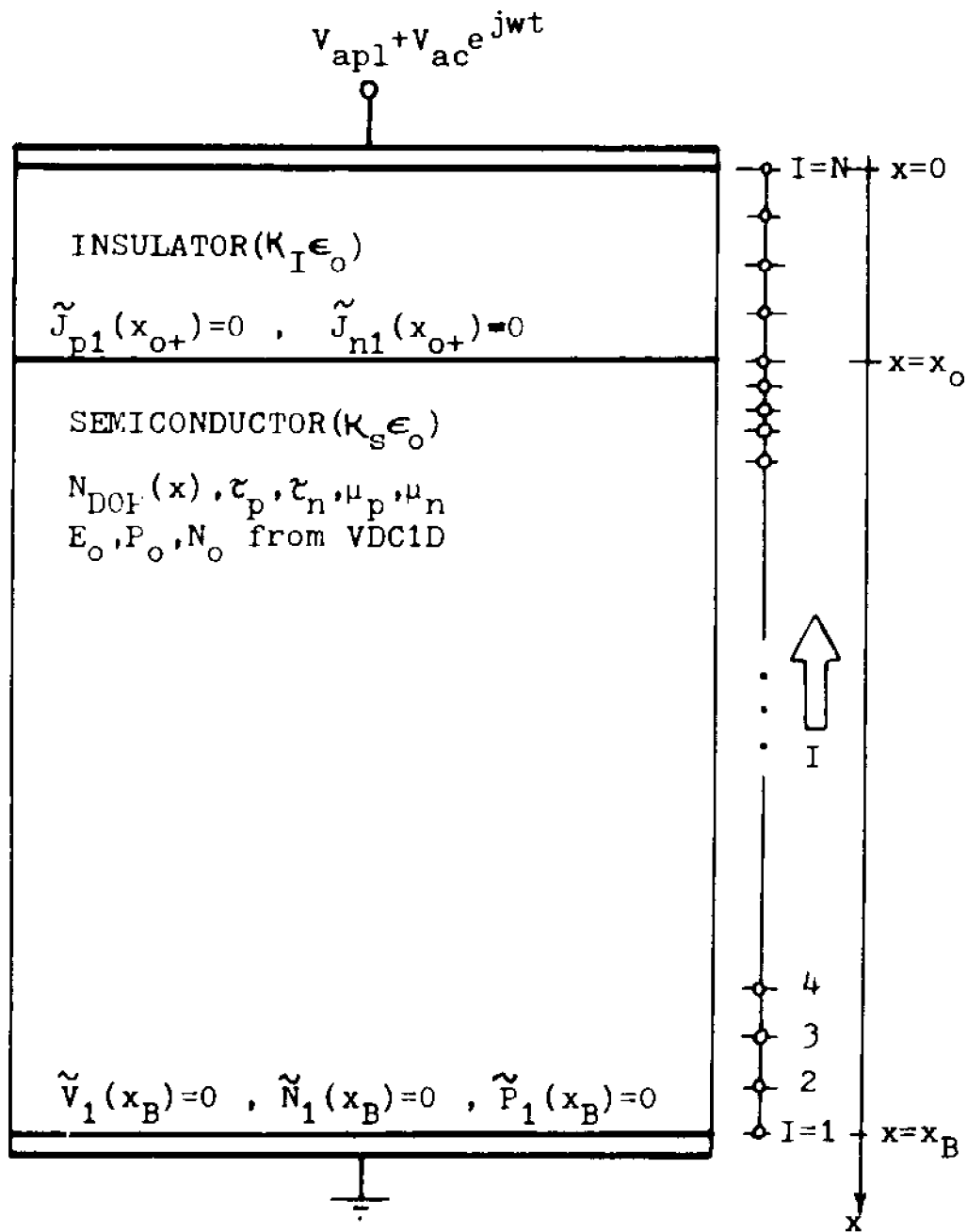


Figure 3.3. The one dimensional MIS structure with boundary conditions, grid and x axis assignments.

node by $\tilde{V}_1(x_{0-})$ and given the applied potential difference of the gate with respect to the reference node, \tilde{V}_{ac} , the solution for $\tilde{V}_1(x)$ is a linear function of distance, and the electric field in the insulator is a constant $\tilde{E}_1(\text{insulator}) = -(\tilde{V}_{ac} - \tilde{V}_1(x_{0-}))/x_0$. Gauss' Law may be expressed as

$$\kappa_S \epsilon_0 \tilde{E}_1(x=x_{0+}) - \kappa_I \epsilon_0 \tilde{E}_1(x=x_{0-}) = 0 \quad (3.2.34)$$

In the above expression, no AC sheet charge densities are assumed to exist at that interface resulting in a zero in the right hand side of Eq. 3.2.34. Substituting the relations above in Eq. 3.2.34 one obtains

$$\kappa_S \epsilon_0 \tilde{E}_1(x_{0+}) = \kappa_I \epsilon_0 \left(\frac{\tilde{V}_1(x_{0-}) - \tilde{V}_{ac}}{x_0} \right) \quad (3.2.35)$$

Furthermore, since $V_1(x_{0-})$ is an unknown, an independent relation is needed to change it to boundary data.

Since the AC potential difference \tilde{V}_1 is everywhere continuous, $\tilde{V}_1(x_{0-}) = \tilde{V}_1(x_{0+})$ at $x = x_0$. This changes Eq. 3.2.35 to

$$\kappa_S \epsilon_0 \tilde{E}_1(x_{0+}) = \kappa_I \epsilon_0 \left(\frac{\tilde{V}_1(x_{0+}) - \tilde{V}_{ac}}{x_0} \right) \quad (3.2.36)$$

which is a relation between \tilde{E}_1 , \tilde{V}_1 and the given applied AC potential difference \tilde{V}_{ac} independent of the ones derived for \tilde{V}_1 , \tilde{n}_1 , \tilde{p}_1 , \tilde{J}_{n1} , and \tilde{J}_{p1} elsewhere. The six

independent boundary data are shown in Fig. 3.3.

The inclusion of the solution of Laplace's equation into the boundary data has made possible the reduction of the number of variables from six in the semiconductor and one in the insulator to just the six in the semiconductor. This consequently reduces the problem to solving just the set of equations shown in Fig. 3.2 with the proper boundary data as derived, from $x = x_B$ to $x = x_{0+}$, i.e. in the semiconductor. Finally one may observe that with the boundary data obtained above, the equations have become a linear boundary value problem.

3.3 The numerical Method of Solution - The Method of Complimentary Functions and Reconditioning Operations

It has been found that a successful solution of the equations in Fig. 3.2 may be obtained by a method of complementary functions⁽³⁸⁾. Whereas Shipman and Roberts have a very thorough discussion of this method⁽³⁹⁾, the formulation of Conte⁽⁴⁰⁾ shall be used here for its conciseness. Consider the general first order linear boundary value problem

$$\dot{\underline{y}}(x) = \underline{A}(x)\underline{y}(x) + \underline{f}(x) \quad (3.3.1a)$$

where \underline{A} is an $n \times n$ matrix and \underline{y} and \underline{f} are vectors of length n in the region $x_b \leq x \leq x_c$ with the boundary conditions

$$\underline{B} \cdot \underline{y}(x_b) = \underline{b} \quad (3.3.1b)$$

$$\underline{C} \cdot \underline{y}(x_c) = \underline{c} \quad (3.3.1c)$$

\underline{B} and \underline{C} are an $[(n-r) \times n]$ matrix of rank $(n-r)$ and a $(r \times n)$ matrix of rank r respectively, and \underline{b} and \underline{c} are vectors of length $(n-r)$ and r respectively.

For the linear problem the solution is of the form

$$\underline{y}(x) = \underline{w}(x) + \beta_1 \underline{y}^1(x) + \dots + \beta_r \underline{y}^r(x) \quad (3.3.2)$$

where \underline{y}^k are linearly independent solutions and β_k the corresponding combining constants. Furthermore, expressing these solutions as columns of a matrix $\underline{Y}(x)$ and the

constants as a vector $\underline{\beta}$, Eq. 3.3.2 may be written as

$$\underline{y}(x) = \underline{w}(x) + \underline{Y}(x) \cdot \underline{\beta} \quad (3.3.3)$$

\underline{Y} having rank equal to r and $\underline{\beta}$ being of length r . The solution $\underline{w}(x)$ satisfies the inhomogenous equation and represents the particular solution

$$\dot{\underline{w}}(x) = \underline{A}(x) \cdot \underline{w}(x) + \underline{f}(x) \quad (3.3.4)$$

and the solution matrix $\underline{Y}(x)$ satisfies the homogenous problem

$$\dot{\underline{Y}}(x) = \underline{A}(x) \cdot \underline{Y}(x) \quad (3.3.5)$$

At $x = x_b$, $\underline{w}(x_b)$ is chosen so that it satisfies

$$\underline{B}\underline{w}(x_b) = \underline{b} \quad (3.3.6)$$

forcing $\underline{Y}(x_b)$ necessarily to satisfy

$$\underline{B} \cdot \underline{Y}(x_b) \cdot \underline{\beta} = 0 \quad (3.3.7)$$

At $x = x_c$, applying the relation of Eq. 3.3.1c one obtains

$$\underline{C} \cdot \left[\underline{w}(x_c) + \underline{Y}(x_c) \cdot \underline{\beta} \right] = \underline{c} \quad (3.3.8)$$

The variables $\underline{w}(x_b)$, $\underline{Y}(x_b)$ and $\underline{\beta}$ then are determined by Eqs. 3.3.6, 3.3.7 and 3.3.8. A scheme of solution is as follows:

1. Solve Eq. 3.3.6 for $\underline{w}(x_b)$ and integrate Eq. 3.3.4 forward from $x = x_b$ to $x = x_c$ with this vector; obtain $\underline{w}(x_c)$.

2. Choose r vectors of length n which are linearly independent (they shall be the r columns of $Y(x_b)$) which satisfy

$$\underline{B} \cdot \underline{Y}(x_b) = \underline{0} \quad (3.3.9)$$

This insures that Eq. 3.3.7 is satisfied for nonzero $\underline{\beta}$.

3. Integrate forward with each column of \underline{Y} from $x = x_b$ to $x = x_c$ and obtain $\underline{Y}(x_c)$.
4. At $x = x_c$, apply the relation given by Eq. 3.3.8 with the solutions obtained above in 1 through 3 and solve for $\underline{\beta}$ from

$$\underline{\beta} = [\underline{C} \cdot \underline{Y}(x_c)]^{-1} \cdot [\underline{c} - \underline{C} \cdot \underline{w}(x_c)] \quad (3.3.10)$$

The constants, $\underline{\beta}$, thus obtained will hold for $x_b \leq x \leq x_c$ and the solution $y(x)$ for any x in this region may be found by using $\underline{Y}(x)$, $\underline{w}(x)$ and $\underline{\beta}$ from above, into Eq. 3.3.3.

This method essentially solves the boundary value problem as if it were an initial value problem. If Kronecker delta values were used for the vector components of \underline{Y} , then $\underline{\beta}$ is really the missing boundary data at x_b . From the theory of linear ordinary differential equations it is known that if one begins integration with a set of independent boundary value vectors, then the solution vectors will remain linearly independent through the course of integration. This insures that at $x = x_c$

$C \cdot Y$ will have an inverse and \underline{g} may be found unambiguously.

Numerical implementation of this procedure to the problem being considered causes several difficulties. First, the assurance of continued linear independence of the shooting vectors can only be made if the integration is performed with infinite precision. Since all machines have finite precision, even in a stable numerical method of integration⁽⁴¹⁾ the accumulation of round-off error may cause the solution vectors to become linearly dependent. Even if linear independence is not lost, but the vectors in $Y(x_c)$ come sufficiently close together such that $CY(x_c)$ has a high condition number⁽⁴²⁾, great difficulty may be expected in finding its inverse and \underline{g} accurately.

A second source of the same problem is the nature of the o.d.e. itself. If the problem is ill-conditioned or "stiff" then the same buildup of linear dependence may be found as integration progresses. This ill-conditioning may be defined on the "big" matrix of the problem, as defined by Bickley and McNamee⁽⁴³⁾, where the ratio of the largest eigenvalue to the smallest is much greater than 1. Example of this behavior shown by ill-conditioned systems may be found in Fox⁽⁴⁴⁾, Shipman and Roberts⁽⁴⁵⁾ and others⁽⁴⁶⁾. An indication of this ill-conditioning is the several-orders-of-magnitude difference in the coefficients of the "big" matrix.

The power of the reconditioning method is that it will successfully handle these problems when necessary.

If the r independent integrations are conducted in parallel then at each integration node, some check on the linear independence may be performed and, if a threshold condition is exceeded, reorthonormalization via a Gram-Schmidt⁽⁴⁰⁾ process is used before the integration is continued.

Reconditioning

For problems which are well behaved and for few nodes of integration, one may safely dispense with reorthonormalization; but for most other applications, some reconditioning may be required for a successful solution. The Gram-Schmidt process is but one method to reorthonormalize the solution vectors. Matrix transformations which will change $\underline{Y}(x)$ to $\underline{Y}^*(x)$ where \underline{Y}^* has columns which are orthonormal, or even just orthogonal, are also suited to recondition \underline{Y} and are used by others⁽⁴⁷⁾ with success. The Gram-Schmidt has great appeal in that it may be easily coded and, as is seen, becomes an integral part of the independence checking algorithm.

The Gram-Schmidt process as described in any number of texts (see for example DeRusso, Roy and Close⁽⁴⁸⁾) is implemented. Given that the columns of \underline{Y} shall be orthonormalized at a given point x_i , the process may be described as:

1. Take the first column of $\underline{Y}(x_i)$, \underline{y}_i and normalize it with respect to its magnitude, consider this to be \underline{y}_1^*

$$\underline{y}_1^* = \underline{y}_1 / |\underline{y}_1| \quad (3.3.11)$$

2. Take the second column of $\underline{Y}(x_i)$, \underline{y}_2 and subtract from it the component of \underline{y}_2 which lies in the \underline{y}_1^* direction

$$\underline{n}_2 = \underline{y}_2 - \langle \underline{y}_2, \underline{y}_1^* \rangle \cdot \underline{y}_1^* \quad (3.3.12)$$

note that the symbol $\langle \cdot, \cdot \rangle$ is used to denote the vector product and that \underline{y}_1^* is a unit vector.

3. To obtain \underline{y}_2^* , normalize \underline{n}_2 with respect to the magnitude of \underline{n}_2

$$\underline{y}_2^* = \underline{n}_2 / |\underline{n}_2| \quad (3.3.13)$$

4. Repeat this process for the third column of \underline{Y} , \underline{y}_3 ; the component of \underline{y}_3 in the \underline{y}_1^* and \underline{y}_2^* directions are removed from \underline{y}_3

$$\underline{n}_3 = \underline{y}_3 - \langle \underline{y}_3, \underline{y}_1^* \rangle \cdot \underline{y}_1^* - \langle \underline{y}_3, \underline{y}_2^* \rangle \cdot \underline{y}_2^* \quad (3.3.14)$$

and then normalized,

$$\underline{y}_3^* = \underline{n}_3 / |\underline{n}_3| \quad (3.3.15)$$

The vectors $\{\underline{y}_1^*, \underline{y}_2^*, \underline{y}_3^*\}$ are orthogonal and of unit magnitude. For the small signal AC equations, the AC variables are complex quantities, therefore the above vectors have components which are complex and the scalar product operation above must be defined accordingly.

Thus, the operation on any two vectors of length n,

with complex coefficients is

$$\langle \tilde{\mathbf{u}}, \tilde{\mathbf{y}} \rangle = \sum_{i=1}^N \tilde{u}_i \cdot \tilde{y}_i \quad (3.3.16)$$

where the prime denotes the complex conjugate. Using this definition, the length of a vector is

$$|\tilde{\mathbf{u}}| = \sqrt{\sum_{i=1}^N \tilde{u}_i \cdot \tilde{u}_i} \quad (3.3.17)$$

Beside the type of reconditioning method employed, a question of prime importance is when should reconditioning be applied. The literature is of little help in this matter since procedures for determining the optimum number of reconditioning operations for a given problem are not known. The problem may be restated in the following manner; as the integration proceeds, the columns of $\underline{\mathbf{Y}}$ not only may lose their orthonormal character but may even become linearly dependent. Whereas loss of orthonormality may be tolerated, and one may still obtain an accurate solution, loss of linear independence causes the loss of completeness of the solution. This may lead to inaccuracies which may not be tolerable. A check on the linear dependence of the columns of $\underline{\mathbf{Y}}$ shows very little until the columns are linearly dependent, in which case, one cannot apply the Gram-Schmidt procedure, since one of the orthogonal directions has already been lost. Therefore a criteria

has to be developed to check how rapidly one is "losing" linear independence and perform a reconditioning operation when this criteria exceeds a threshold. The word "losing" is in quotes since a set of vectors will either be, or not be, linearly dependent, there is no intermediate condition. One parameter which may be checked is how close vectors are coming to each other. Conte⁽⁴⁰⁾ suggests checking the pairwise linear independence of the vectors by calculating the normalized dot products of all vectors with all other vectors. When any one of these products becomes arbitrarily close to unity, perform a reconditioning transformation. The fallacy with this method is that even when the pairwise dot products remain smaller than unity by an epsilon, any three vectors may become coplanar. The same may be true for higher combinations of vectors in more than three dimensional space. Thus Conte's criteria checks solely for colinearity of the vectors and fails in general for more than two dimensional vector space. In this chapter one is dealing with six dimensional vectors; in Chapter 4, vectors of over 30 dimensions are common. If the Gram-Schmidt process is performed at every step and the resulting \underline{Y}^* kept only when necessary, a simple algorithm to check linear independence and how close the vectors are coming together is:

1. Perform the Gram-Schmidt and save in a temporary location \underline{Y}^* .

2. Obtain the dot product of each of the columns of \underline{Y} before orthonormalization and after. Normalize with respect to the magnitude of columns of \underline{Y} .
3. If any one of these dot products is less than ϵ , (e.g., $\epsilon = 0.1$), substitute \underline{Y}^* for \underline{Y} ; keep the orthonormalized set.

This criteria may be expressed algebraically as

$$\min_j \{ \langle \underline{y}_j / |\underline{y}_j|, \underline{y}_j^* \rangle \} \leq \epsilon \quad (3.3.18)$$

The reasoning behind this criterion is illustrated in the following manner. Consider the second vector: if after one has subtracted from it everything in the first vector's direction one is left with a vector (normalized with respect to its magnitude) which when dotted with the original (also normalized) gives a dot product less than ϵ , then the second vector before orthonormalization had a large component in the direction of the first vector. One may say, even though they are linearly independent, that they are "becoming" colinear or "coming together". With subsequent vectors, after the orthonormalization is performed, calculating the dot product of the original vector with the new orthonormalized one, checks how much of the original vector was in the direction of the previous ones. If any one of these dot products are less than a prescribed number ϵ , then

the orthonormalized set is kept, if not, then the integration continues with the old set.

The only drawback of this method is that the Gram-Schmidt procedure must be performed at every step whether or not the new vectors are kept. On the other hand, one must consider that in one way or another some check on the linear independence of the vectors must be made at every step (which will also use computation time and perhaps extra storage space). In this case the linear independence checking routine and the orthonormalization routine are one and the same, a savings in complexity of coding and subsequent debugging time. No effort has been spent in finding other linear independence checking routines and comparing the efficiency of a prospective method with the one implemented.

Application of reorthonormalization is essentially a matrix transformation and care must be exercised in interpreting the results. For example, suppose the orthonormalization criterion is exceeded at some point in the integration, e.g. at $x=x_i$; then, at this point a set of orthonormal vectors is produced from the old

$$\underline{Y}^*(x_i) = \underline{Y}(x_i)\underline{P}_i \quad (3.3.19)$$

where \underline{P}_i is the $(r \times r)$ transformation matrix. For simplicity assume that only one transformation was necessary and integration has carried \underline{Y}^* all the way to x_c .

There, Eq. 3.3.10 is used to solve for the proper β 's. In this case, though, the $\underline{\beta}$ obtained is actually a $\underline{\beta}^*$ and can only combine the \underline{Y}^* to a solution in $x_i \leq x \leq x_c$, that is, $\underline{\beta}^*$ holds only in that region. To find the proper β 's in the region $x_b \leq x \leq x_i$, the inverse transformation of Eq. 3.3.11 must be performed, i.e. if

$$\underline{y}(x) = \underline{Y}^*(x_i)\underline{\beta}^* = \underline{Y}(x_i)\underline{P}_i\underline{\beta}^* = \underline{Y}(x_i)\underline{\beta} \quad (3.3.20)$$

then the relationship between $\underline{\beta}$ and $\underline{\beta}^*$ is

$$\underline{\beta} = \underline{P}_i\underline{\beta}^* \quad (3.3.21)$$

If the \underline{Y} matrix has been stored at every point of integration, just saving the \underline{P} matrices at the orthonormalization points would be sufficient if only one pass is made through the region. To minimize memory storage, two passes may be made saving only the \underline{P} 's on the first and obtaining all $\underline{\beta}$'s at the end of that pass. Then, a second pass is done where, using the $\underline{\beta}$'s found in the first pass, a solution is found at every point by use of Eq. 3.3.3. If only the solution is required at the last region of orthonormalization then only one pass is needed. As is shown in Section 3.4, such is the case in the calculation of the small signal AC admittance.

Returning to the small signal AC problem, the \underline{A} matrix is shown in Fig. 3.2. The forcing vector $\underline{f}(x)$ is in this case the null vector $\underline{0}$, making the system homogeneous. The \underline{y} vector has the following components:

$$\tilde{y} = \begin{bmatrix} \tilde{J}_{p1} \\ \tilde{P}_1 \\ \tilde{E}_1 \\ \tilde{V}_1 \\ \tilde{N}_1 \\ \tilde{J}_{n1} \end{bmatrix} \quad (3.3.22)$$

The matrix \underline{B} and the vector \underline{b} may be found from the boundary conditions:

$$\underline{B} = \begin{bmatrix} 0 & 1 & 0 & 0 & 0 & 0 \\ 0 & 0 & 0 & 1 & 0 & 0 \\ 0 & 0 & 0 & 0 & 1 & 0 \end{bmatrix} ; \quad \underline{b} = \begin{bmatrix} 0 \\ 0 \\ 0 \end{bmatrix} \quad (3.3.23)$$

and similarly, the matrix \underline{C} and vector \underline{c} are:

$$\underline{C} = \begin{bmatrix} 1 & 0 & 0 & 0 & 0 & 0 \\ 0 & 0 & 0 & 0 & 0 & 0 \\ 0 & 0 & \frac{\kappa_{Si} \cdot x_0}{\kappa_{SiO_2}} & -1 & 0 & 0 \end{bmatrix} ; \quad \underline{c} = \begin{bmatrix} 0 \\ 0 \\ -V_{ac} \end{bmatrix} \quad (3.3.24)$$

The number of components of \tilde{y} is 6, thus $n=6$ and $r=3$, by the nature of the boundary data. The vector \underline{w} then is totally unnecessary since it may be taken to be the null vector at $x=x_B$, i.e. $\underline{w}(x_B)=0$. Notice that $x_b=x_B$ and $x_c=0$ for this problem, where x_B is the bulk and $x=0$ is the metal-silicon dioxide interface (see Fig. 3.3).

Using Kronecker delta initial conditions for \tilde{J}_{p1} , \tilde{J}_{n1} and \tilde{E}_1 , the \underline{Y} matrix at $x=x_B$ is

$$\underline{Y}(x_B) = \begin{bmatrix} 1 & 0 & 0 \\ 0 & 0 & 0 \\ 0 & 1 & 0 \\ 0 & 0 & 0 \\ 0 & 0 & 0 \\ 0 & 0 & 1 \end{bmatrix} \quad (3.3.25)$$

In Chapter 2 the DC parameters E_0 , p_0 , n_0 are found. One observes that the values obtained for these quantities differ by several orders of magnitude as functions of distance. For any x some of the components of \underline{A} which contain these quantities also differ by several orders of magnitude. It is recognized then that this problem has the potential of being ill-conditioned⁽⁴⁹⁾. The use of orthonormalization may become necessary and the problem must therefore be coded with that capability.

The region $0 \leq x \leq x_B$ is discretized into N points, as shown in Fig. 3.3, labeled with the subscript I . The values of the DC variables are found from the one dimensional DC algorithm and all other constants in \underline{A} shown in Fig. 3.2 are self-explanatory.

The coding flow chart is given in Fig. 3.4. The method of integration is a stable predictor-corrector and is contained in subroutine (STEP). The discretized equations and formulas used in integration are discussed below.

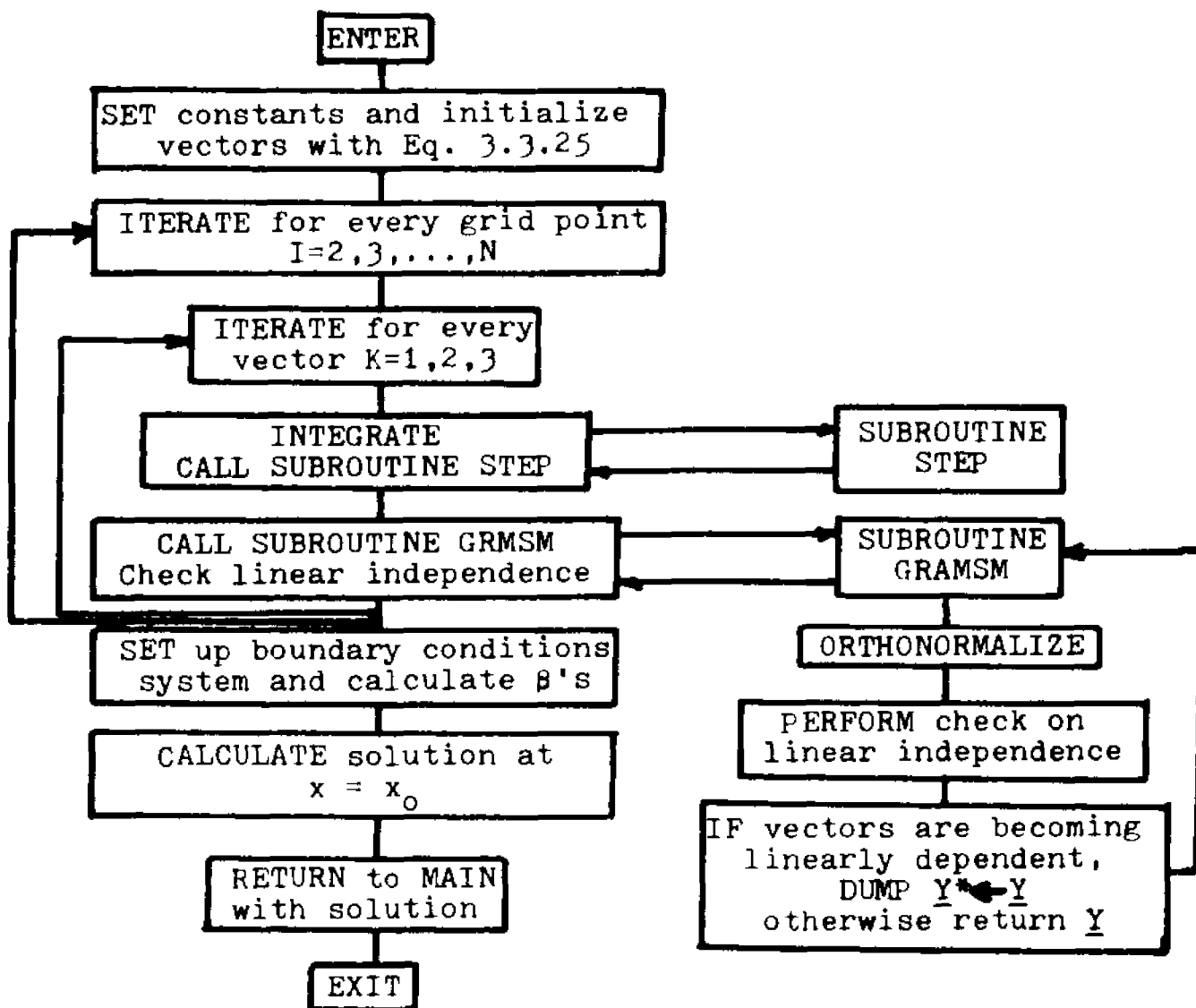


Figure 3.4. Computational flowchart of the algorithm VAC1D.

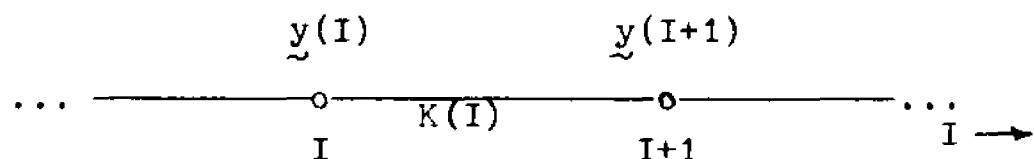
Method of Integration

Whereas any reasonable scheme of integration which exhibits stability over the region of computation may be used, a simple predictor-corrector method has been found satisfactory. Schemes which include more grid points may be more accurate, but the scheme used herein requires less memory allocation, less computation and is much simpler to encode. The scheme is as follows.

Consider integrating

$$\dot{\underline{y}}(x) = \underline{A}(x) \underline{y}(x) \quad (3.3.26)$$

over the following two grid points:



where $K(I)$ is the grid length between $I=I_1$ and $I=I_2$.

The prediction step is:

$$\underline{y}^* = \underline{y}(I) + K(I) \cdot \underline{A}(I) \cdot \underline{y}(I) \quad (3.3.27)$$

where \underline{y}^* is the intermediate solution vector. The correction step is:

$$\underline{y}(I+1) = \underline{y}(I) + K(I) \cdot \left[\underline{A}(I) \cdot \underline{y}(I) + \underline{A}(I+1) \cdot \underline{y}^* \right] / 2 \quad (3.3.28)$$

Application of this scheme to the equations in Fig. 3.2 yields

$$\begin{aligned}
JP1 &= U(1) - K(I) * (CPW * U(2) + RP) \\
P1 &= U(2) + K(I) * (-CP(I) * U(1) + \left(\frac{EO(I)}{VT}\right) * U(2) + PO(I) * C2 * U(3)) \\
E1 &= U(3) + K(I) * C1 * (U(2) - U(5)) \\
V1 &= U(4) - K(I) * U(3) \\
N1 &= U(5) + K(I) * (CN(I) * U(6) - \left(\frac{EO(I)}{VT}\right) * U(5) - NO(I) * C2 * U(3)) \\
JN1 &= U(6) + K(I) * (CNW * U(5) + RP)
\end{aligned}
\tag{3.3.29}$$

The corrector step

$$\begin{aligned}
JP2 &= U(1) - (K(I)/2) * (CPW * (U(2) + P1) + RP + RC) \\
P2 &= U(2) + (K(I)/2) * (-CP(I) * (U(1) - CP(I+1) * JP1) + \left(\frac{EO(I) + EO(I+1)}{VT}\right) * \\
&\quad (U(2) + P1) + PO(I) + PO(I+1) * C2 * (U(3) + E1)) \\
E2 &= U(3) + (K(I)/2) * C1 * (U(2) + P1 - U(5) - N1) \\
V2 &= U(4) - (K(I)/2) * (U(3) + E1) \\
N2 &= U(5) + K(I)/2 * (N(I) * U(6) + CN(I+1) * JN1 - \left(\frac{EO(I) + EO(I+1)}{VT}\right) * \\
&\quad U(5) + N1) - (NO(I) + NO(I+1)) * C2 * (U(3) + E1) \\
JN2 &= U(6) + K(I)/2 * (CNW * (U(5) + N1) + RP + RC)
\end{aligned}
\tag{3.3.30}$$

where 1 refers to the results of the predictor and 2 to the results of the corrector and the \underline{u} vector is defined

$$\text{as } \underline{u} = \begin{bmatrix} U(1) \\ U(2) \\ U(3) \\ U(4) \\ U(5) \\ U(6) \end{bmatrix} = \begin{bmatrix} \hat{J}_{p1} \\ \tilde{p}_1/n_i \\ \tilde{E}_1 \\ \tilde{V}_1 \\ \tilde{n}_1/n_i \\ \hat{J}_{n1} \end{bmatrix}
\tag{3.3.31}$$

The recombination terms are:

predictor

$$RP = \frac{Q * NI * (NO(I) * U(2) + PO(I) * U(5))}{TP(I) * (NO(I) + NI) + TN(I) * (PO(I) + NI)} \quad (3.3.32)$$

corrector

$$RC = \frac{Q * NI * (NO(I+1) * D1 + PO(I+1) * N1)}{TP(I+1) * (NO(I+1) + NI) + TN(I+1) * (PO(I+1) + NI)} \quad (3.3.33)$$

The remaining parameters are:

$$CN(I) = 1 / (Q * NI * UN(I) * VT)$$

$$CP(I) = 1 / (Q * NI * UP(I) * VT)$$

$$CNW = CMPLX(0, Q * NI * W)$$

$$CPW = CMPLX(0, Q * NI * W)$$

$$C1 = (Q * NI) / (KSI * E)$$

Figure 3.5 shows the flow chart of the integration which is a subroutine of the one dimensional AC program and is called STEP.

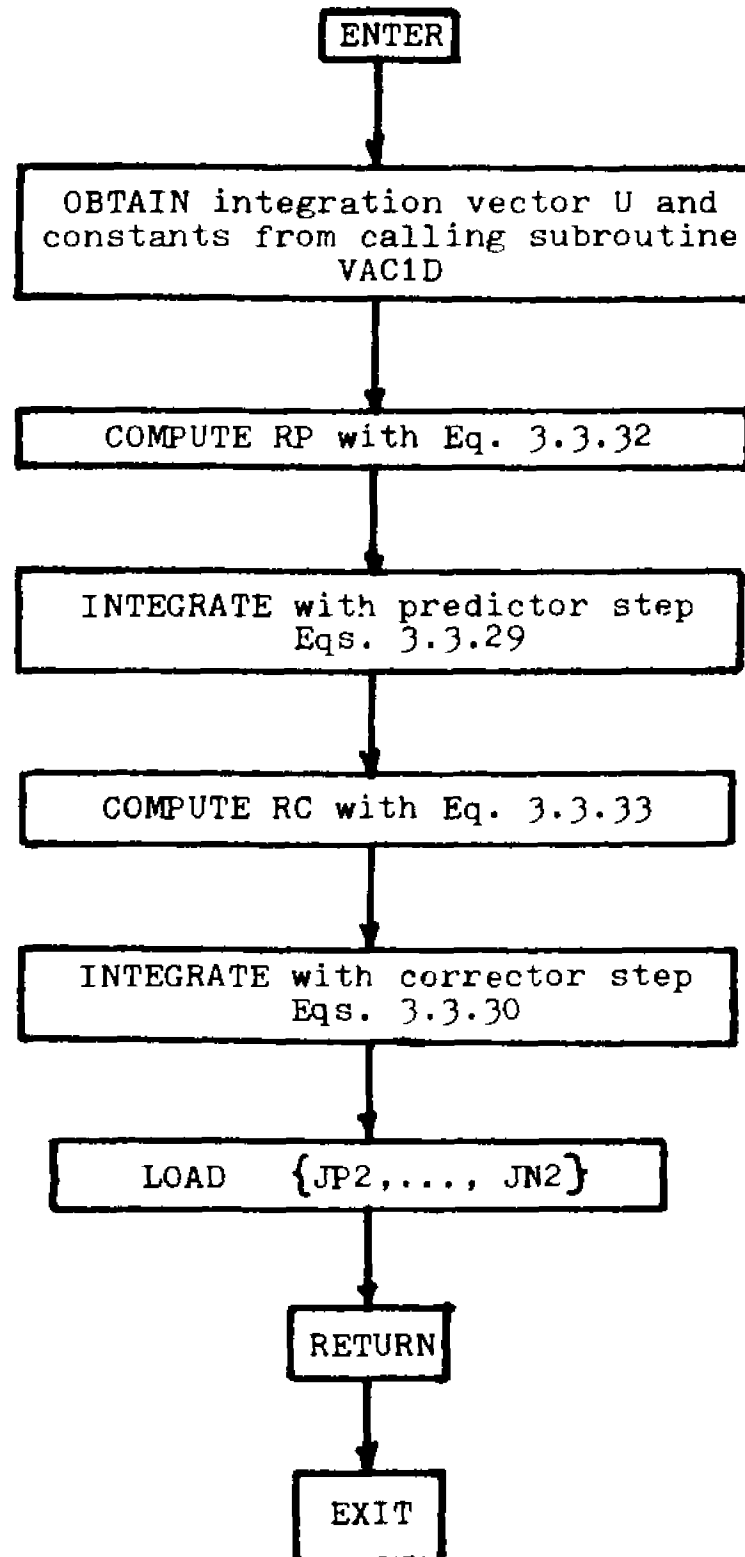


Figure 3.5. Computational flowchart of the integration subroutine STEP.

3.4 The Calculation of the Small Signal AC Admittance in One Spatial Dimension

The device under consideration in one dimension, the MIS capacitor, may be considered a one port device, characterized by its DC operating point and a small signal AC admittance. The complex admittance may be defined as the ratio of the small signal alternating current phasor to the small signal voltage phasor.⁽⁵⁰⁾ This is measured and calculated by impressing a small signal AC bias in series with the DC bias and observing the AC current which flows (see Fig. 3.1). To obtain the small signal current in the device, one must keep in mind that it is a series device (i.e. every grid node is serially connected to every other grid node) and that the total current is constant. The current then may be calculated at any grid point, and since the easiest expression to evaluate is the current in the insulator, it shall be calculated there. Since most quantities of interest are described per unit area (capacitance, conductance, etc.) for the one dimensional device, it is appropriate to use current densities henceforth in place of currents. (Note should be taken that \sim over a variable signifies a complex quantity.) The defining relationship for admittance per unit area is

$$\frac{\tilde{Y}}{A} = \frac{\tilde{J}_{ac}}{\tilde{V}_{ac}} \quad (3.4.1)$$

\tilde{V}_{ac} is the applied AC bias voltage and \tilde{J}_{ac} shall be calculated with the algorithm. In the insulator, the point relationship between current density and electric field is:

$$\tilde{J}_{ac} = j\omega K_I \epsilon_o \tilde{E}_1 \quad (3.4.2)$$

which is the small signal form of Eq. 1.3.17. The small signal AC electric field in the oxide may be easily calculated from the definition of the electric field in terms of the AC voltage

$$\tilde{E}_1 = - \frac{d\tilde{V}_1}{dx} \hat{a}_x \quad (3.4.3)$$

which may be discretized by a forward difference scheme at the top contact point as (see Fig. 3.3)

$$\tilde{E}_1 \cong - \left(\frac{\tilde{V}_1(N-1) - \tilde{V}_1(N)}{Hx(N-1)} \right) \quad (3.4.4)$$

and since $\tilde{V}_1(N) = \tilde{V}_{ac}$ the applied voltage,

$$\tilde{E}_1 = \frac{\tilde{V}_{ac} - \tilde{V}_1(N-1)}{Hx} \quad (3.4.5)$$

The admittance may be rewritten as

$$\tilde{Y} = j\omega K_I \epsilon_o \left(\frac{\tilde{V}_{ac} - \tilde{V}_1(N-1)}{Hx} \right) / \tilde{V}_{ac}$$

To obtain the solution at grid point (N-1) only one pass of the integration is required. Due to the method of integration, upon arrival at the top contact, the independent solution values of all six variables are saved at the (N-1) and at (N) grid points. The combining constants (or β 's) used to match boundary conditions are found and the value of the potential at (N-1) easily reconstructed using the solutions and β 's appropriately

$$\tilde{V}_1(N-1) = \tilde{U}_1(4) * \beta(1) + \tilde{U}_2(4) * \beta(2) + \tilde{U}_3(4) * \beta(3) \quad (3.4.6)$$

where the U's are the independent solution vectors at (N-1) and the subscript (4) refers to the location of the potential solution within that vector. The equivalent circuit component values are calculated from the admittance

$$\frac{\tilde{Y}}{A} = \frac{G}{A} + j\omega \frac{C}{A} \quad (3.4.7)$$

where G and C are the equivalent parallel conductance and capacitance, calculated directly as

$$\frac{G}{A} = \text{Re} \left\{ j\omega K_I \epsilon_o \left(\frac{\tilde{V}_{ac} - \tilde{V}_1(N-1)}{Hx} \right) / v_{ac} \right\} \quad (3.4.8)$$

and

$$\frac{C}{A} = \text{Im} \left\{ j K_I \epsilon_o \left(\frac{\tilde{V}_{ac} - \tilde{V}_1(N-1)}{Hx} \right) / v_{ac} \right\} \quad (3.4.9)$$

It is clear that due to the nature of this algorithm,

only one pass needs to be made to obtain the above small signal parameters. This algorithm is used in several studies:

1. Validity of the model in predicting the small signal admittance compared to the existing theory.
2. Modeling of an experimental capacitance-voltage curve to check the physical validity of the algorithm, equations used and underlying assumptions.
3. Studies of the admittance of devices with inhomogeneous profiles, including comparison to experimental evidence.
4. Modeling the admittance of three level MOS capacitor and comparison to theory.

General Studies

Typical normalized capacitance versus voltage curves are shown in Fig. 3.6 and 3.7. The capacitance is commonly normalized with respect to the oxide capacitance and this practice has been followed where applicable. The excitation frequency is 1 MHz, the usual measurement frequency for "high frequency" response. Figure 3.6 curves have the same uniform background doping (p type, $N_A=1 \times 10^{15}$ ions/cm³) but varying oxide thickness. The grid data is shown in the figure. No problems were encountered at any of the devices modeled in AC solution stability or convergence of the DC algorithm.

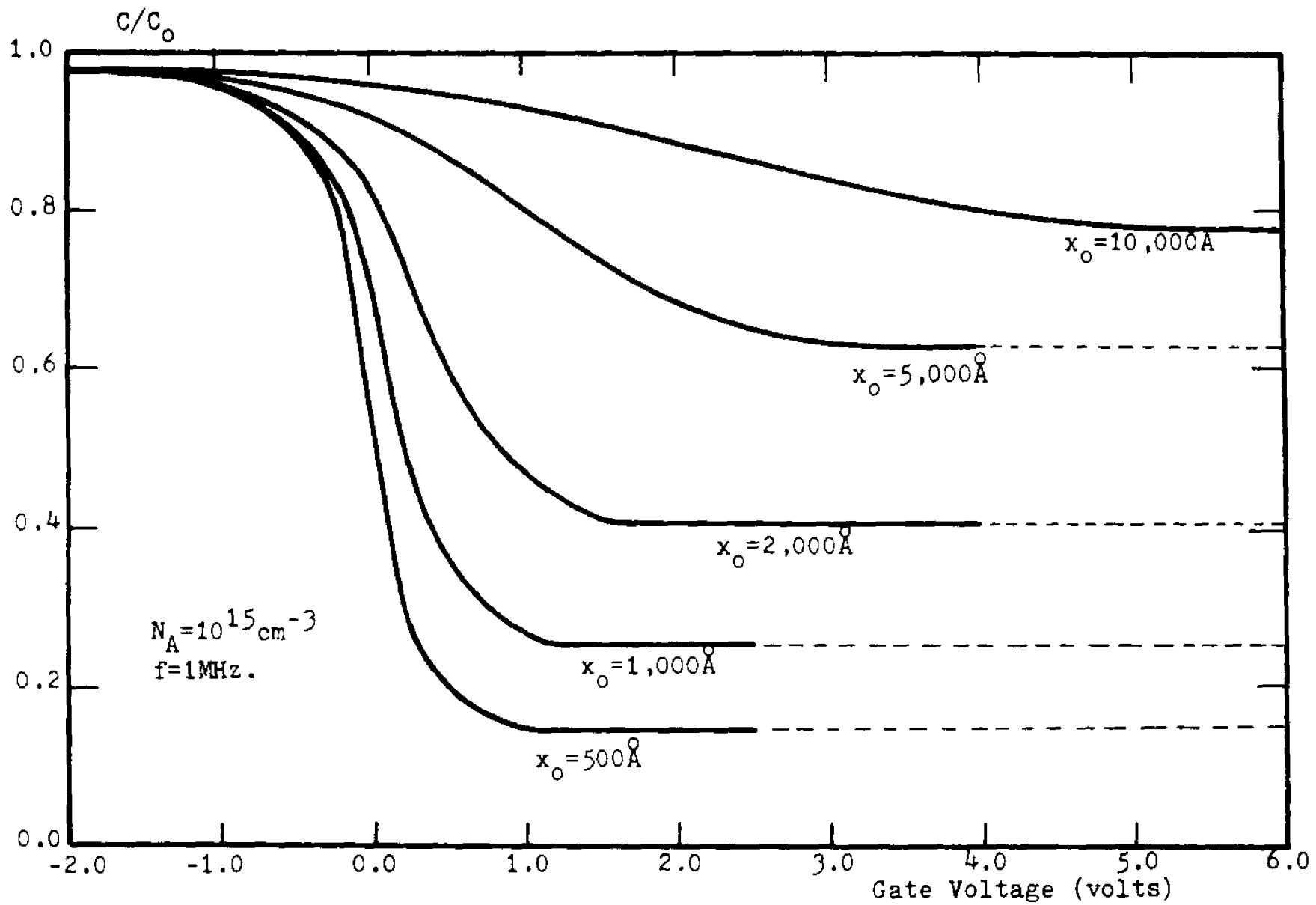


Figure 3.6. Capacitance-voltage curves for varying oxide thicknesses.

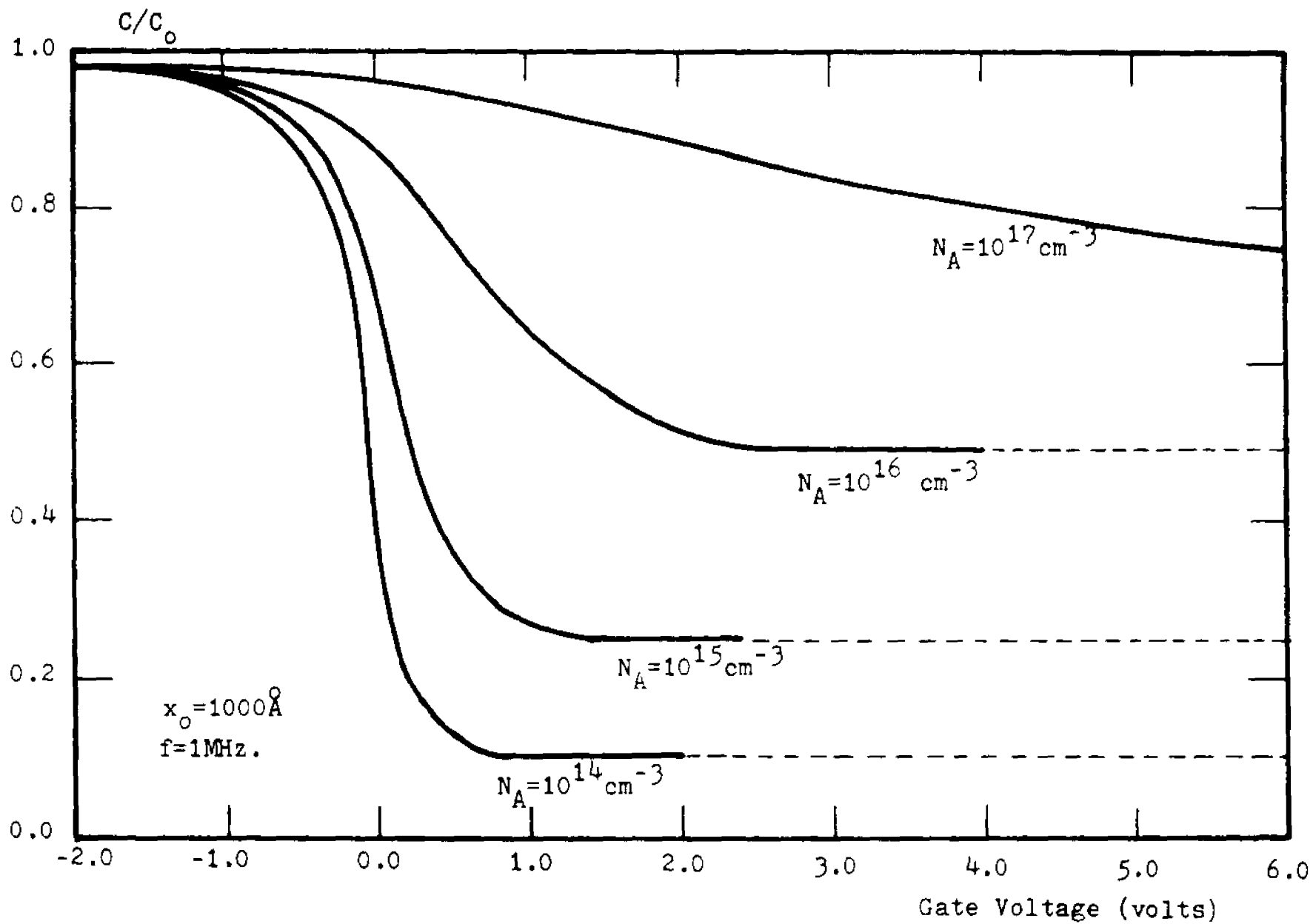


Figure 3.7. Capacitance-voltage curves for varying doping densities.

The only restriction imposed by the use of the Boltzman distribution for carriers has been the limiting of the surface potential to remain within the band gap. If larger applied biases were used to exceed this restriction, several things occurred: a) the carrier concentrations quickly became extremely large and occasionally overflowed the machine and more importantly, b) the solution was in gross error since for large biases the Fermi energy level is driven close to or above the conduction band (or below the valance band), Fermi-Dirac statistics for carrier concentrations must be brought to bear and the Boltzman statistics are no longer applicable.⁽⁵¹⁾ Since, upon reaching strong inversion the capacitance remains constant (at high or low frequencies) driving the device much beyond this point is unnecessary to test the model produced. The results in Fig. 3.6 show, as expected, that the minimum value of the capacitance at this frequency increases for increasing oxide thickness.

In Fig. 3.7 the minimum value capacitance increases as the doping level increases. This is due to the diminution of the maximum depletion width in higher doped materials and is expected. These curves are in excellent agreement with the results of Grove⁽⁵²⁾ and Goetzberger⁽⁵³⁾.

For the uniformly doped MOS capacitor, the inversion capacitance is a function of the signal frequency. It is well known that the capacitance voltage curves exhibit

different shapes at different frequencies, this has been measured and modeled by several authors.⁽⁵⁴⁾⁽⁵⁾ There are two clearly recognized states: the "low frequency" and the "high frequency" CV curves. The "low frequency" curve is characterized by the inversion capacitance returning to the oxide capacitance level (accumulation) after decreasing during depletion. On the other hand, for "high frequencies" the inversion capacitance reaches a low level and remains there. The CV curve at 1 MHz (considered "high frequency") and at 0.1 Hz (very "low frequency") are shown in Fig. 3.8 and bear out this phenomena. Also plotted is the incremental capacitance calculated using the DC model alone (as explained in Section 2.4). The correlation between the incremental and "low frequency" curves are evident. A study is made in Section 3.5 of this phenomena.

The inversion capacitance for a simple structure has been calculated as a function of frequency and is plotted in Figs. 3.9 and 3.10. The transition from high to low frequency levels of capacitance is evidenced and in Fig. 3.10 a comparison is made to the incremental capacitance level. In this case, a discrepancy occurs between the present model and those of others (see Collins) and experimental results as well. The range of transition frequencies from low to high capacitance appears to be, in this model, two decades below that found by others⁽⁵⁾. This discrepancy is partially explained since at low

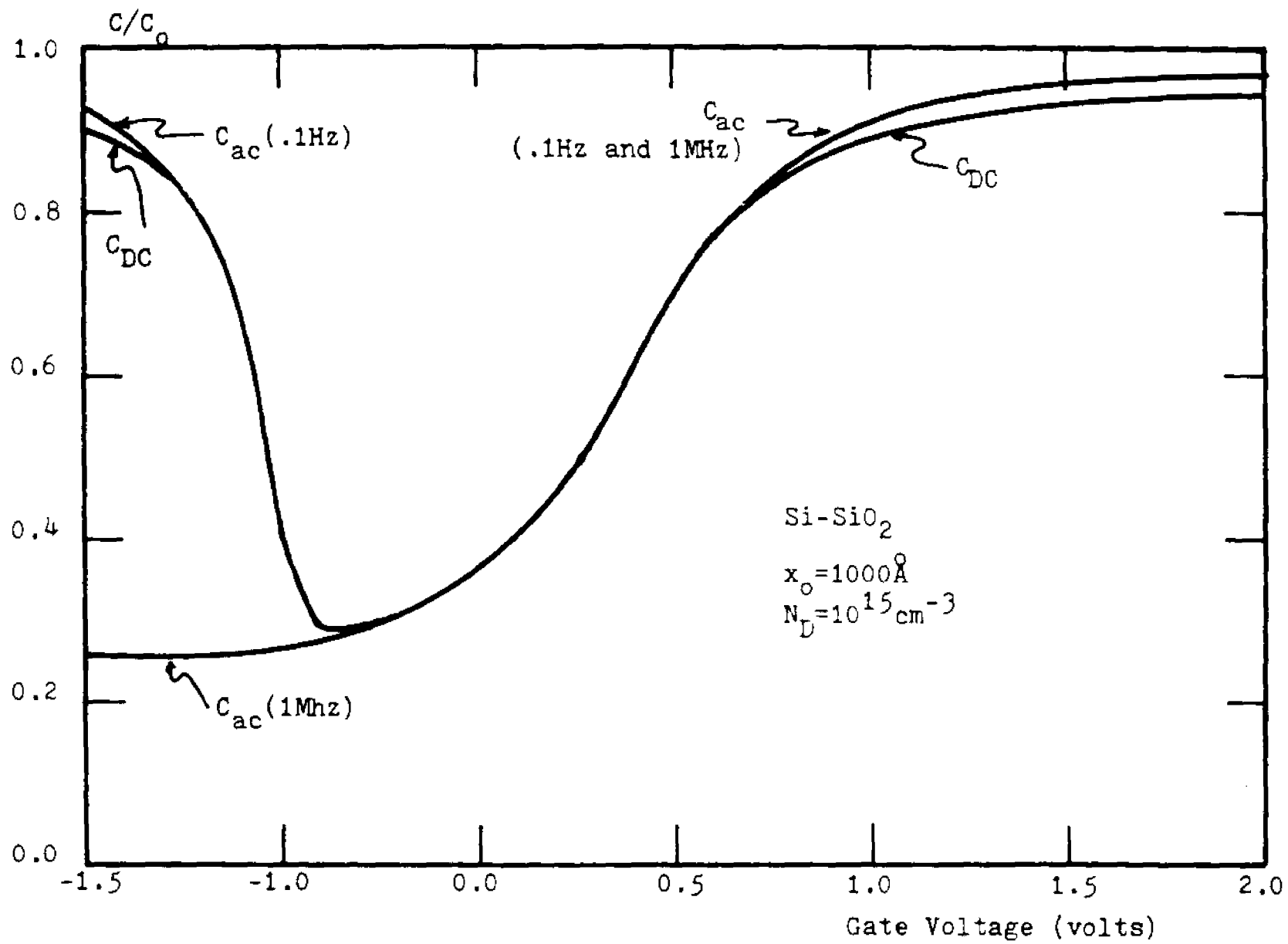


Figure 3.8. Comparison of the calculated incremental, "high" and "low" frequency capacitance.

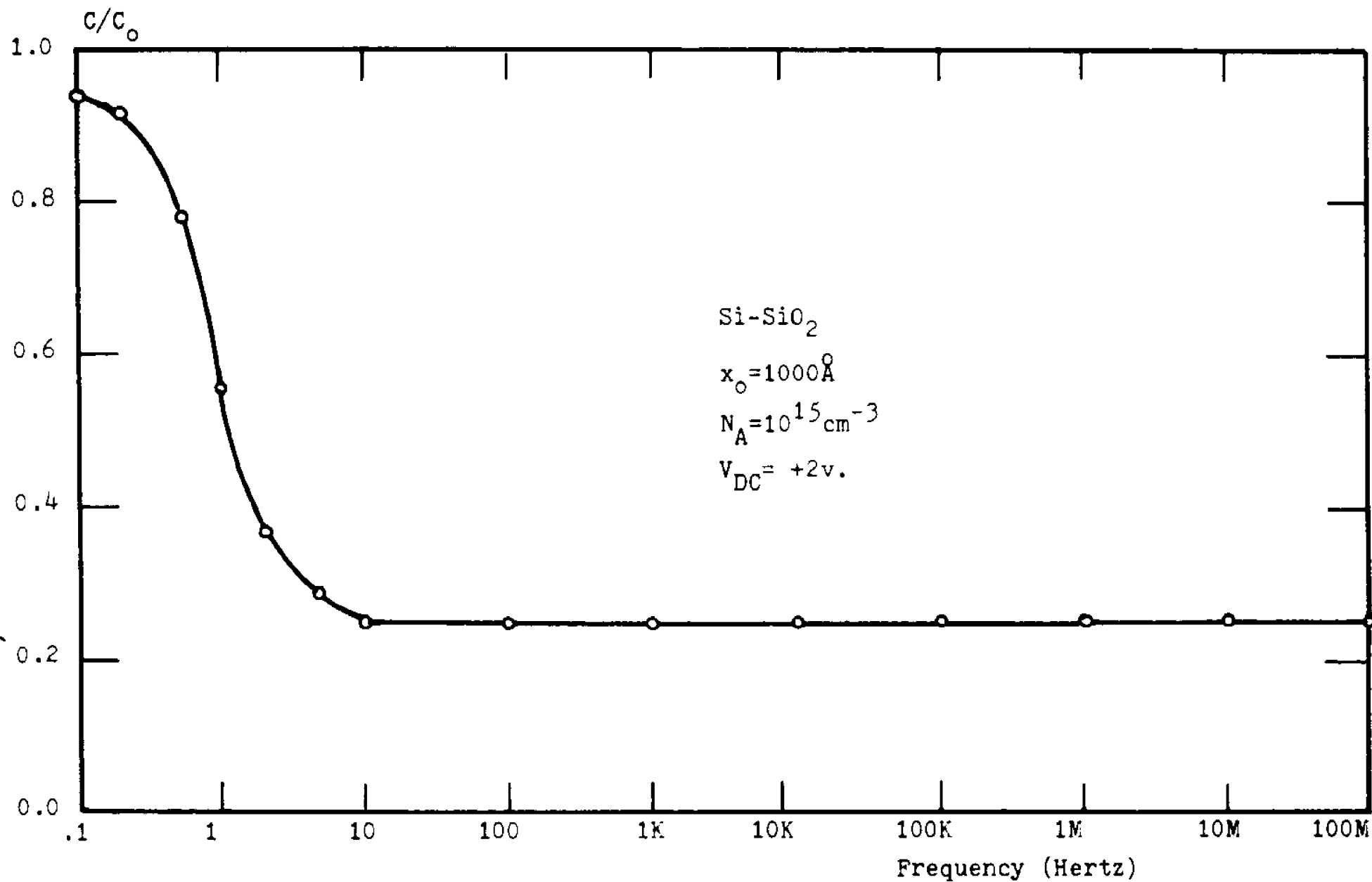


Figure 3.9. Calculated frequency dependence of the inversion capacitance of an MOS capacitor.

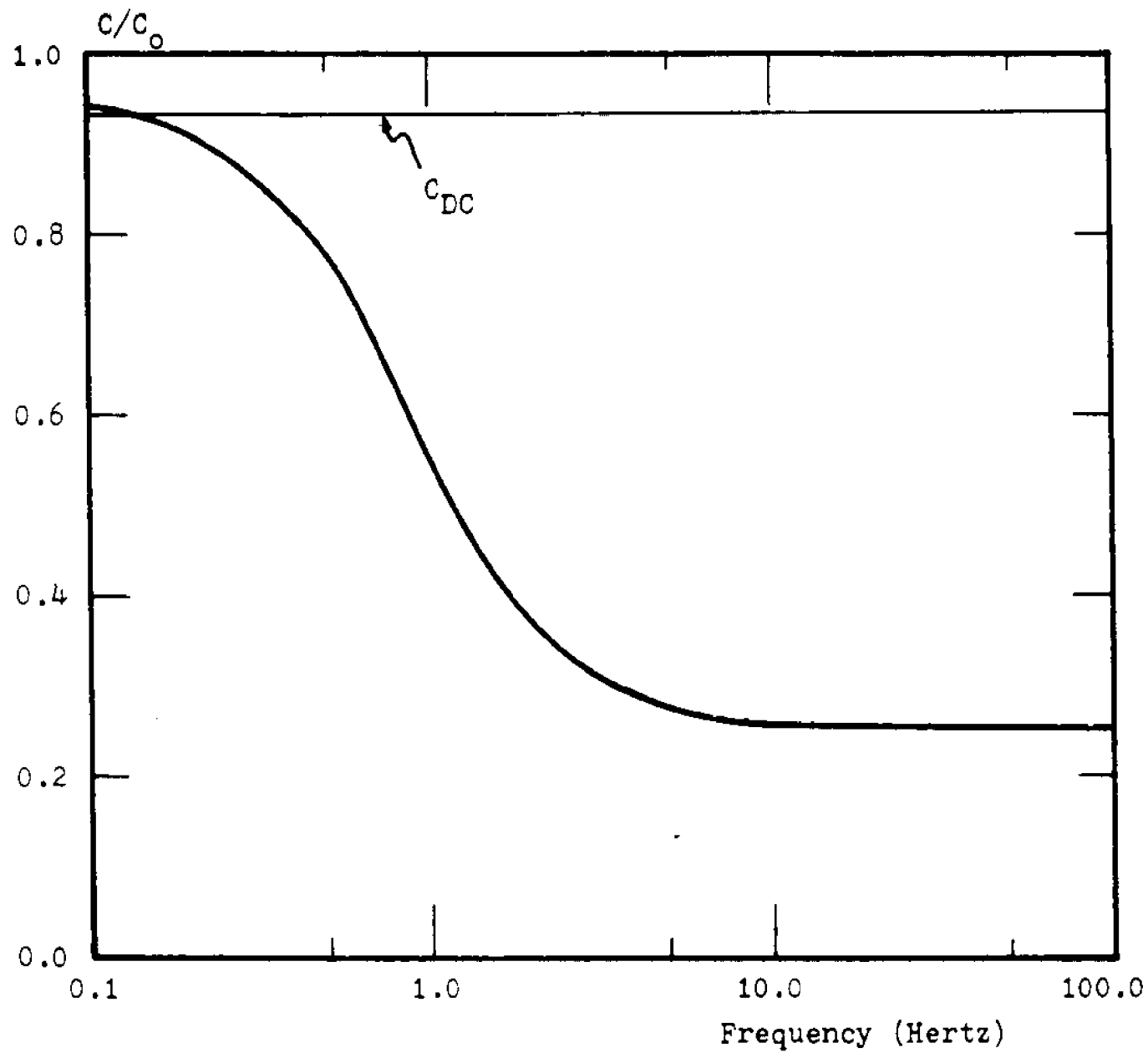


Figure 3.10. Detail of Fig. 3.9.

frequencies the generation recombination mechanism should swamp out any frequency dependence. In this case it does not since it has been linearized and is not the complete term. Normally, the full non-linearized recombination term must be used, as is discussed by Collins.⁽⁵⁾ Inclusion of the full nonlinear term (as derived in Appendix A) would make the equations to be solved nonlinear and harder to solve. It was decided to use the linearized model with its inherent drawbacks for the purpose of this work. The transition from high to low frequencies is observed, although a drawback of the recombination equation shows up here and should be addressed in future work.

Experimental and Theoretical Results

Several "one dimensional" MOS capacitance structures have been fabricated and tested. A particular capacitor that had undergone several processing steps and had the capacitance measured after each step is shown in Fig. 3.11. Basically, starting with p type material with a background doping of $N_A = 3 \times 10^{15}$ ions/cm³, the following procedure was used:

1. A dry oxide of approximately 1000^oA (60 min @ 1000^oC., dry O₂) was grown on a clean wafer.
2. Aluminum was deposited and 10 mil. diameter dots were photolithographically etched.
3. C-V curve number 1 was generated.

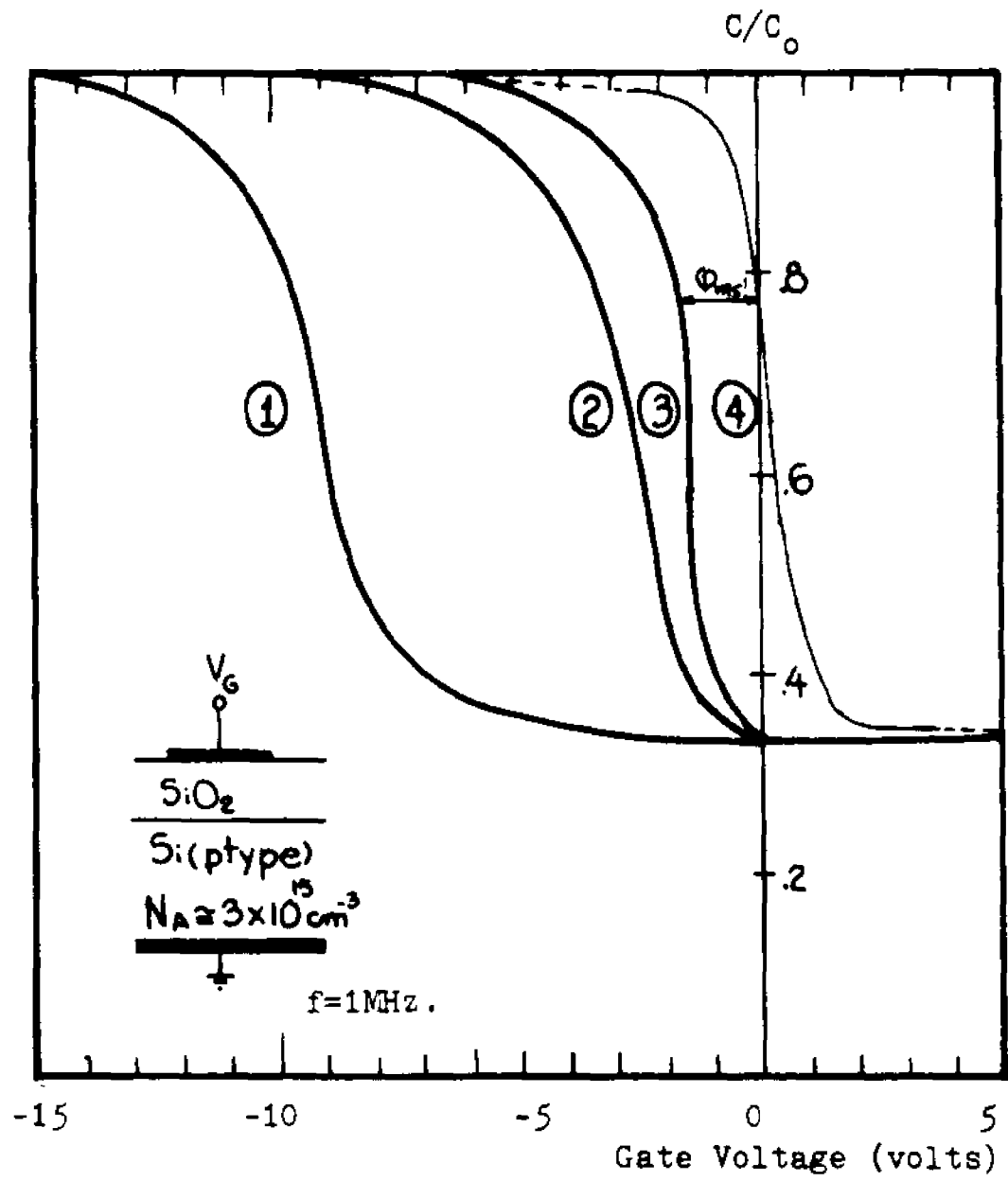


Figure 3.11. Experimental and modeled capacitance of an MOS capacitor.

4. The aluminum was removed and the wafer returned to the furnace @ 1000°C. for a dry N₂ anneal of 20 min. Step 2 was repeated.

5. C-V curve number 2 was generated.

6. The wafer was heated @ 350°C. for 15 min.

7. C-V curve number 3 was generated.

8. Analyze the measured C-V curves by the procedure outlined in Appendix C and generate the computer model shown by curve 4.

All C-V measurements were made with a Boonton 72AD capacitance meter at 1 MHz. The capacitance was normalized with respect to the highest accumulation capacitance measured, assumed to be the oxide capacitance. This particular set of curves was chosen because it demonstrates the effect of the different parameters usually encountered in processing (such as, positive interface surface charge density, surface states, etc.) and how our model meets or fails to meet the data. Curve number 1 corresponds to the basic process in growing a dry oxide, it has the correct shape for p type material and the C_{\min}/C_o inversion ratio meets that predicted for the value of resistivity quoted by the manufacturer and the oxide thickness calculated. It is noted that there is a large flat-band voltage shift, due primarily to a large positive charge in the oxide, Q_{ss} . This is expected for this processing. After annealing in N₂, the expected reduction in Q_{ss} (noted by a positive flat-band voltage shift)

is seen in curve number 2. Comparing these two curves to the model (curve 4) one observes that the slope of the capacitance curve in the transition region (between accumulation and inversion) is quite different. This effect is primarily due to surface states in the silicon, N_{SS} , which have not been reduced in manufacturing and are not taken into account in the model. Annealing in H_2 at lower temperature reduces the effect of N_{SS} considerably and good correlation between curve 3 and the model curve, number 4, now exists. The positive shift in the flat-band voltage is now due only to the metal-semiconductor work function, ϕ_{MS} , which is not included in the ideal model but may easily be computed from given tables (see Appendix C).

Inhomogeneously Doped Varactor

A structure of interest, as a diagnostic tool for more complex structures such as FET's or on its own merits as a circuit element is the inhomogeneously doped MOS capacitor. The two presently available methods of doping the semiconductor bulk are by diffusion and, more recently, ion implantation. The basic doping profile in both cases may be defined by a Gaussian distribution of ions in the surface region superimposed on a constant bulk doping level. The general doping profile for a diffusion may be represented as shown in Fig. 3.12. For ion implantation, the peak of the surface

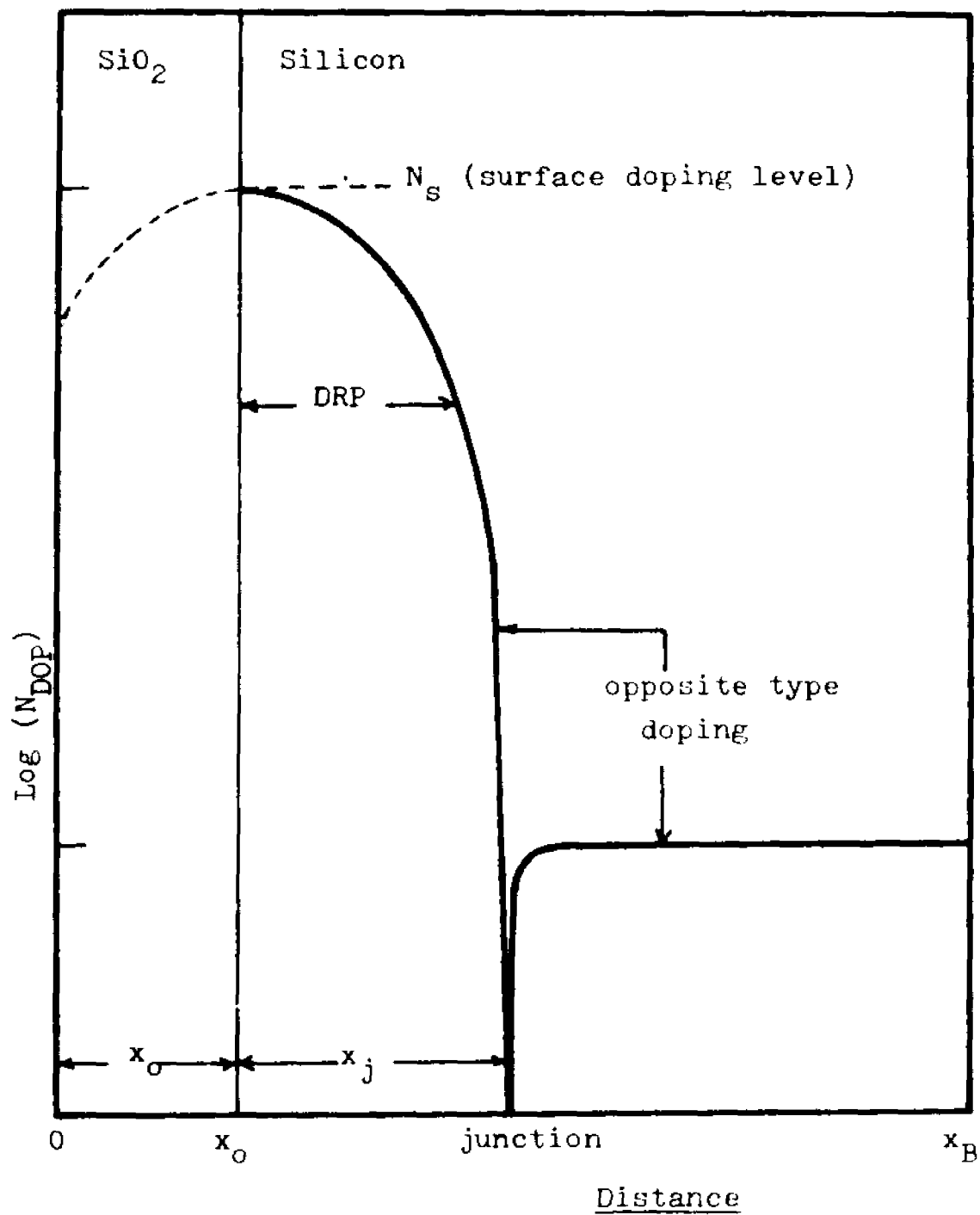


Figure 3.12. General gaussian complementary doped profile.

doping need not lie exactly at the Si-SiO₂ interface but may occur at a point before or after it. The describing equation for the present inhomogeneous profile is

$$N(x) = N_S \exp(-(x-x_c)^2/2\sigma^2) + N_{BULK} \quad (3.4.10)$$

For the diffused profiles the mean (x_c) lies exactly at the interface, thus $x_c = x_0$ and the relationship between the junction depth, x_j , and the standard deviation is

$$\sigma^2 = \frac{x_j^2}{2 \ln\left(\frac{N_{BULK}}{N_S}\right)} \quad (3.4.11)$$

For diffused device, two parameters may be varied and their effect noted: N_S , surface doping, the peak of the diffusion, and x_j , the junction depth. Only devices with complimentary diffusions are considered although one need not be limited to such since the algorithm will handle any $N(x)$.

In Fig. 3.13, the capacitance-voltage curves for an n type 1000Å oxide, $N_{BULK} = 10^{15}$ ions/cm³ device that has a diffusion of $N_S = 1 \times 10^{15}$ ions/cm³ Boron ions with varying junction depths are shown. Two characteristic points should be noted:

1. As the junction depth increases, there is a flat-band voltage shift.
2. For devices which have a junction depth approximately or greater than the maximum depletion width

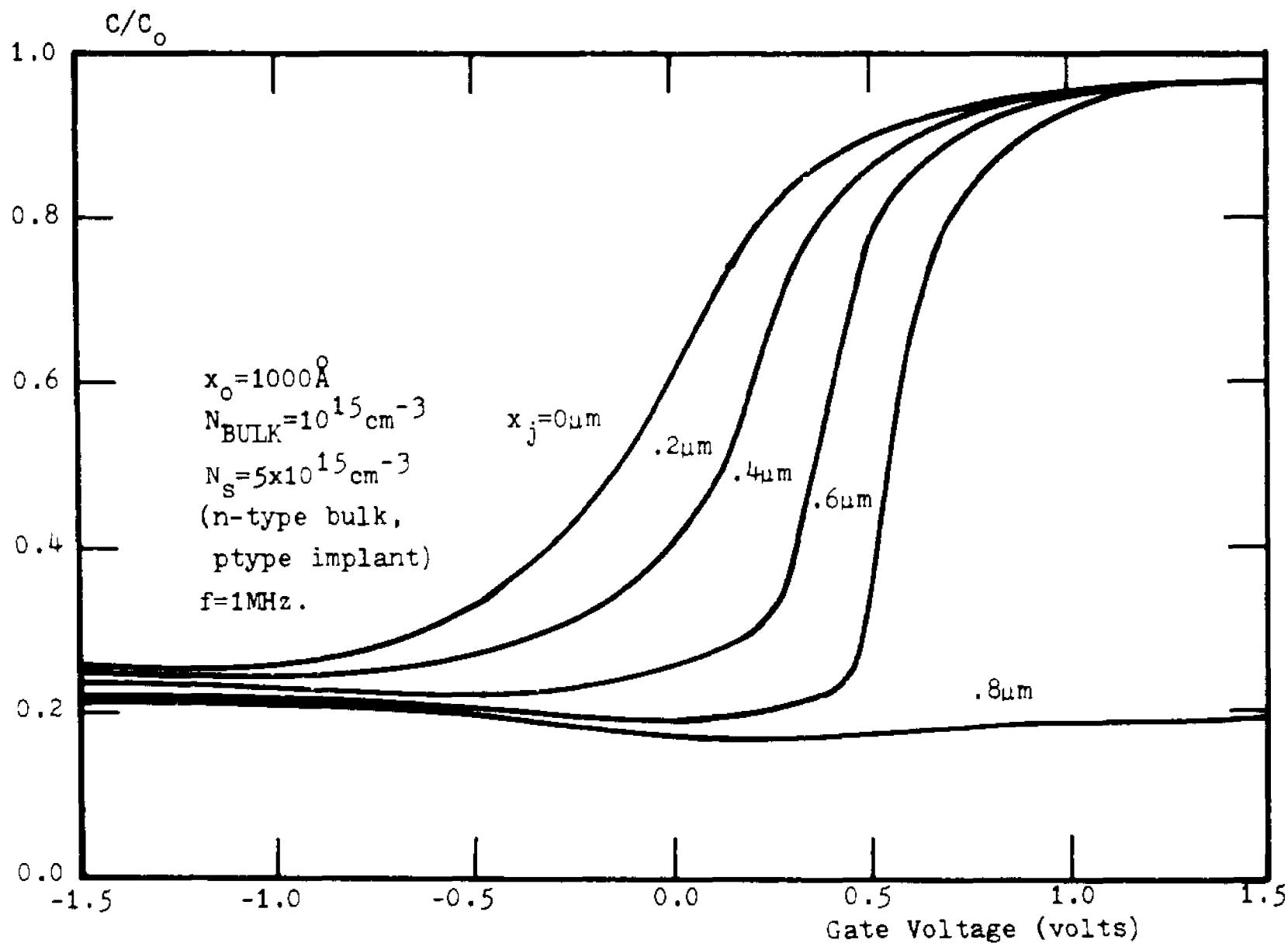


Figure 3.13. Capacitance-voltage curves of an inhomogeneously doped MOS capacitor for varying junction depths.

($x_{\text{DMAX}}=0.85\mu$ in this case) the diffused region is swept of carriers causing the voltage shift.

For junction depths greater than x_{DMAX} , the junction barrier prevents minority carriers from coming to the surface even more than the depletion region did for the homogeneously doped device, thus the low values of capacitance is exhibited even when the surface is accumulated. At this point, the junction capacitance figures prominently in the total capacitance, with the applied bias dropping across the junction, the depletion region the surface, and the oxide in a nonlinear fashion. Essentially, there are three capacitances in series: the oxide capacitance C_o , the diffusion layer capacitance C_s and the junction capacitance C_j , the last two having a nonlinear voltage dependence. Figure 3.14 shows the three regions in an energy band diagram and the equivalent small signal model capacitance with the corresponding capacitance-voltage curves.

Variation of surface doping while keeping the junction depth constant produce results similar to those just described. The capacitance-voltage curves for these devices have been calculated and are shown in Fig. 3.15. In this case, for increasing surface doping, which have decreasing depletion widths, the shielding effect of the junction on minority carriers is felt by field effect. In other words, the higher the doping density at the surface, the less the field penetrates

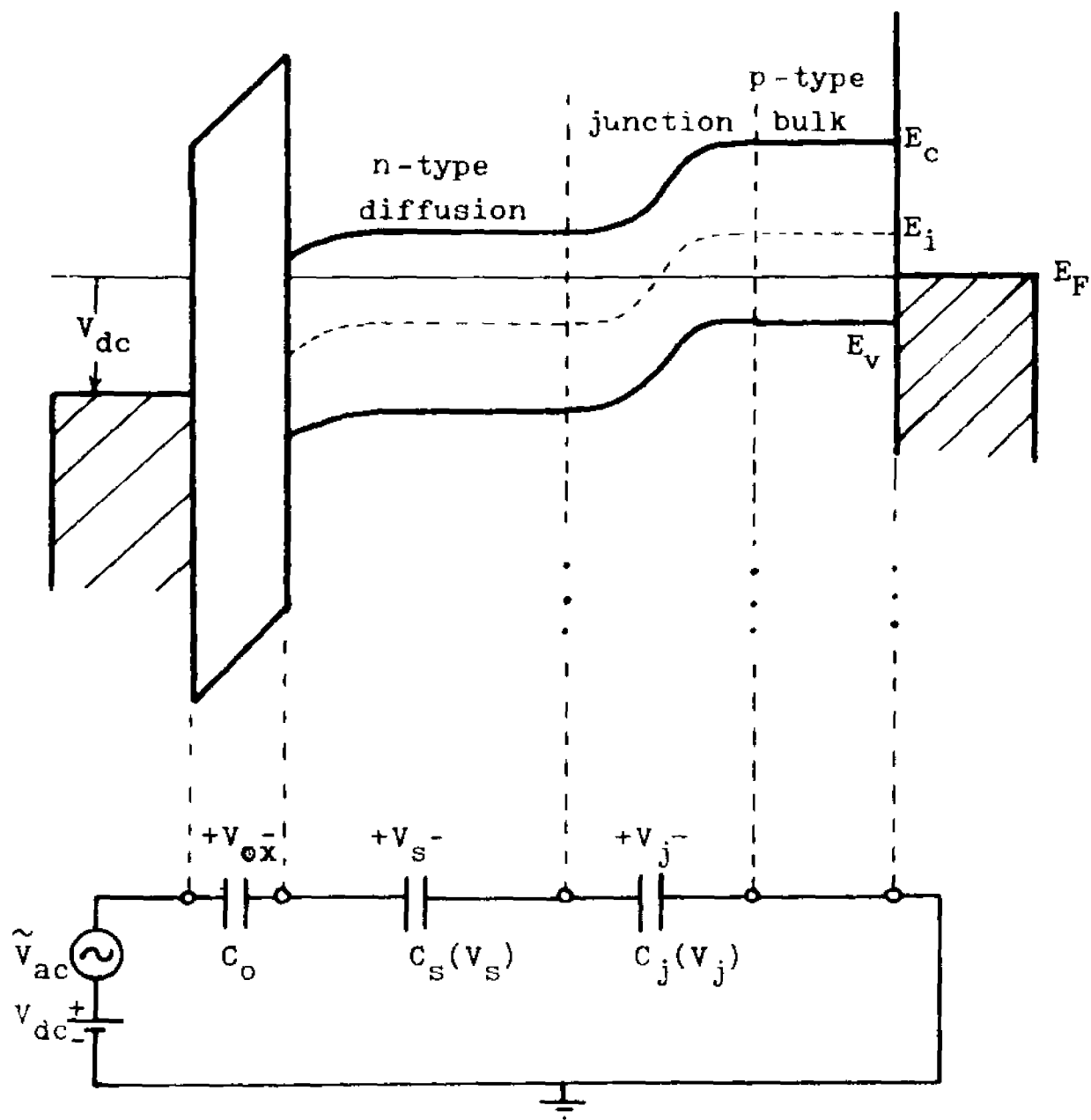


Figure 3.14. Energy band diagram and equivalent circuit of an inhomogeneously doped MOS capacitor.

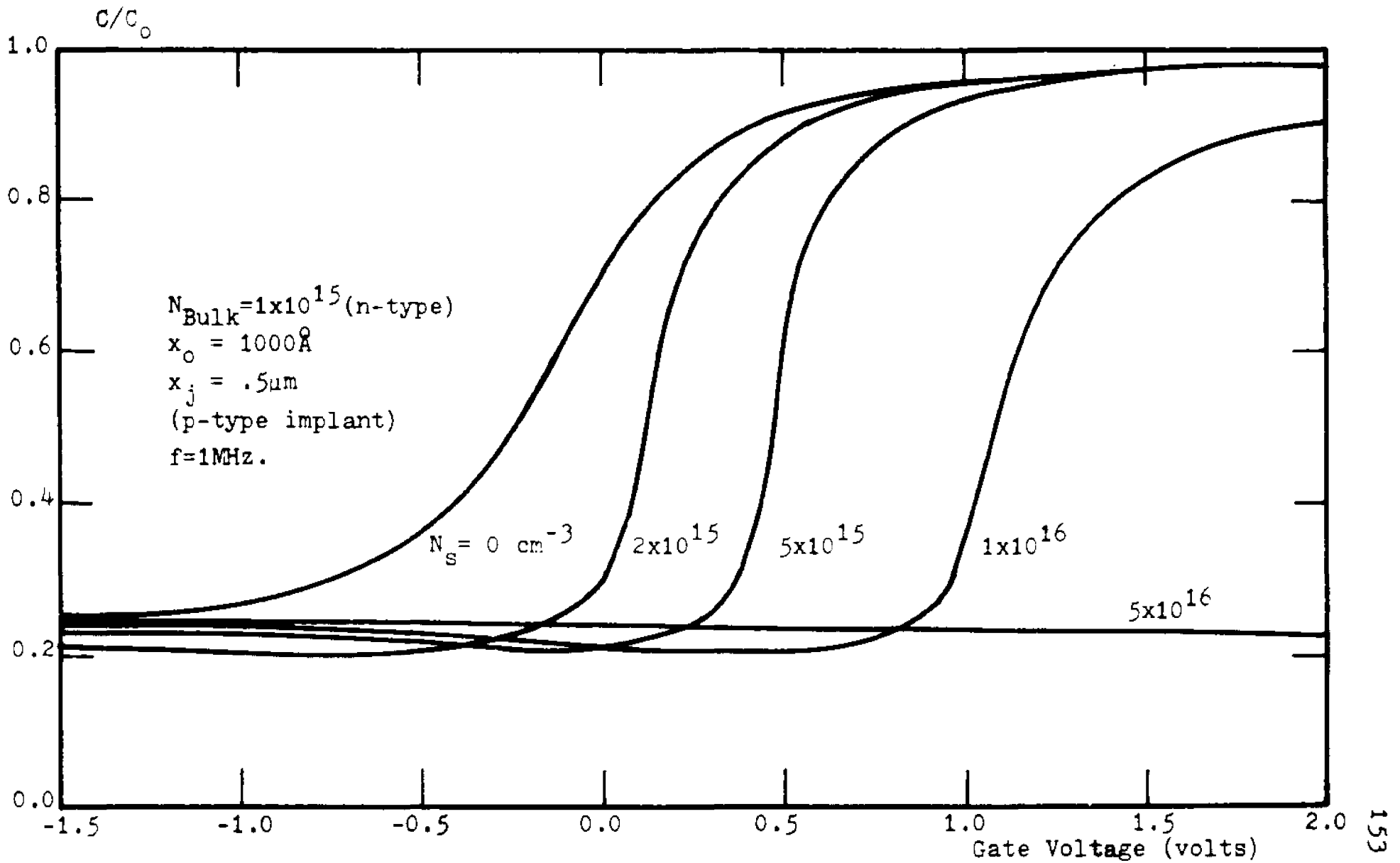


Figure 3.15. Capacitance-voltage curves for inhomogeneously doped MOS capacitors of varying surface doping.

into the silicon, preventing the sweeping out of the surface region by the applied voltage and causing the shielding of the junction. For the curve shown, where the capacitance is essentially constant, the surface doping is $N_s = 5 \times 10^{16}$ ions/cm³, p-type, which has an x_{DMAX} of 0.25 μ m, placing the surface depletion region away from the junction which is at $x_j = 0.5\mu$ m.

Ion implanted MOS FET's have been recently fabricated with the desired controlable flat-band voltage shift. MOS capacitors fabricated on the same wafer with the same profile as the gates of the FET's provide useful diagnostic tools for the fabrication process. These devices and associated capacitors have been reported by Hswe et. al.⁽⁵⁵⁾; their experimental C-V results are modeled herein. This provides a further test on the validity of the algorithms and indicates a use in the design of ion implanted devices.

From the process data given in Hswe's paper, a set of doping profiles is derived and a plot of them shown in Fig. 3.16. A C-V calculation for each of the capacitors was made and plotted, together with Hswe's data, on Fig. 3.17. Good correlation between the model and experiment is noted, with the discrepancies attributed to the following:

1. Other indications of the oxide capacitance should be used than the usual $C_o \cong C_{MAX}$ made by most experimenters. A better way would be to have homogene-

ously doped MOS capacitors (such as device A) next to the implanted ones to provide useful device data such as C_o and N_{BULK} .

2. If the devices were fabricated on different wafers, which seems reasonable but not mentioned by the authors, then the background doping, oxide thickness, and amount of positive surface charge in the oxide, Q_{SS} , may be slightly different for all the devices.

For the purpose of this modeling effort the same Q_{SS} and ϕ_{MS} was ascribed to all devices. The correlation of the experiment and model may be considered as quite reasonable.

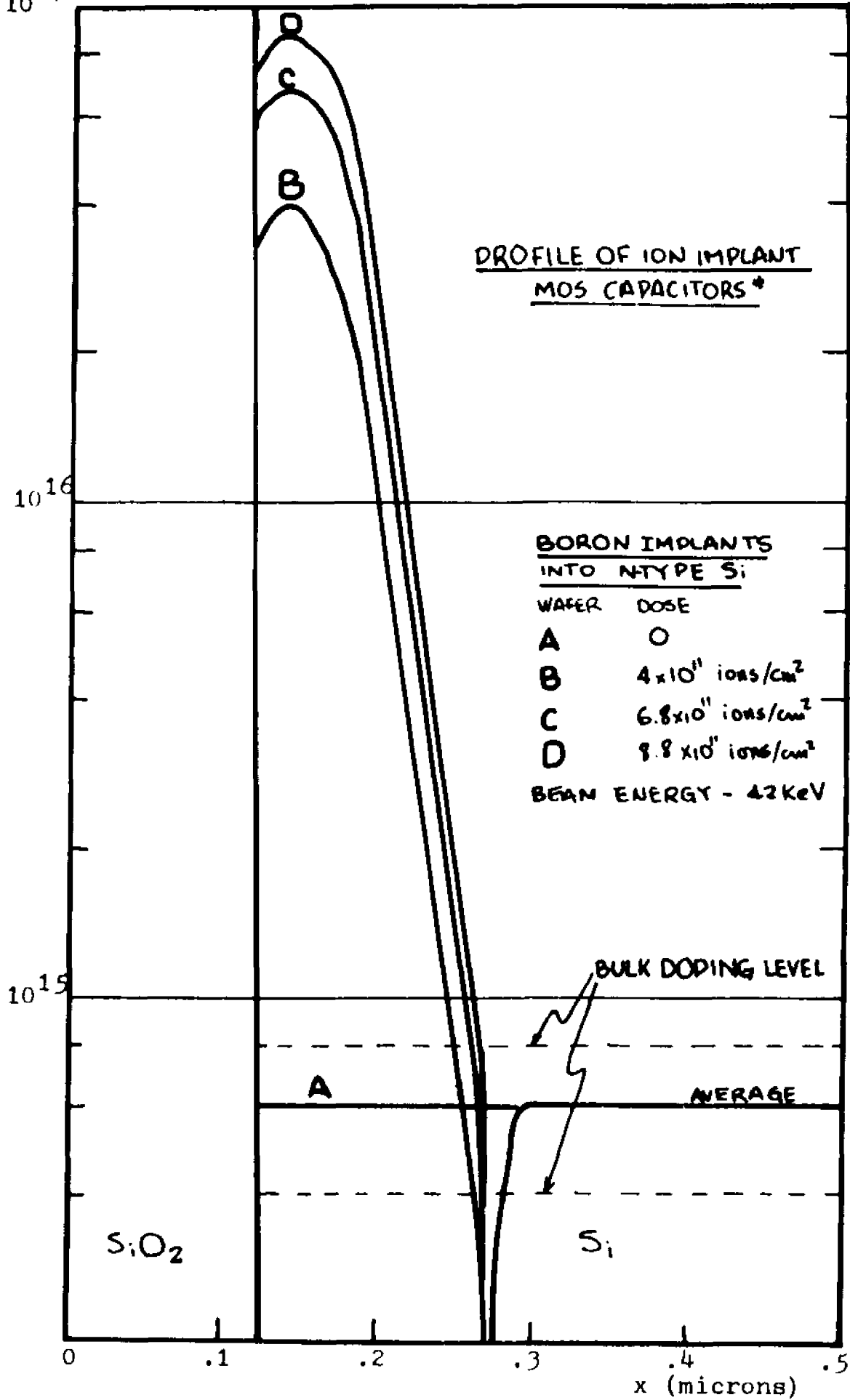


Figure 3.16. Doping profiles of the Hswe, et.al. capacitor.

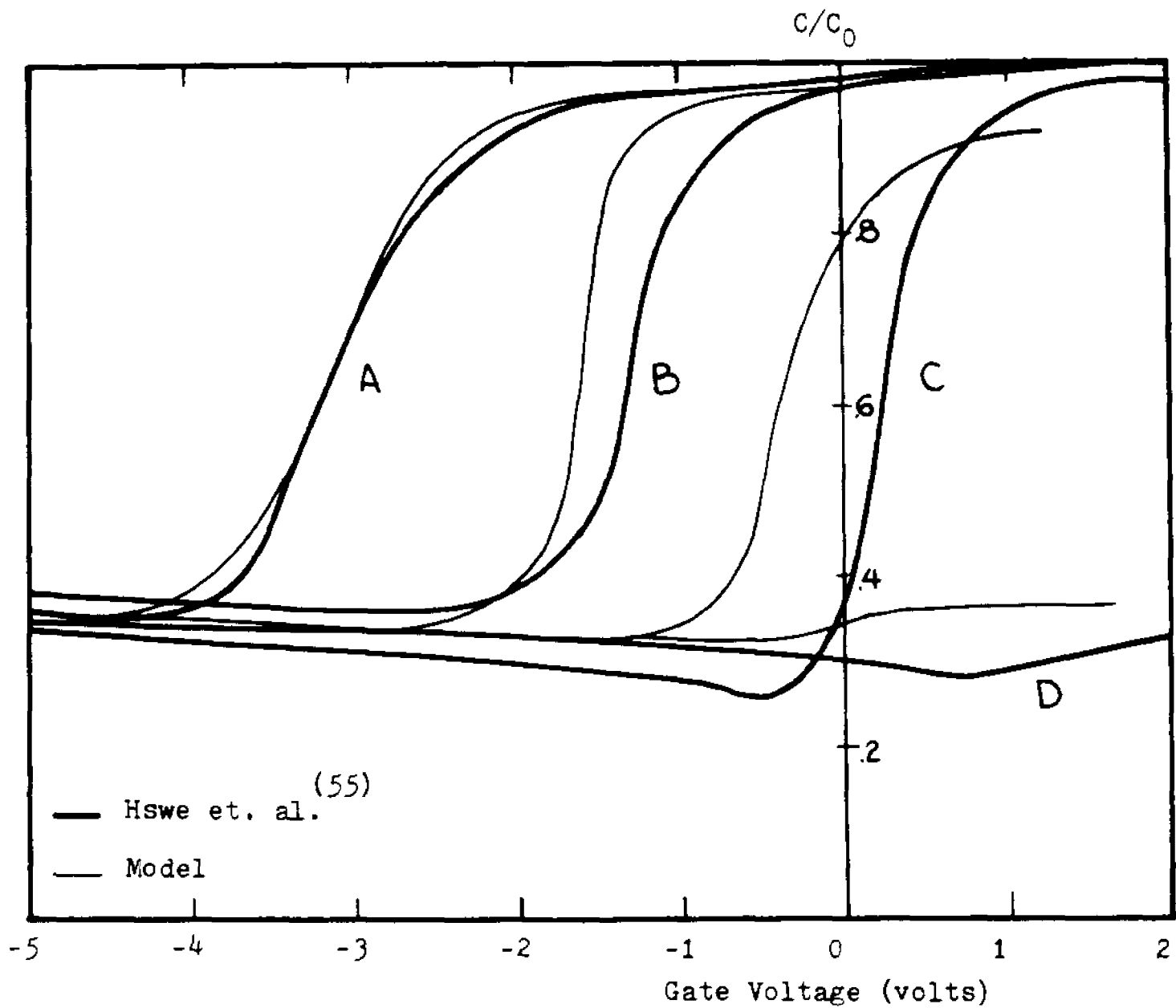


Figure 3.17. Experimental and modeled capacitance-voltage curves of ion-implanted MOS capacitors.

The M-Level MOS Capacitor

An interesting device which stems from the manipulation of the turn-on voltage of MOS capacitors is the M-level varactor. The turn-on voltage of a capacitor is defined as that voltage at which the minimum capacitance is reached when sweeping the bias from accumulation into inversion. If (M-1) MOS capacitors with a two state capacitance voltage curve which have varying turn-on voltages are connected in parallel, total capacitance, being the sum of all capacitances, will exhibit M distinct capacitance levels.

As an example, a three level varactor using two MOS capacitors is described in Fig. 3.18. The turn-on voltage of each is controlled by the Q_{SS} level, the oxide thickness and bulk doping⁽⁵⁶⁾

$$V_{T_0} = \frac{Q_{SS} x_o}{\kappa_{SI} \epsilon_o} + \phi_{MS} + 2\phi_F + \frac{qN_{BULK} x_{dmax} x_o}{\kappa_{SI} \epsilon_o A} \quad (3.4.12)$$

These devices have been fabricated and tested experimentally and their C-V curves modeled. Two oxide thicknesses of approximately 5000\AA and 500\AA were grown on a substrate of greater than $50\Omega\text{cm}$ resistivity. Aluminum contacts of varying area were deposited defining the desired devices. The experimental and model C-V curves have been plotted on Figs. 3.19, 3.20 and 3.21. The device characteristics of the model and manufactured and process parameters are given on each curve. A photo-

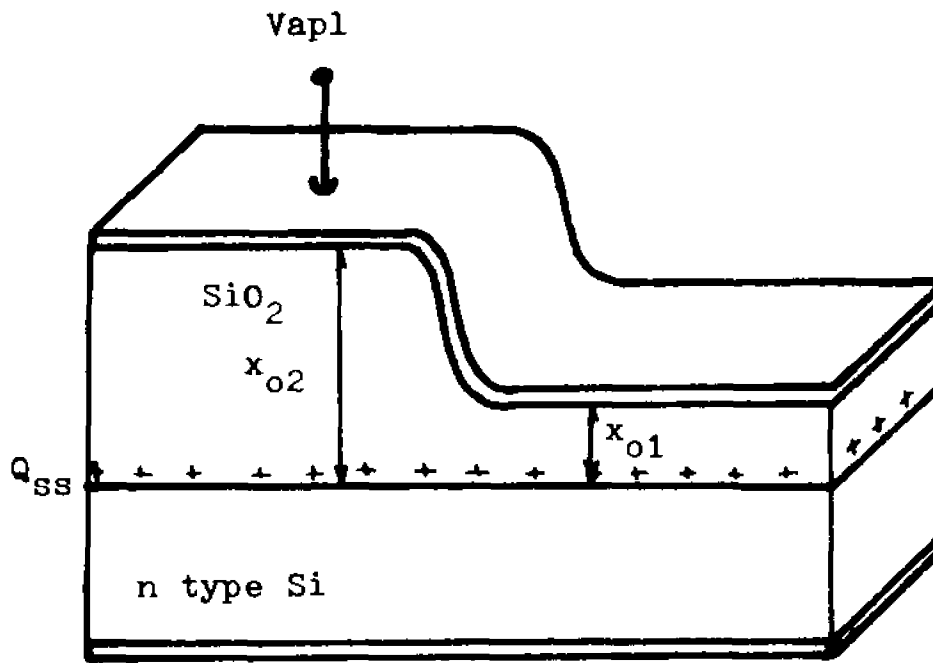
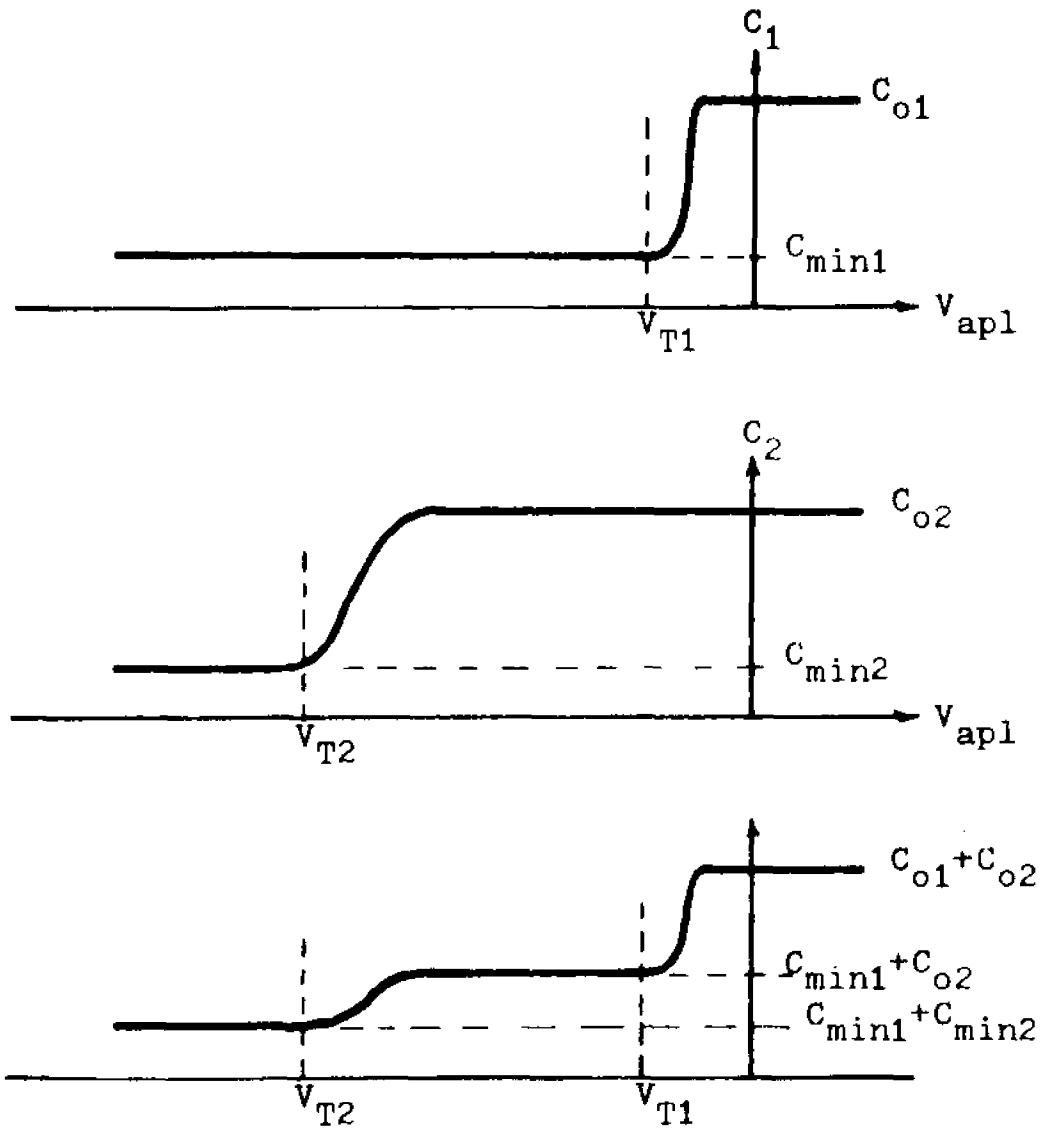


Figure 3.18. Two-level MOS capacitor and resulting C-V curve (at high frequency).



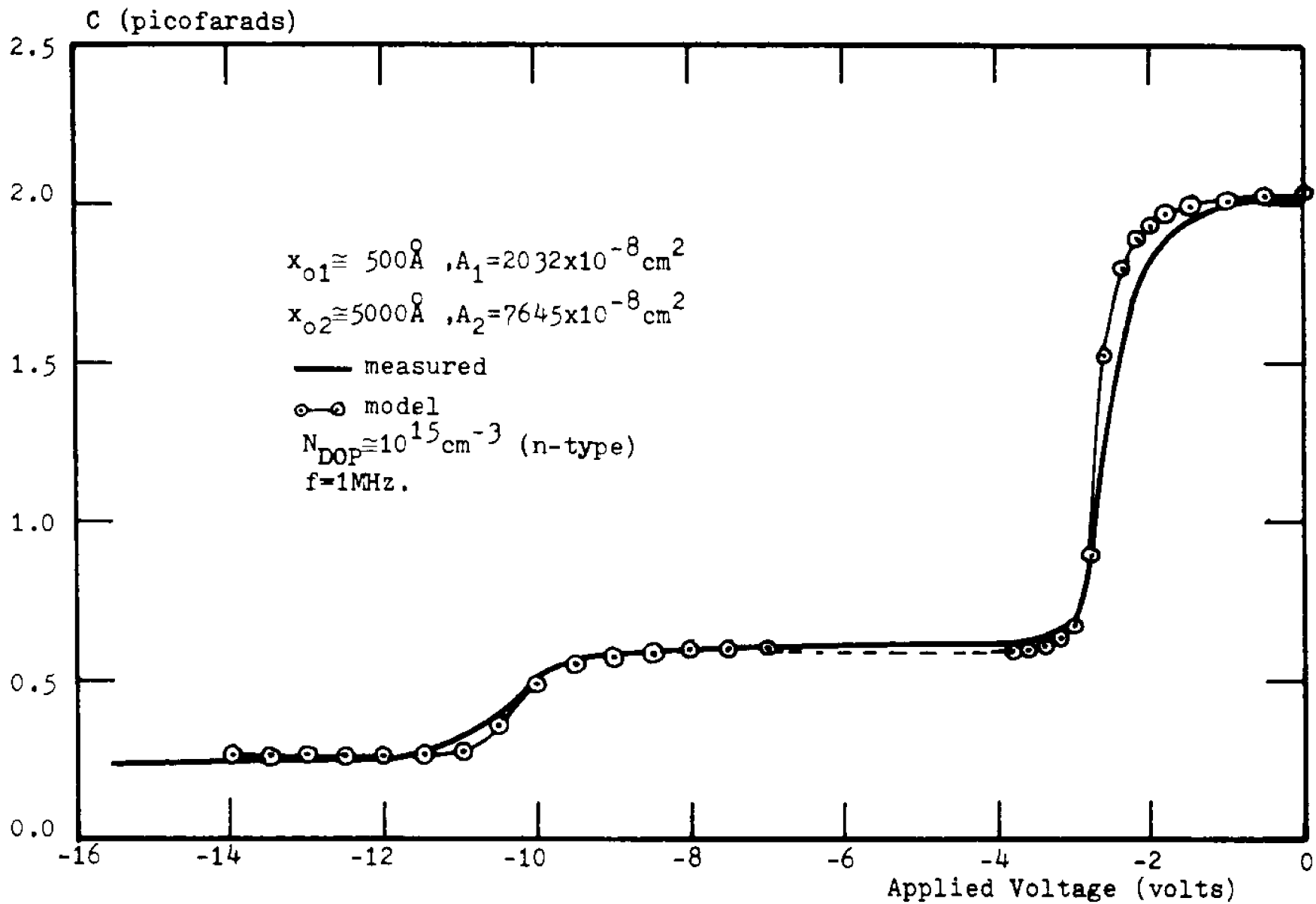


Figure 3.19. Capacitance-voltage curve of three level MOS capacitor (model and experiment).

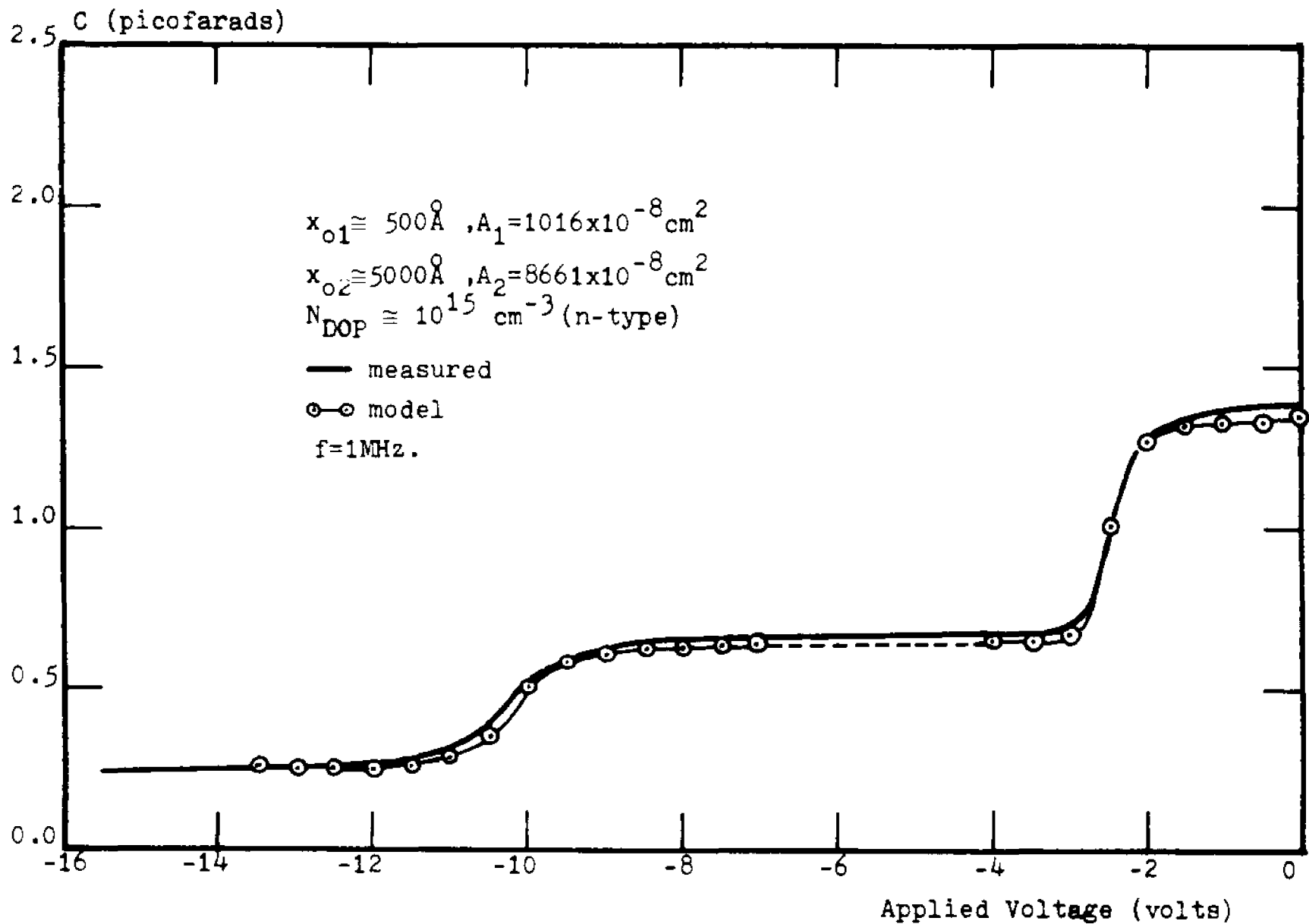


Figure 3.20. Capacitance-voltage curve of a three level MOS capacitor (model and experiment).

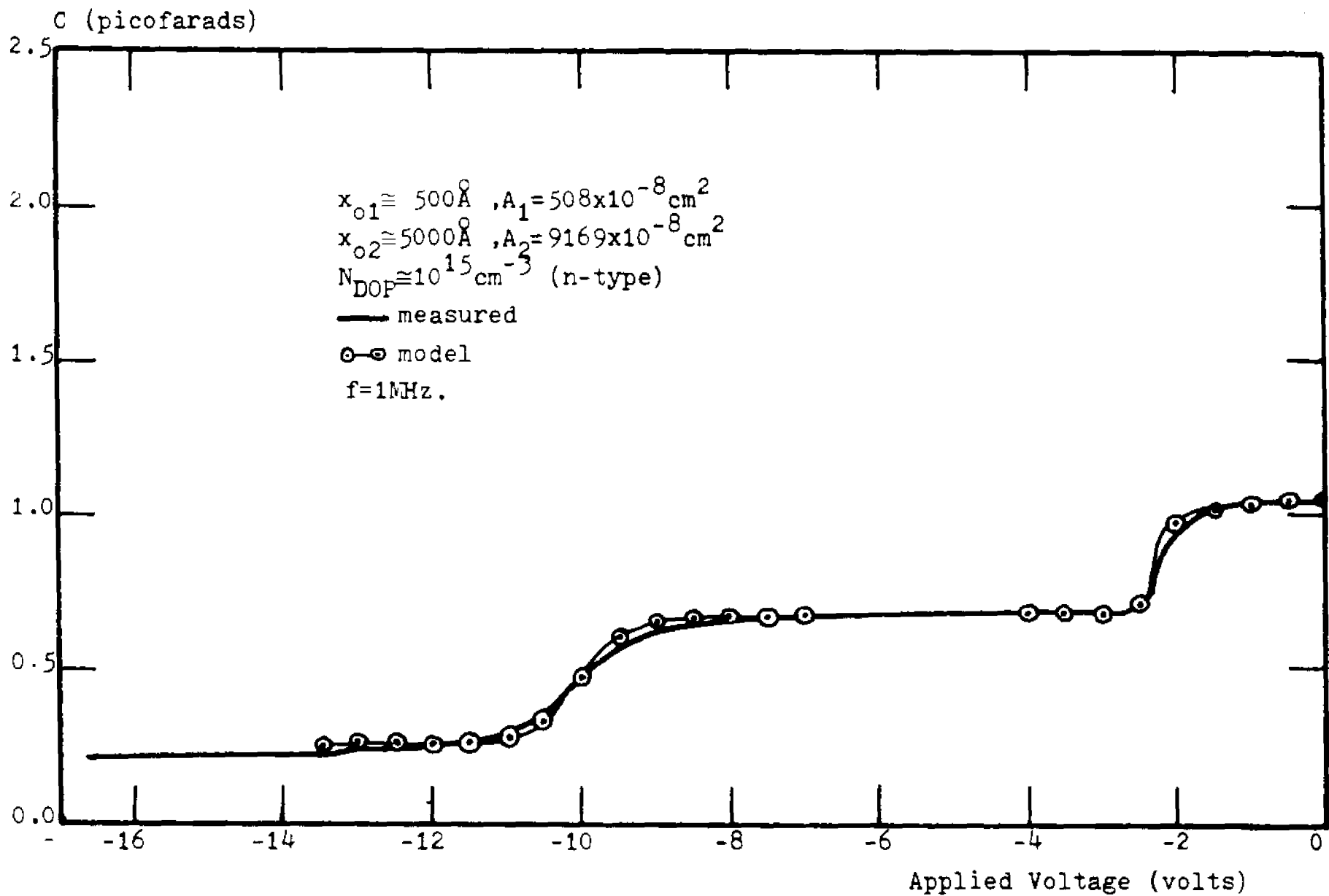


Figure 3.21. Capacitance-voltage curves of a three level MOS capacitor (model and experiment).



Figure 3.22a. Two three-level MOS capacitors.



Figure 3.22b. Detail of three-level MOS capacitor.

micrograph of the devices is shown in Fig. 3.22.

Excellent agreement between the model and experiment is observed. The modeling technique for this structure, slightly more complex than for a single varactor, is developed in Appendix C.

The Conductance

Little has been said so far about the real part of the admittance: the conductance. Although this algorithm can calculate both conductance and capacitance, the reason for stressing capacitance in this section is twofold:

1. Capacitance is usually the parameter of interest in MOS capacitors, whereas conductance is usually minimized for high Q devices or unimportant for design purposes.

2. Most measurements are made of capacitance since it is normally the larger of the two components and most easily measured.

Typical conductance/frequency versus voltage results are shown in Fig. 3.23, device data and grid are given on the graph. Figure 3.24 gives the conductance versus voltage of the ⁽⁵⁵⁾HSwe capacitors as modeled with the algorithm.

Further discussions of conductance curves are given in Section 3.6 where they are used to provide an indication of the accuracy of the algorithm.

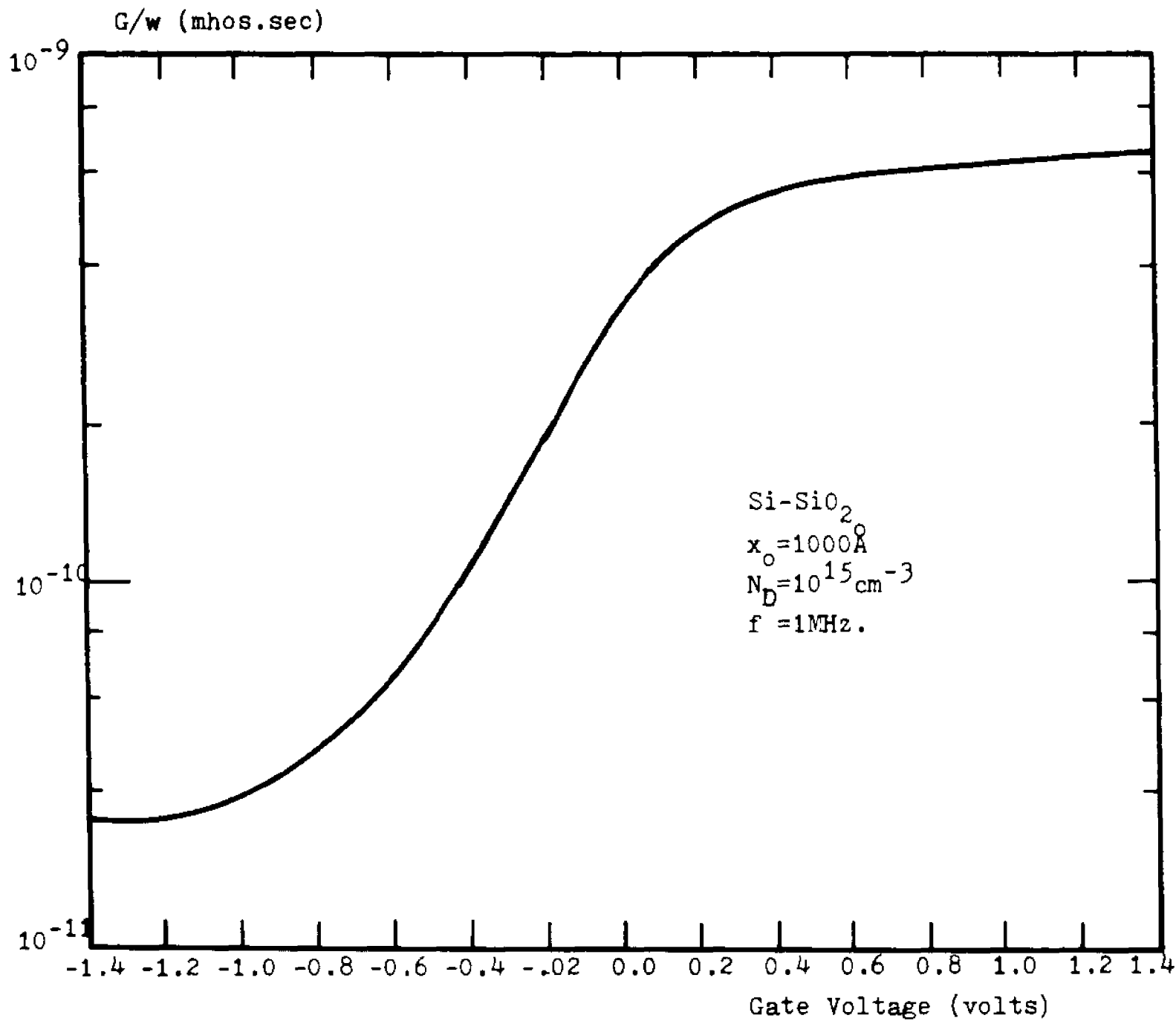
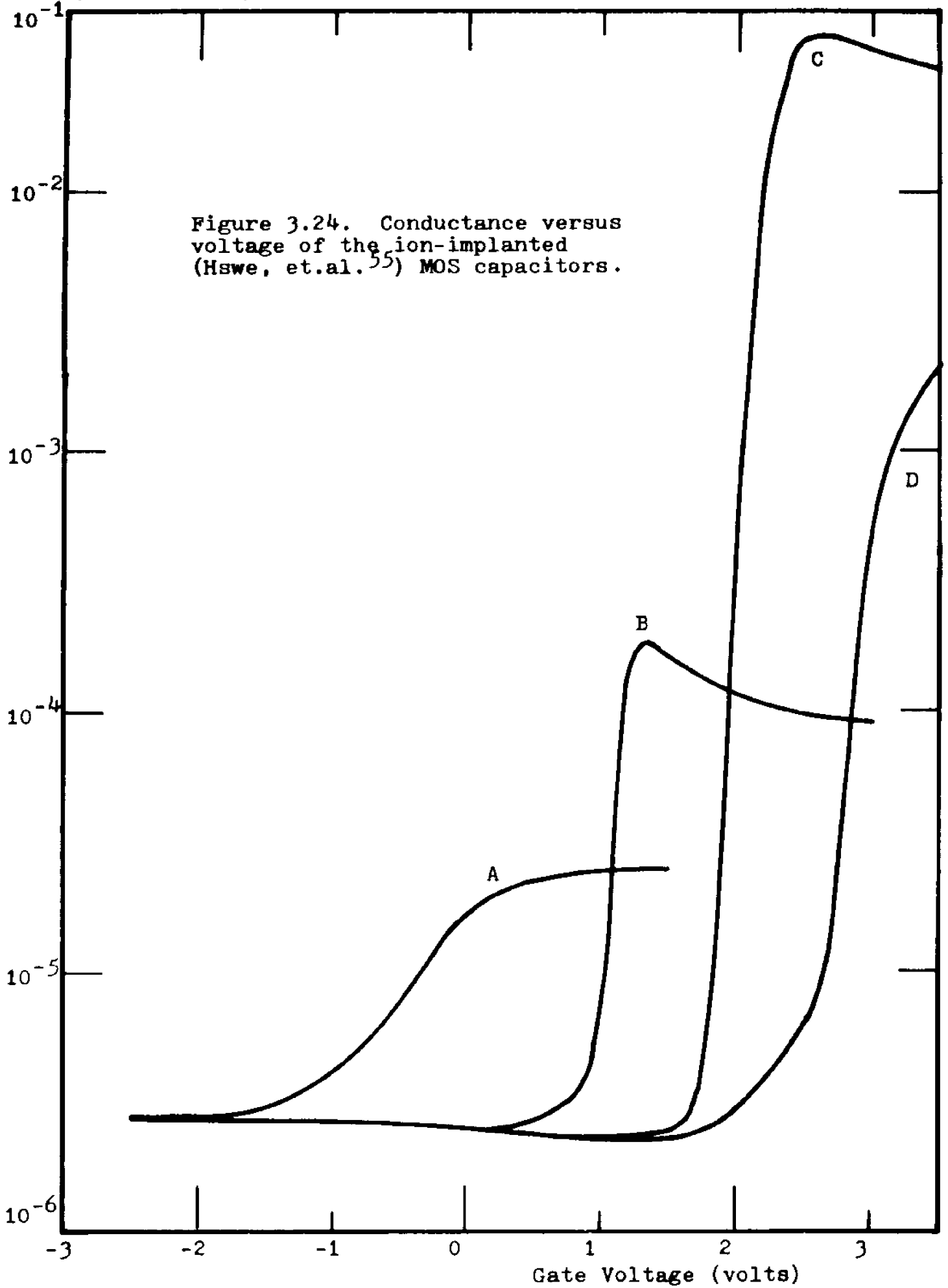


Figure 3.23. Typical high frequency conductance-voltage curve of an MOS capacitor.



3.5 The Total Solution

As described in Section 3.3, to obtain the total solution using the method of complimentary functions it is necessary to perform two passes. This minimizes storage requirements, a prime advantage of this method over others. As applied to the one dimensional method the memory savings realized is of the order: 3 independent vectors x 6 variables x N grid points x complex*16 dimension = 288 N bytes. By performing only one pass and obtaining the solution everywhere, the independent solutions at every point must be saved and then recombined into a complete solution when the combining constants have been found. To minimize memory requirements, a first pass is made without saving the independent solutions with the only aim being to reach the other boundary and obtain the combining constants. A second pass is then performed, which at the same time, generates the independent solutions again (see Section 3.3); and combines them with the constants found in the first pass into a total solution. It is evident that a trade-off between computation time and storage space has taken place. For the complete solution computation time is essentially doubled, but it is a fast algorithm which maintains its viability even in computing the total solution.

Implementation of the Second Pass to the Small Signal
AC Problem

The theory of the second pass, including reconditioning is discussed in Section 3.3. Essentially if no reconditioning has taken place in the course of the integration, then the β vector found at the second boundary can be used to recombine all independent solutions into a total solution throughout the second pass. On the other hand, if reconditioning has taken place at one or more intermediate points more than one set of β 's will be needed. (The exact number is one more than the number of reconditioning nodes since there is a β vector in each region between nodes.) The relationship between a β vector to one in a following region is given by Eq. 3.3.21.

$$\underline{\beta} = \underline{P}_i \underline{\beta}^* \quad (3.3.21)$$

The \underline{P}_i matrices are stored in the course of the first pass as reconditioning takes place. (This does not add considerably to memory requirements since orthonormalization is done on the average 10 to 12 times for 250 grid points. It has never been found necessary to use more than 20 reconditioning points. \underline{P} is a 3x3 matrix with usually COMPLEX*16 coefficients.) At the end of the integration, starting with the $\underline{\beta}_{r+1}$ vector all the other $\underline{\beta}$'s may be found by

$$\underline{\beta}_t = \underline{P}_t \underline{\beta}_{t+1} \quad 1 \leq t \leq r \quad (3.5.1)$$

where r is the number of reconditioning operations performed. Upon finding all $\underline{\beta}$'s, the second pass may be initiated and the total solution computed. The method may be summarized as follows:

1. Perform one pass through the device, calculating and saving the \underline{P} matrices at every reconditioning point and noting the location of the node.
2. Calculate the $\underline{\beta}$ vector to force the boundary conditions at the second boundary, this is $\underline{\beta}_{r+1}$.
3. Calculate the $\underline{\beta}$'s in reverse order by using Eq. 3.5.1 and the stored \underline{P} 's.
4. Repeat the integration, combining the generated solutions in each region with the appropriate $\underline{\beta}$'s, to obtain the total solution.

At each node in which reconditioning was performed in the first pass, reconditioning of the solution vectors must also be done and the next $\underline{\beta}$ used from that node to the next reconditioning node.

The \underline{P} matrices in the small signal AC problem are calculated using Eq. 3.3.11

$$\underline{Y}_i^* = \underline{Y}_i \underline{P}_i \quad (3.3.11)$$

where \underline{Y}_i^* and \underline{Y}_i are (3x6) matrices having columns which are vectors designated $\{y_1^* y_2^* y_3^*\}$ and $\{y_1, y_2, y_3\}$ respectively and \underline{P}_i is then a (3x3) matrix which transforms \underline{Y}_i into \underline{Y}_i^* . To obtain the coefficients of \underline{P}_i , use must be made of the definition of the Gram-Schmidt operation

$$\underline{n}_1 = \underline{y}_1 \quad (3.5.2)$$

$$\underline{y}_1^* = \underline{n}_1 / |\underline{n}_1| \quad (3.5.3)$$

$$\underline{n}_2 = \underline{y}_2 - \langle \underline{y}_2, \underline{y}_1^* \rangle \cdot \underline{y}_1^* \quad (3.5.4)$$

$$\underline{y}_2^* = \underline{n}_2 / |\underline{n}_2| \quad (3.5.6)$$

$$\underline{n}_3 = \underline{y}_3 - \langle \underline{y}_3, \underline{y}_2^* \rangle \cdot \underline{y}_2^* - \langle \underline{y}_3, \underline{y}_1^* \rangle \cdot \underline{y}_1^* \quad (3.5.7)$$

$$\underline{y}_3^* = \underline{n}_3 / |\underline{n}_3| \quad (3.5.8)$$

The coefficients of \underline{P}_i are derived from the above to

obtain

$$P_{11} = \frac{1}{|\underline{n}_1|} \quad (3.5.9)$$

$$P_{21} = (0, 0) \quad (3.5.10)$$

$$P_{31} = (0, 0) \quad (3.5.11)$$

$$P_{12} = \frac{\langle \underline{y}_2, \underline{y}_1^* \rangle}{|\underline{n}_2| |\underline{n}_1|} \quad (3.5.12)$$

$$P_{22} = \frac{1}{|\underline{n}_2|} \quad (3.5.13)$$

$$p_{32} = (0,0) \quad (3.5.14)$$

$$p_{13} = \frac{-\langle y_3, y_1^* \rangle}{|n_3| |n_1|} + \frac{\langle y_3, y_2^* \rangle \cdot \langle y_2, y_1^* \rangle}{|n_3| \cdot |n_2| \cdot |n_1|} \quad (3.5.15)$$

$$p_{23} = \frac{-\langle y_3, y_2^* \rangle}{|n_3| \cdot |n_2|} \quad (3.5.16)$$

$$p_{33} = \frac{1}{|n_3|} \quad (3.5.17)$$

Since, as a reconditioning operation is performed, the above quantities are readily available or may be easily computed, the above coefficients may be obtained without much difficulty. The \underline{P} matrix is upper diagonal which is consistent with the Gram- Schmidt procedure.

Results

The flow chart of Fig. 3.25 was implemented to produce a second pass and calculate the total solution. A quantity of interest in the device under study is the total current density. This parameter is a measure of the goodness of the solution since it must meet several requirements for the solution to be thought of as correct:

1. It must be constant throughout the device since the nodes are all serially connected.
2. Its magnitude and angle must yield the right value of admittance which is checked experimentally.

The total current density in the semiconductor is

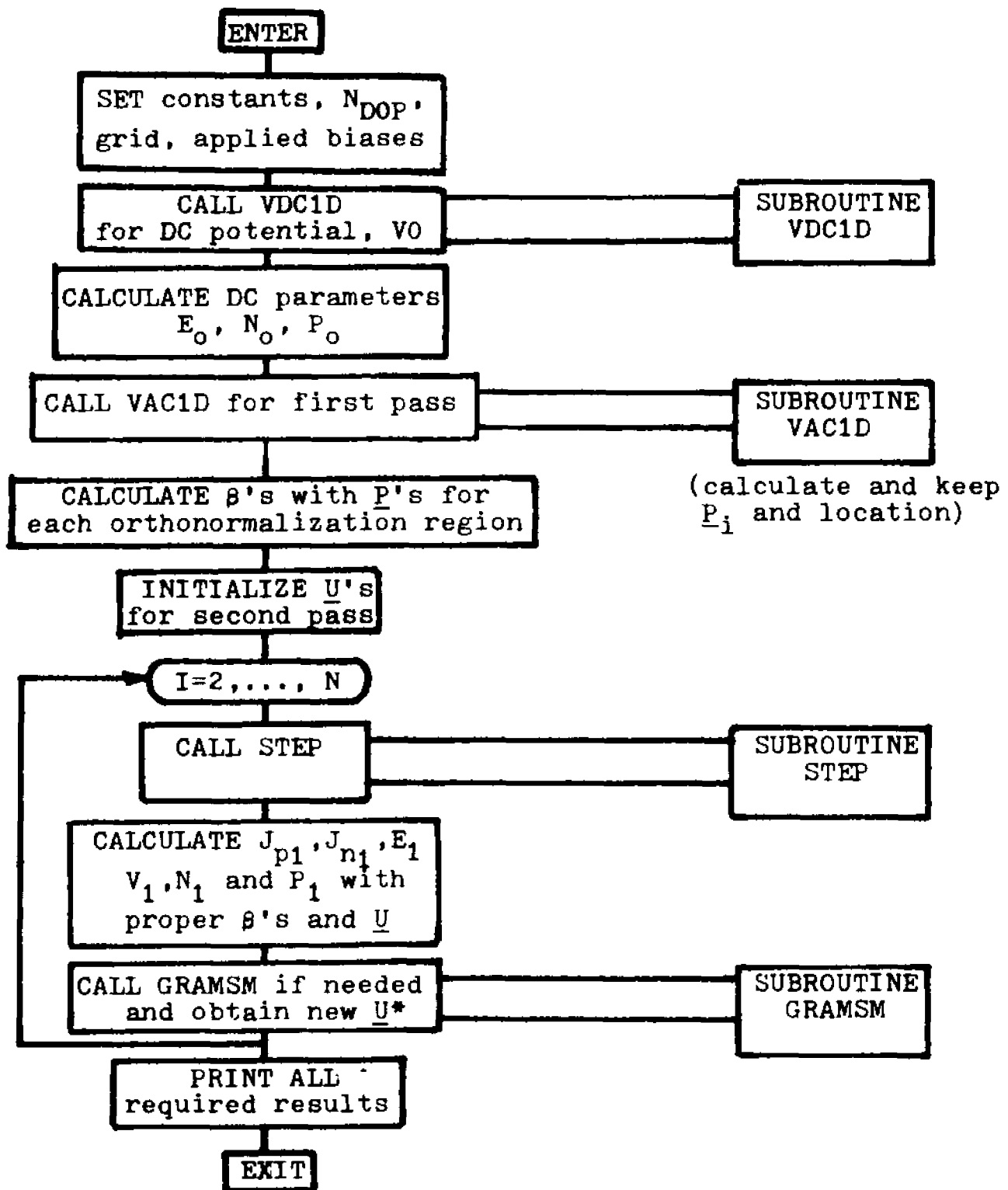


Figure 3.25. Computational flowchart of VACSTUDY, employed to calculate the total solution.

$$\tilde{J}_{\text{tot}} = \tilde{J}_{\text{disp}} + \tilde{J}_{p_1} + \tilde{J}_{n_1} \quad (3.5.18)$$

where \tilde{J}_{disp} is defined as

$$\tilde{J}_{\text{disp}} = j\omega K_{SI} \epsilon_0 \tilde{E}_1 \quad (3.5.19)$$

and \tilde{E}_1 , \tilde{J}_{p_1} , and \tilde{J}_{n_1} are part of the total solution being calculated.

The second pass and subsequent calculation of the total solution were implemented for two reasons:

1. Check on the validity of the total algorithm by making sure the solutions obtained made physical sense and overall results checked with experiments.
2. Check the effect reconditioning has on the solution.

The test case chosen to study 1 and 2 above is an ideal MOS capacitor with a 1000Å^o oxide and homogeneously doped n type bulk of 10¹⁵(1/cm³) doping concentration. Although all variables calculated (\tilde{J}_{p_1} , \tilde{J}_{n_1} , \tilde{n}_1 , \tilde{p}_1 , \tilde{E}_1 , \tilde{V}_1) were printed for every point only the current densities are shown in the figures following this discussion. They are the most instructive parameters from which to verify the algorithm. Test runs were made for four easily identifiable biasing conditions: accumulation, flat-band, depletion, and inversion. Furthermore, high and low frequency operating conditions were simulated by operating at signal frequencies of⁽⁵⁸⁾

1 MHz and 0.1 Hz respectively. These frequencies were chosen for the following reasons:

1. 1 MHz is the accepted measurement frequency for obtaining the high frequency admittance of MOS devices.
2. Operation at 0.1 Hz is representative of low frequency operation as discussed in Section 3.4.

The results are plotted in Fig. 3.26 through 3.33 and are quite remarkable. It is clear that the total current density in each case is constant. Its magnitude and angle are correct since the calculated capacitance is physically reasonable and checks with that calculated and measured by others⁽⁵⁷⁾. The way in which different current densities contribute to the total at different bias conditions is interesting. For example, Fig. 3.26 shows that under inversion (under high frequency conditions) the minority current density in the bulk is very small and peaks near the surface. This peak, though not sufficient for the minority current to contribute significantly to the total, is due to the large DC minority carrier concentrations in the surface region. Under the same DC conditions, but at low frequencies, as shown in Fig. 3.27, the minority carrier density dominates all others throughout the semiconductor. This supports the well known fact that at high frequencies the bulk cannot supply sufficient minority carriers to the surface for it to react to the applied signal

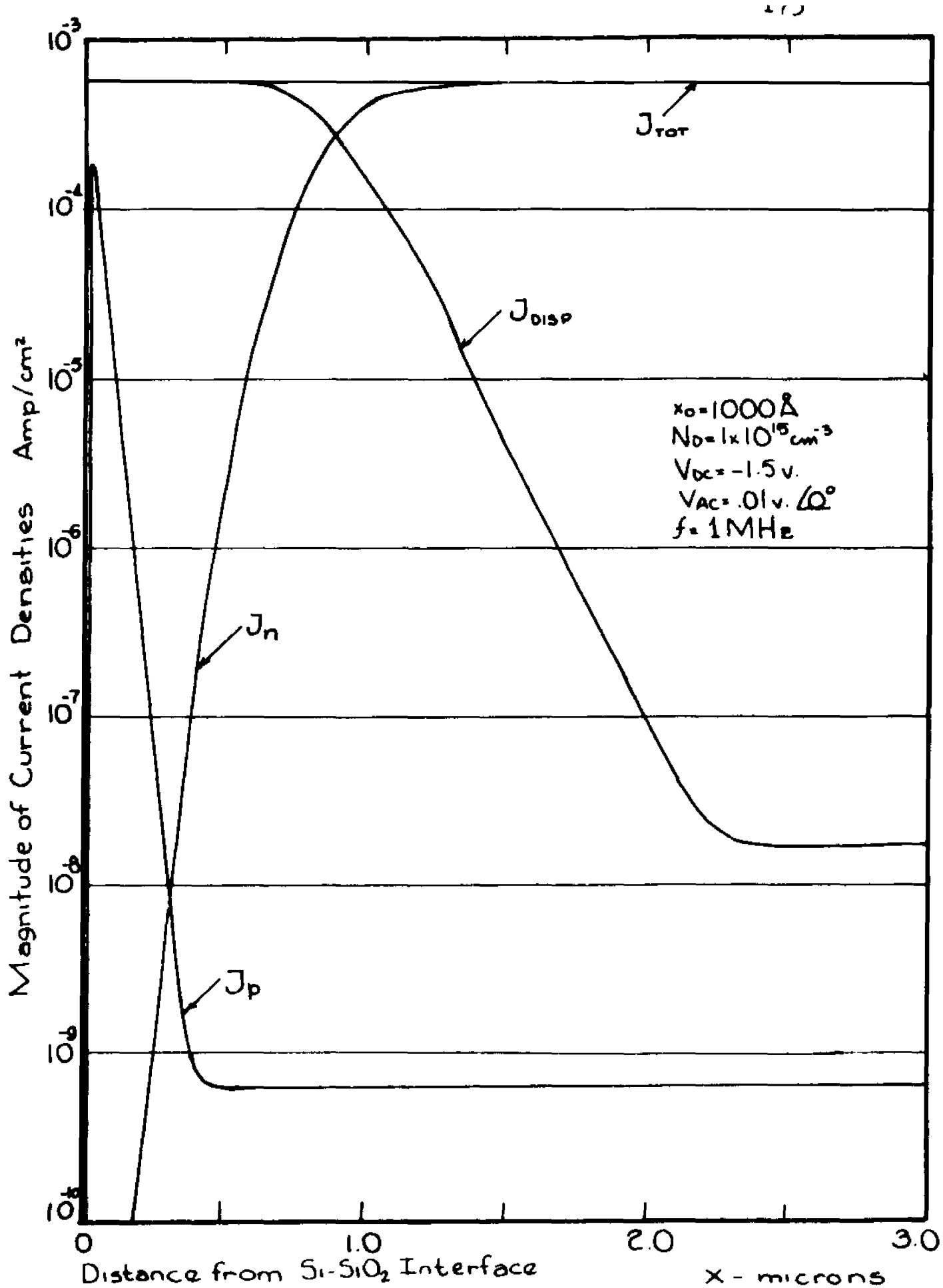


Figure 3.26. Small signal AC current densities in an MOS capacitor in inversion (high frequency).

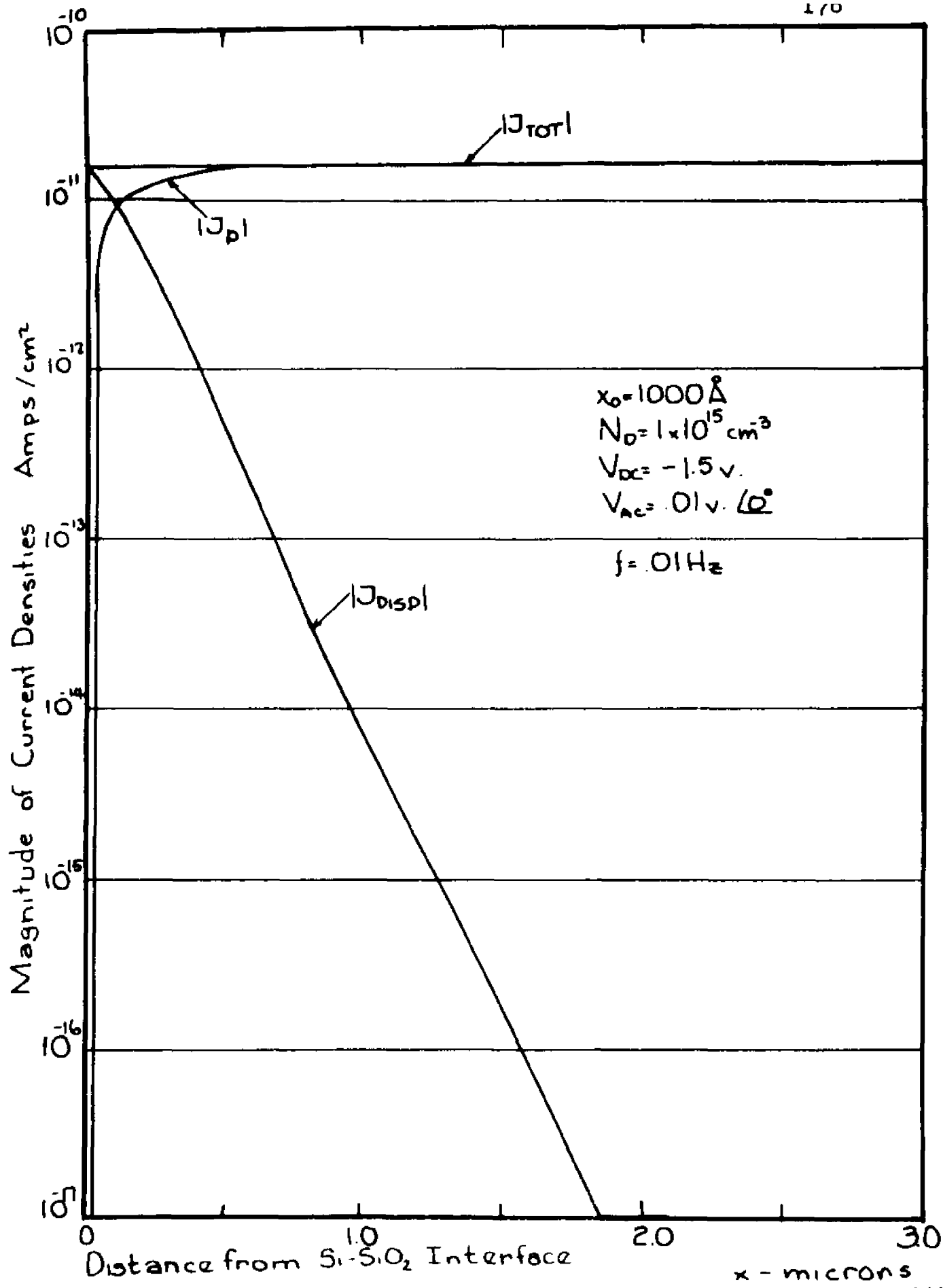


Figure 3.27. Small signal AC current densities in an MOS capacitor in inversion (low frequency).

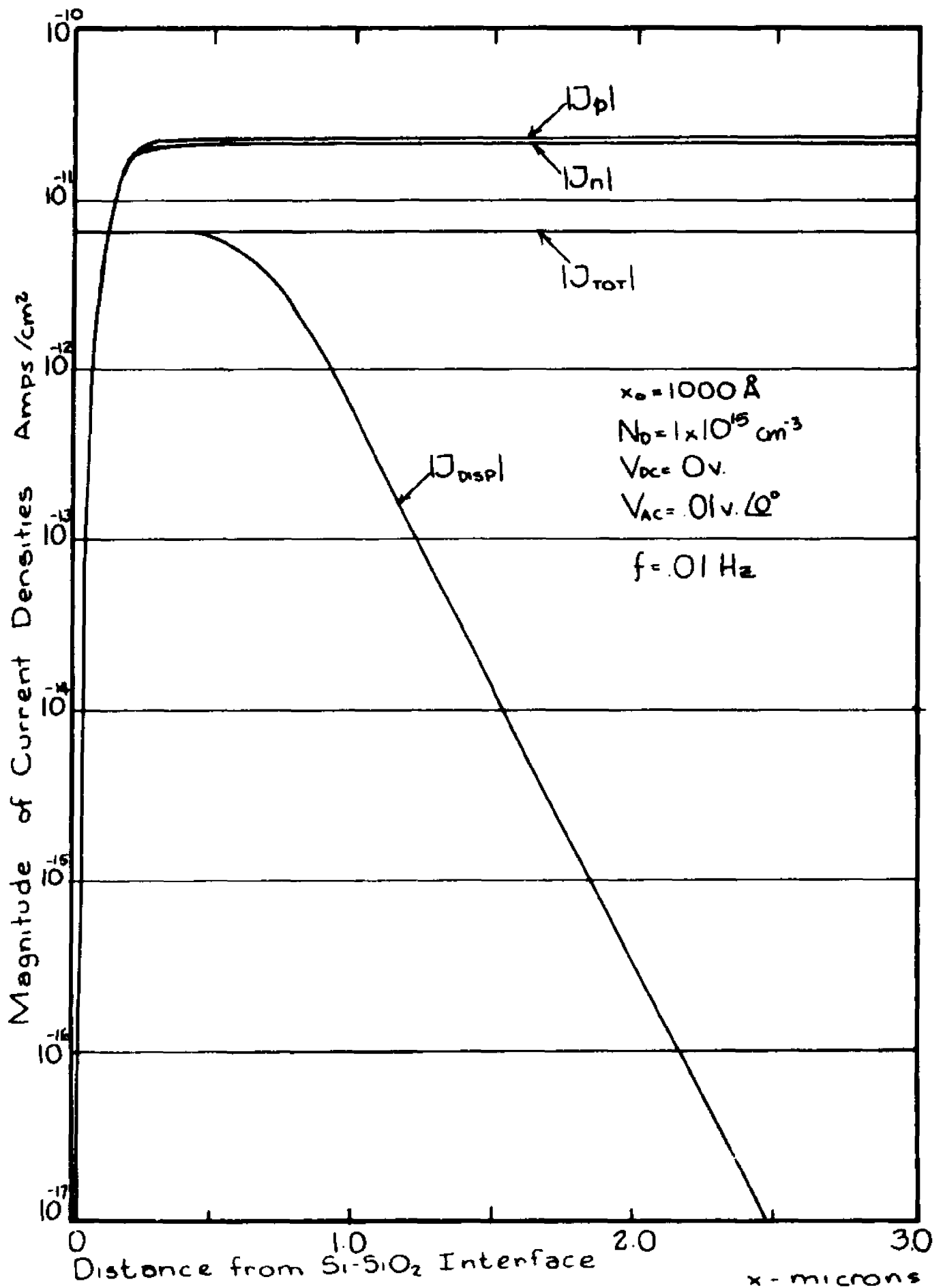


Figure 3.28. Small signal AC current densities in an MOS capacitor in flat-band (low frequency).

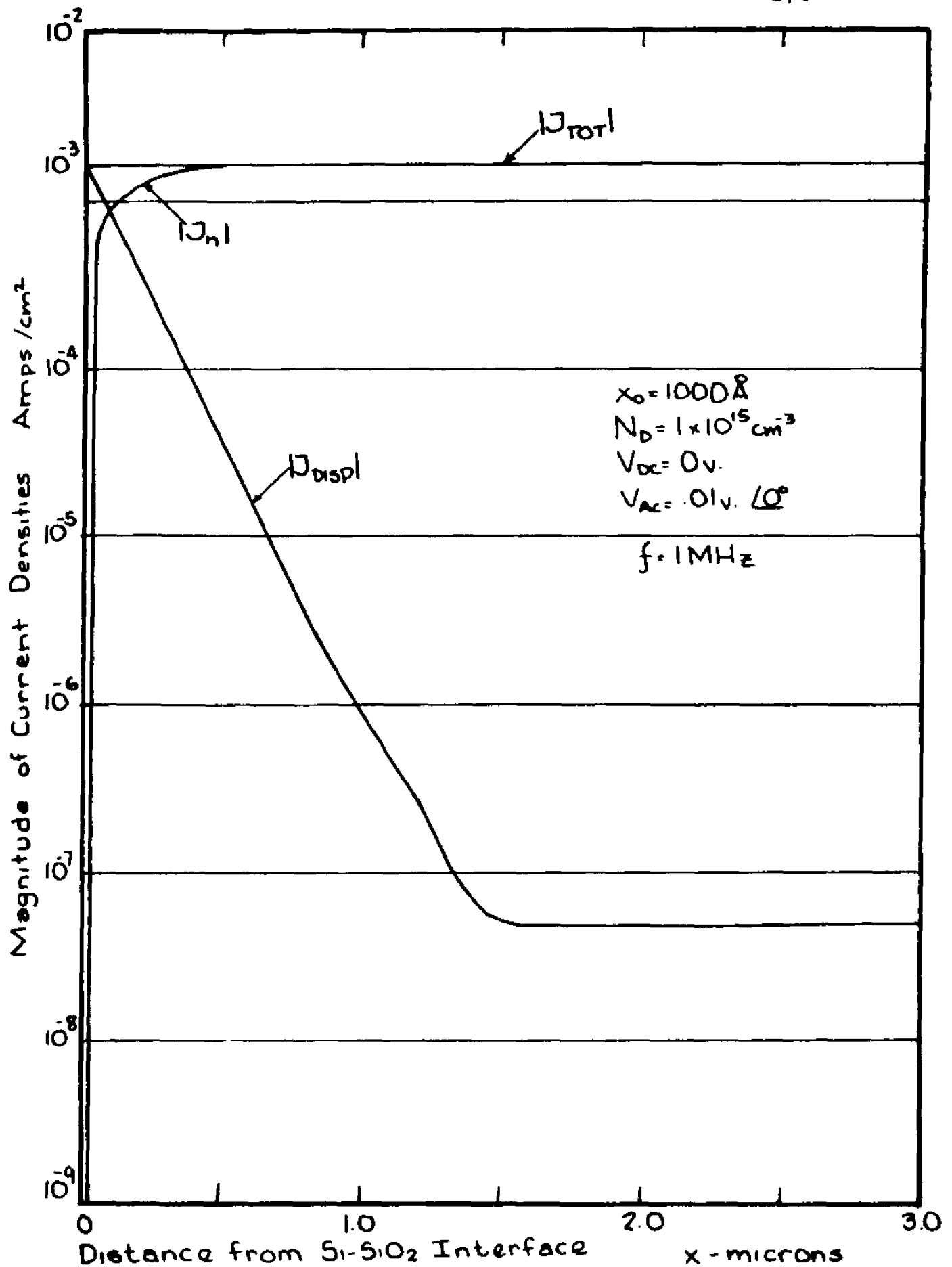


Figure 3.29. Small signal AC current densities in an MOS capacitor in flat-band (high frequency).

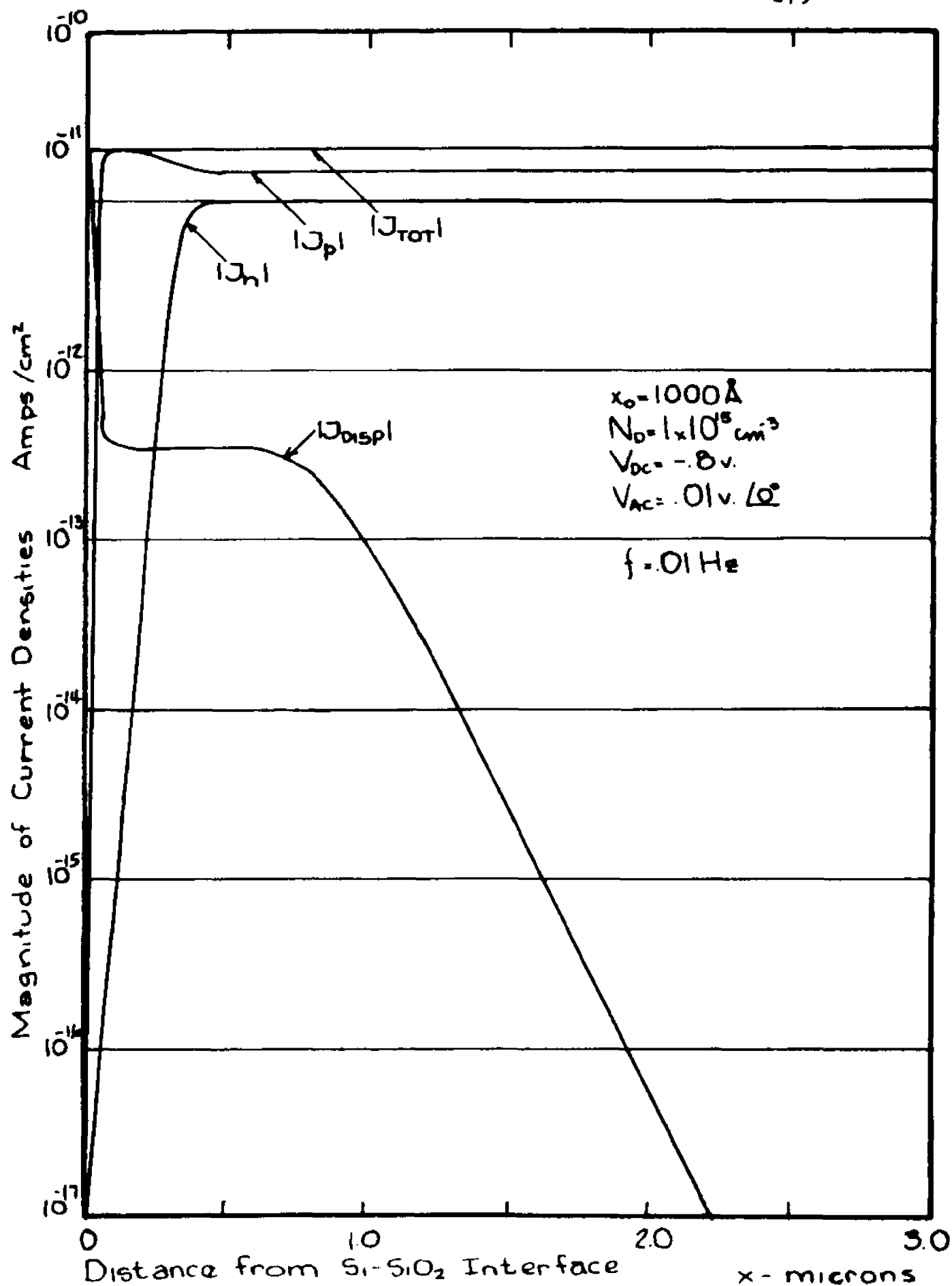


Figure 3.30. Small signal AC current densities in an MOS capacitor in depletion (low frequency).

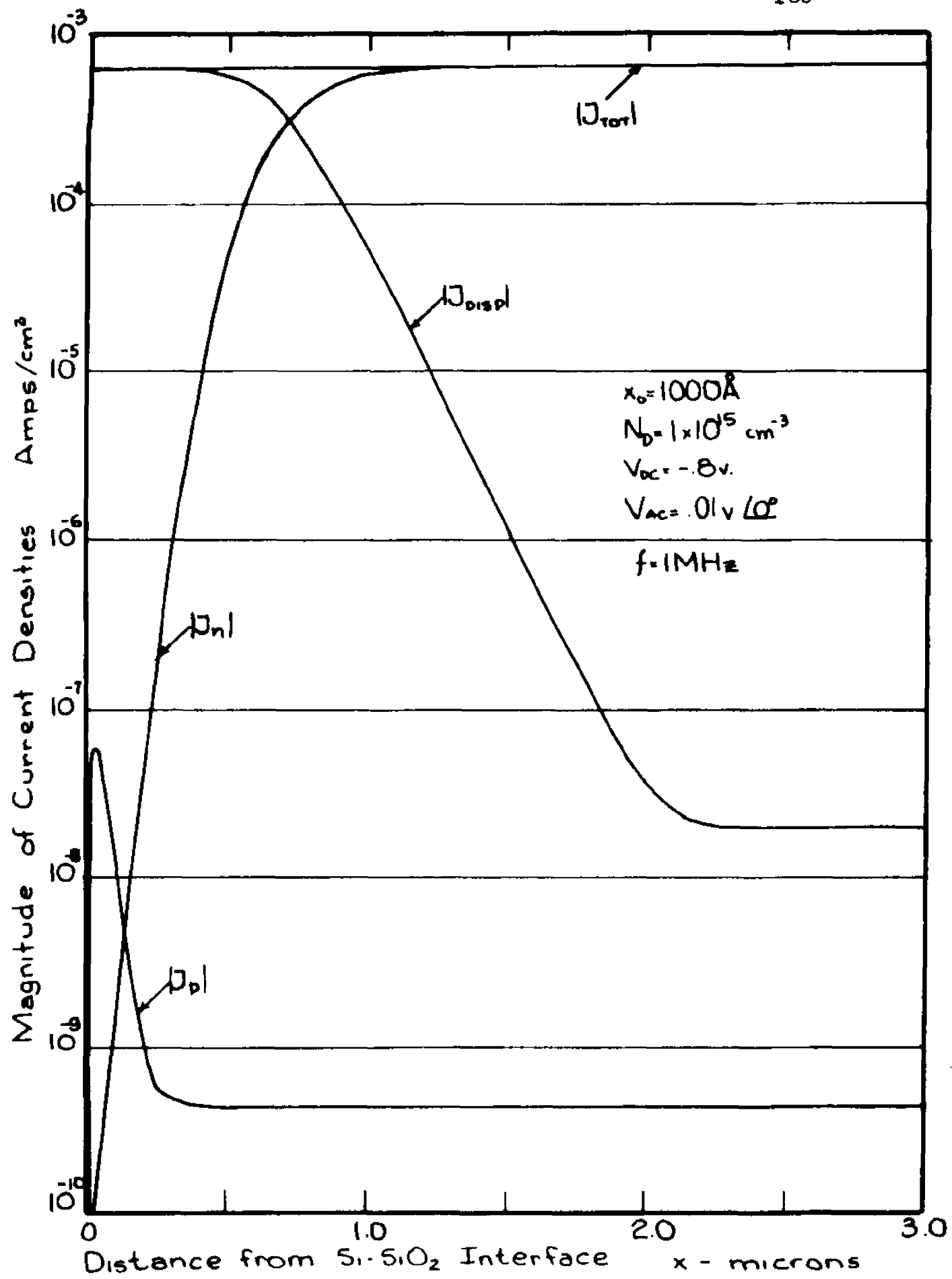


Figure 3.31. Small signal AC current densities in an MOS capacitor in depletion (high frequency).

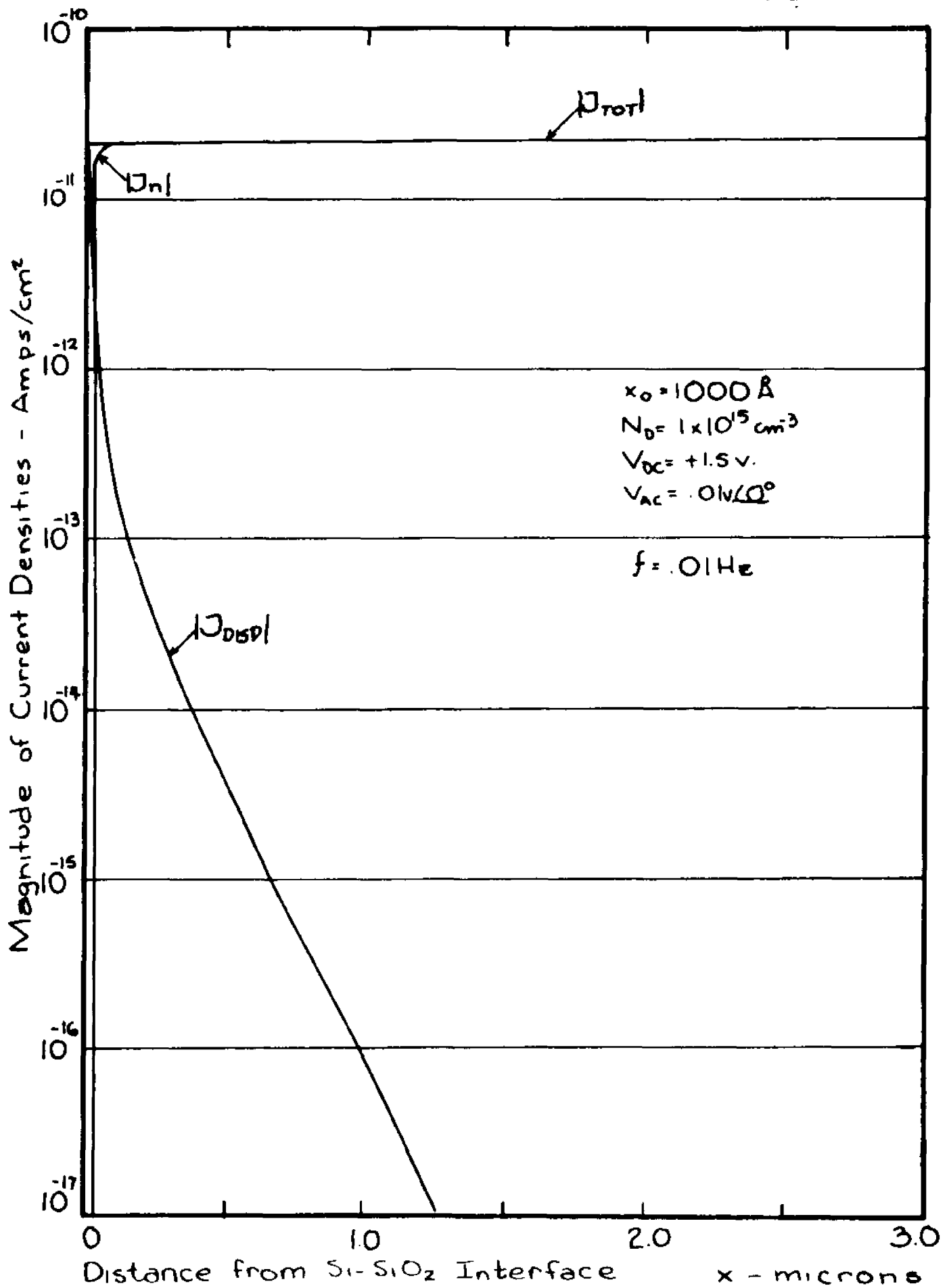


Figure 3.32. Small signal AC current densities in an MOS capacitor in accumulation (low frequency)

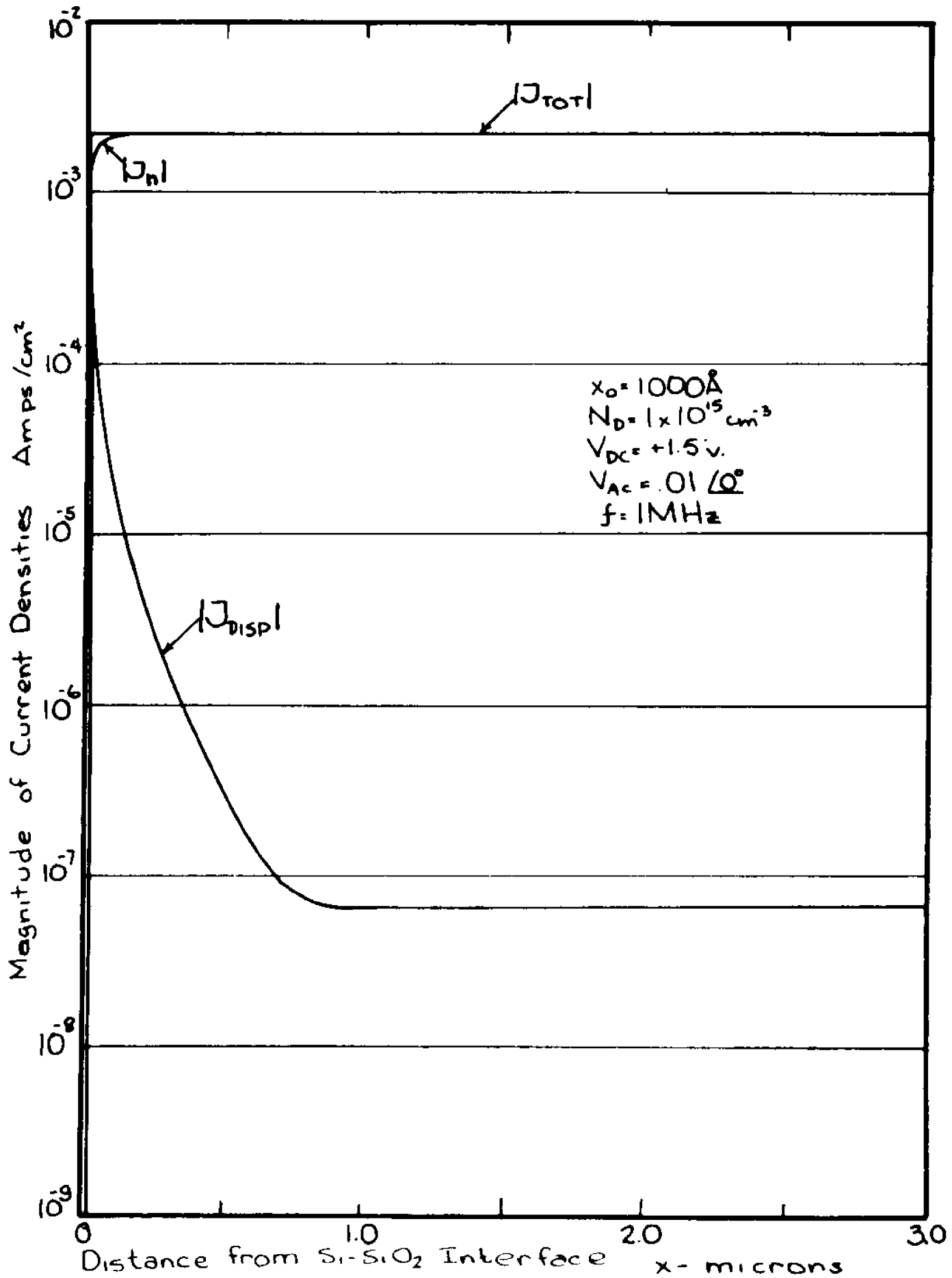


Figure 3.33. Small signal AC current densities in an MOS capacitor in accumulation (high frequency).

swing thus obtaining a high frequency capacitance which remains low in inversion. On the other hand, at low frequency, the bulk can supply sufficient minority carriers to the surface, as seen by the large bulk minority current density, and the capacitance at inversion returns to the high value of the oxide capacitance.

Note should be taken of the fact that at the surface, the carrier current densities become many orders of magnitude smaller than the largest current (orders of magnitude greater than the precision employed), i.e. essentially zero. Also, the displacement current density dominates in the surface and is approximately the total current density in the oxide. An interesting case is that of low frequency at flat-band, Fig. 3.28, where the minority and majority carrier densities are both higher than the total current densities but cancel to give the total current density.

The study of the effect of reconditioning yields mixed results. Only the case for $\epsilon = 0.8$ was tested (since this value of ϵ yielded the best results in modeling C-V curve) and their results compared to the no reconditioning calculation. Whereas the admittance under all bias conditions was the same for both cases and the total current density remained constant (angle and magnitude) throughout the device, a jump across a reconditioning point produced small anomalies in the quantities which were 10 to 12 orders of magnitude

below the dominant quantity. The anomalies may produce a 50% worst-case difference in magnitude. These very small quantities are calculated at a reconditioning node point before and after reconditioning. Physically it is clear that this quantity should be the same at the node point, whether calculated before or after reconditioning. The discrepancy prevailed in the bulk, closer to the first boundary or start of the integration, and not at the surface or end of integration. At that point are quantities before and after orthonormalization were the same to the number of digits printed. The source for this discrepancy is due to buildup of roundoff error in calculation of the β 's, which are less accurate at the beginning of the integration since the last β 's have been obtained through many matrix transformations from the first set of β 's calculated. The last $\underline{\beta}$ vector to be calculated, the one which holds in the first reconditioning interval, is obtained from the first $\underline{\beta}$ vector calculated (β_{r+1}) by

$$\underline{\beta}_1 = \underline{P}_1 \cdot \underline{P}_2 \cdot \dots \cdot \underline{P}_{r+1} \cdot \underline{\beta}_{r+1} \quad (3.5.19)$$

which involve r matrix multiplications. This may easily produce roundoff error to change the very small quantities 50% across a reconditioning point.

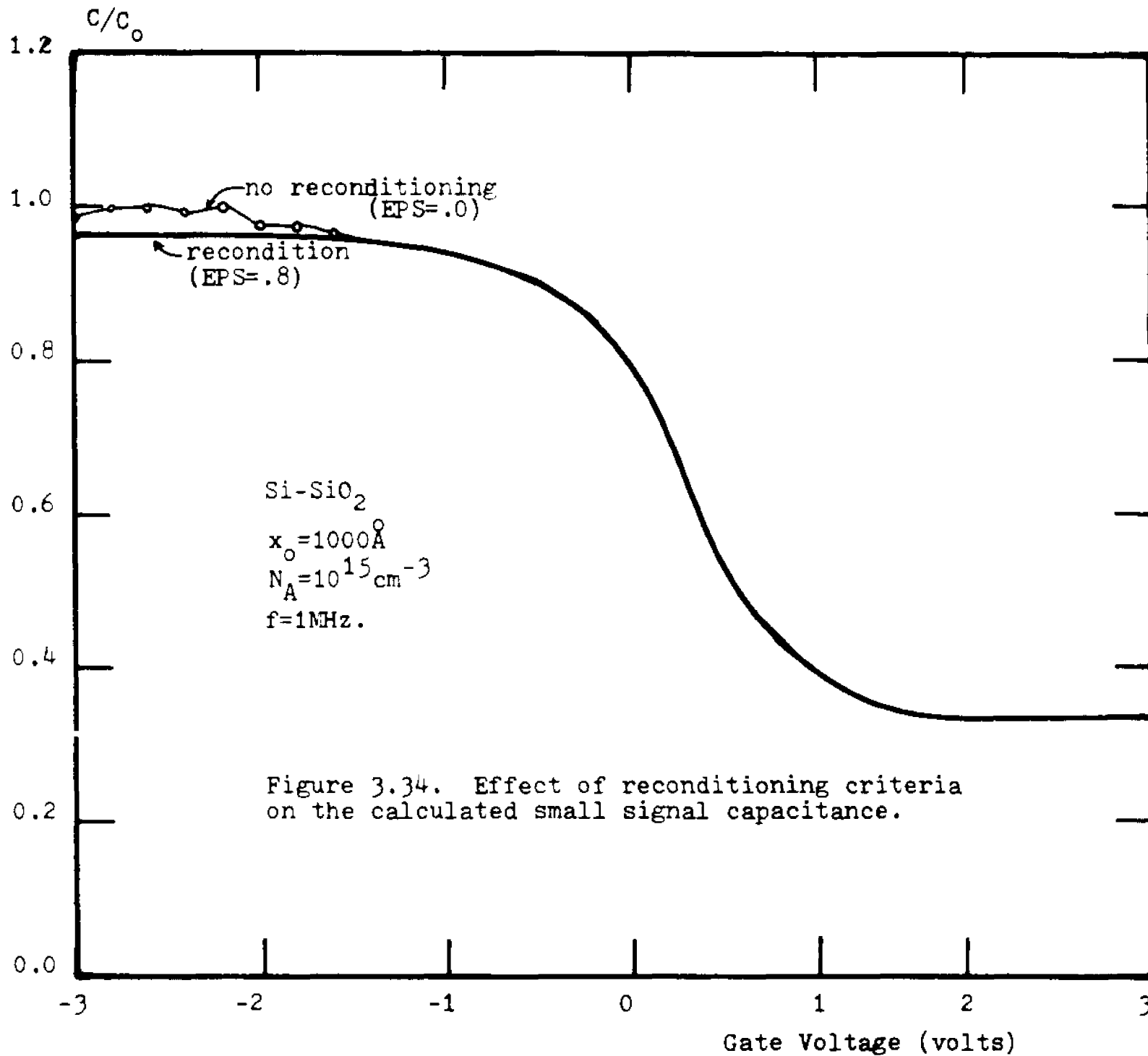
3.6 Studies of the Gram-Schmidt Results and Other Observations on the Algorithm

In executing the algorithm model in the various devices previously discussed, several observations concerning the model parameters were made and are presented in this section.

A question of great interest is the proper use of the orthonormalization routine. In the application of the algorithm, the following has been experienced:

1. If the orthonormalization is not performed at all in the course of the integration, the calculated admittance is usually a smooth and accurate function of the applied DC potential. As an example, an MOS capacitor was modeled with an oxide thickness of 1000\AA and a background doping of $N_A = 1 \times 10^{15} \text{ ions/cm}^2$ and acceptable results were obtained. On the other hand, the same device with a 900\AA oxide and $N_A = 3 \times 10^{15} \text{ ions/cm}^2$ yielded unacceptable results. The capacitance in this case exhibited instabilities in accumulation as shown in Fig. 3.3. The conductance exhibited instabilities throughout the whole bias range as shown in Fig. 3.3.

2. If the Gram-Schmidt is applied whenever the dot product of any vector before and after orthonormalization (see Section 3.3) is less than .8, then acceptable results were obtained in most cases. For the case above, the results are shown in Figs. 3.3 and 3.3 and contrasted with the no orthonormalization results.



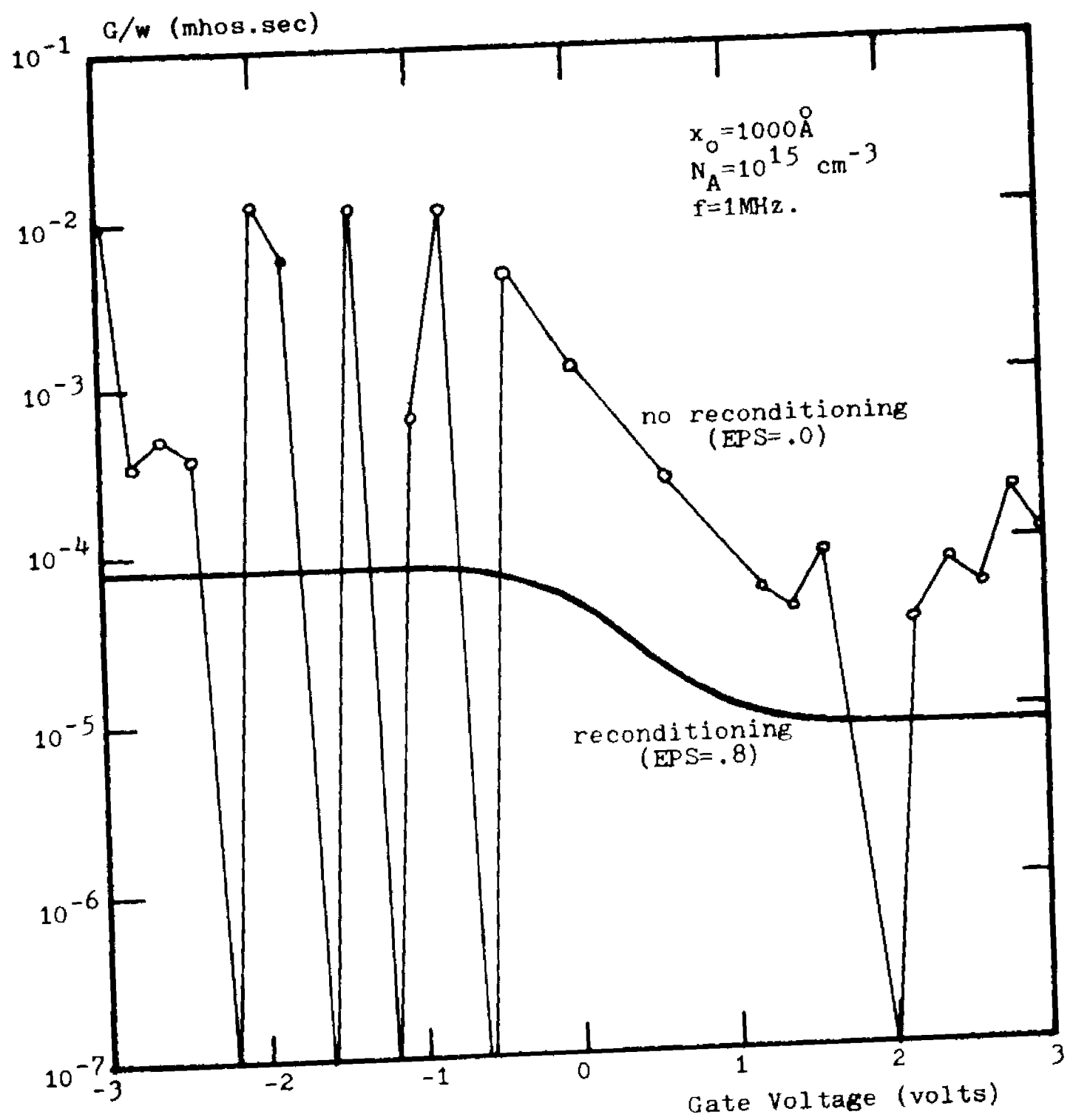


Figure 3.35. Effect of reconditioning on the calculated small signal conductance.

3. If the Gram-Schmidt is done too often then the results are extremely poor, with marked instabilities of several orders of magnitude in the calculated admittance.

4. As discussed in Section 3.5, the total current density through the device is relatively unaffected by reconditioning, but small components may vary widely when the Gram-Schmidt is applied compared to when it is not.

5. Device doping density may effect the buildup of linear dependence. In some cases this is very fast and small steps may be necessary, as is the case for highly doped materials. In such cases the application of reconditioning was not of much help, the grid had to be varied to obtain acceptable results. Generally, for highly doped materials the grid steps must be smaller.

The reason for this phenomena and this particular correction is easier to see when an integration method is employed. If very large integration steps are taken in regions where charge densities are changing rapidly with position, the finite machine precision forces an uncontrolled roundoff error. In more highly doped materials, field effect junctions are much sharper than in lightly doped material thus causing steeper charge gradients, which are conducive to error.

It may also be seen that the application of the Gram-Schmidt routine will be of little use if, after

a particular step, the vectors are so close to being linearly dependent that an error will not be bounded but propagate. This points to the optimum use of the Gram-Schmidt orthonormalization: it is only applicable when the vectors are moving toward linear dependence slowly as a function of grid position. A grid selection algorithm may be implemented based on this observation and more grid points introduced in a region where the orthonormalization criteria has sharp gradients.

The methods of Camisa⁽¹⁾ and Gockhale⁽⁵⁸⁾ have been classified as the classical method, the variables they employ being the quasi-fermi potentials, as defined by Shockley⁽⁵⁹⁾. Table 3.1 gives a brief tabular comparison of the classical method and the method of complimentary functions as applied to the small signal AC problem.

	Classical	Shooting Method
Variables	V_{p_1}, V_{n_1}, V_1	$J_{p_1}, J_{n_1}, p_1, n_1, E_1, V_1$
Number of Equations	3	6
Order of Equations	2 nd	1 st
Storage for Variables (N grid points)	3N	18
Peripheral Storage	Storage of 13 Bands for Two Carrier Problem=13N	None for the admittance
Storage for DC solution	N	N
Solution	Total Solution Available Upon Inversion of Matrix	a. One Pass For Admittance b. Two Passes for Total Solution
Extra Storage To Obtain Total Solution	None	36 x Number of Reconditioning Operations (20)

Table 3.1 One Dimensional Solution of the Small Signal AC Problem
A Comparison of Classical and Shooting Methods

	Classical	Shooting Method
Method of Solution	Matrix Inversion	Integration
Reconditioning	No	Yes
Accuracy	<ul style="list-style-type: none"> a. Iterative Refinement May Improve Accuracy b. Truncation Error of Discretization Scheme c. Accuracy of $((N-2) \times (N-2))$ Matrix Inversion 	Depends On: <ul style="list-style-type: none"> a. How Often Reconditioning Is Performed b. Order of Integration c. Only a 3×3 Matrix Needs to be Inverted
Computational Complexity	Simple	Complex

Table 3.1 (cont'd)

CHAPTER 4

THE SMALL SIGNAL AC MODEL IN
TWO SPATIAL DIMENSIONS4.1 Introduction

The extension of the problem discussed in the previous chapter to two spatial dimensions is not trivial and sophisticated techniques to obtain a solution are herein discussed.

As has been the practice in past chapters, a description of the structure and derivation of the pertinent equations with boundary conditions is performed first, in Section 4.2. Next, the theory of the method of complementary functions in two dimensions is given for elliptic partial differential equations in a rectangle. Special emphasis is paid to the Laplacian operator to illustrate the method. The reconditioning operation is described in Section 4.3. The application of the method to the small signal AC equations is performed in Section 4.4. The integration method employed is described, and a discussion of some preliminary results given. Small signal AC operation is normally superimposed on some DC operating point, which in the cases studied, is given by the two dimensional algorithm of Chapter 2. The total solution in one dimension for the small signal case, obtained with the method of

Chapter 3, is employed as the lateral boundary condition where appropriate.

This meshing of all the algorithms developed is brought to bear on the study of the electronic operation of the three terminal varactor. The results of the study are given in Section 4.5.

4.2 The Structure and Small Signal AC Equations in Two Spatial Dimensions

The small signal AC simulation described in this chapter is solved in two spatial dimensions for MIS devices which have the general structure shown in Chapter 2, Fig. 2.5. The DC operation of these devices is analyzed using the techniques of Chapter 2, providing the DC parameters necessary for the small signal AC analysis in two dimensions.

The purpose of this section is to derive the describing AC equations and related boundary conditions. The derivation for each type of media shall be made separately to improve the clarity of presentation.

The Semiconductor

The equations describing the operation of the semiconductor region of the device are those discussed in Chapter 1, reproduced here for completeness:

The carrier continuity equations

$$\frac{\partial p}{\partial t} = -R - \frac{1}{q} \nabla \cdot \tilde{J}_p \quad (1.3.1)$$

$$\frac{\partial n}{\partial t} = -R + \frac{1}{q} \nabla \cdot \tilde{J}_n \quad (1.3.2)$$

The current density equations

$$\tilde{J}_p = -q\mu_p V_T \nabla p - q\mu_p p \nabla V \quad (1.3.3)$$

$$\underline{J}_n = + q\mu_p V_T \nabla n - q\mu_n n \nabla V \quad (1.3.4)$$

Poisson's Equation

$$\nabla^2 V = \frac{-q}{\kappa_S \epsilon_0} (p-n + N_{DOP}) \quad (1.3.5)$$

It is convenient at this point to use the definition of the electric field intensity

$$\underline{E} = -\nabla V \quad (1.3.16)$$

to obtain

$$\underline{J}_p = -q\mu_p V_T \nabla p + q\mu_p p \underline{E} \quad (4.2.1)$$

$$\underline{J}_n = +q\mu_n V_T \nabla n + q\mu_n n \underline{E} \quad (4.2.2)$$

$$\nabla \underline{E} = \frac{q}{\kappa_S \epsilon_0} (p-n + N_{DOP}) \quad (4.2.3)$$

As in Chapter 3 where the small signal AC equations were derived in one dimension, each scalar variable is expressed as

$$A = A_0 + \tilde{A}_1 e^{j\omega t} \quad (4.2.4)$$

and each vector variable as

$$\underline{B} = \underline{B}_0 + \tilde{\underline{B}}_1 e^{j\omega t} \quad (4.2.5)$$

where the (o) variables are DC components and the (1) variables are AC components considered to be much smaller than the DC terms; i.e. $|\hat{A}_1| \ll |A_0|$ and $|\hat{E}_1| \ll |E_0|$. Rewriting each component in Eqs. 1.3.1 through 1.3.5 along the lines of Eqs. 4.2.4 and 4.2.5, one obtains

$$j\omega \tilde{p}_1 e^{j\omega t} = -\tilde{R}_1 \frac{1}{q} \nabla \cdot (\tilde{J}_{p_0} + \tilde{J}_{p_1} e^{j\omega t}) \quad (4.2.6)$$

$$j\omega \tilde{n}_1 e^{j\omega t} = -\tilde{R}_1 \frac{1}{q} \nabla \cdot (\tilde{J}_{n_0} + \tilde{J}_{n_1} e^{j\omega t}) \quad (4.2.7)$$

$$\tilde{J}_{p_0} + \tilde{J}_{p_1} e^{j\omega t} = -q\mu_p V_T \nabla \cdot (p_0 + \tilde{p}_1 e^{j\omega t}) + q\mu_p (p_0 + \tilde{p}_1 e^{j\omega t}) \cdot (\tilde{E}_0 + \tilde{E}_1 e^{j\omega t}) \quad (4.2.8)$$

$$\tilde{J}_{n_0} + \tilde{J}_{n_1} e^{j\omega t} = +q\mu_n V_T \nabla \cdot (n_0 + \tilde{n}_1 e^{j\omega t}) + q\mu_n (n_0 + \tilde{n}_1 e^{j\omega t}) \cdot (\tilde{E}_0 + \tilde{E}_1 e^{j\omega t}) \quad (4.2.9)$$

$$\nabla \cdot (\tilde{E}_0 + \tilde{E}_1 e^{j\omega t}) = \frac{q}{K_S \epsilon_0} (p_0 + \tilde{p}_1 e^{j\omega t} - n_0 - \tilde{n}_1 e^{j\omega t} + N_{DOP}) \quad (4.2.10)$$

Again, as in Chapter 3, the second order terms in Eqs. 4.2.8 and 4.2.9 are neglected yielding

$$\tilde{J}_{p_0} + \tilde{J}_{p_1} e^{j\omega t} = -q\mu_p V_T \nabla \cdot (p_0 + \tilde{p}_1 e^{j\omega t}) + q\mu_p p_0 \tilde{E}_0 + (\tilde{p}_1 \tilde{E}_0 + p_0 \tilde{E}_1) e^{j\omega t} \quad (4.2.11)$$

$$\tilde{J}_{n_0} + \tilde{J}_{n_1} e^{j\omega t} = +q\mu_n V_T \nabla \cdot (n_0 + \tilde{n}_1 e^{j\omega t}) + q\mu_n n_0 \tilde{E}_0 + (\tilde{n}_1 \tilde{E}_0 + n_0 \tilde{E}_1) e^{j\omega t} \quad (4.2.12)$$

Collecting the AC terms in the above equations yields five equations for the AC variables

$$j\omega\tilde{p}_1 = -\tilde{R}_1 - \frac{1}{q} \nabla \cdot \tilde{J}_{p_1} \quad (4.2.13)$$

$$j\omega\tilde{n}_1 = -\tilde{R}_1 + \frac{1}{q} \nabla \cdot \tilde{J}_{n_1} \quad (4.2.14)$$

$$\tilde{J}_{p_1} = -q\mu_p V_T \nabla \cdot p + q\mu_p p_o \tilde{E}_1 + q\mu_p \tilde{p}_1 E_o \quad (4.2.15)$$

$$\tilde{J}_{n_1} = +q\mu_n V_T \nabla \cdot n_1 + q\mu_n n_o \tilde{E}_1 + q\mu_n \tilde{n}_1 E_o \quad (4.2.16)$$

$$\nabla \cdot \tilde{E}_1 = \frac{q}{\kappa_S \epsilon_o} (\tilde{p}_1 - \tilde{n}_1) \quad (4.2.17)$$

Whereas the above set of first order equations is complete, adding a sixth variable, the AC potential, makes the application of the boundary conditions easier as is seen later in this section. Thus Eq. 1.3.16 may be solved for the gradient of the scalar potential

$$\nabla(V_o + \tilde{V}_1 e^{j\omega t}) = -(\tilde{E}_o + \tilde{E}_1 e^{j\omega t}) \quad (4.2.18)$$

where application has been made of the small signal approximation.

The AC potential is found from

$$\nabla \cdot \tilde{V}_1 = -\tilde{E}_1 \quad (4.2.19)$$

As a form of normalization, the carrier densities may be converted to charge densities. Consider new variables defined as

$$\tilde{P}_1 = q \cdot \tilde{p}_1 \quad (4.2.20)$$

$$\tilde{N}_1 = q \cdot \tilde{n}_1 \quad (4.2.21)$$

$$P_0 = q \cdot p_0 \quad (4.2.22)$$

$$N_0 = q \cdot n_0 \quad (4.2.23)$$

The equations then become

$$j\omega\tilde{P}_1 = -q\tilde{R}_1 - \nabla \cdot \tilde{J}_{p_1} \quad (4.2.24)$$

$$j\omega\tilde{N}_1 = -q\tilde{R}_1 + \nabla \cdot \tilde{J}_{n_1} \quad (4.2.25)$$

$$\tilde{J}_{p_1} = -\mu_p V_T \nabla \cdot \tilde{P}_1 + \mu_p P_0 \tilde{E}_1 + \mu_p \tilde{P}_1 E_0 \quad (4.2.26)$$

$$\tilde{J}_{n_1} = +\mu_n V_T \nabla \cdot \tilde{N}_1 + \mu_n N_0 \tilde{E}_1 + \mu_n \tilde{N}_1 E_0 \quad (4.2.27)$$

$$\nabla \cdot \tilde{E}_1 = \frac{1}{\kappa_S \epsilon_0} (\tilde{P}_1 - \tilde{N}_1) \quad (4.2.28)$$

The next step in the derivation is to separate the vector equations into scalar equations. Equations 4.2.26 and 4.2.27 then become

$$\tilde{J}_{p_1 x} = -\mu_p V_T \frac{\partial \tilde{P}_1}{\partial x} + \mu_p P_0 \tilde{E}_{1x} + \mu_p \tilde{P}_1 E_{0x} \quad (4.2.29)$$

$$\tilde{J}_{n_1 x} = +\mu_n V_T \frac{\partial \tilde{N}_1}{\partial x} + \mu_n N_0 \tilde{E}_{1x} + \mu_n \tilde{N}_1 E_{0x} \quad (4.2.30)$$

$$\tilde{J}_{p1x} = \mu_p V_T \frac{\partial \tilde{P}_1}{\partial x} + \mu_p P_o \tilde{E}_{1y} + \mu_p \tilde{P}_1 E_{oy} \quad (4.2.31)$$

$$\tilde{J}_{n1y} = +\mu_n V_T \frac{\partial \tilde{N}_1}{\partial y} + \mu_n N_o \tilde{E}_{1y} + \mu_n \tilde{N}_1 E_{oy} \quad (4.2.32)$$

Since the method of solution entails integration of the equations in the y direction, the next step is to rewrite all expressions containing terms in the \hat{a}_x direction as functions of terms in the \hat{a}_y direction. Equation 4.2.24 and 4.2.25 are rewritten with the gradient term expanded

$$j\omega \tilde{P}_1 = -q\tilde{R}_1 - \frac{\partial \tilde{J}_{p1x}}{\partial x} - \frac{\partial \tilde{J}_{p1y}}{\partial y} \quad (4.2.33)$$

$$j\omega \tilde{N}_1 = -q\tilde{R}_1 + \frac{\partial \tilde{J}_{n1x}}{\partial x} + \frac{\partial \tilde{J}_{n1y}}{\partial y} \quad (4.2.34)$$

Taking the partial derivative of Eqs. 4.2.29 and 4.2.30 with respect to x provides an expression useful in the above

$$\begin{aligned} \frac{\partial \tilde{J}_{p1x}}{\partial x} &= -\mu_p V_T \frac{\partial^2 \tilde{P}_1}{\partial x^2} + \mu_p P_o \frac{\partial \tilde{E}_{1x}}{\partial x} + \mu_p \frac{\partial P_o}{\partial x} \tilde{E}_{1x} + \mu_p \tilde{P}_1 \frac{\partial E_{ox}}{\partial x} \\ &\quad + \mu_p \frac{\partial \tilde{P}_1}{\partial x} E_{ox} \end{aligned} \quad (4.2.35)$$

$$\begin{aligned} \frac{\partial \tilde{J}_{n1x}}{\partial x} &= +\mu_n V_T \frac{\partial^2 \tilde{N}_1}{\partial x^2} + \mu_n N_o \frac{\partial \tilde{E}_{1x}}{\partial x} + \mu_n \frac{\partial N_o}{\partial x} \tilde{E}_{1x} + \mu_n \tilde{N}_1 \frac{\partial E_{ox}}{\partial x} \\ &\quad + \mu_n \frac{\partial \tilde{N}_1}{\partial x} E_{ox} \end{aligned} \quad (4.2.36)$$

The approximation has been made here that the variation of either mobility with respect to x is slight and may be neglected. In cases where this approximation is seen not to hold, the above equations may be expanded simply to take this into account. Equations 4.2.35 and 4.2.36 are now used in Eqs. 4.2.33 and 4.2.34 which are in turn solved for the derivatives of the currents yielding

$$\frac{\partial \tilde{J}_{p_1 y}}{\partial y} = +(j\omega\tilde{P}_1 + q\tilde{R}_1) - \mu_p V_T \left\{ -\frac{\partial^2 \tilde{P}_1}{\partial x^2} + \frac{P_o}{V_T} \frac{\partial \tilde{E}_{1x}}{\partial x} + \frac{\partial P_o}{\partial x} \frac{\tilde{E}_{1x}}{V_T} + \frac{\tilde{P}_1}{V_T} \frac{\partial E_{ox}}{\partial x} + \frac{\partial \tilde{P}_1}{\partial x} \frac{E_{ox}}{V_T} \right\} \quad (4.2.37)$$

$$\frac{\partial \tilde{J}_{n_1 y}}{\partial y} = -(j\omega\tilde{N}_1 + q\tilde{R}_1) + \mu_n V_T \left\{ \frac{\partial^2 \tilde{N}_1}{\partial x^2} + \frac{N_o}{V_T} \frac{\partial \tilde{E}_{1x}}{\partial x} + \frac{\partial N_o}{\partial x} \frac{\tilde{E}_{1x}}{V_T} + \frac{\tilde{N}_1}{V_T} \frac{\partial E_{ox}}{\partial x} + \frac{\partial \tilde{N}_1}{\partial x} \frac{E_{ox}}{V_T} \right\} \quad (4.2.38)$$

So as not to add an extra variable to the set, \tilde{E}_{1x} is replaced by

$$\frac{\partial \tilde{V}_1}{\partial x} = -\tilde{E}_{1x} \quad (4.2.39)$$

Using this in the above equations, results in

$$\frac{\partial \tilde{J}_{p_1 y}}{\partial y} = -(j\omega\tilde{P}_1 + q\tilde{R}_1) + \mu_p V_T \left\{ \frac{\partial^2 \tilde{P}_1}{\partial x^2} + \frac{P_o}{V_T} \frac{\partial^2 \tilde{V}_1}{\partial x^2} + \frac{\partial P_o}{\partial x} \frac{\partial \tilde{V}_1}{\partial x} \frac{1}{V_T} + \frac{\tilde{P}_1}{V_T} \frac{\partial^2 V_o}{\partial x^2} - \frac{\partial \tilde{P}_1}{\partial x} \frac{E_{ox}}{V_T} \right\} \quad (4.2.40)$$

$$\begin{aligned} \frac{\partial \tilde{J}_{n_1 y}}{\partial y} = & -(j\omega \tilde{N}_1 + q \tilde{R}_1) + \mu_n V_T \frac{\partial^2 \tilde{N}_1}{\partial x^2} - \frac{N_o}{V_T} \frac{\partial^2 \tilde{V}_1}{\partial x^2} - \\ & \frac{\partial N_o}{\partial x} \frac{\partial \tilde{V}_1}{\partial x} \frac{1}{V_T} - \frac{\tilde{N}_1}{V_T} \frac{\partial^2 V_o}{\partial x^2} + \frac{\partial \tilde{N}_1}{\partial x} \frac{E_{ox}}{V_T} \end{aligned} \quad (4.2.41)$$

where use has been made of the relationship between E_{ox} and V_o .

Equations 4.2.31 and 4.2.32 are solved for the charge density partial derivatives in the y direction

$$\frac{\partial \tilde{P}_1}{\partial y} = - \frac{\tilde{J}_{p_1 y}}{\mu_p V_T} + \frac{P_o}{V_T} \tilde{E}_{1y} + \frac{\tilde{P}_1}{V_T} E_{oy} \quad (4.2.42)$$

$$\frac{\partial \tilde{N}_1}{\partial y} = + \frac{\tilde{J}_{n_1 y}}{\mu_n V_T} - \frac{N_o}{V_T} \tilde{E}_{1y} - \frac{\tilde{N}_1}{V_T} E_{oy} \quad (4.2.43)$$

Applying Eqs. 4.2.40 to 4.2.28 yields an expression for the partial derivative of \tilde{E}_{1y} in the y direction

$$\frac{\partial \tilde{E}_{1y}}{\partial y} = \frac{1}{K_S \epsilon_o} (\tilde{P}_1 - \tilde{N}_1) + \frac{\partial^2 \tilde{V}_1}{\partial x^2} \quad (4.2.44)$$

Finally, an expression for the partial derivative of \tilde{V}_1 in the y direction is found from the y direction component of Eq. 4.2.19

$$\frac{\partial \tilde{V}_1}{\partial y} = - \tilde{E}_{1y} \quad (4.2.45)$$

Equations 4.2.40 through 4.2.45 comprise the necessary set to solve the problem. They are reproduced in

Fig. 4.1 together with boundary conditions. The rationale behind this particular method of setting up the equations is presented when the numerical method of solution is discussed in Section 4.3.

The Insulator

Using the assumption that the insulator is non-conductive, it is only necessary to solve Laplace's equation in that region. To be compatible with the equations in the semiconductor and to have smooth transitions from one region to another, the second order equation may be rewritten as two first order equations in y

$$\frac{\partial \tilde{E}_{1y}}{\partial y} = \frac{\partial^2 \tilde{V}_1}{\partial x^2} \quad (4.2.46)$$

$$\frac{\partial \tilde{V}_1}{\partial y} = -\tilde{E}_{1y} \quad (4.2.47)$$

Equation 4.2.19 has been applied in this derivation.

The Metal-Semiconductor Boundary

At this boundary, the same assumptions discussed in Chapter 3 will be assumed to hold, namely that the contact is ohmic and no accumulation of carriers exist at this interface. This plane is chosen as the voltage reference node of the device. Consequently the boundary conditions are

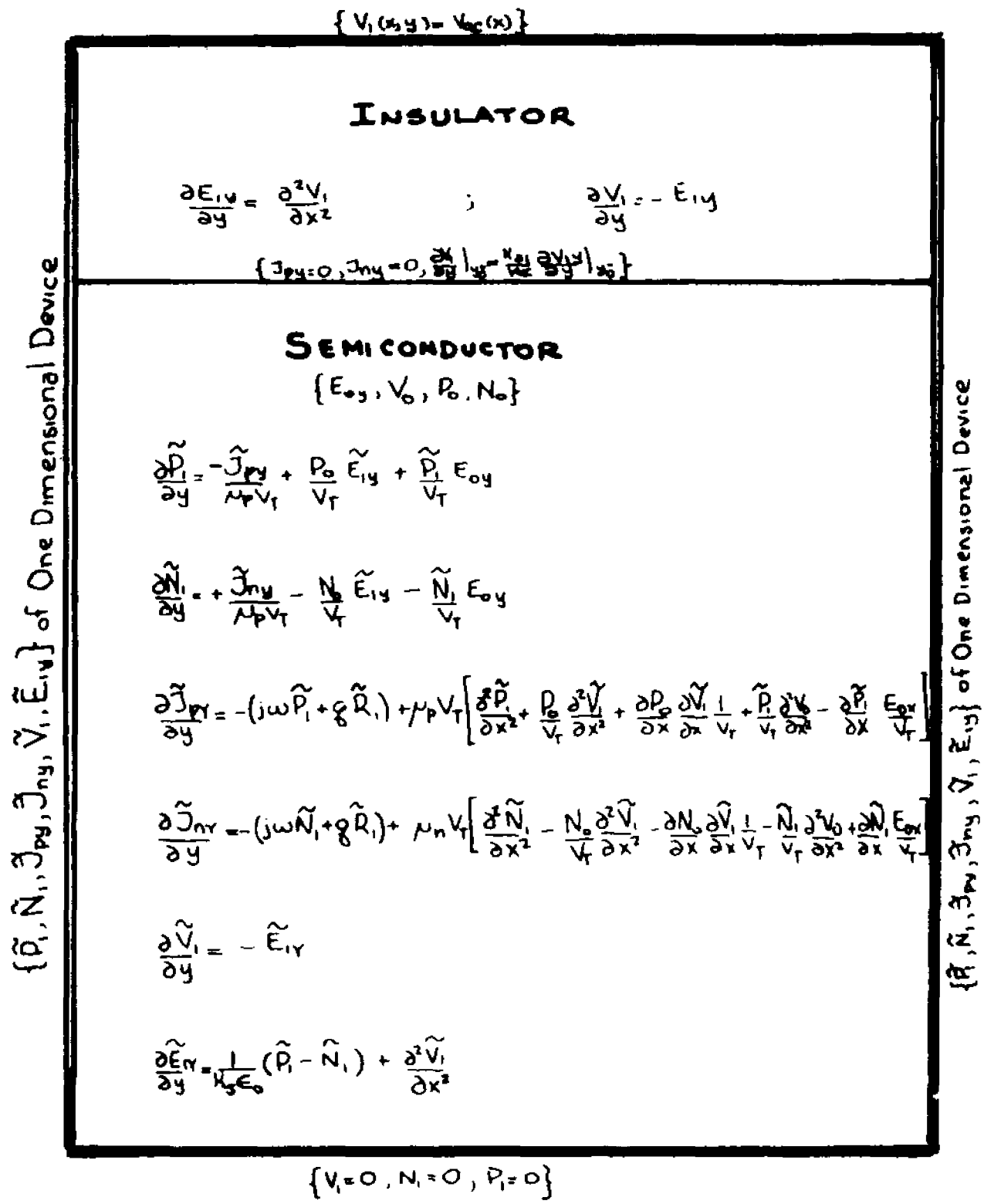


Figure 4.1. Structure, equations and boundary conditions for two dimensional small signal MIS device simulation.

$$\tilde{V}_1(x, y_B) = 0, \tilde{P}_1(x, y_B) = 0, \tilde{N}_1(x, y_B) = 0, x_L \leq x \leq x_R \quad (4.2.48)$$

The Metal-Insulator Boundary

Since the metal contact at this boundary is connected to the external AC signal source, and it is assumed that the AC voltage applied to this contact or set of contacts, as the case may be, is not necessarily constant in the x direction, the boundary condition on \tilde{V}_1 is

$$\tilde{V}_1(x, y=0) = \tilde{V}_{ac}(x), \quad x_L \leq x \leq x_R \quad (4.2.49)$$

The Semiconductor-Insulator Interface

Applying Gauss' Law at the plane of the interface,

$$\hat{n}_1 \cdot \mathcal{D}_1 - \hat{n}_2 \cdot \mathcal{D}_2 = Q \quad (4.2.50)$$

At the interface in question the normal unit vector is in the \hat{a}_y direction thus the above reduces to

$$\kappa_S \epsilon_0 \tilde{E}_{1y}(x, y_0^+) - \kappa_I \epsilon_0 \tilde{E}_{1y}(x, y_0^-) = 0 \quad (4.2.51)$$

where use has been made of the relationship between the electric displacement and field intensity and the fact that the AC interface charge density is zero.

$$\tilde{J}_{p_1y}(x, y_0^+) = 0, \tilde{J}_{n_1y}(x, y_0^+) = 0, x_L \leq x \leq x_R \quad (4.2.52)$$

Whereas the zero recombination velocity assumption makes the boundary conditions simpler to implement, it is not necessary to adhere to it where the physics necessitates a nonzero term. For the present application it was not found necessary to include a nonzero surface recombination velocity.

The Transverse Boundaries

It is not sufficient to specify boundary data on the y boundaries alone since one is dealing here with a set of elliptic partial differential equations. These equations require the specification of boundary data on the whole boundary. It is much easier to implement Dirichlet boundary condition than Neumann or mixed type. For this reason, the assumption is made that at the transverse boundaries a one dimensional solution holds. This solution is obtained from the one dimensional model of Chapter 3. The approximation made here is similar to that made for the transverse boundaries in the DC problem. The effect of this assumption is shown in Appendix D.

4.3 The Theory of the Method of Complementary Functions For Elliptic Partial Differential Equations

In this section the method of complementary functions applied to elliptic partial differential equations is presented. This method is also referred to as a "shooting" method since it involves solving the equations from one boundary to another in a manner analagous to "shooting". In the literature, this method may alternately be called the "reconditioning" method⁽⁶⁰⁾ or the "stabilized march out technique"⁽⁴⁷⁾.

Consider a general second order linear p.d.e

$$\nabla^2 u(x,y) = f(\nabla u, u, x, y,) \quad (4.3.1)$$

which is elliptic. This p.d.e. is to be solved in a region of the Cartesian xy space labeled R; a restriction for numerical computation shall be placed on the boundary, namely that it be rectangular. This is not a general restriction on the method, rather since non-rectangular regions are not considered elsewhere in this work, it is expedient to consider only regions of that type. Figure 4.2a shows the region under study and its associated boundaries. The boundary data is of the proper type for an elliptic p.d.e.: boundary value on the closed boundary. Consider as a first example the Dirichlet boundary data as shown in Fig. 4.2a.

The continuous p.d.e. is now discretized with a rectangular grid, not necessarily uniform in the x and

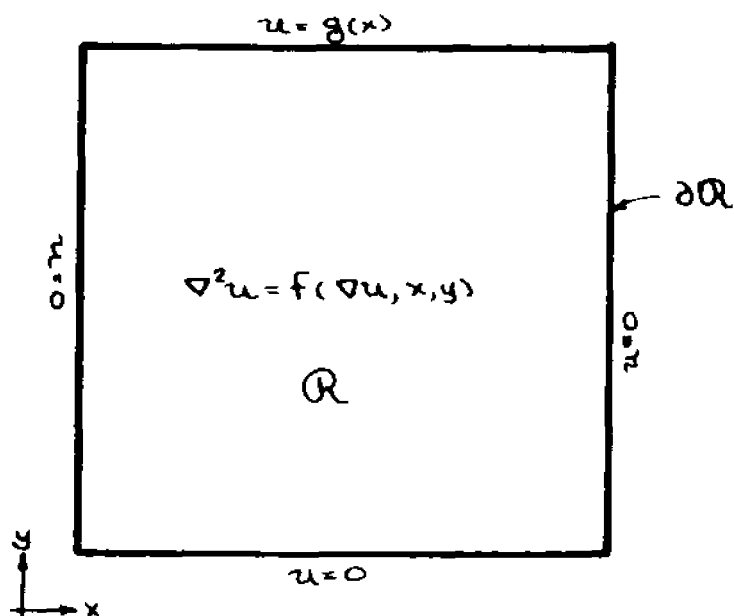


Figure 4.2a. The general two dimensional problem used in developing the shooting method.

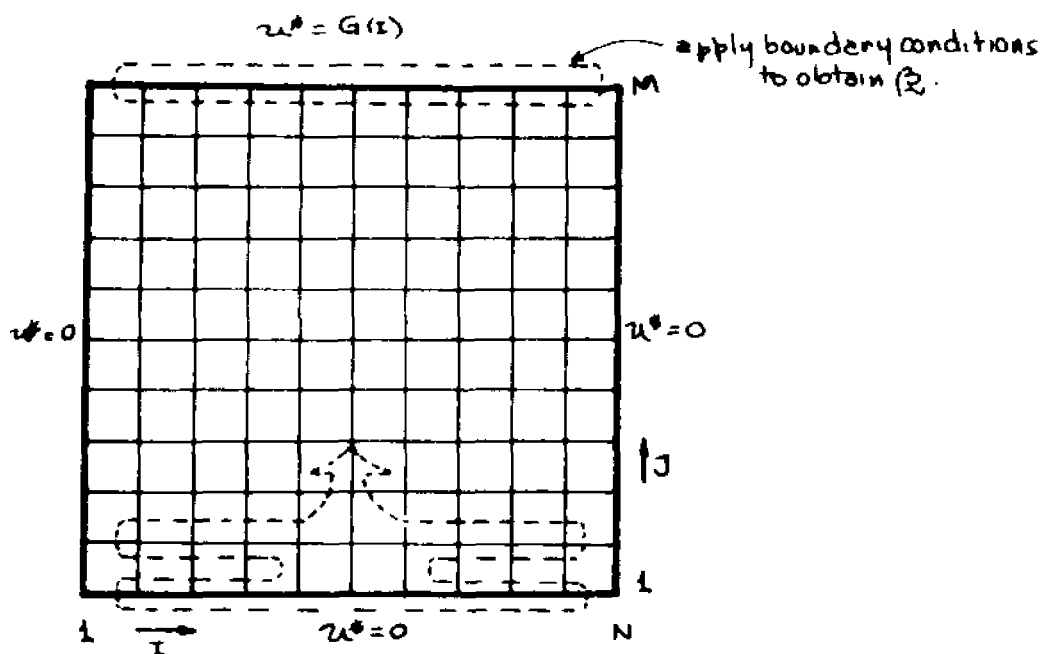


Figure 4.2b. The region above discretized with a grid and shooting direction assigned.

y directions. Some appropriate discretization scheme is employed for the second order partial derivatives and for the first order ones, yielding

$$\Delta^2 u^* = f(Du^*, u^*, x_i, y_j) \quad (4.3.2)$$

where u^* is the discrete analogue of u and Δ^2 and D are the symbols representing the discrete analogues of ∇^2 and ∇ . The grid structure is shown in Fig. 4.2b.

The method of solution of the resulting set of linear algebraic Eq. 4.3.2 consists of solving for the values of u^* for a whole row at a time in terms of the values in the preceding rows. In other words, solving Eq. 4.3.2 for $\{u^*(I, J+1), 2 \leq I \leq N-1\}$ in terms of $\{u^*(I, J) \text{ and } u^*(I, J-1), 2 \leq I \leq N-1\}$. In matrix form, this is expressed as

$$\underline{u}^*(J+1) = \underline{A}\underline{u}^*(J) + \underline{B}\underline{u}^*(J-1) + \underline{C} \quad (4.3.3)$$

where $\underline{u}^*(\cdot)$ is a vector of all the row components $\{u^*(I, \cdot), 2 \leq I \leq N-1\}$. This method is self-starting if, when it begins at one boundary, both the boundary row and one row in from the boundary are known. This condition is true of hyperbolic and parabolic p.d.e's where the variable and its gradient are the given boundary conditions. In this case it is slightly different since either the value of the unknown or its gradient are given, but never both, since that would overstate the boundary conditions. Thus, having the boundary values

or the gradients, is insufficient to start the algorithm. This difficulty is avoided by arbitrarily choosing starting conditions for the unknown values in the necessary row in such a way that as many linearly independent starting row solutions are chosen as unknowns exist. This generates a matrix \underline{U} , the columns of which are the \underline{u}^* each linearly independent from the next. Equation 4.3.3 relates the row solution matrices to each other as

$$\underline{U}(J+1) = \underline{A} \underline{U}(J) + \underline{B} \underline{U}(J-1) + \underline{C} \quad (4.3.4)$$

It is seen that if \underline{A} , \underline{B} and \underline{C} are matrices of rank $(N-2)$ equal to their order $(N-2)$, and either one or both of the matrices $\underline{U}(J)$ and $\underline{U}(J-1)$ have linearly independent columns (which means their rank and order are $(N-2)$) then $\underline{U}(J+1)$ will have rank equal to its order $(N-2)$. This will result in $\underline{U}(J+1)$ having columns linearly independent.

This generation of matrices of linearly independent row solutions continues until the opposite boundary is reached. Here these solutions will not necessarily satisfy the boundary conditions individually but may be combined with some weights to match those boundary conditions

$$\underline{U}(M) \cdot \underline{\beta} = \underline{u}^*(M) \text{ given} \quad (4.3.5)$$

There are as many combining constants in the vector $\underline{\beta}$ as there are unknowns arbitrarily chosen at the beginning. This is not coincidental; if the arbitrary starting values were Kronecker delta conditions, then the $\underline{\beta}$ found from solving Eq. 4.3.5 are the required unknown values in the second row. The Kronecker delta starting condition is easily implemented as

$$\underline{U}(2) = \underline{I} \quad (4.3.6)$$

where \underline{I} is the identity matrix and $\underline{U}(2)$ is the row matrix one row from the starting boundary. Once the combining constants have been found, the solution at any one row may be computed from

$$\underline{u}^*(J) = \underline{U}(J) \cdot \underline{\beta} \quad (4.3.7)$$

Since $\underline{U}(J)$ for $J=2$ is the identity matrix \underline{I} , then it is seen that indeed $\underline{u}^*(2)$, the unknown starting row values are the weights $\underline{\beta}$.

For boundary data which is nonzero at the transverse and lower boundaries, the solution is divided into two parts: the homoneneous solution and the response due to the nonzero boundaries. Figure 4.3 shows this decomposition. Since the p.d.e. in question, and all subsequent ones considered in this chapter, are linear, this separation and final sum of solutions is admissible since superposition is valid. The homogeneous problem is the same as considered previously up to but not including

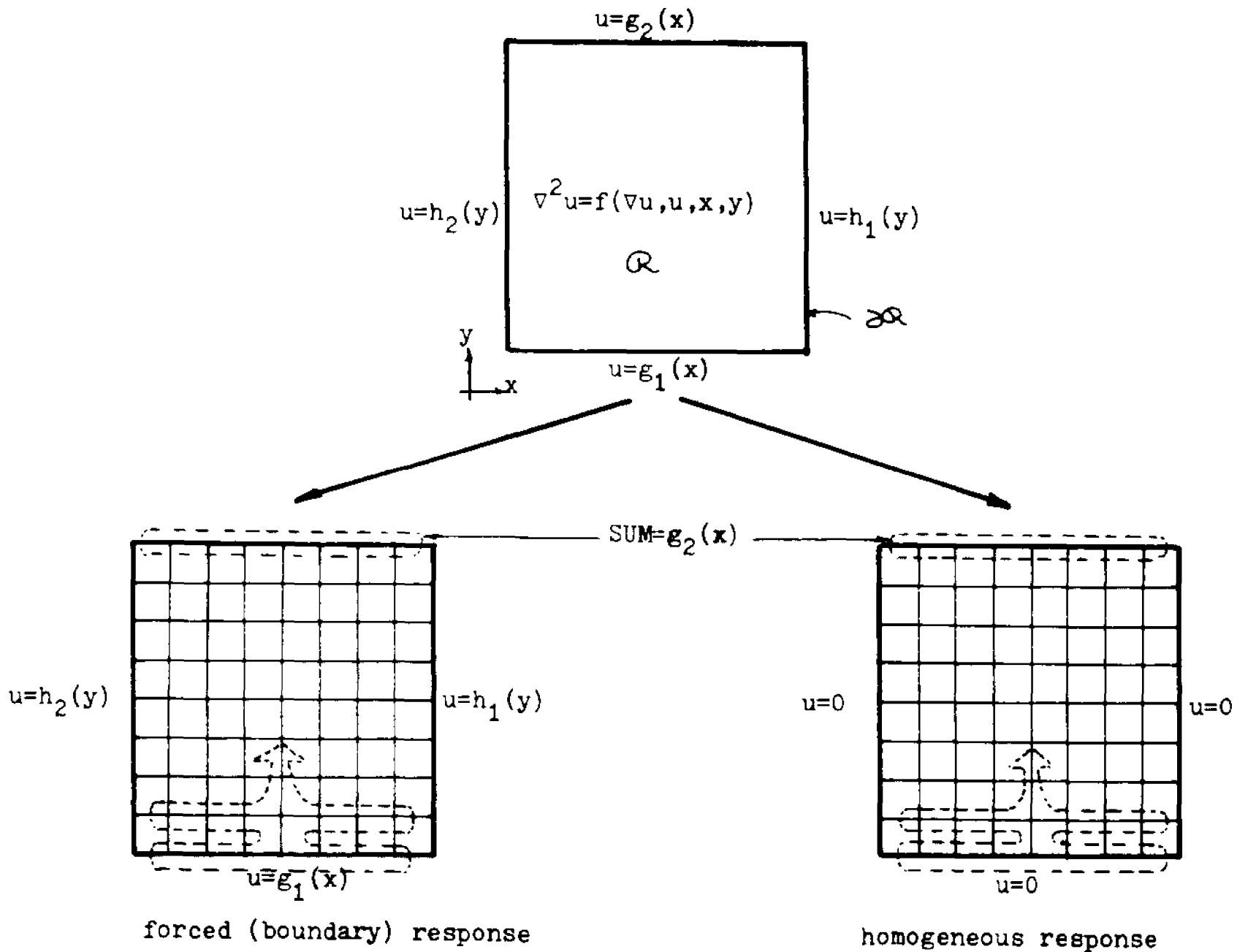


Figure 4.3. Scheme of computation using the shooting method.

Eq. 4.3.7. The zero or homoneneous boundary values are used on three sides up to the fourth boundary. This homogeneous solution makes use of the arbitrary starting vectors and is necessarily a matrix for row values. The forced response will be a single row solution vector which has the proper given boundary values on the boundaries, with the information used where appropriate. To start this computation the $\underline{u}^*(2)$ row is assumed to be zero. At the upper boundary, the homogeneous response must be combined with the weights to be found and added to the forced response to yield the given boundary values

$$\underline{U}(M)_{\text{homogeneous}} \cdot \underline{\beta} + \underline{u}^*(M)_{\text{forced}} = \underline{u}^*(M)_{\text{given}} \quad (4.3.8)$$

This equation may be solved for the weights $\underline{\beta}$. It is seen that in both cases (Eqs. 4.3.7 and 4.3.8) enough equations are provided for the number of unknowns in $\underline{\beta}$ (its length is $(N-2)$). The solution in the interior may be found from

$$\underline{u}^*(J) = \underline{U}(J)_{\text{homogeneous}} \cdot \underline{\beta} + \underline{u}^*(J)_{\text{forced}} \quad (4.3.9)$$

Again if the identity matrix is used as the arbitrary linearly independent vectors of the homogeneous response and since a zero vector is used for $\underline{u}^*(2)$ in the forced solution, the combining constants $\underline{\beta}$ are the missing row values for row $J=2$.

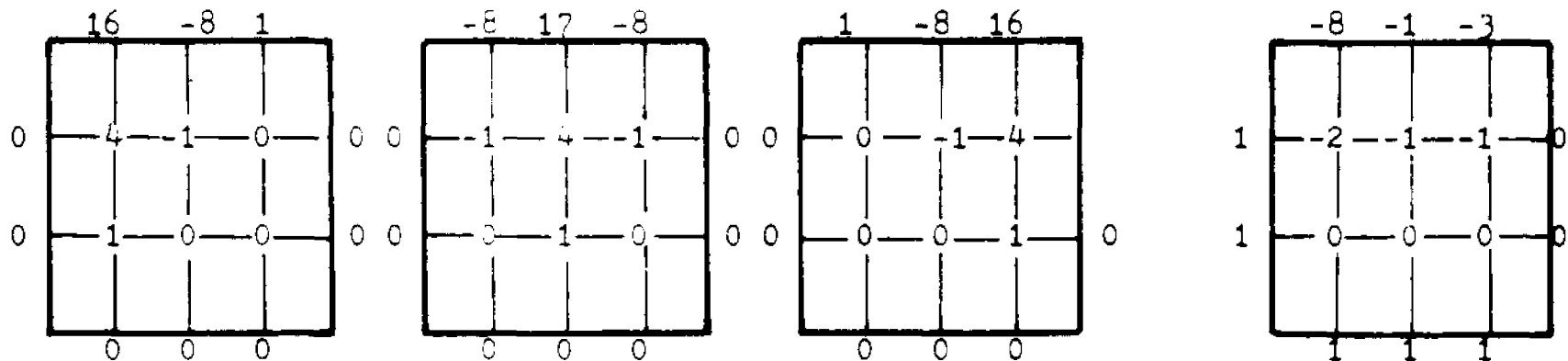
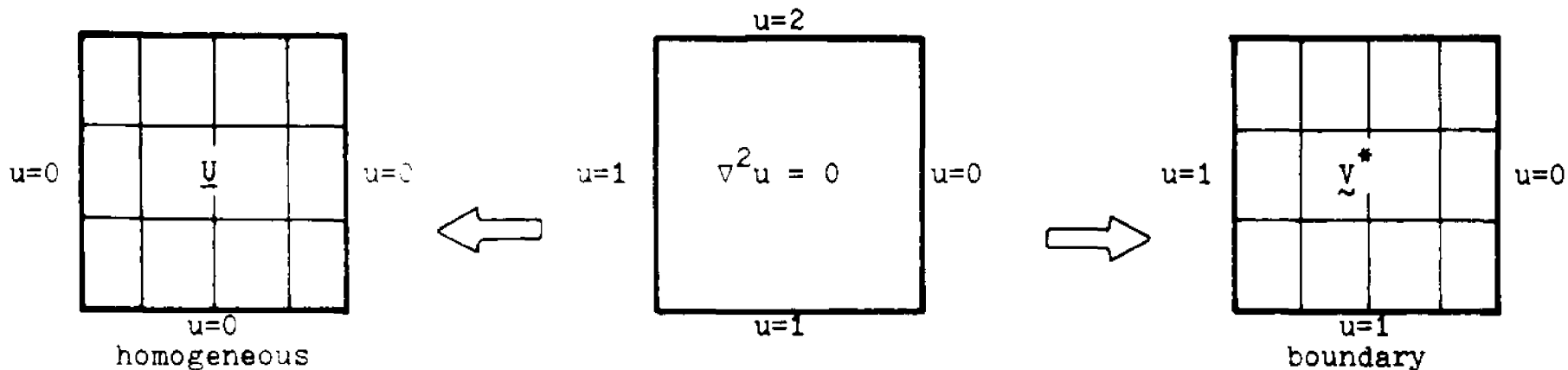
To illustrate this method of computation, Laplace's equation in a rectangle is solved. A five point formula

is employed for the discretization of the Laplacian. A simple example is shown in Fig. 4.4, demonstrating the main algorithmic steps.

The application of a five point formula for the discretization of the Laplacian is not suitable in this case since the resulting scheme is unstable. This is due to the excessive buildup of roundoff error incurred by computing this scheme with a finite arithmetic machine. It may be observed from this simple example presented that the matrix multiplying the $\underline{\beta}$ vector has main diagonal elements which are $\sim 4^2$ above the smallest element. This is a sign of ill-conditioning and will cause errors in the calculation of $\underline{\beta}$. In a problem which has $M \times N$ interior nodes, the resulting matrix multiplying the $\underline{\beta}$ vector will have elements which differ by $\sim 4^{M-N}$, increasing the difficulty in obtaining an accurate solution for $\underline{\beta}$. An analysis by the Fourier method⁽⁶¹⁾ may be made of this scheme to test its stability. Consider again Laplace's equation

$$\frac{\partial^2 u}{\partial x^2} + \frac{\partial^2 u}{\partial y^2} = 0 \quad (4.3.10)$$

A five point formula with h and k equal step sizes in the x and y direction is employed with the positive y axis as the shooting direction. The result is

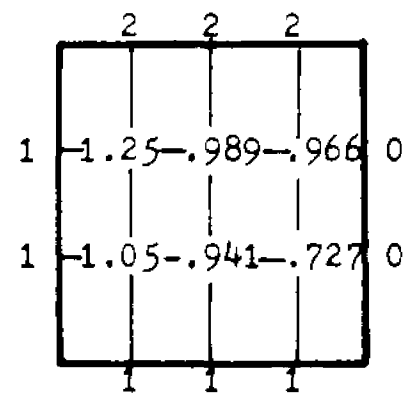


$$(16) \cdot \beta_1 + (-8) \cdot \beta_2 + (1) \cdot \beta_3 - 8 = 2$$

$$(-8) \cdot \beta_1 + (17) \cdot \beta_2 + (-8) \cdot \beta_3 - 1 = 2$$

$$(1) \cdot \beta_1 + (-8) \cdot \beta_2 + (16) \cdot \beta_3 - 3 = 2$$

$$\begin{bmatrix} \beta_1 \\ \beta_2 \\ \beta_3 \end{bmatrix} = \begin{bmatrix} 1.05 \\ .941 \\ .727 \end{bmatrix}$$



$$\text{Total Response} = \underline{u} \cdot \beta + \tilde{v}^*$$

Figure 4.4. Example of the application of the shooting method to Laplace's equation.

$$u^*(x, (n+1)k) = 2u^*(x, nk) - u^*(x, (n-1)k) - \lambda u^*(x+h, nk) - \lambda u^*((x-h), nk) + 2u^*(x, nk) \quad (4.3.11)$$

where $\lambda = k^2/h^2$ and the scheme has been expressed for the value of u^* at the $(n+1)^{\text{th}}$ row. A Fourier decomposition of $u^*(x, nk)$ may be expressed as

$$u^*(x, nk) = \sum_{\nu=-\infty}^{\infty} a_{\nu} b_{\nu}^n e^{j\nu x} \quad (4.3.12)$$

where ν is some discrete frequency, $j = \sqrt{-1}$, and a_{ν} is the appropriate Fourier coefficient. Applying it to Eq. 4.3.11 and equating terms of the same frequency, one obtains

$$a_{\nu} b_{\nu}^{n+1} e^{j\nu x} = 2(1+\lambda) a_{\nu} b_{\nu}^n e^{j\nu x} - a_{\nu} b_{\nu}^{n-1} e^{j\nu x} - \lambda a_{\nu} b_{\nu}^n e^{j\nu(x+h)} - \lambda a_{\nu} b_{\nu}^n e^{j\nu(x-h)} \quad (4.3.13)$$

Factoring $a_{\nu} b_{\nu}^{n-1} e^{j\nu x}$ and employing the appropriate trigonometric identity yields

$$b_{\nu}^2 - [2(1+\lambda) - 2\lambda \cos \nu h] b_{\nu} + 1 = 0 \quad (4.3.14)$$

Solving for b_{ν} using the quadratic formula and taking the largest value of b_{ν} one obtains

$$b_{\nu} = [1 + \lambda(1 - \cos \nu h)] + \sqrt{[1 + \lambda(1 - \cos \nu h)]^2 - 1} \quad (4.3.15)$$

For all values of $\lambda > 0, b_y \geq 1$, which means that the scheme is unstable.

A stable scheme, in which this roundoff error is bounded is a predictor-corrector method. This requires the formulation of the equations as a first order set. Thus an alternative formulation of the problem, still involving the same method, is to rewrite Eq. 4.3.1 as two first order p.d.e.'s in y . This may be done by defining the gradient of the variable in a direction normal to the starting boundary as well as the variable as the two dependent variables and introducing it into Eq. 4.3.1. This results in a coupled set of first order equations in y

$$\frac{\partial u}{\partial y} = v \quad (4.3.16)$$

$$\frac{\partial v}{\partial y} = f(\nabla u, u, x, y) - \frac{\partial^2 u}{\partial^2 x} \quad (4.3.17)$$

Now, given either u or v on the boundary, the other variable is unknown and becomes the arbitrary solution. Again, as many arbitrary linearly independent starting vectors are needed as there are grid points in a row. The solution method is exactly the same as that described earlier with one exception: Eqs. 4.3.16 and 4.3.17 need not be discretized along the lines of Eq. 4.3.2. This results in the introduction of more accurate and stable methods of integration, for example, a predictor-corrector method with arbitrary order of accuracy. This method

is employed in the actual solution of the small signal AC equations derived in Section 4.2 and is developed in Section 4.4.

Reconditioning Operations

This operation is entirely analogous to the method used in one dimension (see Section 3.3) and the reasons for performing reconditioning are similar. The Gram-Schmidt method is used to maintain linear independence of the solution vectors. A test for linear independence is done via the Gram-Schmidt by performing it on the required vectors and noting the angle between the unconditioned and conditioned vectors. (This is analogous to the method discussed in Section 3.3.) If this angle is close to 90° , then reconditioning is necessary; if it is equal to 90° , then it is too late to recondition since an orthogonal solution direction has been lost.

The Gram-Schmidt, as shown in Chapter 3, is essentially a matrix multiplication operation at some point

$J=L$

$$\underline{U}'(L) = \underline{U}(L) \cdot \underline{P}_i \quad (4.3.18)$$

The combining constants $\underline{\rho}$ found at the final boundary are not valid for the entire solution space; it is valid from that boundary to the last row before reconditioning was performed. An appropriate set of weights for the next region between reconditioning is found from the

\underline{P} matrix and the last \underline{g}

$$\underline{g}_i = \underline{P}_i \cdot \underline{g}_{i+1} \quad 1 \leq i \leq r \quad (4.3.19)$$

where r is the number of reconditioning operations performed.

As is seen, the mechanics of this method of reconditioning may be more complex to express in an algorithm but in principle are completely analogous to the derivation, for one spatial dimension, of Chapter 3. Again, other methods of reconditioning may be applicable (e.g. Edwards and Hansen⁽⁴⁷⁾) and may provide some improvements over the Gram-Schmidt orthonormalization. This has not been investigated.

4.4 The Small Signal AC Equations in Two Dimensions- Numerical Method of Solution and Implementation of the Algorithm

The method described here to solve the equations derived in Section 4.2 is modeled after the alternative derivation of the previous section (see Eqs. 4.3.16 and 4.3.17).

The region in which a solution is desired is rectangular and a rectangular grid shall be superimposed on it (see Fig. 4.5). For the present application, due to the nature of the geometry and materials, it is found convenient to shoot along the y direction as shown in Fig. 4.2. At each point in the grid, there are six variables which are the unknowns: the small signal carrier current densities and electric field in the y direction, \tilde{J}_{ny} , \tilde{J}_{py} , \tilde{E}_{1y} ; and the small signal carrier densities and potential, \tilde{n}_1 , \tilde{p}_1 and \tilde{V}_1 . (The x direction variables have been expressed in terms of these six and substituted into the six equations relating the above, and do not explicitly appear. This leads to the equations derived in Section 4.2: Eqs. 4.2.37, 4.2.38, 4.2.39, 4.2.41 and 4.2.42.)

Consider an interior row as shown in Fig. 4.5 and write the solution vector which satisfies the six p.d.e.'s (appropriately discretized) at these (N-2) points. This vector is 6x(N-2) long. Consider further that one is at such a point in the solution that a whole row is

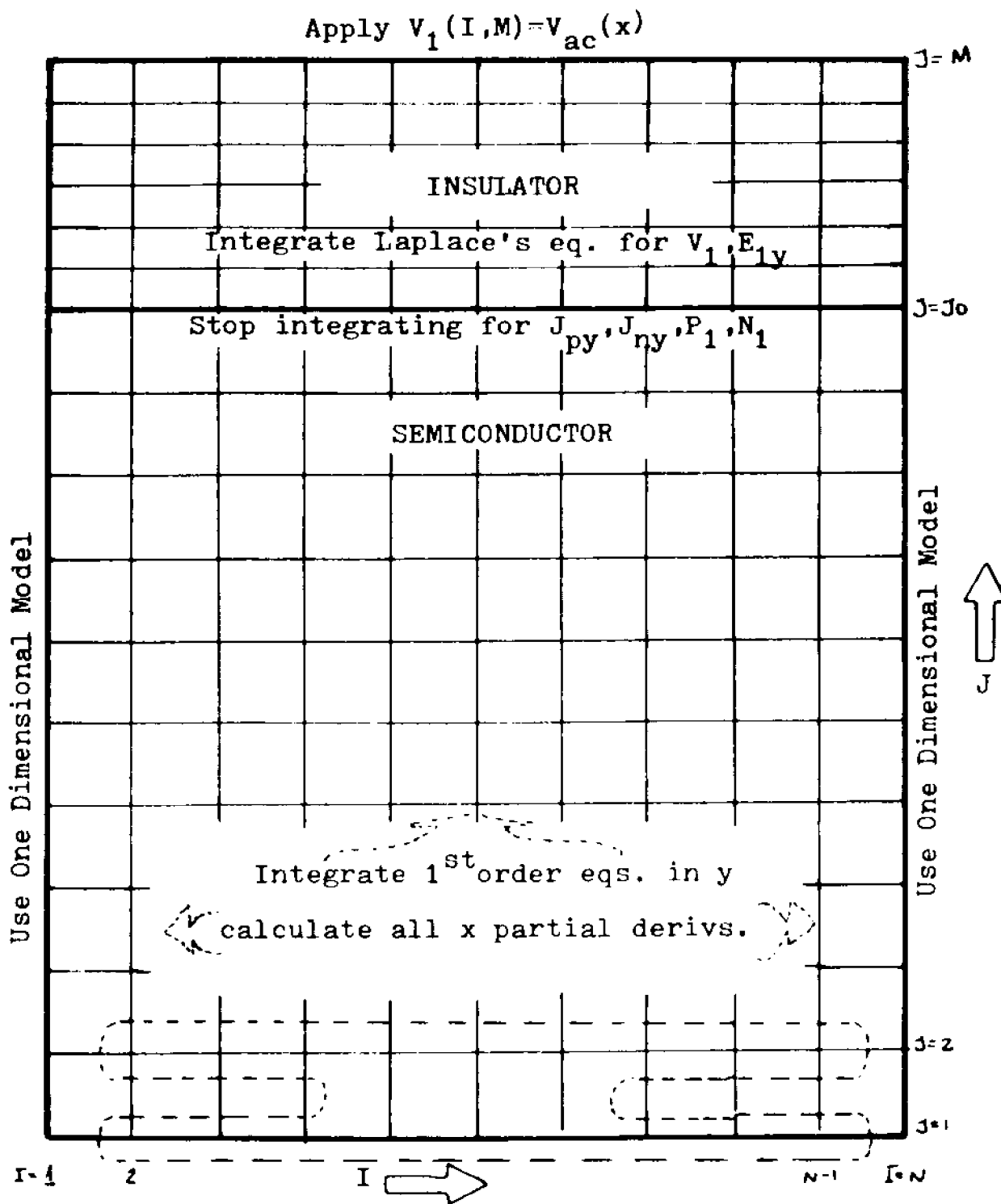


Figure 4.5. Scheme of computation for the two dimensional small signal AC problem by application of the shooting method.

known; the solution to the row above it may be found by integrating, through some stable integration routine, the above mentioned equations. Continuing with the solution just found, the solution to the next row above it may be found by the same method until the upper boundary is reached. This procedure could be used to span the whole solution space by beginning at one horizontal boundary and integrating one's way to the other horizontal boundary.

To visualize the application of a stable integration method, consider the pertinent equations rewritten in the following form

$$\frac{\partial \tilde{J}_{py}}{\partial y} = f_1(\tilde{P}_1, \tilde{N}_1, \tilde{V}_1, P_0, V_0, E_0) \quad (4.4.1)$$

$$\frac{\partial \tilde{J}_{ny}}{\partial y} = f_2(\tilde{P}_1, \tilde{N}_1, \tilde{V}_1, N_0, V_0, E_0) \quad (4.4.2)$$

$$\frac{\partial \tilde{P}_1}{\partial y} = f_3(\tilde{P}_1, \tilde{E}_{1y}, \tilde{J}_{py}, E_{0y}) \quad (4.4.3)$$

$$\frac{\partial \tilde{N}_1}{\partial y} = f_4(\tilde{N}_1, \tilde{E}_{1y}, \tilde{J}_{ny}, E_{0y}) \quad (4.4.4)$$

$$\frac{\partial \tilde{E}_{1y}}{\partial y} = f_5(\tilde{P}_1, \tilde{N}_1, \tilde{V}_1) \quad (4.4.5)$$

$$\frac{\partial \tilde{V}_1}{\partial y} = f_6(\tilde{E}_{1y}) \quad (4.4.6)$$

For the present application, use was made of a simple predictor-corrector method although greater

accuracy may be achieved with a higher order method.

This was used mainly for preliminary results and suffices for the purpose of this dissertation. If a whole solution row is known, then the x partial derivatives may be computed for that row, J, and the right hand side functions of Eqs. 4.3.1 through 4.3.7 are calculated. They are, in turn, used to predict the value of the variables at the next row

$$\tilde{J}_{py}^* = F_1[\tilde{P}_1(J), \tilde{N}_1(J), \tilde{V}_1(J), \tilde{P}_0(J), \tilde{V}_0(J), \tilde{E}_{ox}(J)] * HY(J) + \tilde{J}_{py}(J) \quad (4.4.7)$$

$$\tilde{J}_{ny}^* = F_2[\tilde{P}_1(J), \tilde{N}_1(J), \tilde{V}_1(J), \tilde{N}_0(J), \tilde{V}_0(J), \tilde{E}_{ox}(J)] * HY(J) + \tilde{J}_{ny}(J) \quad (4.4.8)$$

$$\tilde{P}_1^* = F_3[\tilde{P}_1(J), \tilde{E}_{1y}(J), \tilde{J}_{py}(J), \tilde{E}_{oy}(J)] * HY(J) + \tilde{P}_1(J) \quad (4.4.9)$$

$$\tilde{N}_1^* = F_4[\tilde{N}_1(J), \tilde{E}_{1y}(J), \tilde{J}_{ny}(J), \tilde{E}_{oy}(J)] * HY(J) + \tilde{N}_1(J) \quad (4.4.10)$$

$$\tilde{E}_{1y}^* = F_5[\tilde{P}_1(J), \tilde{N}_1(J)] * HY(J) + \tilde{E}_{1y}(J) \quad (4.4.11)$$

$$\tilde{V}_1^* = F_6[\tilde{E}_{1y}(J)] + \tilde{V}_1(J) \quad (4.4.12)$$

The discretization schemes for second and first order partial derivatives in the x direction are centered difference schemes. The capital 'F' replacing the lower case 'f' in the continuous p.d.e.'s of Eqs. 4.4.1 through 4.4.6 represent the change from continuous to discrete functions. Also, note must be taken that the functions

are now functions of solution vectors of the variables in the whole row. This stems from the discretization scheme of the derivatives in the x direction which necessitates the inclusion of variable values at the transverse grid points for the solution at any one grid point.

The corrector step may now be taken by using the predicted values (denoted by the star(*)) and averaging the functions over the two rows to generate a corrected solution at row (J+1)

$$\tilde{J}_{py}(J+1) = (\tilde{F}_1 + \tilde{F}_1^*) * \frac{HY(J)}{2} + \tilde{J}_{py}(J) \quad (4.4.13)$$

$$\tilde{J}_{ny}(J+1) = (\tilde{F}_2 + \tilde{F}_2^*) * \frac{HY(J)}{2} + \tilde{J}_{ny}(J) \quad (4.4.14)$$

$$\tilde{P}_1(J+1) = (\tilde{F}_3 + \tilde{F}_3^*) * \frac{HY(J)}{2} + \tilde{P}_1(J) \quad (4.4.15)$$

$$\tilde{N}_1(J+1) = (\tilde{F}_4 + \tilde{F}_4^*) * \frac{HY(J)}{2} + \tilde{N}_1(J) \quad (4.4.16)$$

$$\tilde{E}_1(J+1) = (\tilde{F}_5 + \tilde{F}_5^*) * \frac{HY(J)}{2} + \tilde{E}_1(J) \quad (4.4.17)$$

$$\tilde{V}_1(J+1) = (\tilde{F}_6 + \tilde{F}_6^*) * \frac{HY(J)}{2} + \tilde{V}_1(J) \quad (4.4.18)$$

where the $HY(J)$ is the J^{th} grid step.

To begin this method at one boundary, knowledge of all six variables at all grid points in the boundary row must be known. From the discussion of the boundary data available (see Section 4.2), only three (\tilde{n}_1, \tilde{p}_1 and \tilde{V}_1) are known at the lower boundary leaving three unknown ($\tilde{J}_{ny}, \tilde{J}_{py}, \tilde{E}_{1y}$). This is analogous to the one dimensional

situation and a similar treatment has been applied. Since there are three unknowns at each node and $(N-2)$ nodes in the boundary row, there are a total of $3x(N-2)=L$ unknowns in the row solution vector. Thus $3x(N-2)$ linearly independent solution vectors must be carried to obtain a complete solution. The starting vectors are given arbitrary values that satisfy the linear independence condition. The easiest form of generation of such vectors is to give the value of zero to all variables in a particular solution vector K and the value of $(1+j0)$ for the current densities and electric field. Such a starting matrix for $J=2$ is shown in Fig. 4.6, it includes only values for the interior points, the boundary points at $J=1$ and N are all set to zero for the homogeneous response. The matrix for row $J=1$ of the homogeneous response is the null matrix due to the zero boundary conditions on \tilde{V}_1 , \tilde{n}_1 and \tilde{p}_1 as derived in Section 4.2 and the fact that \tilde{E}_{1y} , \tilde{J}_{py} , and \tilde{J}_{ny} are set to zero here due to the nature of the solution.

Boundary value information is carried in an extra column of the solution matrix, $K=3x(N-2)+1$, and it starts out as zero for $(1 \leq J \leq N, \text{ and } I=1,2)$ but has the correct values at the transverse boundaries for both I levels. This transverse boundary value is found from the total solution given by the one dimensional AC simulation described in Section 3.5 and submitted to the program as data. This is in keeping with the treatment

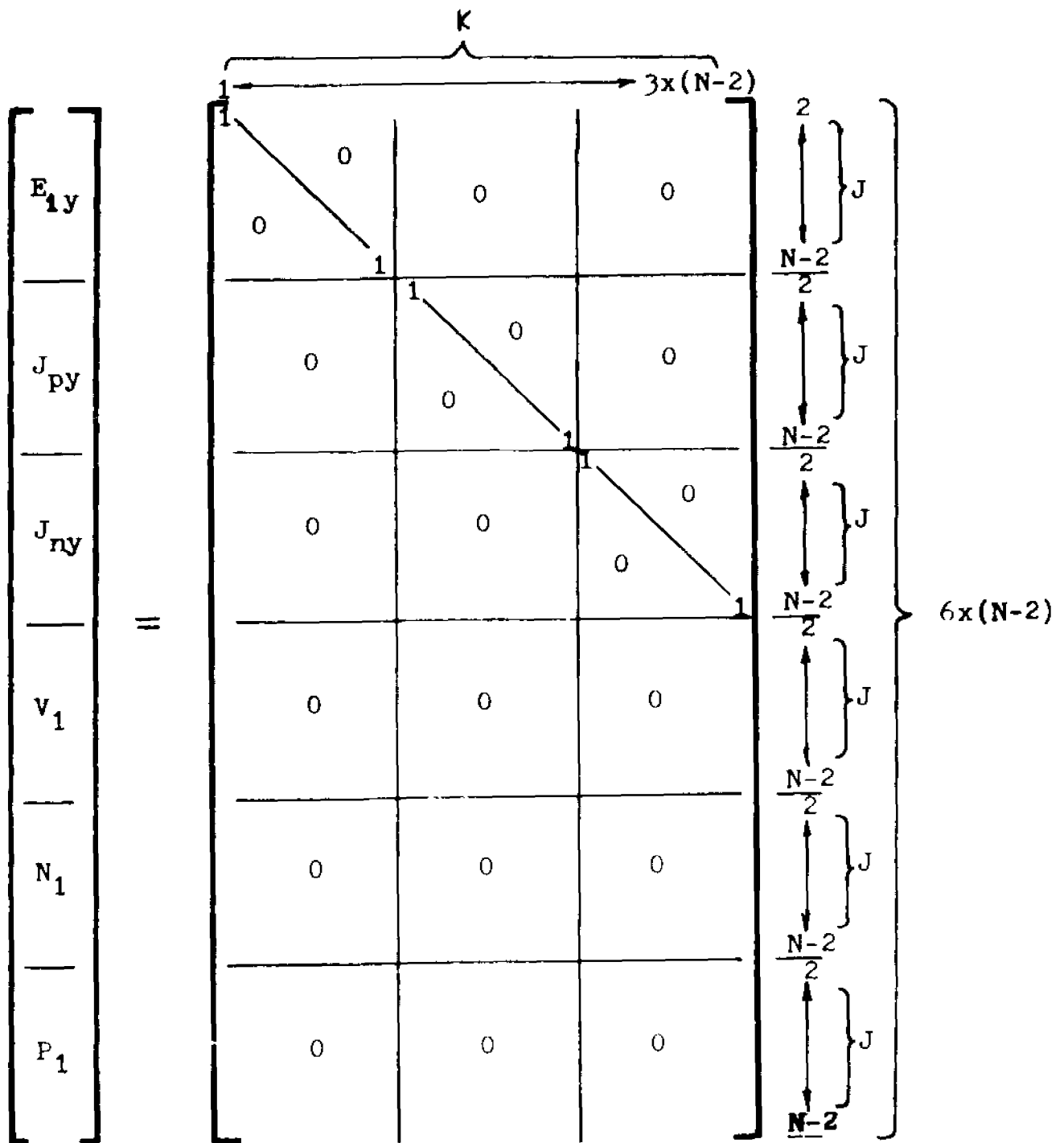


Figure 4.6. Arbitrary starting vectors as columns of $V(2)$, employed in the small signal AC simulation.

of the boundaries as described in Section 4.2.

Integration of the above vectors is performed from the substrate-metal boundary to the insulator-semiconductor boundary. Since the insulator is assumed ideal, no carrier or carrier current densities exist in this media, thus integration of the carrier current density equations and continuity equations stop at this interface. The potential, and associated electric field in the y direction, are carried across the interface by application of Gauss' Law. In the insulator the potential satisfies Laplace's equation; integration of the two first order equations (the alternative formulation, see Section 4.3) carries the solution to the top boundary. The predictor-corrector integration applied to Eqs. 4.2.43 and 4.2.44 is:

predictor

$$\tilde{\mathbf{E}}_{1y}^* = D_x^2 \tilde{\mathbf{V}}_1(J) * HY(J) + \tilde{\mathbf{E}}_{1y}(J) \quad (4.4.19)$$

$$\tilde{\mathbf{V}}_1^* = -\tilde{\mathbf{E}}_{1y}(J) * HY(J) + \tilde{\mathbf{V}}_1(J) \quad (4.4.20)$$

corrector

$$\tilde{\mathbf{E}}_{1y}(J+1) = D_x^2 (\tilde{\mathbf{V}}_1^* + \tilde{\mathbf{V}}_1(J)) * \frac{HY(J)}{2} + \tilde{\mathbf{E}}_{1y}(J) \quad (4.4.21)$$

$$\tilde{\mathbf{V}}_1(J+1) = -(\tilde{\mathbf{E}}_{1y}^* + \tilde{\mathbf{E}}_{1y}(J)) * \frac{HY(J)}{2} + \tilde{\mathbf{V}}_1(J) \quad (4.4.22)$$

where D_x^2 represents the discrete analogue of the second derivative with respect to x.

The boundary conditions are applied at the top to find the weights, $\underline{\beta}$, using the matrix equation shown in Fig. 4.7. This yields as many combining constants, $\underline{\beta}$, as there are unknowns, L. The resulting matrix which multiplies the $\underline{\beta}$ vector must be inverted with as much precision as possible. It is a full matrix and has complex coefficients. A Gaussian elimination routine is implemented in complex space to invert this matrix. A flow chart of the algorithm is shown in Fig. 4.8.

Performing a reconditioning operation and testing for its need at any one row is done as described in the previous section. Only one pass is necessary in the calculation of admittance, as is described in Section 4.5. To obtain the total solution, two passes with accompanying computation of the $\underline{\beta}$'s for each reconditioning region must be performed. Since only the admittance was the parameter of interest in this work, the total solution algorithm was not implemented.

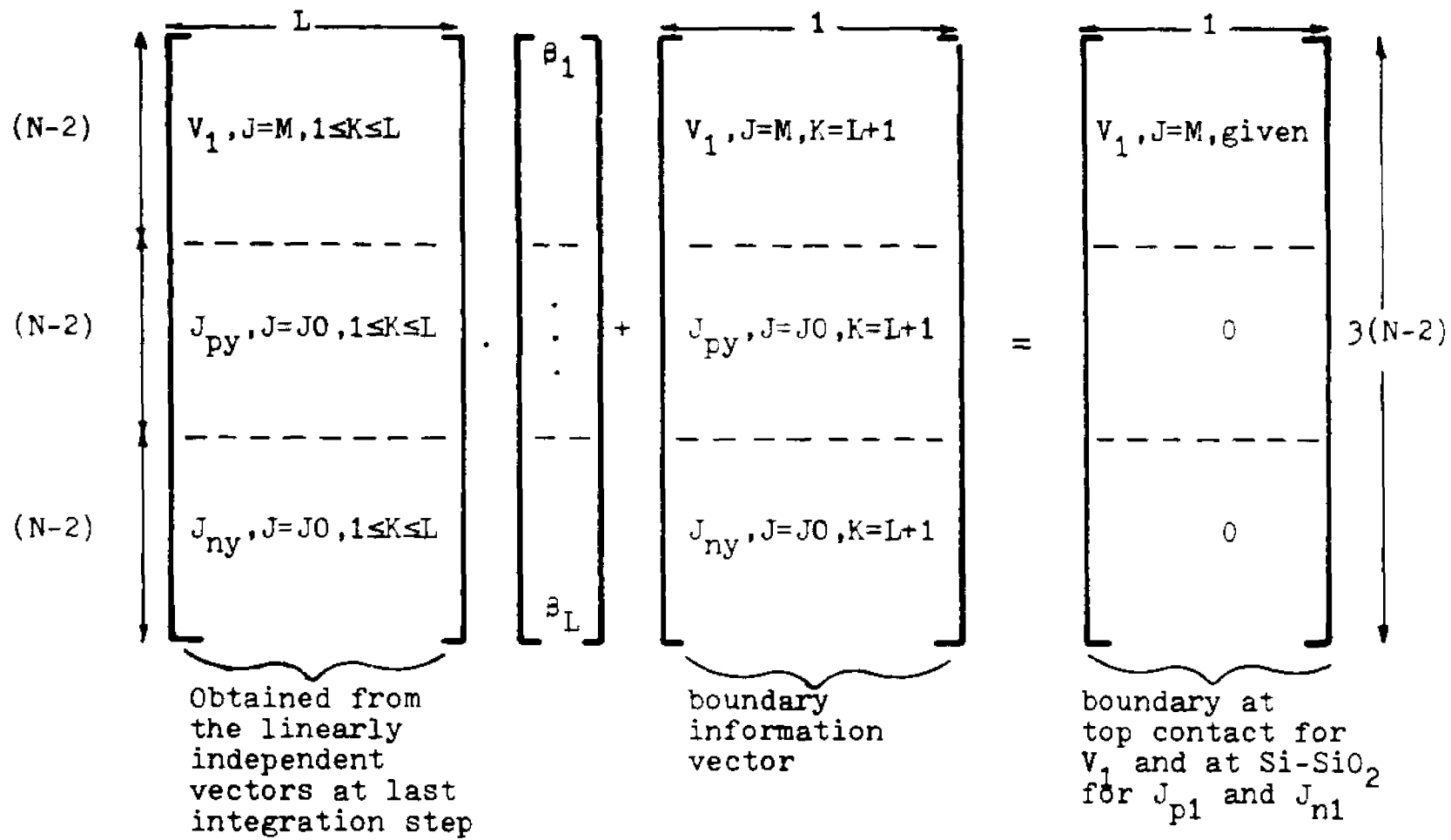


Figure 4.7. Application of boundary conditions (at $J=M$ for V_1 and at $J=J_0$ for J_{py} and J_{ny}) in the small signal AC problem.

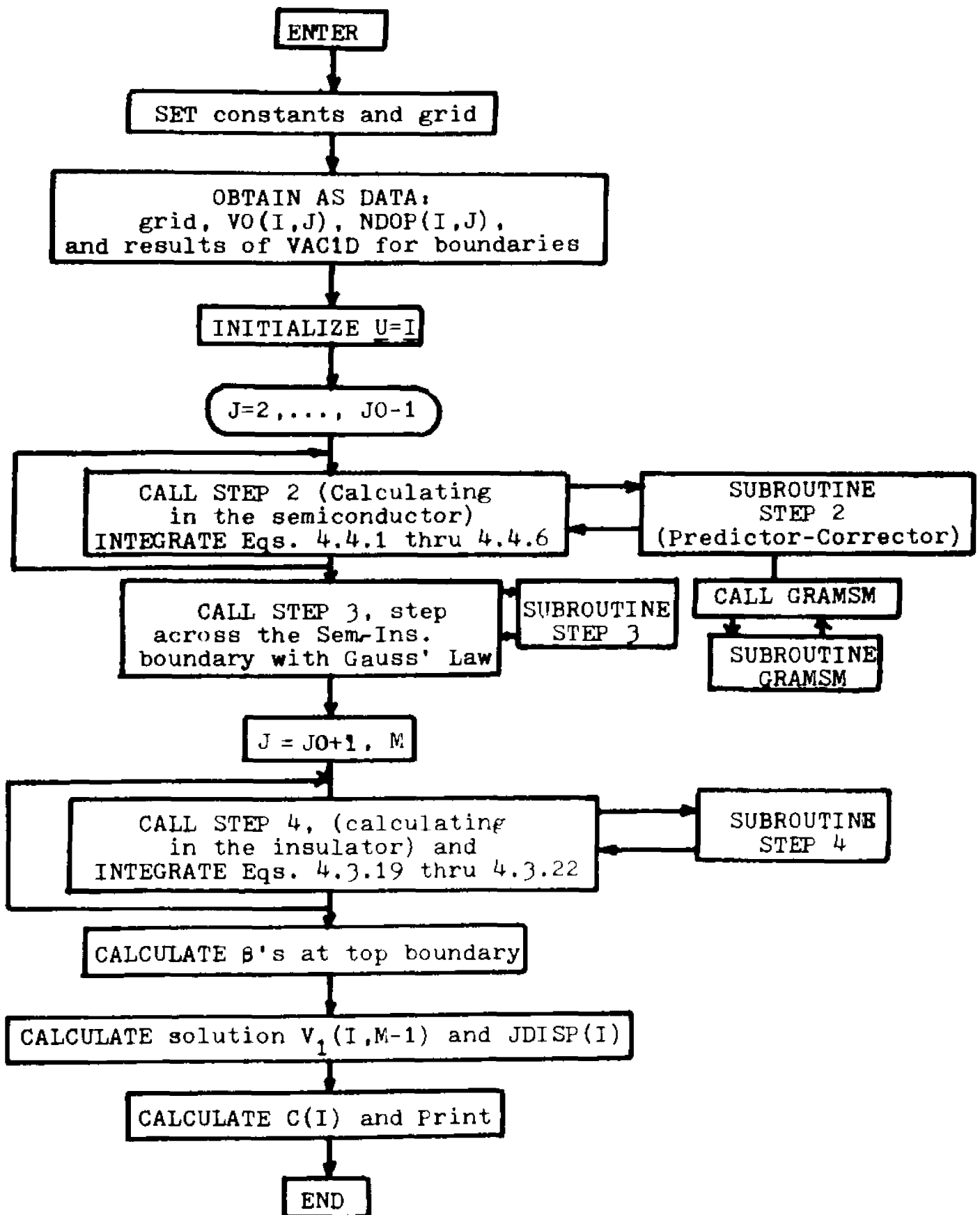


Figure 4.8. Computational flowchart of VAC2D.

4.5 The Three Terminal Varactor-Small Signal Analysis in Two Dimensions

The device used to test the algorithm of Section 4.3 is the "Three Terminal Varactor"⁽²⁾. The structure and grid employed is shown in Fig. 2.30 where the necessary DC parameters were obtained. In this section the small signal admittance shall be calculated and studied as a function of DC bias. The small signal AC potential is superimposed on the DC biases as shown in Fig. 4.9. The device modeled consists of a uniformly doped ($N_A = 1.10^{15}$ ions/cm³) silicon substrate with a 1000Å oxide (SiO₂), a substrate contact and two top plates separated by a distance x_d . The grid used in the analysis is uniform with 25x60 grid points in the x and y directions respectively ($H_x = .1\mu\text{m}$ and $H_y = .025\mu\text{m}$). There are 25x10 grid points in the insulator with uniform .01μm steps in the y direction and .1μm steps in the x direction. The AC solution is not sought outside this region (as is in the DC model) since the AC bias is assumed small and the gap region is assumed to be at AC ground. This assumption is reasonable since it is anticipated that the AC potential drops quite rapidly along the air-insulator surface, as experienced for the DC case (see Fig. 2.39). The main interest here is the calculation of the small signal capacitance of one of the top leads as a function of bias voltages. For this purpose a small signal capacitance, $C(I)$, is defined at each of the grid nodes

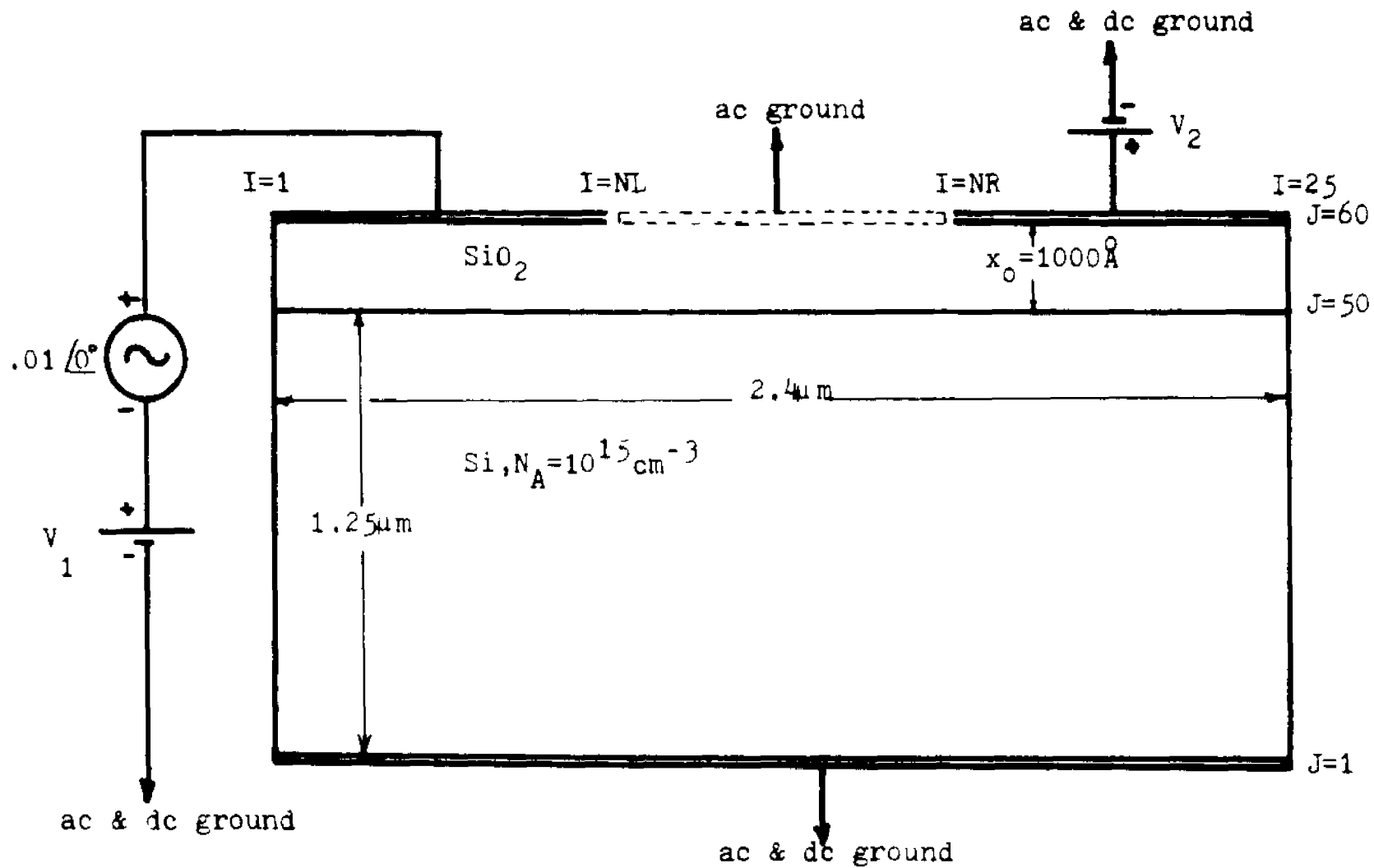


Figure 4.9. Structure and biasing of the three terminal varactor.

of the plate in question as shown in Fig. 4.10a. This lumped value capacitance is calculated from the normal displacement current density at each plate node as shown in Fig. 4.10b, (\hat{a}_y is the normal direction to the plate). Calculation of the displacement current yields

$$\tilde{J}_{\text{disp}} \cdot \hat{a}_y = -j\omega \kappa_I \epsilon_o \tilde{E}_1 \cdot \hat{a}_y \quad (4.5.1)$$

The electric field at the plate ($J=60$) may be expressed in terms of the AC potential as

$$\tilde{E}_1 Y(I,60) = -(\tilde{V}_1(I,60) - \tilde{V}_1(I,59)) / HY(59) \quad (1 \leq I \leq NL) \quad (4.5.2)$$

Since $V_1(I,60) = V_{ac}$, the applied small signal AC bias, the definition of capacitance as discussed in Chapter 3 may be re-expressed as

$$C_{ac}(I) = \frac{\kappa_I \epsilon_o}{HY(59)} \cdot \text{IM} \left\{ \frac{\tilde{V}_{ac} - \tilde{V}_1(I,59)}{\tilde{V}_{ac}} \right\} \frac{f}{\text{cm}^2} \quad (1 \leq I \leq NL) \quad (4.5.3)$$

The capacitance is normalized with respect to the oxide capacitance. By this it is meant that an oxide capacitance

$$C_o(I) = \frac{\kappa_I \epsilon_o}{x_o(I)} \frac{f}{\text{cm}^2} \quad (4.5.4)$$

may be defined for each node point and used as a normalizing constant. This is useful since the capacitance

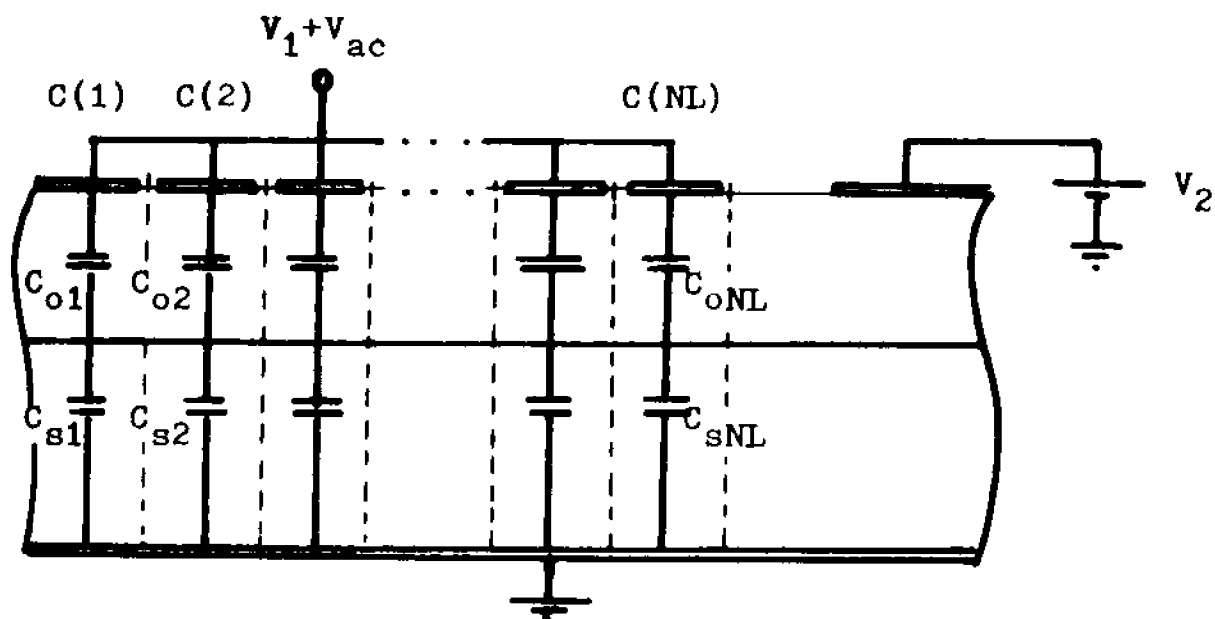


Figure 4.10a. Distributed capacitance circuit showing definitions of pertinent capacitances in the three terminal varactor studied.

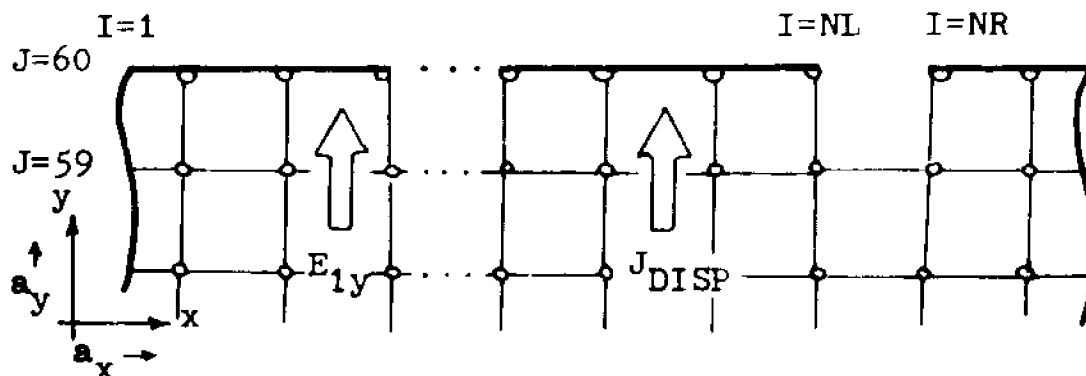


Figure 4.10b. Grid and variables employed in the small signal AC capacitance calculation.

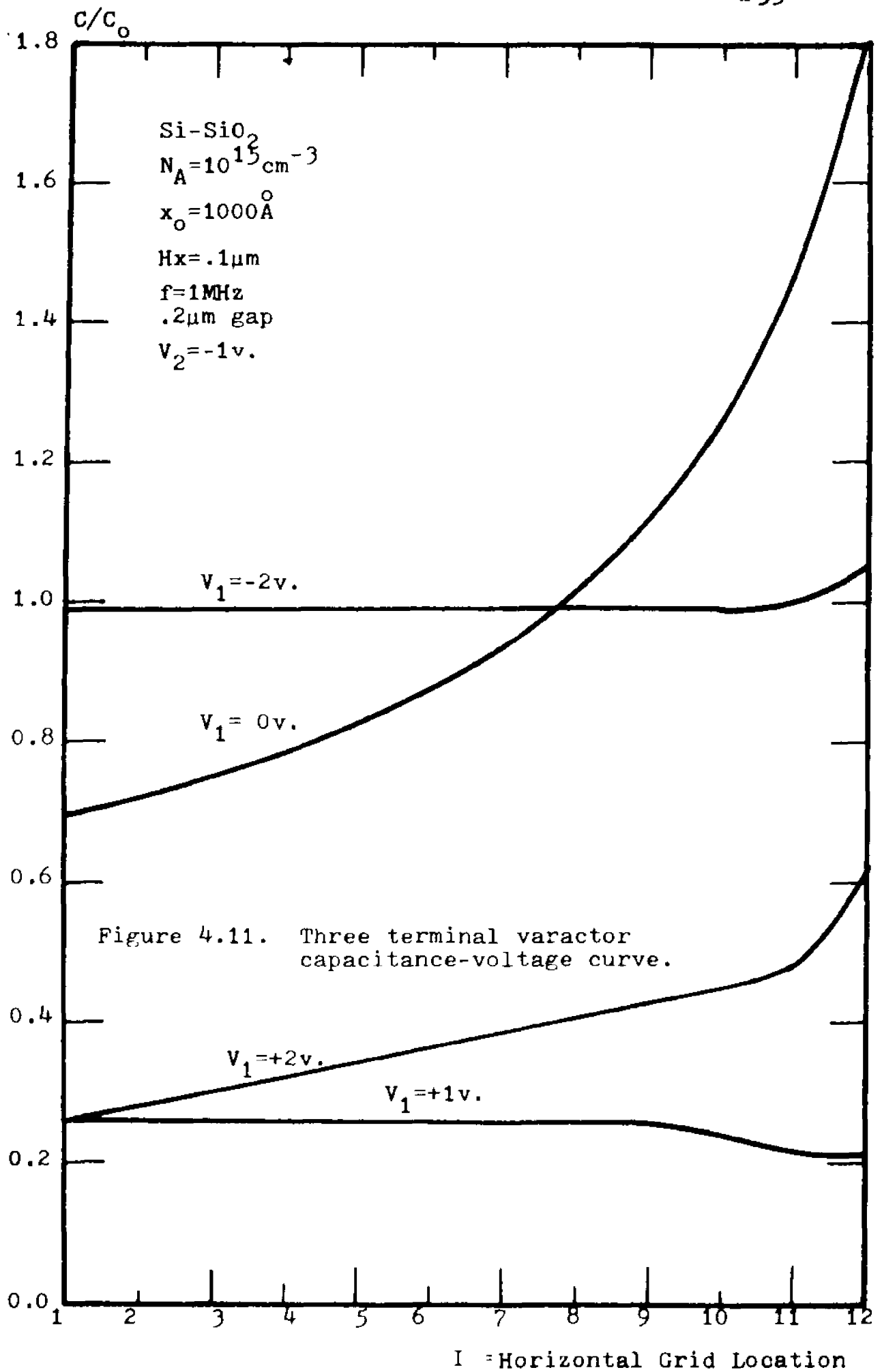
level for a strip, being considered a one dimensional device, is easily found from a plot of $C(I)$ versus I . Furthermore, the effect of capacitance change due to the DC bias conditions is easily noticed and related to its cause. Lastly, any fringing effect due to finite plate dimension is easily observable. All these points are discussed in greater detail when particular examples are considered. The capacitance calculated is that of Eq. 4.5.3 normalized by Eq. 4.5.4 to yield

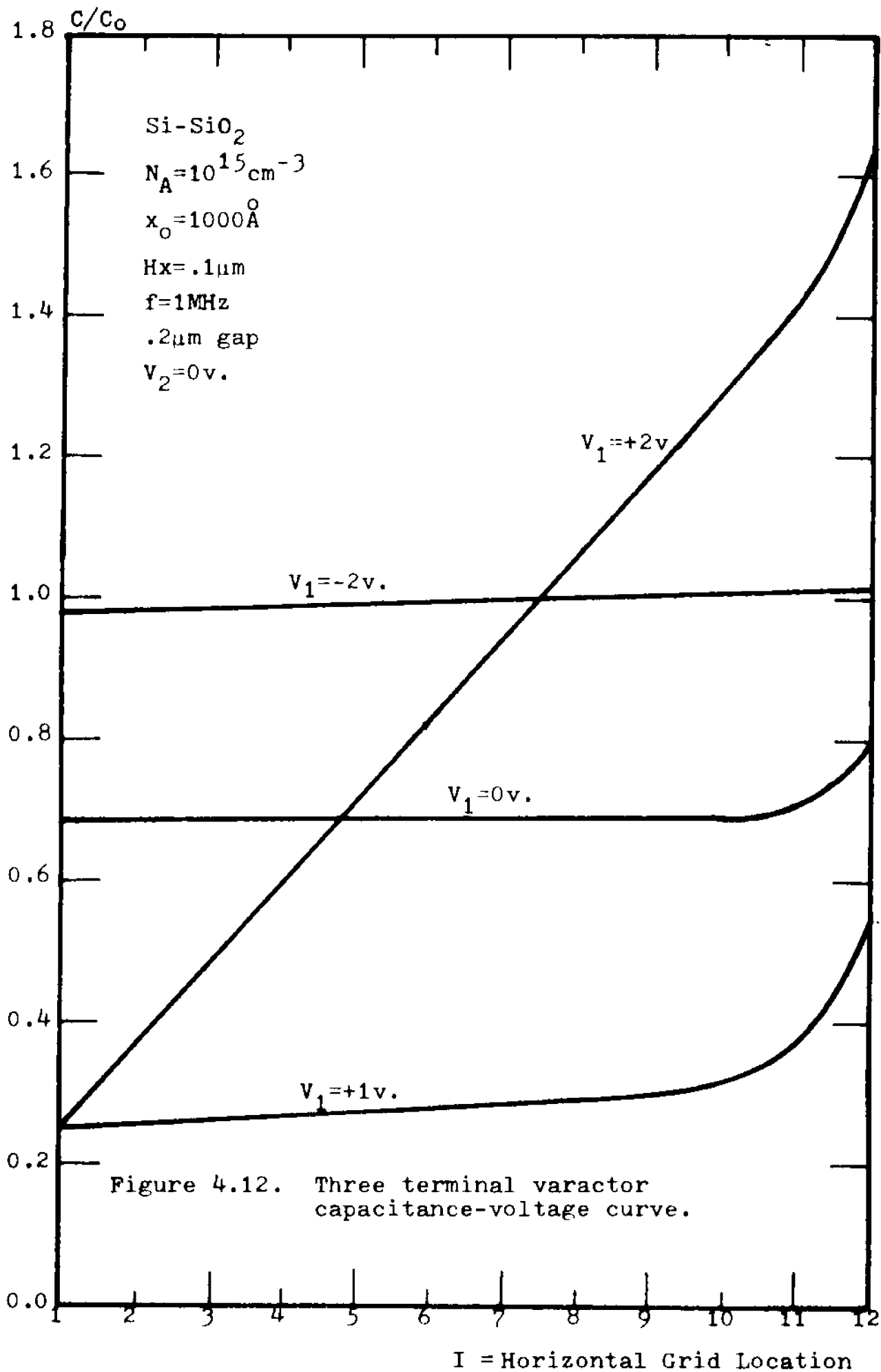
$$C(I) = \frac{C_{ac}(I)}{C_o(I)} = \frac{1}{10} \cdot IM \left\{ \frac{(\tilde{V}_{ac} - \tilde{V}_1(I, 59))}{V_{ac}} \right\} \quad (4.5.5)$$

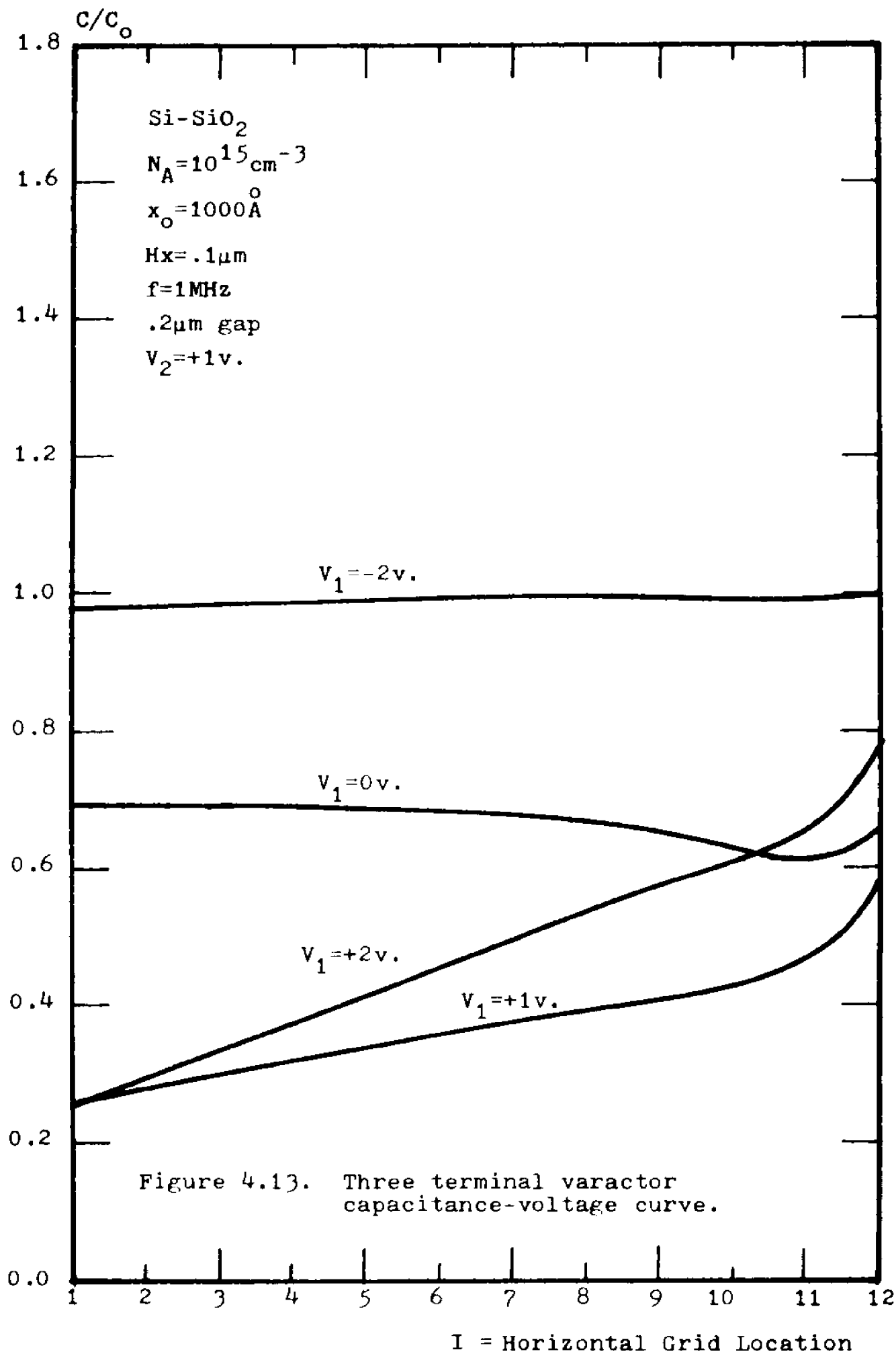
Use has been made of the fact that the oxide thickness is constant in the example being considered and divided into ten grid steps in the \hat{a}_y direction. The underlying assumption is that one may view $C(I)$ as a collection of individual MOS capacitors in parallel as is shown in Fig. 4.10a.

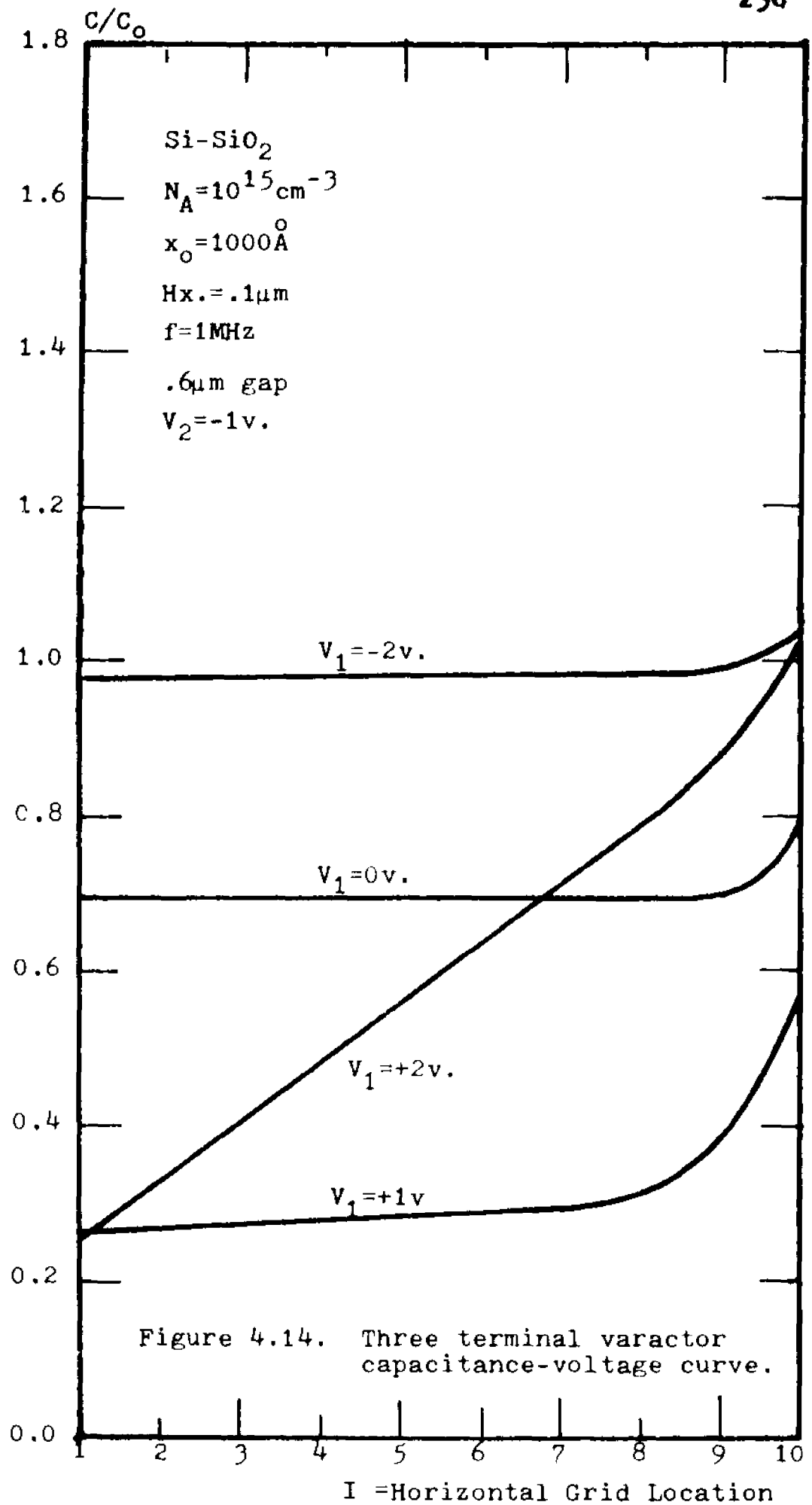
The capacitance function is calculated for two different lead separations, $0.2\mu\text{m}$ and $0.6\mu\text{m}$, in an effort to demonstrate the effect of lead separation on plate to plate coupling. The resulting functions are plotted in Figs. 4.11, 12, and 13 for the narrow gap case and Figs. 4.14, 15 and 16 for the wide gap case as bias voltage 2 is varied as -1, 0, and +1 volt respectively.

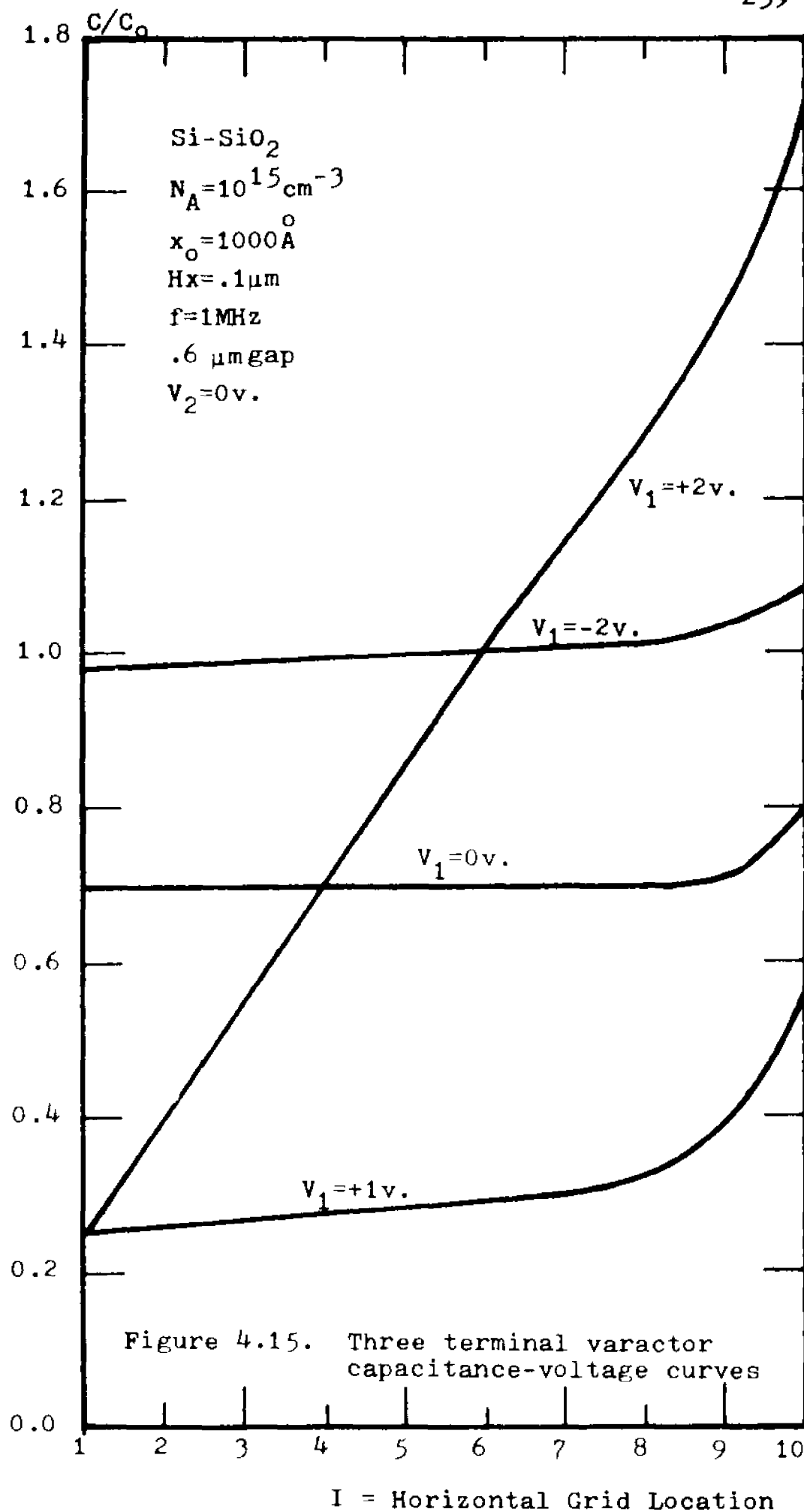
For both devices, the capacitance at accumulation ($V_1 = -2\text{v}$) is little affected by the varying bias on V_2 .

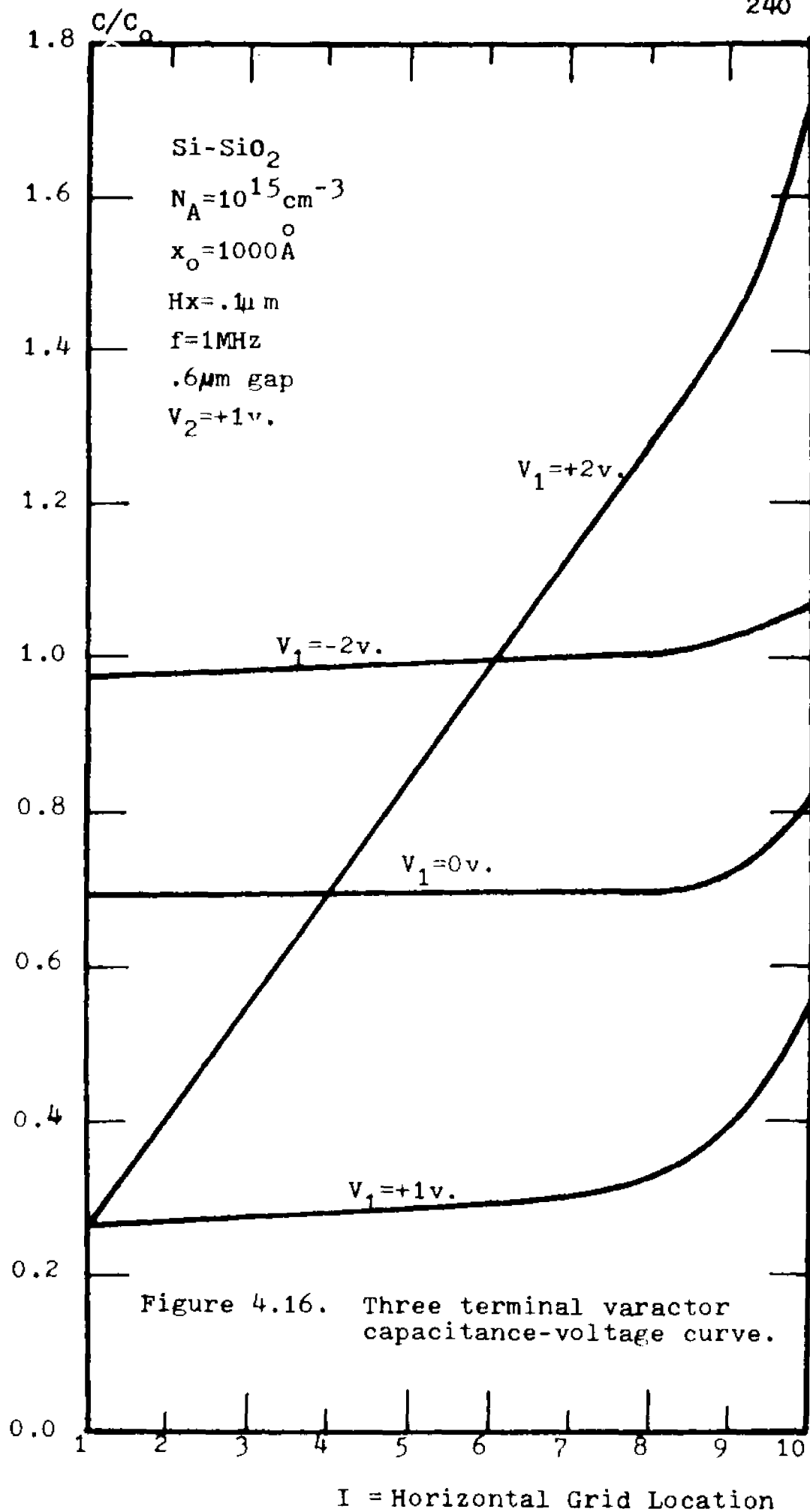












There is an exception, the capacitance value of the right edge of the plate, $I=12$, is slightly higher in all but one case ($V_1=-2$, $V_2=+1$) for the short gap device. The reason for this higher value is fringing. This rightmost region is not terminated by an accumulated charge sheet of the same length as the plate, but one that, due to the large bias on V_1 , extends past the region below the plate. This increases the equivalent C_0 for the rightmost capacitor and increases the overall capacitance at this point. The bias $V_1=-2$ is a very strong one in that it holds the semiconductor deep in accumulation, the surface condition under the lead is relatively unaffected by the nearby lead bias. (See Chapter 2 where the DC conditions are described.) Only when the two leads are sufficiently together, e.g. the $.2\mu\text{m}$ gap device, and the bias on the other lead sufficiently strong, $V_2=+1\text{v.}$, is a change noticeable. In this case, a decrease in the accumulation region fringing brings with it a decrease in capacitance.

For $V_2=0\text{v.}$ the results for both type gaps are nearly identical if superimposed (Figs. 4.12 and 4.15). This points to the fact that operation for this bias condition is totally dependent on fringing. This V_2 bias condition allows the introduction of the idea of a sidewall depletion capacitance due to field effect, which increases the overall capacitance, as shown in Fig. 4.17a. This condition may easily be disturbed by applying a negative or a positive bias, to V_2 , both reducing the overall capacitance.

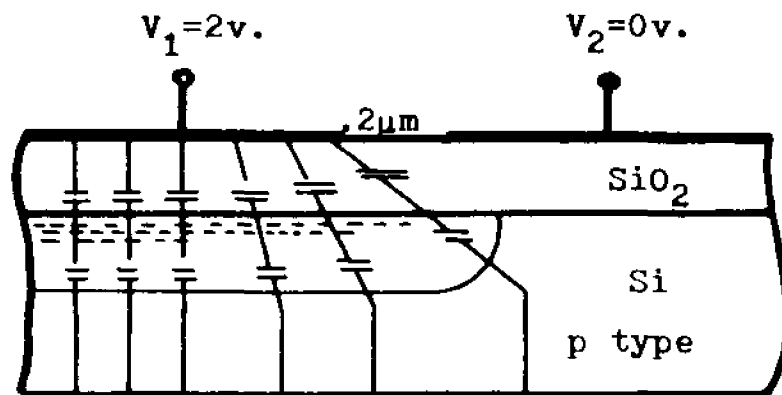


Figure 4.17a. Inversion under lead 1, showing lateral spread of inversion region.

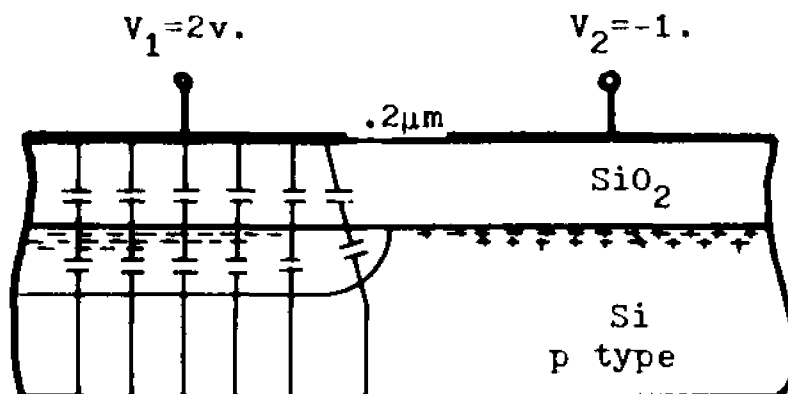


Figure 4.17b. Reduction of lateral inversion region under lead 1 by accumulation under lead 2.

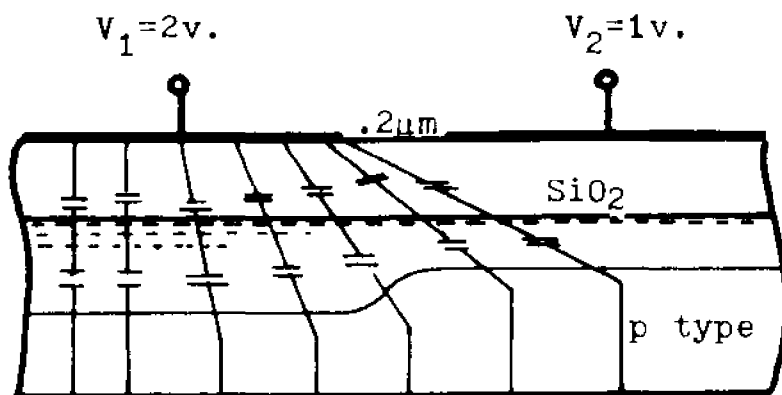


Figure 4.17c. Increase in lateral inversion by the inversion lead 2.

In the second case, depletion under lead 2 destroys the sidewall depletion and removes that capacitance, reducing the overall capacitance. This is further documented by the wide gap device for $V_1=+2v$, $V_2=+1v$. In that case the depletion regions do not meet and the sidewall capacitance is still present.

From the three V_2 bias conditions on the wide gap devices, shown in Figs. 4.14 through 4.16, it is clear that at this distance ($.6\mu m$) the effect of V_2 on C_1 is minimal. For $V_2=0v$ and $V_2=+1v$ and most of $V_2=-1v$, the curves are exactly the same as a function of V_1 . Only when $V_2=-1v$ and $V_1=+2v$ is the capacitance different. This is again due to the decrease in the depletion under lead 1 due to the accumulation under lead 2. Even at this distance ($.6\mu m$) the effect of V_2 is noticeable. This is because for 1×10^{15} ions/cm³ doped material, $x_{DMAX} \cong .85\mu m$, thus the depletion region extends widely.

An interesting effect is observed for bias conditions $V_1=0v$ and $V_2=-1v$, shown in Fig. 4.18a. Here, as in no other case shown, the capacitance of lead 1 became very large. This is peculiar to a narrow gap device and is due to the accumulation region under lead 2 extending to under lead 1. Since most of the semiconductor under lead 1 is not at flat-band, but partly accumulated, its capacitance is higher ($C_{accum} > C_{FB}$). Also, the fringing capacitance increases the edge capacitances, as shown in Fig. 4.18a.

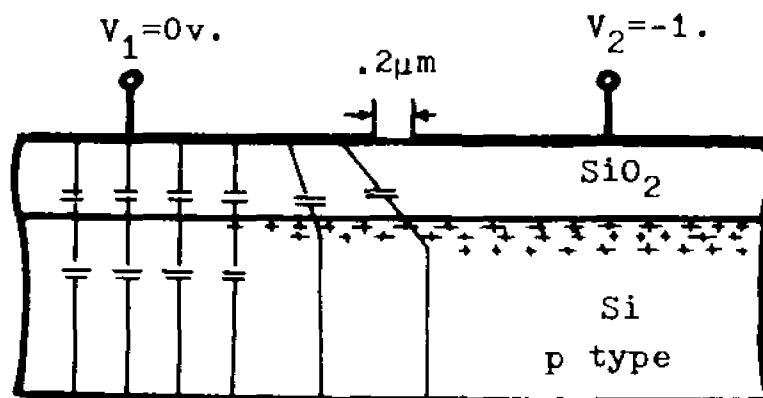


Figure 4.18a. The influence of a nearby accumulation region on the capacitance of a short gap device.

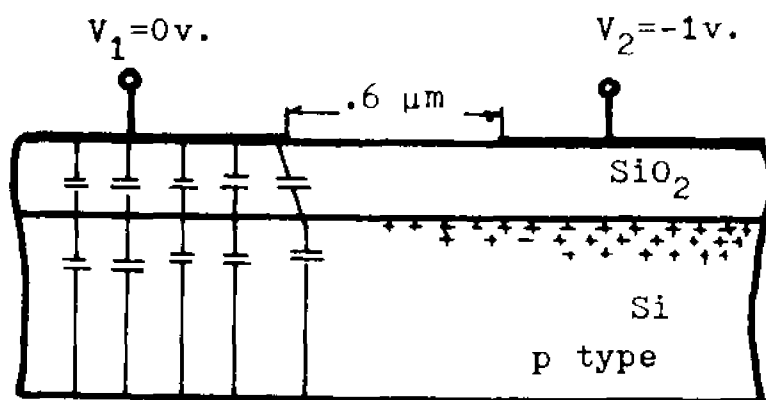


Figure 4.18b. Reduction of the influence of the accumulation region by the increase in gap width.

The question of direct coupling between the leads may be explored by observing the zero bias conditions in both devices. Under this condition, the energy bands are flat over the whole device. The capacitance values as a function of distance, if superimposed with the rightmost edges matching, are identical. This points to the fact that direct coupling is minimal since separating the leads has no noticeable effect on the capacitance. The slight increase in capacitance at the gap edge in both cases is due, not to lead-to-lead fringing, but to the slightly larger C_0 at that edge. This increase is due to lead edge to semiconductor surface fringing for lead 1. Furthermore, since lead 2 is AC grounded, a calculation of the AC current density at lead 2 metal-insulator boundary shows it to be several orders of magnitude below that in lead 1.

This may be confirmed by observing that for a wider gap device, this extension of the accumulation region does not occur as seen in Fig. 4.18b and no corresponding large capacitance increase occurs.

The conclusions which may be drawn from this study are the following:

1. Variation of the admittance of one lead by varying biases on a nearby lead is a short range phenomena.
2. For gaps $>.6\mu\text{m}$, the effect is minimal for the structure studied.

3. For gaps $< .2\mu\text{m}$, or even overlapping electrodes, some control of the fringing capacitance is possible.

CHAPTER 5

SUMMARY

In the course of the present work several things are accomplished:

1. Development of the differential equations describing MIS device operation into the proper set for DC and small signal AC analysis in one and two spatial dimensions.

2. Investigation of various methods used to solve the above equations numerically. Several of these methods are novel in application to semiconductor device modeling.

3. The study of several MIS devices with one and two dimensional character. The admittance of inhomogeneously doped MOS capacitors, the three level capacitor and the three terminal varactor are investigated.

The algorithms developed are described below:

1. One dimensional DC operation of an MOS capacitor (subroutine VDC1D). Solves the semiconductor nonlinear Poisson equation with a method similar to Gummel's algorithm.

2. Two dimensional DC operation of an MOS device (program VDC2D). It obtains the potential in an MOS device equilibrium by solving the semiconductor nonlinear

Poisson equation. This is performed with a one step SOR-Newton iterative scheme.

3. One dimensional small signal AC operation of an MOS capacitor (program VAC1D). Solves the small signal AC differential equations with a shooting method. Employs reconditioning to damp instability of the solution arising from the recognized ill-conditioning of the problem. It is employed to calculate the admittance with a minimum amount of memory compared to classical methods. The complete solution in the interior of the device is also available for slightly more memory and computation time.

4. Two dimensional small signal AC operation of an MOS device (program VAC2D). This program employs the method of complimentary functions extended to two spatial dimensions. It is employed to study the three terminal varactor.

These models were derived as free from limiting assumptions as possible. The only fundamental assumptions made were:

1. Use of Boltzman statistics in place of full Fermi Dirac ones, limiting the range of applied DC bias to the devices.

2. Employment of Dirichlet boundary conditions in certain cases as an approximation to the proper type of boundary condition.

3. Termination of moment taking of the Boltzman

equation at the first moment by assuming no temperature gradients. This allows the generation of six describing equations for a two carrier model.

Recommended Further Work

The application of the algorithms developed to devices other than the ones studied is envisioned as an immediate continuation of this work. The use of the two dimensional small signal AC algorithm in the analysis of devices in nonequilibrium situations is proposed, such as the calculation of the admittance of MOSFET's under varying bias conditions.

The closer investigation of the frequency dependence of the MIS admittance and the employment of full Fermi statistics is desirable.

The automation of the algorithms for a wide range of device parameters to alleviate the need for operator intervention. Coding of the step-by-step optimized relaxation parameter for the DC problem, as discussed in Appendix B, is also projected.

Lastly, the study of the large signal AC and transient response of devices in more than one spatial dimension is a problem to be addressed in the future.

Appendix A

Model of The

Generation-Recombination Mechanism

This appendix is concerned with the derivation of a linearized small signal generation-recombination mechanism to be included in the equations of Chapters 3 and 4.

The generation-recombination (G-R) model given by Shockley and Read ⁽⁶²⁾ and Hall ⁽⁶³⁾ shall be the starting point of analysis with

$$R = \frac{\sigma_p \sigma_n v_{th} N_T (p n - n_i^2)}{\sigma_n n + N_c \exp\left(\frac{E_c - E_T}{kT}\right) + \sigma_p p + N_v \exp\left(\frac{E_T - E_v}{kT}\right)} \quad (\text{A.1})$$

where

R = Thermal generation-recombination rate for both electrons and holes.

σ_p, σ_n = Capture cross sections of traps for both holes and electrons respectively.

N_v, N_c = Effective density of states at the valance and conduction band edges respectively.

N_T = Effective density of the trap states.

By defining the intrinsic carrier concentration, n_i , one may factor out of the denominator the terms $N_c \exp\left(\frac{E_c - E_i}{kT}\right)$ and $N_v \exp\left(\frac{E_v - E_i}{kT}\right)$ and replace them by n_i^2 ⁽⁵⁹⁾. One also may define two terms which simplify

Eq. A.1 and have physical significance

$$\tau_p = \frac{1}{\sigma_p v_{th} N_T} \quad (A.2)$$

and

$$\tau_n = \frac{1}{\sigma_n v_{th} N_T} \quad (A.3)$$

These shall be referred to as the "minority" G-R lifetimes of holes and electrons respectively. Physically they may be thought of as the average time between an electron-hole pair recombining at a trapsite and being subsequently generated by that trap state. The reason for the name "minority" lifetime is that the thermal G-R mechanism removes a greater percentage of minority carriers from the conduction process than majority carriers. This is true since it is assumed that the G-R term R is the same for both electrons and holes, i.e. $R_p = R_n = R$. The G-R term then becomes

$$R = \frac{p \cdot n - n_i^2}{\tau_p \{n + n_i \exp(E_T - E_i)/kT\} + \tau_n \{p + n_i \exp(E_i - E_T)/kT\}} \quad (A.4)$$

It has been assumed ⁽⁶²⁾⁽⁶³⁾ that a single trap state having an activation energy of E_T exists. The closer the trap energy level is to the intrinsic energy level, the more efficient is the trap, i.e. R is larger. Recombination is maximized for the trap lying exactly at the intrinsic Fermi energy level, $E_T = E_i$. Since the G-R mechanism is strongest for such trap, it is

assumed as the worst-case yielding

$$R = \frac{p \cdot n - n_i^2}{\tau_p(n+n_i) + \tau_n(p+n_i)} \quad (\text{A.5})$$

Equation A.5 is then the general G-R term derived for a single trap state of activation energy equal to the intrinsic Fermi energy.

Making the small signal approximation for the holes and electrons concentrations

$$p = p_0 + \tilde{p}_1 \exp j\omega t \quad ; \quad n = n_0 + \tilde{n}_1 \exp j\omega t$$

yields

$$R = \frac{p_0 \cdot n_0 + \tilde{p}_1 n_0 \exp j\omega t + \tilde{n}_1 p_0 \exp j\omega t + \tilde{p}_1 \tilde{n}_1 \exp j2\omega t - n_i^2}{\tau_p(n_0 + \tilde{n}_1 \exp j\omega t + n_i) + \tau_n(p_0 + \tilde{p}_1 \exp j\omega t + n_i)} \quad (\text{A.6})$$

Since, by the small signal approximation $|\tilde{p}_1| \ll p_0$ and $|\tilde{n}_1| \ll n_0$, one may linearize Eq. A.6 by making the following assumptions:

$$\tilde{p}_1 \cdot \tilde{n}_1 \cdot \exp j2\omega t \cong 0$$

$$n_0 + \tilde{n}_1 \exp j\omega t + n_i \cong n_0 + n_i$$

$$p_0 + \tilde{p}_1 \exp j\omega t + n_i \cong p_0 + n_i$$

and obtain

$$R \cong \frac{p_0 \cdot n_0 - n_i^2 + (\tilde{p}_1 n_0 + \tilde{n}_1 p_0) \exp j\omega t}{\tau_p(n_0 + n_i) + \tau_n(p_0 + n_i)} \quad (\text{A.7})$$

In the MOS structures in question, no direct current is allowed to flow and thus $p_0 \cdot n_0 = n_i^2$, further reducing the G-R term to

$$\tilde{R}_{ac} = \frac{\tilde{p}_1 \cdot n_0 + \tilde{n}_1 \cdot p_0}{\tau_p (n_0 + n_i) + \tau_n (p_0 + n_i)} \quad (\text{A.8})$$

where R in this case is $\tilde{R}_{ac} \exp j\omega t$.

APPENDIX BStability Analysis of the Numerical Method Used
in the Solution of the Nonlinear Poisson Equation

The nonlinear partial differential equations encountered in Chapter 2 were solved numerically. Due to the nonlinearity in the Poisson equation (see for example, Eq. 2.3.1) and the method used to obtain a solution (SOR-Newton), there may be cases in which the iteration diverges rather than converges. There is no question that if the method were applied to a corresponding linear set of equations, the scheme would be found to be unconditionally stable. When applied to the equations under study, the stability of the schemes, the regions where stability may be established and convergence towards a final solution are questions of great importance. In the following material these questions are addressed, analyzing the schemes by applying stability criteria and obtaining a criteria for choosing successful relaxation parameters and starting vectors.

The main theorem used in the following analysis is given by Stern⁽⁶⁴⁾:

Th^m 1: Given a continuously differentiable function $\phi(x)$, if

$$\left\| \frac{\partial \phi(x)}{\partial x} \right\| \leq c < 1 \quad (\text{B.1})$$

then $\phi(x)$ is a contraction

Here $\frac{\partial \phi(x)}{\partial x}$ denotes the Jacobian matrix, the underlying x denotes a vector or a vector function and the matrix norm to be used throughout shall be

$$\|A\| = \max_i \sum_j (a_{ij})$$

The following definition of a vector norm shall also be used

$$\|x\| = \max_i \{x_i\}$$

The equations of Section 2.2, after discretization and assuming constant but not necessarily equal step sizes in the x and y directions, may be written as

$$F_{I,J}(V) = \frac{V_{I+1,J} + V_{I-1,J} - 2V_{I,J}}{DXS} + \frac{V_{I,J+1} + V_{I,J-1} - 2V_{I,J}}{DY} - C_1 \sinh V_{I,J} + C_2 = 0 \quad (\text{B.2})$$

in the semiconductor, and

$$F_{I,J}(V) = \frac{V_{I+1,J} + V_{I-1,J} - 2V_{I,J}}{DXI} + \frac{V_{I,J+1} + V_{I,J-1} - 2V_{I,J}}{DY} = 0 \quad (\text{B.3})$$

in the insulator, and

$$F_{I,J}(V) = K_I \epsilon_0 \left(\frac{V_{I,J} - V_{I-1,J}}{DXI} \right) - K_S \epsilon_0 \left(\frac{V_{I+1,J} - V_{I,J}}{DXS} \right) - Q_{SSI} = 0 \quad (\text{B.4})$$

at the interface between insulator and semiconductor at a $y=\text{constant}$ curve. Picking a specific example for the interface equation does not detract from the generalized system since it will be shown that the stability of the system is dominated by the nonlinearity of Eq. B.2. It should be noted that the symbols C_1 and C_2 denote two constants which may be obtained by comparing Eq. B.2 and those in Chapter 2, and are introduced here to simplify the analysis notation.

The solution sought is a vector \underline{v}_e which satisfies the above set of algebraic equations, given a complete set of boundary conditions. One is operating, as may be observed, in an N dimensional vector space (for N number of interior grid points) with each component of the solution vector lying in a mutually orthogonal direction to the rest. To find a solution vector, one begins at some coordinate location somewhere in the N dimensional space at some initial vector \underline{v}_0 and uses a scheme to approach the solution vector \underline{v}_e by a series of iterations. The scheme to be used is

$$\underline{v}_{I,J}^{k+1} = \underline{v}_{I,J}^k - w_{I,J} \frac{F_{I,J}(\underline{v}^k)}{F'_{I,J}(\underline{v}^k) \cdot \underline{a}_{I,J}} \quad (\text{B.5})$$

where $F'_{I,J}(\underline{v}^k)$ denotes the Jacobian of $F_{I,J}(\underline{v}^k)$. This is dotted with the unit vector $\underline{a}_{I,J}$ of the N dimensional space and produces $\frac{\partial F_{I,J}(\underline{v}^k)}{\partial \underline{v}_{I,J}}$. The parameter $w_{I,J}$ is

the local accelerating parameter with a value $0 < \omega \leq 2$ used to accelerate convergence of the algorithm. The superscript k and $k+1$ refer to the old and new iterate value of the (I,J) component of $V_{I,J}$.

It should be pointed out that in this scheme all other components of \underline{v} except the (I,J) are considered constant and iteration toward a solution is performed along a curve $z = F_{I,J}(\underline{v}^*, V_{I,J})$ on a plane $\underline{v}^* = \text{constant}$ where \underline{v}^* is the current \underline{v} vector without $V_{I,J}$ in it, i.e. \underline{v}^* has $N-1$ components.

For this scheme with a general $\underline{F}(\underline{v})$, Householder⁽⁶⁵⁾ shows that if one commences the iteration with a starting vector \underline{v}_0 close enough to the solution vector \underline{v}_e , then the iteration converges. This is to say that this scheme is locally stable in a neighborhood of the solution vector. Normally one may not know that a \underline{v}_0 picked at random, or even with a sophisticated physical insight, will be within this neighborhood. Convergence of the scheme may be monitored as the iteration progresses; it is the purpose of this appendix to derive such a scheme. The strategy for its development is:

1. Apply the iteration scheme of Eq. B.5 to Eqs. B.2, B.3 and B.4 and rewrite into proper form for stability analysis
2. Apply Theorem 1 to the set above derived.
3. Develop a criteria to be applied to the k^{th} iterate of \underline{v} to show it will produce a contrac-

tion mapping when the scheme is applied to it.

Application of Eq. B.5 to Eqs. B.2 through B.4 yields in the semiconductor

$$V_{I,J}^{k+1} = V_{I,J}^k - w_{I,J}$$

$$\left\{ \frac{\frac{V_{I+1,J}^k + V_{I-1,J}^{k+1} - 2V_{I,J}^k}{DXS} + \frac{V_{I,J-1}^k + V_{I,J-1}^{k+1} - 2V_{I,J}^k}{DYS} - C_1 \sinh V_{I,J} + C_2}{\left(-\frac{2}{DXS} - \frac{2}{DY} - C_1 \cosh V_{I,J}\right)} \right\} \quad (B.6)$$

and in the insulator

$$V_{I,J}^{k+1} = V_{I,J}^k - w_{I,J} \left\{ \frac{\frac{V_{I+1,J}^k + V_{I-1,J}^{k+1} - 2V_{I,J}^k}{DXI} + \frac{V_{I,J}^k + V_{I,J-1}^{k+1} - 2V_{I,J}^k}{DYI}}{\left(-\frac{2}{DXI} - \frac{2}{DY}\right)} \right\} \quad (B.7)$$

and at the interface

$$V_{I,J}^{k+1} = \frac{\kappa_S \epsilon_0 V_{I-1,J}^{k+1} + \kappa_I \epsilon_0 V_{I+1,J}^k}{\left(\frac{\kappa_S \epsilon_0}{DXS} + \frac{\kappa_I \epsilon_0}{DXI}\right)} \quad (B.8)$$

Note should be taken of the fact that this scheme calls for immediate substitution of the new (k+1) iterate for the old (k) iterate as it becomes available during the iteration. This is a feature of successive relaxation techniques and has been employed here.

As is evident, the above equations are in the proper form for application of Theorem 1, thus one may proceed directly to accomplish part 2. The Jacobian of the above set is simply obtained by noting that this system of equations is solved by iterating one equation at a time,

that is, in the (I,J) equation all other variable values at (I+1,J), (I-1,J), (I,J+1) and (I,J-1) are considered constant. The Jacobian in this case has a diagonal form; the diagonal element being $\frac{\partial \phi_{I,J}}{\partial V_{I,J}}$.

In the semiconductor

$$\frac{\partial \phi_{I,J}}{\partial V_{I,J}} = 1 - w_{I,J} \left\{ \frac{-\frac{2}{DXS} - \frac{2}{DY} - C_1 \cosh(V_{I,J})^2 - (-C_1 \sinh V_{I,J}) * F_{I,J}(V)}{(-\frac{2}{DXS} - \frac{2}{DY} - C_1 \cosh V_{I,J})^2} \right\} \quad (B.9)$$

in the insulator

$$\frac{\partial \phi_{I,J}}{\partial V_{I,J}} = 1 - w_{I,J} \quad (B.10)$$

and at the interface

$$\frac{\partial \phi_{I,J}}{\partial V_{I,J}} = 0 \quad (B.11)$$

The last result is expected since a straight forward computation, not an iteration, is used. The term $F_{I,J}(V)$ used in Eq. B.9 is that defined in Eq. B.2. Also, it may be seen, that for any value of V the iteration in the oxide will always yield a contraction mapping (for $0 < w_{I,J} \leq 2$). In the semiconductor application of the matrix norm, previously defined, on the Jacobian in Eq. B.9 yields

$$\frac{\partial \phi_{I,J}}{\partial \underline{v}} = \max_{I,J} \left| 1 - w_{I,J} \left(\frac{\left(\frac{-2}{DXS} - \frac{2}{DY} - C_1 \cosh V_{I,J} \right)^2 - (-C_1 \sinh V_{I,J} * F_{I,J}(\underline{v}))}{\left(\frac{-2}{DXS} - \frac{2}{DY} - C_1 \cosh V_{I,J} \right)^2} \right) \right| \quad (B.12)$$

To satisfy the hypothesis to Theorem 1, \underline{v} in the above equation must satisfy

$$\max_{I,J} \left| 1 - w_{I,J} \left(\frac{\left(\frac{-2}{DXS} - \frac{2}{DY} - C_1 \cosh V_{I,J} \right)^2 - (-C_1 \sinh V_{I,J} * F_{I,J}(\underline{v}))}{\left(\frac{-2}{DXS} - \frac{2}{DY} - C_1 \cosh V_{I,J} \right)^2} \right) \right| \ll 1 \quad (B.13)$$

If \underline{v} satisfies Eq. B.13, then it produces a contraction mapping. It is this expression which may be used to test the current \underline{v}^k to see if it will map into \underline{v}^{k+1} as a contraction. This by itself does not insure that the resulting vector, \underline{v}^{k+1} , will also produce a contraction mapping when acted on by $F_{I,J}(\underline{v})$. Thus from Eq. B.13, one may only monitor stability of the scheme, step by step. If and when a given \underline{v}^k does not produce a contraction mapping then corrective action may be taken such as to choose a new starting vector \underline{v}_0 and commence anew or modify the iteration (by changing $w_{I,J}$ for example) to bring about stability and continue the approach to the solution \underline{v}_0 . This latter approach is used to yield a criteria on $w_{I,J}$ which proves useful. Rewriting Eq. B.13 as

$$\max_{I,J} \left| 1 - w_{I,J} + \left[\frac{w_{I,J}(-C_1 \sinh V_{I,J} * F_{I,J}(\underline{V}))}{\left(\frac{-2}{DXS} + \frac{-2}{DY} - C_1 \cosh V_{I,J}\right)^2} \right] \right| \leq 1 \quad (\text{B.14})$$

and further, as

$$\max_{I,J} \left| 1 - w_{I,J} \left\{ 1 + \frac{C_1 \sinh V_{I,J} * F_{I,J}(\underline{V})}{\left(\frac{+2}{DXS} + \frac{2}{DY} + C_1 \cosh V_{I,J}\right)^2} \right\} \right| \leq 1 \quad (\text{B.15})$$

For the above inequality to be satisfied, it is sufficient that

$$0 \leq \max_{I,J} \left| w_{I,J} \left\{ 1 + \frac{C_1 \sinh V_{I,J} * F_{I,J}(\underline{V})}{\left(\frac{+2}{DXS} + \frac{2}{DY} + C_1 \cosh V_{I,J}\right)^2} \right\} \right| \leq 2 \quad (\text{B.16})$$

rewriting

$$0 < \max_{I,J} \left| 1 + \frac{C_1 \sinh V_{I,J} * F_{I,J}(\underline{V})}{\left(\frac{2}{DXS} + \frac{2}{DY} + C_1 \cosh V_{I,J}\right)^2} \right| \leq \frac{2}{w_{I,J}} \quad (\text{B.17})$$

At this point one observes that $w_{I,J}$ can be made as small as necessary to place an upper limit on the middle term in the above expression. Thus for all \underline{V} , an $w_{I,J}$ may be found for Eq. B.17 to be satisfied. This fact is further appreciated if one notices that for small $w_{I,J}$ one is iterating toward the solution slowly and for large $w_{I,J}$, much faster. Thus for any \underline{V}_0 , the $w_{I,J}$ can be adjusted at each (I,J) and for each (k) as the iteration progresses, and maintain stability. If one is far away from a solution, especially in regions with few stable paths, it is unwise to take large steps and the above expression will yield the largest $w_{I,J}$

which is possible to be used and maintain stability.

As one gets closer to a solution, $F_{I,J}(\underline{y})$ gets closer to zero and the allowable $w_{I,J}$ becomes larger.

The name given the scheme for various values of w are: ⁽⁶⁶⁾

1. $0 < w \leq 1$ successive under-relaxation
2. $w = 1$ Gauss-Seidel
3. $1 < w \leq 2$ successive over-relaxation

For $F_{I,J}(\underline{y}_0) = 0$ (i.e. $\underline{y} = \underline{y}_0$ or the solution vector), w equals 2, the largest value it may attain. This stability analysis suggests several things:

1. Underrelaxation is a more stable method since it operates with smaller w 's,
2. As a solution is reached, one can accelerate convergence by going to larger w 's and still satisfy Eq. B.17,
3. An w may be chosen at each (I,J) for each iteration or a blanket w chosen for that iteration which satisfies the worst case over all (I,J) .

The main drawback in implementing this analysis is that it requires computation time above that used in finding \underline{y}^{k+1} . On the other hand, this may accelerate convergence where less iterations are needed, thus realizing a savings in computation time. This technique has not been programmed or tried on the problem at hand but should be used in a fully automatic program to assure convergence in all cases.

Appendix C

Analysis of Measured MIS Capacitance-Voltage Curves

This appendix concerns the procedure found useful in analyzing the capacitance-voltage curve of an MIS capacitor. This procedure is used extensively for modeling the small signal AC admittance of the MIS capacitor as a function of DC bias. The structure is shown in Fig. C.1a. The data will consist of a set of data points or a recorder plot of gate capacitance versus applied voltage, V_{apl} . Figure C.1b shows a typical result for p type bulk and describes the nomenclature used in the text. Several assumptions are made which are reasonable and simplify the analysis.

1. It shall be assumed that in strong accumulation (large negative bias for the curve shown in Fig. C.1b) the measured capacitance is a constant, C_{max} , and is the insulator capacitance. The oxide capacitance being that of a parallel plate capacitor having the insulator thickness and dielectric constant, that is

$$C_{max} = C_o = K \epsilon_o \frac{A}{x_o} \quad (C.1)$$

An approximate correction factor may be used if a slope to the C-V curve exists at the bias point picked for measuring C_{max} ⁽⁶⁷⁾. Otherwise, if the device is

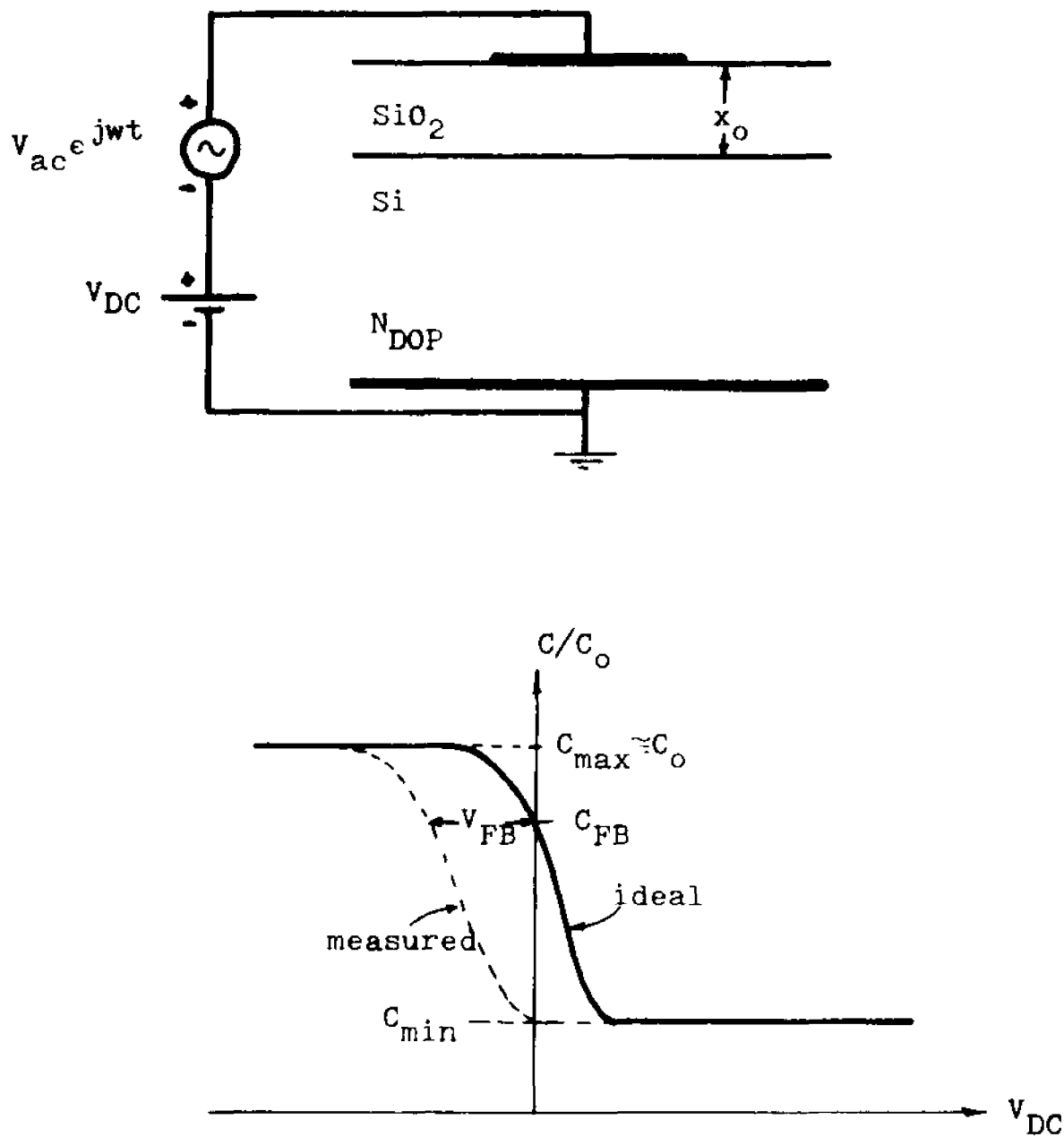


Figure C.1. Definition of terms in the modeling of the capacitance of an MIS capacitor.

homogeneously doped, then the approximation given by Eq. C.2 is valid.

2. The substrate is homogeneously doped. If this is not the case, analysis must proceed in a different manner and the assumption above may not be made.

3. The fringing capacitance due to the finite dimensions of the gate plate are neglected. This is reasonable if the dimensions of the plate are much larger than the insulator thickness, as is usually the case.

The procedure under these assumptions is:

1. From measurements of the area of the device (obtained from original mask measurements, microscopic examination, etc.), the measured C_{\max} and the type of insulator material, obtain the oxide thickness

$$x_o = \frac{\kappa_I \epsilon_o A}{C_{\max}} \quad (C.2)$$

Compare this result with the insulator color (for oxides on silicon⁽⁶⁸⁾) and growth data as a check.

2. Obtain the ratio of C_{\min}/C_{\max} . If approximate curves are available using this ratio and the insulator thickness obtained in 1 determine the approximate value of the semiconductor doping level. (For silicon dioxide on silicon, these curves are widely available, see Sze⁽⁶⁹⁾ for example) Using a fixed strong inversion bias and the insulator thickness from 1, vary the doping level about the approximate level found above and iteratively deter-

mine a more exact figure. If an approximate doping level is not available, a sweep for inversion conditions may need to be done for this determination.

3. At this point the theoretical C-V curve may be generated for biases from accumulation to inversion.

Several things must be kept in mind:

- a. the algorithm as is presently stated will not compute the capacitance accurately for biases which bring the surface intrinsic energy level beyond the band gap limits. The surface potential calculated may be monitored for each generated point and maintained within limits (+.55 to -.55 volts for silicon under the assumptions of the algorithm).
- b. several passes may be needed to obtain the curve for the full bias range (permitted by the limits on surface potential) unless consultation of published results is made for surface potential versus gate biases curves, to determine gate bias limits (for silicon these may be found in Goetzberger⁽⁵³⁾).

4. Normally in all measured C-V curves there is a fair amount of voltage shift, due to the metal semiconductor work function, and other physical causes. This shift may be measured if one has knowledge of the flat-band capacitance. It is found by using a bias voltage of 0 volts and the parameters from above on the algorithm.

This value of $\frac{C_{FB}}{C_0}$ is found on the measured C-V curve, the bias at this point being the flat-band voltage.

5. The amount of positive interface charge residing in the insulator may be found from

$$\frac{Q_{SS}}{q} = -(V_{FB} - \phi_{MS}) \frac{\kappa_I \epsilon_0}{qx_0} \quad (C.3)$$

The metal semiconductor work function ϕ_{MS} , is found from published results (for silicon-aluminum, see Wolf⁽⁷⁰⁾).

Example:

A pattern of 10 mil diameter aluminum dots were deposited over a dry (O₂) oxide grown @ 1000°C. for 60 min., and annealed in N₂ for 10 min. The oxide color is tan to brown. The substrate was p type silicon of resistivity 4 to 4.6 Ωcm as specified by the manufacturer. The C-V measurements were made with a Boonton 72AD capacitance meter at 1 MHz. The resulting normalized C-V curve is plotted in Fig. C.2.

The measured C_{max} is 19pf., thus the oxide thickness is x_o = 922Å which compares favorably with the growth data and color information.

The ratio of $\frac{C_{min}}{C_{max}}$ is .33. From the curve in Sze⁽⁷¹⁾ the approximate background doping is N_B ≈ 2x10¹⁵ ions/cm³. Sweeping from 1x10¹⁵ to 3x10¹⁵ in .2x10¹⁵ steps the $\frac{C_{min}}{C_{max}}$ ratio at 2.8x10¹⁵ is found to be .333 and is selected. The applied voltage is +2.0V, which drives the device into inversion. Indeed, such is the

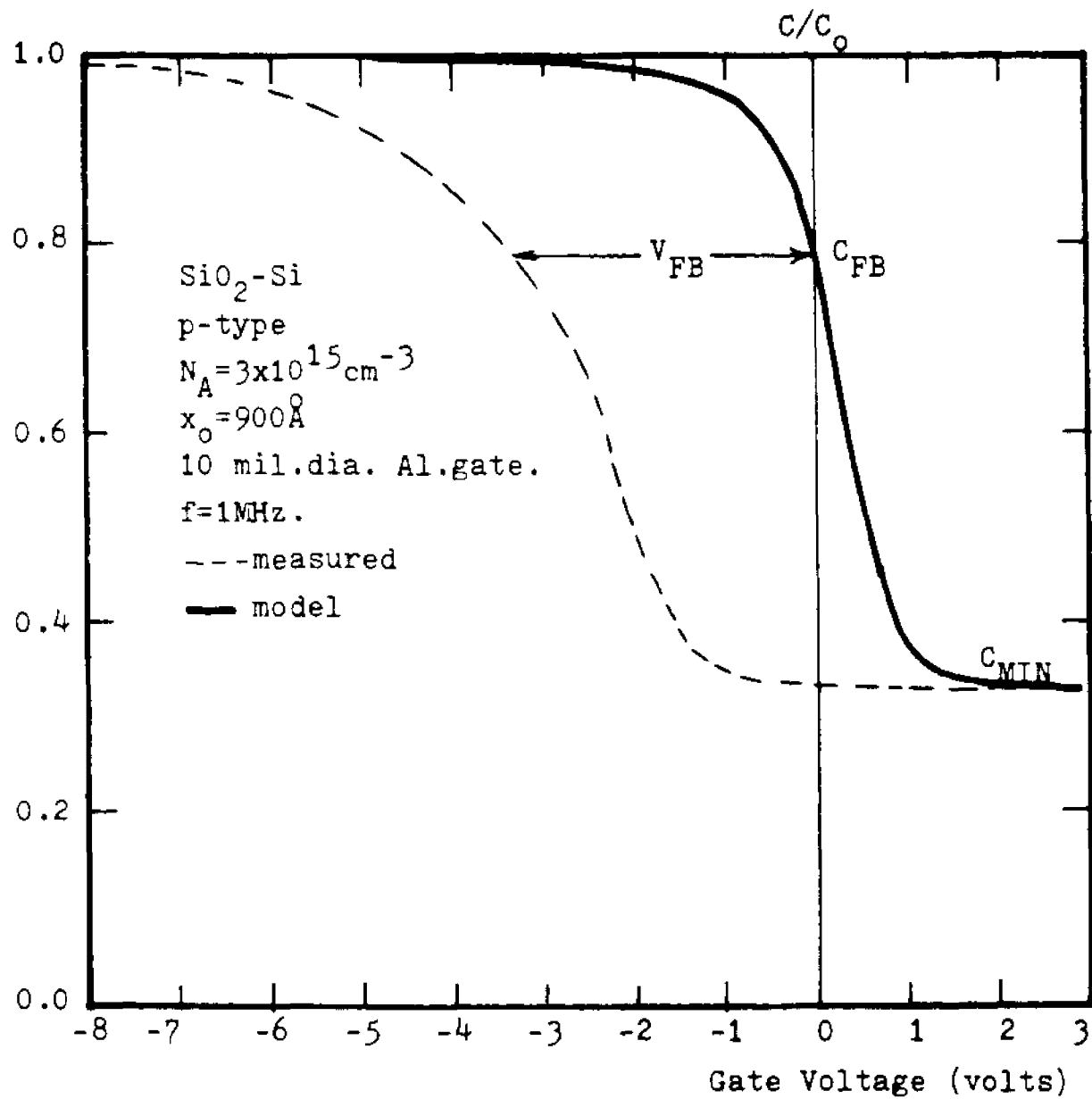


Figure C.2. Measured and calculated capacitance-voltage curve.

case since at 2.8×10^{15} and $V_{ap} = +2V$, the surface potential was $.4V$, which lies more than $2|V_F|$ away from the reference level ($V_F = .3$). This doping level relates well to the specified resistivity.

The full ideal C-V curve was then generated for $x_o = 922 \text{ \AA}$ and $N_B = 2.8 \times 10^{15}$ ions/cm³. It is also plotted on Fig. C.2. For zero applied bias, the flat-band capacitance (normalized) is found to be $C_{FB}/C_o = .785$. The flat-band voltage is then calculated as $V_{FB} = -3.2V$. The metal semiconductor work function difference for this case is $\phi_{MS} = -.92$ which leads to the calculation of the Q_{ss}/q level.

$$\frac{Q_{ss}}{q} = -(V_{FB} - \phi_{MS}) \frac{k_I \epsilon_o}{qx_o} = \frac{(-3.2 + .92) \cdot 3.9 \cdot 8.86 \times 10^{-14}}{.0922 \times 10^{-4} \cdot 1.6 \times 10^{-19}}$$

which yields

$$\frac{Q_{ss}}{q} = 6.98 \times 10^{11} \text{ cm}^{-2}$$

Inhomogeneously Doped Devices

Several differences appear in the C-V curve of inhomogeneously doped devices. These noticeable differences have been shown theoretically and experimentally in Chapter 3 and are:

1. A flat-band voltage shift due to the inhomogeneity besides the usual causes of shift;

2. Change in the C_{\min}/C_{\max} ratio;
3. In some cases, the C_{\max} is not equal to C_0 or may not be measured due to the high voltage levels the device must be driven to obtain accumulation.

In these cases, independent knowledge of oxide thickness and doping profile must be known a priori and used with the model. This information may be derived from measurements (such as ellipsometry data for oxide thickness) or fabrication data which has been processed to yield this information.

An alternate solution exists which may be incorporated in the process. A homogeneous capacitor may be planned to be fabricated alongside the homogeneously doped one. Working up the C-V data from this device with the procedure described here, yields oxide thickness, background doping and flat-band voltage shift due to ϕ_{MS} , and Q_{SS} . This information can be used in the analysis of the inhomogeneous device.

Stepped Oxide Devices

Devices which have more than two capacitance levels due to insulator steps may be analyzed as follows. The device data and unknowns are shown in Fig. C.3.

The relationship of all the parameters is

$$C' = C_{O1} + C_{O2} \quad (C.4)$$

$$C'' = C_{o2} + C_{\min 1} \quad (C.5)$$

$$C''' = C_{\min 2} + C_{\min 1} \quad (C.6)$$

where C_{o1} and C_{o2} are the oxide capacitances of the capacitors under A_1 and A_2 and are

$$C_{o1} = \kappa_{\text{SiO}_2} \epsilon_o \frac{A_1}{x_{o1}} \quad (C.7)$$

$$C_{o2} = \kappa_{\text{SiO}_2} \epsilon_o \frac{A_2}{x_{o2}} \quad (C.8)$$

and the minimum capacitances are

$$C_{\min 1} = \alpha_1(x_{o1}, N_{\text{DOP}}) \cdot C_{o1} \quad (C.9)$$

$$C_{\min 2} = \alpha_2(x_o, N_{\text{DOP}}) \cdot C_{o2} \quad (C.10)$$

Thus introducing the relations of equations C.7 through C.10 into equations C.4 through C.6, one obtains

$$C' = \kappa_{\text{SiO}_2} \epsilon_o \left(\frac{A_1}{x_{o1}} + \frac{A_2}{x_{o2}} \right) \quad (C.11)$$

$$C'' = \kappa_{\text{SiO}_2} \epsilon_o \left(\frac{A_2}{x_{o2}} + \alpha_1(x_{o1}, N_{\text{DOP}}) \cdot \frac{A_1}{x_{o1}} \right) \quad (C.12)$$

$$C''' = \kappa_{\text{SiO}_2} \epsilon_o \left(\alpha_2(x_{o2}, N_{\text{DOP}}) \frac{A_2}{x_{o2}} + \alpha_1(x_{o1}, N_{\text{DOP}}) \frac{A_1}{x_{o1}} \right) \quad (C.13)$$

In these three equations the only unknowns are x_{o1} , x_{o2} and N_{DOP} and may be solved for iteratively. The parameter

$\alpha(\cdot)$ may be found approximately from Sze⁽⁷²⁾ for example and more accurately from the one dimensional AC program derived in Chapter 3.

The amount of shift measured for each step may be converted in V_{FB} of each capacitor once the oxide thicknesses and doping concentrations are known.

$$V_{FB1} = V'_{FB} \quad (C.14)$$

where V'_{FB} is measured at a capacitance level of

$$C'_{FB} = C_{O1} + C_{FB2} \quad (C.15)$$

and C_{FB2} calculated for x_{O2} and N_{DOP} with $V_G=0$ volts and the one dimensional algorithm. The second flat-band voltage is

$$V_{FB2} = V''_{FB} - V'_{FB} \quad (C.16)$$

where V''_{FB} is measured at a capacitance level

$$C''_{FB} = C_{FB1} + C_{1 \min} \quad (C.17)$$

with C_{FB1} and $C_{1 \min}$ found as explained above.

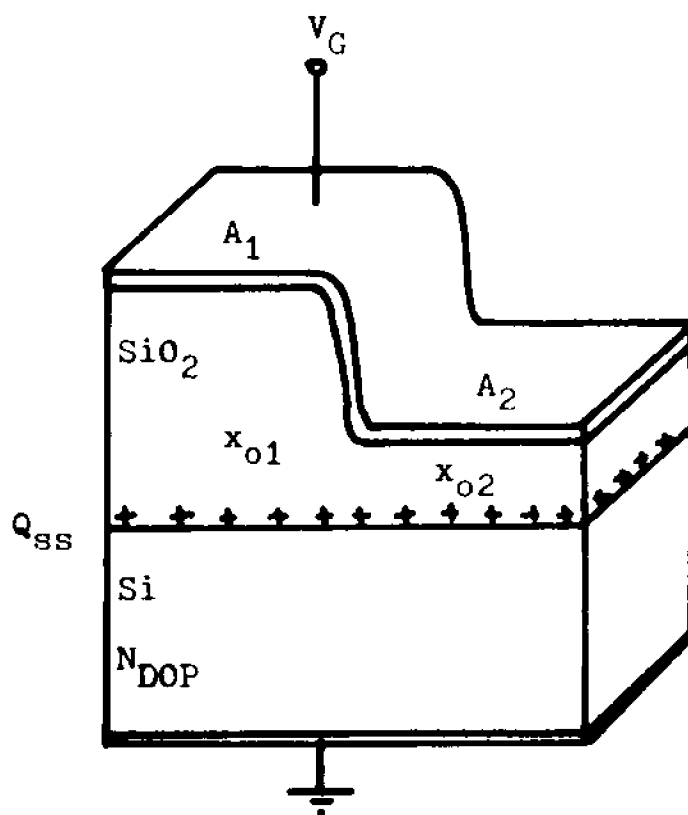


Figure C.3a. Structure of a three level MOS capacitor.

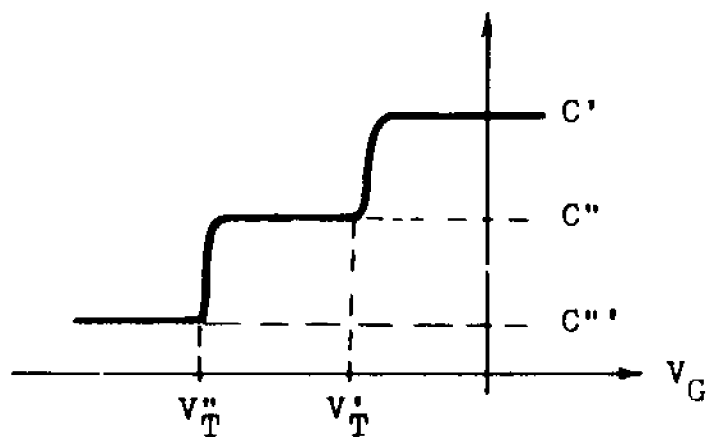


Figure C.3b. Definition of terms in the example of a three level MOS varactor.

APPENDIX D

Verification of the Lateral Boundary Approximation in the Two Dimensional Problem

Consider the structure shown in Fig. D.1a. The object of this appendix is to obtain an estimate of the error in using a linear approximation to the solution at some lateral boundary, b away from the center of the device. The structure is an infinite strip in the x direction of finite width b . The problem is essentially a solution of Laplace's equation for the potential given the boundary conditions shown.

A solution is simply obtained by decomposing the problem into the sum of three subproblems, as shown in Figs D.1b and D.1c. This is possible due to the superposition of solutions of a linear problem. The solution to 1 is a straightforward linear voltage drop from the top contact to the bottom

$$v_1(x,y) = v_0 \cdot \left(\frac{y}{a}\right) \quad (D.1)$$

Problems 2 and 3 are essentially the same and shall be treated by a general solution. Consider their generalization shown in Fig. D.2.

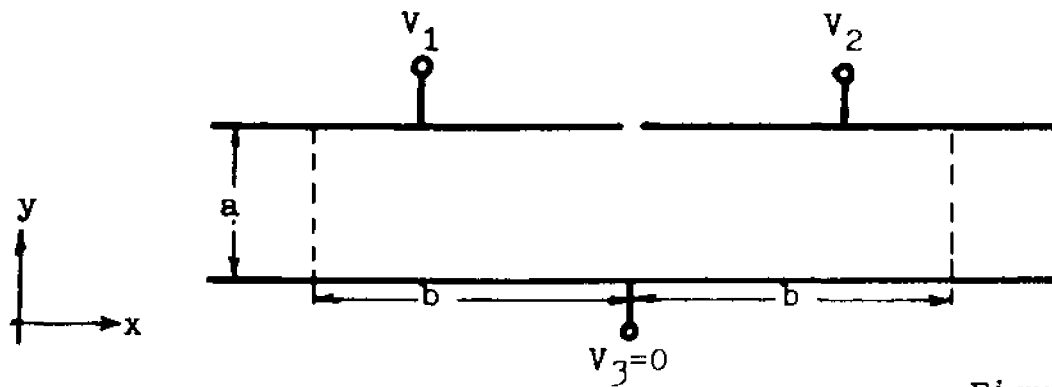


Figure D.1a.

$$V_1 = V_o + (V_1 - V_o) \quad V_2 = V_o + (V_2 - V_o)$$

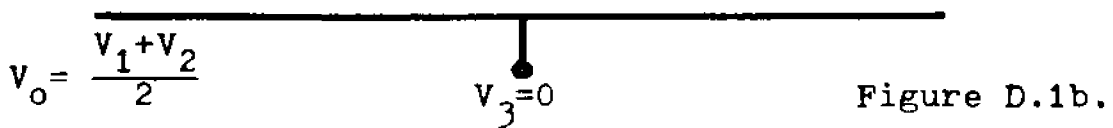


Figure D.1b.

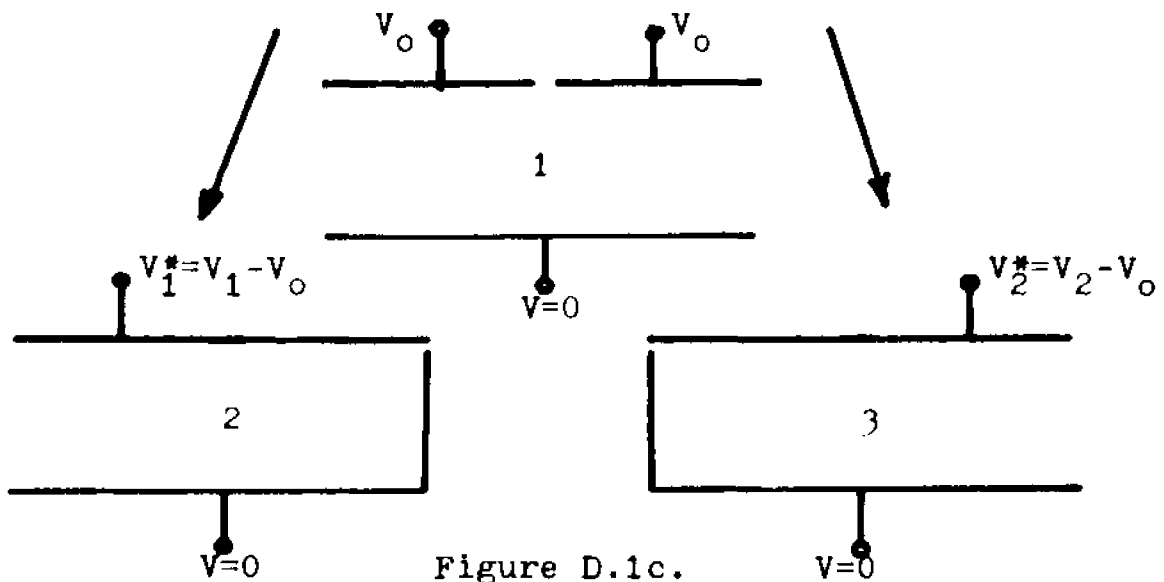


Figure D.1c.

Figure D.1. Structure and decomposition of the problem.

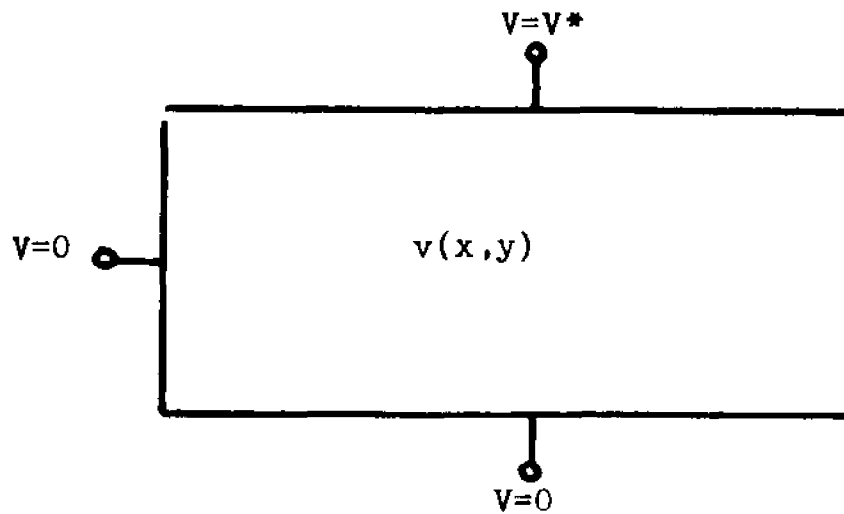


Figure D.2. Redefinition of the boundary conditions.

Separate a linear component in $v(x,y)$ as

$$v(x,y) = \frac{V^*y}{a} + v'(x,y) \quad (D.2)$$

where $v'(x,y)$ is a correction factor. This factor is the one of interest, specially how rapidly it goes to zero as x increases. Since $v(x,y)$ must satisfy Laplace's equation, so must $v'(x,y)$ and the problem may be redefined to solve for $v'(x,y)$, as shown in Fig. D.3

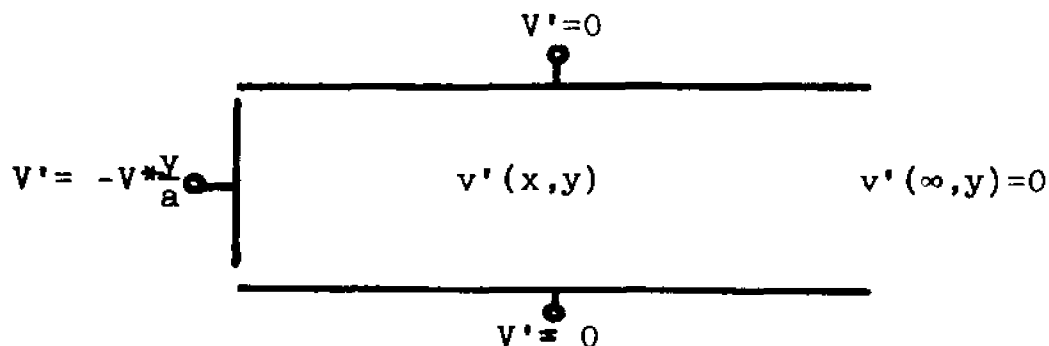


Figure D.3. Further redefinition of the boundary conditions.

Solving Laplace's equation for $v'(x,y)$ with the boundary conditions shown, yields

$$v'(x,y) = \sum_{\text{nodd}}^{\infty} \frac{V^*}{2n\pi} e^{-\frac{n\pi x}{a}} \sin\left(\frac{n\pi}{a} y\right) \quad (\text{D.4})$$

and $v(x,y)$

$$v(x,y) = V^* \frac{y}{a} + \sum_{\text{nodd}}^{\infty} \frac{V^*}{2n\pi} e^{-\frac{n\pi x}{a}} \sin\left(\frac{n\pi}{a} y\right) \quad (\text{D.5})$$

Combining all three solutions for the subproblems, one obtains the total solution to the problem shown in Fig. D.1b

$$v(x,y) = \begin{cases} V_1 \frac{y}{a} + \sum_{\text{nodd}}^{\infty} \frac{V_2 - V_1}{2} \cdot \frac{1}{2n\pi} e^{-\frac{n\pi x}{a}} \sin\left(\frac{n\pi}{a} y\right) & x \geq 0 \\ V_2 \frac{y}{a} + \sum_{\text{nodd}}^{\infty} \frac{V_2 - V_1}{2} \cdot \frac{1}{2n\pi} e^{+\frac{n\pi x}{a}} \sin\left(\frac{n\pi}{a} y\right) & x \leq 0 \end{cases} \quad (\text{D.6})$$

The solution above is represented as the sum of a linear term and a correction factor. The question to be answered is at what $x = b$ does the approximation of neglecting the correction factor become meaningful? Since $\sin\left(\frac{n\pi}{a} y\right) \leq 1$, and substituting $(x) = b$ one sees that this factor is

$$F \leq \sum_{\text{nodd}}^{\infty} \frac{V_1 - V_2}{2} \frac{1}{2n\pi} e^{-\frac{n\pi b}{a}} \quad (\text{D.7})$$

The first term in this series is

$$F_1 = \frac{(V_1 - V_2)}{4\pi e \frac{\pi b}{a}} \quad (\text{D.8})$$

which for a (b/a) ratio of unity is

$$F_1 \cong \frac{V_1 - V_2}{300}$$

Appendix EAlgorithm Listing

The following computer code listings are representative of all the programs written and implemented in this work.

VDC2D - solves the two dimensional semiconductor Poisson equation by a one-step SOR-Newton scheme. It has VDC1D as a subroutine.

VAC1D - solves the small signal AC equations in one dimension by the method of complementary functions. Computes total solution, admittance and incremental capacitance. Typical output for admittance and a plotting routine are given.

VAC2D - solves the two dimensional small signal AC equations by the method of complementary functions. Requires two dimensional DC solution and one dimensional AC boundary solutions as input data.

VDC2D

```

//          JCB REGION=200K, TIME=5
// *MAIN LINES=5
// EXEC FORTC
// FCRT. SYSIN DC *, DCB=BLKSIZE=2000
    REAL*8  MX, HY
    CCMCN  HX(74), FY(59)
    REAL*8  V0(25,60), V010(60), VOUT(21,11)
    REAL*8  CSS(25)
    REAL*8  MAINES(25), MAINPS(25), NMAIN(25,50), NPASS(50)
    REAL*8  QMS, XO, CHL, PI
    REAL*8  G, NI, EPSO, KSIC2, KSI, VT
    DC 40  J=1,49
    HY(J)=.025E-4
    DC 41  J=50,59
    HY(J)=.01E-4
    DC 42  I=1,24
    HX(I)=.2E-4
    NR=14
    NL=12
    KSIC2=3.9
    G=1.6E-19
    EPSO=8.96E-14
    XO=.1E-4
40
41
42

```

```

      NI=1.45E10
      REAL*8 CNE
      CNE =1.
      PI=4.*DATAN(CNE)
      CO=(KSIC2*EPS0/XO)*1.E12
      V2=1.
      VT=.0259
      DC 10 I=1,25
      CSS(I)=0.
      DC 10 J=1,50
10  NMAIN(I,J)=-1.E15
      V1=-1.
      I=1
      DC 14 J=1,50
14  NPASS(J)=NMAIN(I,J)
      QMS=CSS(I)
      WRITE(6,104)
      CALL VDC1C(VO1D,V1,NPASS,QMS)
      DC 15 J=1,60
15  VO(I,J)=VO1C(J)
      I=25
      DC 16 J=1,50
16  NPASS(J)=NMAIN(I,J)
      QMS=CSS(I)
      WRITE(6,104)
      CALL VDC1C(VO1C,V7,NPASS,QMS)
      DC 17 J=1,60
17  VO(I,J)=VO1C(J)
      CHL=0.
      DC 18 I=2,13
      CHL=CHL+HX(I-1)
      DC 18 J=1,60
      K=I+12
      VO(I,J)=VO(1,J)
18  VO(K,J)=VO(25,J)
      CHL=CHL+HX(13)

```

```

CC 30 I=1,10
CC 30 J=2,11
TEMP=J-1
TEMP=TEMP/(11-I)
VOUT(I,J)=(V0(25,60)-V0(1,60))*ATAN(TEMP)/PI
VCUT(I,J)=VCUT(I,J)+V0(1,60)
30 CONTINUE
CC 36 I=12,21
CC 36 J=2,11
TEMP=J-1
TEMP=TEMP/(11-I)
VOUT(I,J)=(V0(1,60)-V0(25,60))*ATAN(TEMP)/PI
VCUT(I,J)=VCUT(I,J)+V0(25,60)
36 CONTINUE
DC 31 J=2,11
VOUT(11,J)=(V0(1,60)+V0(25,60))/2.
31 CCNTINUE
ISTART=NL+1-2
ISTOP=NR-1-2
J=1
IF(ISTART.EQ.ISTOP)GC TO 32
DC 32 I=ISTART,ISTOP
VCUT(1,J)=((V0(1,60)-V0(25,60))/(NR-NL))*(NL-I+2)+V0(25,60)
32 CCNTINUE
VOUT(11,1)=(V0(1,60)+V0(25,60))/2.
ISTOP=NL-2
DC 33 I=1,ISTOP
VOUT(1,1)=V0(1,60)
33 CONTINUE
ISTART=NR-2

```

```

      DC 34 I=1,21
      VOUT(I,1)=VO(25,60)
34    CONTINUE
      V=V1
      WRITE(6,105)
      CALL VDC2C(NMAIN,VO,QSS,VOUT,NR,NL)
      DC 20 J=1,50
      WRITE(6,101)J
      DC 25 I=1,25
      MAINES(I)=NI*DEXP(VO(I,J)/VT)
      MAINPS(I)=NI*DEXP(-VO(I,J)/VT)
25    CONTINUE
      WRITE(6,102)
      WRITE(6,103)(I,VO(I,J),MAINES(I),MAINPS(I),I=1,25)
20    CONTINUE
      DC 26 J=51,60
      WRITE(6,106)(J,I,VO(I,J),I=1,25)
26    CONTINUE
      WRITE(6,107)
      DC 27 J=1,11
      WRITE(6,108)(J,I,VOUT(I,J),I=1,21)
27    CONTINUE
100  FORMAT(1H ,I3,2X,F10.3,2(2X,1PE10.3))
101  FORMAT(1H0,'RESULTS FOR ROW=',I4)
102  FORMAT(1H0,5X,'I',6X,'VO',6X,'NES',6X,'NPS')
103  FORMAT(25(1H0,1X,I4,1X,F10.3,2(1X,E10.3),/))
104  FORMAT(1H0,'ENTERING VDC1C')
105  FORMAT(1H0,'ENTERING VDC2C')
106  FORMAT(1HC,25('ROW=',I4,'CCL=',I4,'VO=',F10.3,/,1H ))
107  FORMAT(1H0' ***** COMPUTING OUTSIDE *****')
108  FORMAT(1HC,21('ROW=',I4,'CCL=',I4,'VO=',F10.3,/,1H ))
      END
      SUBROUTINE VDC1C(VOIC,VAPL,DN,QSS)
      REAL*8 HX,HY
      COMMON HX(24),HY(59)
      REAL*8 VCLD(59),FP(50),FM(50),VOID(60)

```

```

REAL*8 A(59),P(59),C(59),D(59)
REAL*8 BETA(59),GAMMA(59),DN(50)
REAL*8 C1,CQS,SUM
REAL*8 C2(50)
REAL*8 KK12
REAL*8 C,NI,EPS0,KSIC2,KSI,VT
EPS=1.E-14
EPS0=8.86E-14
NI=1.45E10
C1=3.2E-7*NI
DC 20 J=1,50
C2(J)=DN(J)/(2.*NI)
20 CCNTINUE
VT=.0259
SN=1.
IF (DN(1).LT.0.)SN=-1.
VOID(1)=SN*VT*DLOG(DABS(DN(1))/NI)
VOID(60)=VAPL+VCID(1)
DC 1 J=2,50
SN=1.
IF(DN(J).LT.0.)SN=-1.
VCLD(J)=SN*VT*DLOG(DABS(DN(J))/NI)
1 CCNTINUE
DC 2 J=51,59
VCLD(J)=VCLD(J-1)+VAPL/10.
2 CONTINUE
JJ=0
50 CCNTINUE
KK12=HY(2)*(HY(2)+HY(1))/2.
FM(2)=KK12*C1*(DSINH(VCLD(2)/VT)-C2(2))

```

```

FP(2)=KK12*C1*CCOSH(VCLD(2)/VT)/VT
R(2)=- (HY(1)+HY(2))/HY(1)-FP(2)
C(2)=1.
D(2)=FM(2)-VOLC(2)*FP(2)-VOID(1)*HY(2)/HY(1)
DC 3 J=3,49
  KK12=HY(J)*(HY(J-1)+HY(J))/2.
  FM(J)=KK12*C1*(CSINH(VCLD(J)/VT)-C2(J))
  FP(J)=KK12*C1*CCOSH(VCLD(J)/VT)/VT
  A(J)=HY(J)/HY(J-1)
  B(J)=- (HY(J-1)+HY(J))/HY(J-1)-FP(J)
  C(J)=1.
  D(J)=FM(J)-VOLC(J)*FP(J)
3 CONTINUE
  A(50)=11.7/HY(49)
  B(50)=- (3.9/HY(50)+11.7/HY(49))
  C(50)=3.9/HY(50)
  D(50)=-QCS/EP50
DC 5 J=51,59
  A(J)=HY(J)/HY(J-1)
  R(J)=- (HY(J-1)+HY(J))/HY(J-1)
  C(J)=1.
  D(J)=0.
5 CONTINUE
  D(59)=-VOID(60)*HY(59)/HY(58)
  BETA(2)=P(2)
  GAMMA(2)=C(2)/BETA(2)
DC 6 J=3,59
  BETA(J)=P(J)-(A(J)*C(J-1)/BETA(J-1))
6 GAMMA(J)=(D(J)-(A(J)*GAMMA(J-1)))/BETA(J)
  VOID(59)=GAMMA(59)
  SUM=0.
DC 7 J=2,58
  L=60-J
  VOID(L)=GAMMA(L)-(C(L)*VOID(L+1)/BETA(L))
  SUM=SUM+DABS(VOID(L)-VOLC(L))
  VOLC(L)=VOID(L)

```

```

7 CCNTINUE
  VCLD(59)=VOID(59)
  JJ=JJ+1
  IF(JJ.EQ.100) GC TO 9
  IF(SUM.GT.EPS)GC TO 50
9 CCNTINUE
  WRITE(6,100)JJ,SUM
100  FORMAT(1H0,'JJ=',I4,'SUM=',E10.3)
  RETURN
  END
  SUBROUTINE VDC2D(N,VO,QS,VOUT,NR,NL)
    REAL*8 HX,HY
    COMMON HX(24),FY(59)
    REAL*8 VO(25,60),C2(25,50),VOUT(21,11)
    REAL*8 QS(25)
    REAL*8 N(25,50),NES(25),NPS(25)
    REAL*8 DX2,DY2,SUM,DFSI,FSI
    REAL*8 K22,H22,DYOUT
    REAL*8 VNEW,C1,C3,C4,WOX,WSI,FP,FM,FOX,FOUT,WOUT
    REAL*8 L1,L2,L3,PI
    REAL*8 C,NI,EPSO,KSIC2,KSI,VT
    REAL*8 CNE
    ONE =1.
    PI=4.*DATAN(CNE)
    EPSO=8.86 E-14
    EPS=1.E-4
    NI =1.45E10
    VT=.0259
    C1=3.2E-7*NI
    DYOUT=HX(13)

```

```

DC 9 J=1,50
DC 9 I=1,25
9 C2(I,J)=-N(I,J)/(2.*N(I))
C3=1./(11.7/HY(49)+3.9/HY(50))
L1=(DCOS(PI/24.)+DCOS(PI/9.))*0.5
L2=(DCOS(PI/24.)+DCOS(PI/49.))*0.5
L3=(DCOS(PI/10.)+DCOS(PI/20.))*0.5
WCX=2./(1.+DSQRT(1.-(L1**2)))
WSI=2./(1.+DSQRT(1.-(L2**2)))
WCUT=2./(1.+DSQRT(1.-(L3**2)))
JJ=1
DSUM=0.
1 SUM=0.
DC 14 J=2,49
H22=HY(J)*HY(J-1)*(HY(J-1)+HY(J))/2.
DC 14 I=2,24
K22=HX(I)*HX(I-1)*(HX(I-1)+HX(I))/2.
DX2=(HX(I-1)*VC(I+1,J)+HX(I)*V0(I-1,J))/K22
DY2=(HY(J-1)*VC(I,J+1)+HY(J)*V0(I,J-1))/H22
DX2=DX2-((HX(I-1)+HX(I))*V0(I,J))/K22
DY2=DY2-((HY(J-1)+HY(J))*V0(I,J))/H22
FP=(C1/VT)*DCOS(V0(I,J)/VT)
FM=C1*(DSINH(V0(I,J)/VT)+C2(I,J))
C4=-2.*(1./(HX(I)*HX(I-1))+1./(HY(J)*HY(J-1)))
DFSI=C4-FP
FSI=DX2+DY2-FM
VNEW=V0(I,J)-WSI*(FSI/DFSI)
SUM=SUM+CABS(VNEW-V0(I,J))
14 V0(I,J)=VNEW
DC 15 I=2,24
V0(I,50)=C3*(11.7*V0(I,49)/HY(49)+3.9*V0(I,51)/HY(50)+QS(I)/EP
15 CCNTINUE
DC 16 J=51,59
H22=HY(J)*HY(J-1)*(HY(J-1)+HY(J))/2.
DC 16 I=2,24
K22=HX(I)*HX(I-1)*(HX(I-1)+HX(I))/2.

```

```

DX2=(HX(I-1)*VO(I+1,J)+HX(I)*VO(I-1,J))/K22
DX2=DX2-((HX(I-1)+HX(I))*VO(I,J))/K22
DY2=(HY(J-1)*VO(I,J+1)+HY(J)*VO(I,J-1))/H22
DY2=DY2-((HY(J-1)+HY(J))*VO(I,J))/H22
FCX=DX2+DY2
C4=-2.*(1./(HX(I)*HX(I-1))+1./(HY(J)*HY(J-1)))
VNEW=VO(I,J)-WDX*(FCX/C4)
SUM=SUM+DABS(VNEW-VO(I,J))
16 VO(I,J)=VNEW
   ISTART=NL+1
   ISTOP=NR-1
   DO 21 I=ISTART,ISTOP
     VO(I,60)=VO(I,59)*KSIQ2*DYOUT/HY(59)+VOUT(I-2,2)
     VO(I,60)=VO(I,60)/(1.+KSIQ2*DYOUT/HY(59))
     VCUT(I-2,1)=VO(I,60)
21  CONTINUE
     DO 20 J=2,10
       DO 20 I=2,20
         FCUT=VCUT(I,J)-(VCUT(I+1,J)+VOUT(I-1,J))/4.
         FCUT=FCUT-(VCUT(I,J+1)+VOUT(I,J-1))/4.
         VNEW=VOUT(I,J)-WOUT*(FCUT)
         SUM=SUM+DABS(VNEW-VOUT(I,J))
         VCUT(I,J)=VNEW
20  CONTINUE
       IF(JJ.GT.1)DSUM=(TSUM-SUM)/SUM
       TSUM=SUM
100  FORMAT(1H0,'JJ=',I4,'SUM=',E10.3,'DSUM=',E10.3)
     JJ=JJ+1
     WRITE(6,100) JJ,SUM,DSUM
     IF (JJ.GE.200)GC TO 2
     IF(SUM.GT.EPS)GC TO 1
2  CONTINUE
   RETURN
   END

```

VACD1D

```

REAL*8 VRE(2),VIM(2),YRE,YIM
COMPLEX*8 TEMP
REAL*8 TEMP1,TEMP2
COMPLEX*8 VAC
REAL*8 QG1,QC2
  DIMENSION CCC(50),CRF(50),G(50),VG(50)
  DIMENSION VS(50),QC(50),QUAL(50)
COMPLEX*16 VIPASS
COMPLEX*8 CPW,CNW
REAL*8 VO,EO,PO,NO
REAL*4 K,NPASS
REAL*4 K1,K2,K3,K4
REAL*4 CP,CN,C1,C2
REAL*4 KSI,KSIC2,NI,Q,VT,EPSC
INTECEP*4 I1,I2,I3,I4
REAL*4 TP,IN
COMMON CPW,CNW
COMMON VO(50),EO(490),PC(490),NC(490)
COMMON K(490),NPASS(490)
COMMON K1,K2,K3,K4
COMMON CP,CN,C1,C2
COMMON KSI,KSIC2,NI,Q,VT,EPSC
COMMON I1,I2,I3,I4
COMMON TP,IN
XO=.1E-4
I1=20
I2= 50
I3=100
I4=110

```

```
      ISTCP=I3-1
      K1=.075E-4
-----
      K2=.05E-4
      K3=.01E-4
      K4=X0/10.
      CC 10 J=1, I3
      APASS(J)=1.E15
10 CONTINUE
-----
      NN=31
      CV=.1
      VAPL=-1.6
      F=1.E6
      W=3.14*2.*F
      KSI=11.7
-----
      KSIC2=3.9
      C=1.6F-19
      NI=1.45E10
      VT=.0259
      TP=8.E-6
      TN=TP
-----
      UP=480.
      UN=1350.
      EPSO=8.86 E-14
      CO=(KSIC2*EPSO/X0)*1.E12
      NM=11-1
      CC 1 I=1, NM
1 K(I)=K1
```

```

NM=I2-1
CC 2 I=I1,NM
2 K(I)=K2
NM=I3-1
CC 3 I=I2,NM
3 K(I)=K3
K(I3)=K4
-----
C1=(C*N1)/(KSI*EPS0)
C2=1./(N1*VT)
CP=1./(C*N1*UP*VT)
CN=1./(C*N1*UN*VT)
TPS=C*N1/TP
TNS=C*N1/TN
-----
TNW=C*N1*W
TPW=C*N1*W
CPW=CMPLX(0.,TPW)
CNW=CMPLX(0.,TNW)
CSS=0.
CC 6 J=1,NM
JITER=J
VAPL=VAPL+DV
VC(J)=VAPL
CALL VECIC(VAPL,CSS)
VS(J)=VO(I3)
EO(I)=- (VO(2)-VC(I))/K(I)

```

```

PO(1)=NI*CFXP(-VO(1)/VT)
NO(1)=NI*CEXP(VO(1)/VT)
DC 4 I=2, I3
EO(I)=-((VO(I+1)-VO(I))/K(I)+(VC(I)-VC(I-1))/K(I-1))/2.
PO(I)=NI*CEXP(-VO(I)/VT)
NO(I)=NI*CEXP(VO(I)/VT)

```

```
4 CCNTINUE
```

```

EO(I3)=-((VO(I3)-VO(I3-1))/K(I3-1)
VAC=(.01,0.)
CG1=(VO(I4)-VO(I4-1))*KSID2*EPSC/K4
CG(J)=CG1

```

```
WRITE(6,200) VAPL
```

```
200 FORMAT(1F, 'COMPUTING FOR VAPL=', 1X, F7.2)
```

```
CALL VACIC(VAC, VIPASS, ISTOP, JITER)
```

```
VRE(1)=VAC
```

```
VRE(2)=VIPASS
```

```
VIM(1)=AIMAC(VAC)
```

```
TEMP=VIPASS
```

```
VIM(2)=AIMAG(TEMP)
```

```
CALL YIC(VRE, VIM, XO, W, YRE, YIM)
```

```
CRF(J)=YIM*1.E12/CO
```

```
G(J)=YRE*W
```

```
QUAL(J)=YRE/YIM
```

```
TEMP=VAPL+.005
```

```
CALL VECIC(TEMP, CSS)
```

```
CG2=(VO(I4)-VO(I4-1))*KSID2*EPSC/K4
```

```
CCG=(CG2-CG1)
```

```
WRITE(6,101)
```

```
CVG=.005
```

```
CC(J)=(CCG*1.E12)/(CVG*CO)
```

```
WRITE(6,1C1)
```

```

6 CONTINUE
  WRITE(6,106)
  WRITE(6,101)
  WRITE(6,100) NPASS(1),X0,CC
  WRITE(6,105) F,VO(1)
  WRITE(6,101)
  WRITE(6,102)
  WRITE(6,101)
  CC 5 J=1,NN
  WRITE(6,103)VG(J),G(J),CDC(J),CRF(J),VS(J),QG(J),CLAL(J)
5 CONTINUE
  WRITE(6,101)
  WRITE(6,104)


---


  WRITE(6,101)
  CALL PLOT(VG,CDC,CRF,G,NN)
100 FORMAT(1F,'N=',1PE10.3,'CM-3',/,1X,'XC=',1PE10.3,' CENTIMETER
*,/,1X,'CO=',E10.3,' PICO FARADS/SQ.CM. ')
101 FORMAT(1F,85(' '))
102 FORMAT(7X,'VG',10X,'G',11X,'CDC',10X,'CRF',9X,'VS',9X,'CG',12X
* 'C',/,5X,'VCLTS',7X,'MPOS',2X,2(3X,' PICO FARADS'),5X,'VCLTS',2X
* 'CDUL/CM**2')
103 FORMAT(1F,F10.3,3(3X,E10.3),F10.3,2X,1PE10.3,2X,1PE10.3)
104 FORMAT(1F,' ALL CAPACITANCES ARE PER SQAURE CENTIMETERS')
105 FORMAT(1F,' FREQUENCY=',1PE10.3,' HERTZ',/,1X,'VF=',E10.3,' VCLT
106 FORMAT(1F1)


---


  STOP
  END

```

```

SUBROUTINE VCIC(VAPL,QQS)
REAL*8 VCLC(500),FP(490),FM(450),VDMAX,T
REAL*8 A(500),P(500),C(500),D(500),BETA(500),GAMMA(500)
REAL*4 C2(490)
REAL*4 KK12,KK22,KK32,KK42
COMPLEX*8 CPW,CNW
REAL*8 VO,EQ,PO,NO
REAL*4 K,NPASS
REAL*4 KK1,KK2,KK3,KK4
REAL*4 CP,CN,C1TEMP,C2TEMP
REAL*4 KSI,KSIC2,N1,G,VT,EPSC
INTEGER*4 N1,N2,N3,N4
REAL*4 TP,TN
COMMON CPW,CNW
COMMON VO(500),E0(490),PC(490),NC(490)
COMMON K(490),NPASS(490)
COMMON KK1,KK2,KK3,KK4
COMMON CP,CN,C1TEMP,C2TEMP
COMMON KSI,KSIC2,N1,G,VT,EPSC
COMMON N1,N2,N3,N4
COMMON TP,TN
EPS=.5E-15
CI=3.2E-7*NI
CC 20 J=1,N3
C2(J)=NPASS(J)/(12.*NI)

```

```

20 CONTINUE
  KK12=KK1**2
  KK22=KK2**2
  KK32=KK3**2
  KK42=KK4**2
  TEMP1=KK2/KK1
  TEMP2=1.+TEMP1
  TEMP3=(KK2*(KK1+KK2))/2.
  TEMP4=KK3/KK2
  TEMP5=1.+TEMP4
  TEMP6=(KK3*(KK2+KK3))/2.
  REAL*8 COP
  COP=NPASS(1)
  SN=1.
  IF(NPASS(1).LT.0.)SN=-1.
  VO(1)=SN*VT*(CLCG(CABS(COP/NI)))
  VO(N4)=VAPL+VO(1)
  DO 1 J=2,N3
  SN=1.
  IF(NPASS(J).LT.0.)SN=-1.
  VOLC(J)=SN*VT*ALOG(ABS(NPASS(J))/NI)
1 CONTINUE
  NP=NP+1
  NM=N4-1
  DO 2 J=NP,NM
  VOLC(J)=VOLC(J-1)+VAPL/IC.
2 CONTINUE
  JJ=0
50 FM(2)=KK12*C1*(CSINH(VOLC(2)/VT)-C2(2))
  FP(2)=KK12*C1*ECOSF(VOLC(2)/VT)/VT
  P(2)=-2.-FP(2)

```

```

C(2)=1.
D(2)=FM(2)-VOLC(2)*FP(2)-V0(1)
NP=N1-1
DO 3 J=3,NP
FM(J)=KK12*C1*(DSINH(VOLC(J)/VT)-C2(J))
FP(J)=KK12*C1*DCOSH(VOLC(J)/VT)/VT
A(J)=1.
B(J)=-2.-FP(J)
C(J)=1.
C(J)=FM(J)-VOLC(J)*FP(J)
3 CONTINUE
FM(N1)=TEMP3*C1*(DSINH(VOLC(N1)/VT)-C2(N1))
FP(N1)=TEMP3*C1*DCOSH(VOLC(N1)/VT)/VT
A(N1)=TEMP1
B(N1)=-TEMP2-FP(N1)
C(N1)=1.
C(N1)=FM(N1)-VOLC(N1)*FP(N1)
NP=N1+1
NM=N2-1
DO 4 J=NP,NM
FM(J)=KK22*C1*(DSINH(VOLC(J)/VT)-C2(J))
FP(J)=KK22*C1*DCOSH(VOLC(J)/VT)/VT
A(J)=1.
B(J)=-2.-FP(J)
C(J)=1.

```

```

D(J)=FM(J)-VCLC(J)*FP(J)
4 CONTINUE
FM(N2)=TEMP6*C1*(DSINH(VOLC(N2)/VT)-C2(N2))
FP(N2)=TEMP6*C1*DCOSH(VOLC(N2)/VT)/VT
A(N2)=TEMP4
B(N2)=-TEMP5-FP(N2)
C(N2)=1.
D(N2)=FM(N2)-VCLC(N2)*FP(N2)
NP=N2+1
NM=N3-1
DO 5 J=NP,NM
FM(J)=KK32*C1*(DSINH(VOLC(J)/VT)-C2(J))
FP(J)=KK32*C1*DCOSH(VOLC(J)/VT)/VT
A(J)=1.
B(J)=-2.-FP(J)
C(J)=1.
D(J)=FM(J)-VCLC(J)*FP(J)
5 CONTINUE
A(N3)=11.7/KK3
P(N3)=- (3.9/KK4+11.7/KK3)
C(N3)=3.9/KK4
D(N3)=-CCS/EP50
NP=N3+1
NM=N4-1
DO 10 J=NP,NM
A(J)=1.
B(J)=-2.
C(J)=1.
D(J)=0.
10 CONTINUE
C(NM)=-VO(N4)

```

```

BETA(2)=P(2)
GAMMA(2)=C(2)/BETA(2)
DO 6 J=3,NM
  BETA(J)=B(J)-(A(J)*C(J-1)/BETA(J-1))
6  GAMMA(J)=(D(J)-(A(J)*GAMMA(J-1)))/BETA(J)
  VO(NM)=GAMMA(NM)
  VDMAX=0.
  N2M=N4-2
  DO 7 J=2,N2M
    L=N4-J
    VO(L)=GAMMA(L)-(C(L)*VO(L+1)/BETA(L))
    T=ABS(VO(L)-VOLD(L))
    IF(T.GT.VEMAX)VEMAX=T
    VOLD(L)=VO(L)
7  CONTINUE
  VOLD(NM)=VO(NM)
  JJ=JJ+1
  IF(JJ.EQ.100) GO TO 9
  IF(VDMAX.GT.EPS) GO TO 50
9  CONTINUE
  RETURN
  END

```

SUBROUTINE VACID(VAC,VIPASS,ISTOP,JITER)

COMPLEX*8 CPW,CNW

REAL*8 VO,E0,P0,N0

REAL*4 K,NPASS

REAL*4 K1,K2,K3,K4

REAL*4 CP,CN,C1,C2

REAL*4 KSI,KSIC2,NI,Q,VT,EPSC

INTEGER*4 I1,I2,I3,I4

REAL*4 TP,TN

COMMON CPW,CNW

COMMON VO(500),E0(490),P0(490),N0(490)

COMMON K(490),NPASS(490)

COMMON K1,K2,K3,K4

COMMON CP,CN,C1,C2

COMMON KSI,KSIC2,NI,Q,VT,EPSC

COMMON I1,I2,I3,I4

COMMON TP,TN

COMPLEX*16 VIPASS,P(12,3,3),BETA(20,3),AA(3,3)

REAL*4 K4

INTEGER*2 INDEX(20)

COMPLEX*8 TEMP

COMPLEX*16 A(3,3),B(3),C(3)

COMPLEX*16 U1TEMP(6),U2TEMP(6),U3TEMP(6)

COMPLEX*8 VAC

REAL*4 KSI,KSIC2

REAL*4 MINANG

KSI=11.7

KSIC2=3.9

DO 1 I=1,6

U1TEMP(I)=(0.,0.)

U2TEMP(I)=(0.,0.)

```

U3TEMP(I)=(0.,0.)
1  CCNTINUE
  U1TEMP(1)=(1.,0.)
  U2TEMP(6)=(1.,0.)
  U3TEMP(3)=(1.,0.)
  IPASS=1
  JC=1
  INDEX(20)=0
  CC 8 I=1,ISTCP
  ITER=I
  CALL STEP(U1TEMP,I,ISTOP,IPASS)
  CALL STEP(U2TEMP,I,ISTOP,IPASS)
  CALL STEP(U3TEMP,I,ISTOP,IPASS)
  IF(I.EC.1)WRITE(6,200)
  CALL GRAMI (U1TEMP,U2TEMP,U3TEMP,ITER,INDEX,P,JQ)
200  FCRMAT(1H , 'STEP',5X,'U2*L2',6X,'U3*L3')
  H CCNTINUE
  A(1,1)=U1TEMP(1)*CPW
  A(1,2)=U2TEMP(1)*CPW
  A(1,3)=U3TEMP(1)*CPW
  A(2,1)=U1TEMP(6)*CNW
  A(2,2)=U2TEMP(6)*CNW
  A(2,3)=U3TEMP(6)*CNW
  A(3,1)=(-U1TEMP(3))*K4*10.*(KSI/KSID2)+U1TEMP(4)*CI
  A(3,2)=(-U2TEMP(3))*K4*10.*(KSI/KSID2)+U2TEMP(4)*CI

```

```

A(3,3)=(-U3TEMP(3)*K4*10.*(KSI/KSIO2)+L3TEMP(4))*C1
DC 10 I=1,3
10 C(I)=(0.,C.)
C(3)=VAC
DC 20 I=1,3
DC 20 J=1,3
AA(I,J)=A(I,J)
20 CONTINUE
CALL AINV(A,B,C)
VIPASS=(P(1)*UITEMP(4)+B(2)*L2TEMP(4)+B(3)*L3TEMP(4))*C1
IF(JITER.EC.1) GO TO 21
IF(JITER.EC.8) GO TO 21
IF(JITER.EC.16) GO TO 21
IF(JITER.EC.24) GO TO 21
IF(JITER.EC.31) GO TO 21
RETURN
21 CONTINUE
WRITE(6,100)
100 FORMAT(1F0, 'THE **A** MATRIX')
DC 2 I=1,3
CALL SEP16(AA(I,1),A1,A2)
CALL SEP16(AA(I,2),A3,A4)
CALL SEP16(AA(I,3),A5,A6)
WRITE(6,101)A1,A2,A3,A4,A5,A6
101 FORMAT(1F 23('(',1PE10.1,',',1PE10.1,')',3X))
2 CONTINUE
WRITE(6,102)
102 FORMAT(1F0, 'THE *BETA* VECTOR')
DC 3 I=1,3
CALL SEP16(B(I),B1,B2)
WRITE(6,103)B1,B2

```

```

103  FORMAT(1F , '( ',1PE10.1, ', ',1PE1C.1, ')')
3    CONTINUE
      COMPLEX*16 JP1,P1,E1,V1,N1,JN1,JTOT,JDISP
      IPASS=2
      WRITE(6,105)
105  FORMAT(1F 'CALCULATING ALL BETAS')
      L=INDEX(20)+1
      LL=INDEX(20)
      DO 12 J=1,3
      BETA(L,J)=B(J)
12   CONTINUE
      IF(INDEX(20).EQ.0)GO TO 25
      DO 13 I=1,LL
      L=L-I
      WRITE(6,106) L,INDEX(L)
106  FORMAT(1F0,'L=',I2,4X,'AT STEP=',I2)
      WRITE(6,110)
110  FORMAT(1F0,'THE *BETA* VECTOR',10X,'THE *P*  MATR(X')
      DO 13 J=1,3
      BETA(L,J)=(0.,0.)
      DO 14 JJ=1,3
      BETA(L,J)=BETA(L,J)+P(L,J,JJ)*BETA(L+1,JJ)
14   CONTINUE
      CALL SEP16(BETA(L,J),B1,B2)
      CALL SEP16(P(L,J,1),T1,T2)

```

```

111 CALL SEPI6(P(L,J,2),T3,T4)
13  CALL SEPI6(P(L,J,3),T5,T6)
25  WRITE(6,111)P1,B2,T1,T2,T3,T4,T5,T6
    FORMAT(1F,4(' ',1PE10.1,' ',1PE10.1,' '))
    CCNTINUE
    CCNTINUE
    JC=1
    CC 15 I=1,6
    UTEMP(I)=(0.,0.)
    U2TEMP(I)=(0.,0.)
    U3TEMP(I)=(0.,0.)
    CCNTINUE
15  U1TEMP(1)=(1.,0.)
    U2TEMP(6)=(1.,0.)
    U3TEMP(3)=(1.,0.)
    CC 16 I=1, ISTOP
    CALL STEP(U1TEMP, I, ISTOP, IPASS)
    CALL STEP(U2TEMP, I, ISTOP, IPASS)
    CALL STEP(U3TEMP, I, ISTOP, IPASS)
    JPI=PETA(JC,1)*U1TEMP(I)
    JPI=JPI+PETA(JC,2)*U2TEMP(I)
    JPI=JPI+PETA(JC,3)*U3TEMP(I)
    JPI=JPI*CPW
    PI=PETA(JC,1)*U1TEMP(2)*NI
    PI=PI+PETA(JC,2)*U2TEMP(2)*NI
    PI=PI+PETA(JC,3)*U3TEMP(2)*NI
    EI=PETA(JC,1)*U1TEMP(3)*CI
    EI=EI+PETA(JC,2)*U2TEMP(3)*CI
    EI=EI+PETA(JC,3)*U3TEMP(3)*CI
    VI=PETA(JC,1)*U1TEMP(4)*CI
    VI=VI+PETA(JC,2)*U2TEMP(4)*CI

```

```

V1=V1+BETA(JC,3)*U3TEMP(4)*C1
N1=BETA(JC,1)*U1TEMP(5)*NI
N1=N1+BETA(JC,2)*U2TEMP(5)*NI
N1=N1+BETA(JC,3)*U3TEMP(5)*NI
JN1=BETA(JC,1)*U1TEMP(6)
JN1=JN1+BETA(JC,2)*U2TEMP(6)
JN1=JN1+BETA(JC,3)*U3TEMP(6)
JN1=JN1*CPW
JDISP=(CPW*KSI*EPS0*E1)/(Q*NI)
JTCT=(JP1+JN1)+(CPW*KSI*EPSC*E1)/(Q*NI)
WRITE(6,107)I
107  FORMAT(1F,'AT STEP=',I2)
CALL SEP16(JP1,T1,T2)
CALL SEP16(JN1,T3,T4)
CALL SEP16(JDISP,T5,T6)
CALL SEP16(JTCT,B1,B2)
T7=SQRT(B1**2+B2**2)
T8=ATAN(B2/B1)
WRITE(6,112)T1,T2,T3,T4,T5,T6,B1,B2,T7,T8
CALL SEP16(P1,T1,T2)
CALL SEP16(N1,T3,T4)
CALL SEP16(E1,T5,T6)
CALL SEP16(V1,B1,B2)
T7=SQRT(B1**2+B2**2)
T8=ATAN(B2/B1)

```

```

WRITE(6,112)T1,T2,T3,T4,T5,T6,B1,B2,T7,T8
112  FORMAT(1F,5('(',1PE9.2,',',1PE9.2,')'))
      IF(INDEX(20).EQ.0) GO TO 16
      IF(JC.GT.INDEX(20))GO TO 16
      IF(1.LT.INDEX(JQ))GO TO 16
      JC=JC+1
      WRITE(6,108)
108  FORMAT(1F,'CRITHONORMALIZING')
      CALL GRM2(U1TEMP,U2TEMP,U3TEMP)
      JP1=BETA(JQ,1)*U1TEMP(1)
      JP1=JP1+BETA(JQ,2)*U2TEMP(1)
      JP1=JP1+BETA(JQ,3)*U3TEMP(1)
      JP1=JP1*CPW
      P1=BETA(JQ,1)*U1TEMP(2)*NI
      P1=P1+BETA(JQ,2)*U2TEMP(2)*NI
      P1=P1+BETA(JQ,3)*U3TEMP(2)*NI
      E1=BETA(JQ,1)*U1TEMP(3)*C1
      E1=E1+BETA(JQ,2)*U2TEMP(3)*C1
      E1=E1+BETA(JQ,3)*U3TEMP(3)*C1
      V1=BETA(JQ,1)*U1TEMP(4)*C1
      V1=V1+BETA(JQ,2)*U2TEMP(4)*C1
      V1=V1+BETA(JQ,3)*U3TEMP(4)*C1
      N1=BETA(JQ,1)*U1TEMP(5)*NI
      N1=N1+BETA(JQ,2)*U2TEMP(5)*NI
      N1=N1+BETA(JQ,3)*U3TEMP(5)*NI
      JN1=BETA(JQ,1)*U1TEMP(6)
      JN1=JN1+BETA(JQ,2)*U2TEMP(6)
      JN1=JN1+BETA(JQ,3)*U3TEMP(6)
      JN1=JN1*CPW
      JDISP=(CPW*KSI*EPS0*E1)/(Q*NI)
      JTCT=(JP1+JN1)+(CPW*KSI*EPSC*E1)/(Q*NI)
      CALL SEP16(JP1,T1,T2)
      CALL SEP16(JN1,T3,T4)
      CALL SEP16(JDISP,T5,T6)
      CALL SEP16(JTCT,B1,B2)
      T7=SQRT(B1**2+B2**2)
      T8=ATAN(B2/P1)
      WRITE(6,112)T1,T2,T3,T4,T5,T6,B1,B2,T7,T8
      CALL SEP16(P1,T1,T2)
      CALL SEP16(N1,T3,T4)
      CALL SEP16(E1,T5,T6)
      CALL SEP16(V1,B1,B2)
      T7=SQRT(B1**2+B2**2)
      T8=ATAN(B2/P1)
16  WRITE(6,112)T1,T2,T3,T4,T5,T6,B1,B2,T7,T8
      CONTINUE
      RETURN
      END

```

```

SUBROUTINE STEP(U, I, ISTOP, IPASS)
COMPLEX*16 U(6), E1, E2, V1, V2, P1, P2, N1, N2, JP1, JP2, JN1, JN2
COMPLEX*16 RP, RC
COMPLEX*8 CPW, CNW
REAL*8 VO, EO, PO, NO
REAL*4 K, NPASS
REAL*4 K1, K2, K3, K4
REAL*4 CP, CN, C1, C2
REAL*4 KSI, KSI02, NI, Q, VT, EPS0
INTEGER*4 I1, I2, I3, I4
REAL*4 TP, TN
COMMON CPW, CNW
COMMON VO(500), EO(490), PO(490), NC(490)
COMMON K(490), NPASS(490)
COMMON K1, K2, K3, K4
COMMON CP, CN, C1, C2
COMMON KSI, KSI02, NI, Q, VT, EPSC
COMMON I1, I2, I3, I4
COMMON TP, TN
RP=C*NI*(NO(I)*U(2)+PO(I)*U(5))/CPW
RP=RP/((TP*(NO(I)+NI))+(TN*(PC(I)+NI)))
JP1=U(1)-K(I)*(U(2)+RP)
P1=U(2)+K(I)*(-CP*CPW*U(1)+(EO(I)/VT)*L(2)+PO(I)*C1*C2*U(3))
E1=U(3)+K(I)*(U(2)-U(5))
V1=U(4)-K(I)*U(3)
N1=U(5)+K(I)*(CN*CNW*U(6)-(EO(I)/VT)*L(5)-NC(I)*C1*C2*L(3))
JN1=U(6)+K(I)*(U(5)+RP)
RC=C*NI*(NO(I+1)*P1+PO(I+1)*N1)/CPW
RC=RC/((TP*(NO(I+1)+NI))+(TN*(PC(I+1)+NI)))
JP2=U(1)-(K(I)/2.)*((U(2)+P1)+RP+RC)
P2=U(2)+(K(I)/2.)*(-CP*CPW*(U(1)+JP1)+(EO(I)/VT)*L(2))
P2=P2+(K(I)/2.)*((EO(I+1)/VT)*P1+PC(I)*C1*C2*L(3))
P2=P2+(K(I)/2.)*(PO(I+1)*C1*C2*E1)
E2=U(3)+(K(I)/2.)*(U(2)+P1-U(5)-N1)
V2=U(4)-(K(I)/2.)*(U(3)+E1)
N2=U(5)+(K(I)/2.)*(CN*CNW*(U(6)+JN1)-(EO(I)/VT)*L(5))
N2=N2+(K(I)/2.)*((-EO(I+1)/VT)*N1-NC(I)*C1*C2*L(3))
N2=N2+(K(I)/2.)*(-NO(I+1)*C1*C2*E1)
JN2=U(6)+(K(I)/2.)*((U(5)+N1)+RP+RC)
U(1)=JP2
U(2)=P2
U(3)=E2
U(4)=V2
U(5)=N2
U(6)=JN2
RETURN
END

```

```

SUBROUTINE GRAM1 (Y1,Y2,Y3,ITER,INDEX,P,JQ)
COMPLEX*16 Y1(6),Y2(6),Y3(6),Z1(6),Z2(6),Z3(6),P(12,3,3)
COMPLEX*8 TEMPY,TEMPZ,TEMP1,TEMP2,TEMP3
COMPLEX*8 TEMPZ1,TEMPZ2,TEMPZ3
INTEGER*2 INDEX(20)
EPS=2.
CALL PRCC(Y1,Y1,TEMPZ1)
T1=TEMPZ1
T1=SQRT(T1)
DO 1 I=1,6
1 Z1(I)=Y1(I)/T1
CALL PRCC(Y2,Z1,TEMP1)
DO 2 I=1,6
2 Z2(I)=Y2(I)-TEMP1*Z1(I)
CALL PRCC(Z2,Z2,TEMPZ2)
T2=TEMPZ2
T2=SQRT(T2)
DO 3 I=1,6
3 Z2(I)=Z2(I)/T2
CALL PRCC(Y3,Z1,TEMP2)
CALL PRCC(Y3,Z2,TEMP3)
DO 4 I=1,6
4 Z3(I)=Y3(I)-TEMP2*Z1(I)-TEMP3*Z2(I)
CALL PRCC(Z3,Z3,TEMPZ3)
T3=TEMPZ3
T3=SQRT(T3)
DO 5 I=1,6
5 Z3(I)=Z3(I)/T3
CALL ANGLE(Y2,Z2,ALPHA2)

```

```

CALL ANGLE(Y3,Z3,ALPHA3)
IF(ITER.GT.85)WRITE(6,101)ITER, ALPHA2,ALPHA3
IF(ALPHA2.GT.EPS)GO TO 21
IF(ALPHA3.LT.EPS)GO TO 20
21 CONTINUE
WRITE(6,101)ITER,ALPHA2,ALPHA3
101 FORMAT(1H ,I3,3X,2(1X,1PE10.3))
DO 6 I=1,6
Y1(I)=Z1(I)
Y2(I)=Z2(I)
Y3(I)=Z3(I)
6 CONTINUE
INDEX(JC)=ITER
INDEX(20)=INDEX(20)+1
P(JC,1,1)=1./T1
P(JC,2,1)=(0.,0.)
P(JC,3,1)=(0.,0.)
P(JC,1,2)=-TEMP1/(T1*T2)
P(JC,2,2)=1./T2
P(JC,3,2)=(0.,0.)
P(JC,1,3)=(-TEMP2+(TEMP1*TEMP3)/T2)/(T1*T3)
P(JC,2,3)=-TEMP3/(T2*T3)
P(JC,3,3)=1./T3
JC=JC+1
20 CONTINUE
RETURN
END

```

```
SUBROUTINE GRAM2 (Y1,Y2,Y3)
COMPLEX*16 Y1(6),Y2(6),Y3(6),Z1(6),Z2(6),Z3(6)
COMPLEX*8 TEMPY,TEMPZ,TEMP1,TEMP2,TEMP
CALL PRCC(Y1,Y1,TEMPY)
T=TEMPY
CC 1 I=1,6
1 Z1(I)=Y1(I)/SQRT(I)
CALL PRCC(Y2,Z1,TEMP1)
CC 2 I=1,6
2 Z2(I)=Y2(I)-TEMP1*Z1(I)
CALL PRCC(Z2,Z2,TEMPZ)
T=TEMPZ
CC 3 I=1,6
3 Z2(I)=Z2(I)/SQRT(I)
CALL PRCC(Y3,Z1,TEMP1)
CALL PRCC(Y3,Z2,TEMP2)
CC 4 I=1,6
4 Z3(I)=Y3(I)-TEMP1*Z1(I)-TEMP2*Z2(I)
CALL PRCC(Z3,Z3,TEMPZ)
T=TEMPZ
CC 5 I=1,6
5 Z3(I)=Z3(I)/SQRT(I)
CC 6 I=1,6
Y1(I)=Z1(I)
Y2(I)=Z2(I)
Y3(I)=Z3(I)
6 CONTINUE
20 CONTINUE
RETURN
END
```

```

SUBROUTINE AINV(A,B,CC)
COMPLEX*16 A(3,3),B(3),CC(3),AA(3,3),TEMP,CHECK(3)
REAL*8 T1,T2
INTEGER*2 IC(3)
NN=3
DC 50 N=1,NN
IC(N)=A
50 CONTINUE
DC 51 I=1,NN
B(I)=CC(I)
T1=B(I)
T2=B(I)*(0.,-1.0000)
WR(TE(6,999))I,T1,T2
DC 51 J=1,NN
AA(I,J)=A(I,J)
51 CONTINUE
DC 475 N=1,NN
N1=N+1
D=0.
DC 100 I=N,NN
DC 100 J=N,NN
T1=A(I,J)
T2=A(I,J)*(0.,-1.0000)
IF(CABS(T1**2+T2**2)-D)100,90,90
90 D=CABS(T1**2+T2**2)
II=I
JJ=J
100 CONTINUE
DC 110 I=1,NN
TEMP=A(I,N)
A(I,N)=A(I,JJ)

```

```

110      A(I, JJ)=TEMP
        CCNTINUE
        I=IC(N)
        IC(N)=IC(JJ)
        IC(JJ)=I
        DC 120 J=N, NN
        TEMP=A(N, J)
        A(N, J)=A(II, J)
        A(II, J)=TEMP
120      CCNTINUE
        TEMP=B(N)
        B(N)=B(II)
        B(II)=TEMP
        B(N)=B(N)/A(N, N)
        IF(N-NN)200, 500, 200
200      DC 450 J=N1, NN
        T1=A(N, J)
        T2=A(N, J)*(0., -1.0000)
        IF(T1.NE.0.)CC TO 310
        IF(T2.EQ.0.)CC TO 350
310      CCNTINUE
        A(N, J)=A(N, J)/A(N, N)
        DC 30 I=N1, NN
30      A(I, J)=A(I, J)-A(I, N)*A(N, J)
350      B(J)=B(J)-A(J, N)*B(N)

```

```

450  CCNTINUE
475  CCNTINUE
500  N1=N
      N=N-1
      IF(N)700,700,,J
550  DC 600 J=N1,NN
600  B(N)=P(N)-A(N,J)*B(J)
      GC TC 500
700  CCNTINUE
      DC 950 N=1,NN
      DC 900 I=N,NN
      IF(IC(I)-N)900,750,900
750  TEMP=P(N)
      B(N)=P(I)
      B(I)=TEMP
      GC TC 950
900  CCNTINUE
950  IC(I)=IC(N)
      DC 10 I=1,NN
      T1=P(I)
      T2=P(I)*(0.,-1.0000)
      WRITE(6,999)I,T1,T2
999  FORMAT(1F , 'I=', I2, 2X, 'B= (', IPE12.2, ', ', IPE12.2, ')')
10   CCNTINUE
      DC 12 I=1,NN
      CHECK(I)=(0.,0.)
      DC 13 J=1,NN
      CHECK(I)=CHECK(I)+AA(I,J)*B(J)
13   CCNTINUE
      T1=CHECK(I)
      T2=CHECK(I)*(0.,-1.0000)
      WRITE(6,998)I,T1,T2
998  FORMAT(1F , 'I=', I2, 2X, 'CHECK= (', IPE12.2, ', ', IPE12.2, ')')
12   CCNTINUE
      RETURN
      END

```

```

SUBROUTINE PLOT(V,X1,X2,X3,N)
DIMENSION V(50),X1(50),X2(50),X3(50)
DIMENSION A(51)
DATA CCT/'./',STAR/'*'/,PLUS/'+'/,BLANK/' '/,EX/'X'/
X3(1)=ABS(X3(1))
X3MAX=X3(1)
DO 1 J=1,N
X3(J)=ABS(X3(J))
IF(X3MAX.LT.X3(J))X3MAX=X3(J)
1 CONTINUE
DO 2 J=1,51
2 A(J)=CCT
DO 3 J=1,51,5
A(J)=STAR
3 CONTINUE
WRITE(6,102) X3MAX
102 FORMAT(1P1,'X3MAX=',1X,1PE10.3)
WRITE(6,100)(A(K),K=1,51)
100 FORMAY(7X,51A1)
DO 5 J=1,N
DO 4 JJ=1,51
4 A(JJ)=BLANK
M=X1(J)*50+1
A(M)=STAR
M=X2(J)*50+1
A(M)=PLUS
TEMP=ABS(X3(J))/X3MAX
M=TEMP*50+1
A(M)=EX
A(1)=CCT
A(51)=CCT
WRITE(6,101)V(J),(A(K),K=1,51)
101 FORMAT(F7.3,51A1)
5 CONTINUE
DO 6 J=1,51
6 A(J)=CCT
DO 7 J=1,51,5
A(J)=STAR
7 CONTINUE
WRITE(6,100) (A(K),K=1,51)
RETURN
END

```

```

SUBROUTINE YIC(VRE,VIM,DY,OMEGA,YRE,YIM)
REAL*8 JRE,JIM,KSIN2,VRE(2),VIM(2),YRE,YIM
KSIC2=3.9
EPSO=A.86E-14
TEMP=KSIC2*EPSO/DY
JRE=TEMP*(VIM(2)-VIM(1))
JIM=TEMP*(VRE(1)-VRE(2))
TEMP=VRE(1)**2+VIM(1)**2
YRE=(JRE*VRE(1)+JIM*VIM(1))/TEMP
YIM=(-JRE*VIM(1)+JIM*VRE(1))/TEMP
RETURN
END

```

```

SUBROUTINE SEPI6(X,XRE,XIM)
COMPLEX*16 X
COMPLEX*8 TEMP
TEMP=X
XRE=TEMP
XIM=AIMAC(TEMP)
RETURN
END

```

```
SUBROUTINE ANGLE(U1,U2,ALPHA)
  COMPLEX*16 U1(6),U2(6)
  COMPLEX*8 TEMP,TEMP1,TEMP2
  CALL PRCC(U1,U2,TEMP)
  CALL PRCC(U1,U1,TEMP1)
  CALL PRCC(U2,U2,TEMP2)
  T1=TEMP1
  T2=TEMP2
  T3=TEMP
  T4=AIMAG(TEMP)
  ALPHA=CABS(TEMP)
  ALPHA=ALPHA/SCRT(T1*T2)
  ALPHA=ARCCS(ALPHA)
  RETURN
  END
```

```
SUBROUTINE PRCC(U1,U2,SCPRCC)
  COMPLEX*16 U1(6),U2(6)
  COMPLEX*8 TEMP
  COMPLEX*8 SCPRCC
  SCPRCC=(0.,0.)
  DO I=1,6
    TEMP=U1(I)
    TEMP1=TEMP
    TEMP2=-AIMAG(TEMP)
    TEMP=CMPLX(TEMP1,TEMP2)
    SCPRCC=SCPRCC+TEMP*U2(I)
  I
  RETURN
  END
```

N= J.CCCE 15CM-3
 XC= 1.0C0E-05 CENTIMETERS
 CC= 3.455E 04PICCFARADS/SC.CM.
 FREQUENCY= 1.0C0E 06HERTZ
 WF= 2.886D-01VCLITS

WG	G	CEC	CRF	VS	CG	C
VCLITS	WHCS	PICCFARACS	PICCFARACS	VOLTS	COUL/CM ²	
-1.500	0.357E-05	0.859E 00	0.252E CC	-0.41C	-2.765E-C8	6.518E-05
-1.400	0.358E-05	0.881E 00	0.253E CC	-0.359	-2.461E-C8	6.530E-05
-1.300	0.360E-05	0.853E 00	0.253E CC	-0.386	-2.161E-C8	6.552E-05
-1.200	0.364E-05	0.758E 00	0.254E CC	-0.365	-1.874E-C8	6.594E-05
-1.100	0.372E-05	0.675E 00	0.257E CC	-0.344	-1.615E-C8	6.683E-05
-1.000	0.394E-05	0.424E 00	0.263E CC	-0.30C	-1.421E-C8	6.904E-05
-0.900	0.437E-05	0.293E 00	0.275E CC	-0.224	-1.303E-C8	7.333E-05
-0.800	0.497E-05	0.293E CC	0.290E CC	-0.163	-1.203E-C8	7.901E-05
-0.700	0.576E-05	0.311E 00	0.309E CC	-0.092	-1.099E-C8	8.591E-05
-0.600	0.679E-05	0.334E 00	0.322E CC	-0.026	-9.876E-C9	9.435E-05
-0.500	0.822E-05	0.363E 00	0.361E CC	-0.04C	-8.676E-C9	1.050E-04
-0.400	0.103E-04	0.402E CC	0.395E CC	0.102	-7.361E-C9	1.189E-04
-0.300	0.135E-04	0.454E 00	0.450E CC	0.159	-5.892E-C9	1.381E-04
-0.200	0.186E-04	0.526E 00	0.521E CC	0.21C	-4.211E-C9	1.643E-04
-0.100	0.259E-04	0.612E CC	0.610E CC	0.254	-2.256E-C9	1.959E-04
0.000	0.344E-04	0.656E 00	0.658E CC	0.289	4.956E-14	2.267E-04
0.100	0.420E-04	0.763E 00	0.771E CC	0.316	2.520E-C9	2.510E-04
0.200	0.480E-04	0.911E 00	0.824E CC	0.327	5.239E-C9	2.682E-04
0.300	0.523E-04	0.844E CC	0.861E CC	0.354	8.099E-C9	2.801E-04
0.400	0.555E-04	0.868E CC	0.888E CC	0.369	1.106E-C8	2.884E-04
0.500	0.579E-04	0.885E 00	0.907E CC	0.381	1.409E-C8	2.943E-04
0.600	0.597E-04	0.898E CC	0.921E CC	0.392	1.717E-C8	2.987E-04
0.700	0.611E-04	0.908E CC	0.932E CC	0.401	2.029E-C8	3.020E-04
0.800	0.621E-04	0.915E 00	0.940E CC	0.410	2.344E-C8	3.045E-04
0.900	0.630E-04	0.922E 00	0.947E CC	0.418	2.661E-C8	3.066E-04
1.000	0.637E-04	0.926E 00	0.952E CC	0.426	2.980E-C8	3.082E-04
1.100	0.643E-04	0.931E 00	0.957E CC	0.433	3.301E-C8	3.096E-04
1.200	0.648E-04	0.934E CC	0.961E CC	0.440	3.623E-C8	3.107E-04
1.300	0.652E-04	0.937E 00	0.964E CC	0.446	3.947E-C8	3.116E-04
1.400	0.655E-04	0.929E CC	0.967E CC	0.453	4.271E-C8	3.124E-04
1.500	0.659E-04	0.942E 00	0.969E CC	0.459	4.596E-C8	3.131E-04

ALL CAPACITANCES ARE PER SQUARE CENTIMETERS

VAC2D

```

//      JOB REGION=45CK,TIME=5
// *FCR PAT FR,CCNAME=SYSPRINT,COPIES=C
// *PAIN LINES=2C
// EXEC FCATG
//FCRT.SYSIN CC *,CCB=BLKSIZE=2CCC

CCMPLEX*16 V1,E1Y,JPY,JNY,P1,N1
CCMPLEX*16 VAC,CVL,CVR,VIBACK
CCMPLEX*16 JPYE,JNYB,E1YB,V1B,P1B,N1B
REAL*8 VC
REAL*4 ECX,ECY,PC,NC
REAL*4 TA,TP,MLP,MUN,NCOP
REAL*4 C,NI,VT,EPSC,KSI,KSI2,ANG,CMEGA,C1,MY,MX,XC
CCMPCN V1(25,7C),E1Y(25,7C),JPY(25,7C)
CCMPCN JNY(25,7C),P1(25,7C),N1(25,7C)
CCMPCN VAC(25),CVL,CVR,VIBACK(25,7C)
CCMPCN JPYE(25),JNYB(25),E1YB(25),V1B(25),P1B(25),N1B(25)
CCMPCN VC(25,6C)
CCMPCN ECX(2,25),ECY(2,25),PC(2,25),NC(2,25)
CCMPCN TA,TP,MLP,MUN,NCOP
CCMPCN C,NI,VT,EPSC,KSI,KSI2,ANG,CMEGA,C1,MY,MX,XC
REAL*4 NTEPP
REAL*8 VTEPP
CCMPLEX*16 JTCT,ECISP,JIMAG
CCMPLEX*16 VIRET(25)
CC 1 JJ=1,5C
CC 2 II=1,25
READ(S,10C)J,I,VTEMP,NTEMP
VC(II,J)=VTEMP
ACCP=NTEMP
CCCONTINUE
2

```

```

100  FCRPAT(IX ,Z(14,IX),D25.15,E2C.7)
      CCNTINUE
      REAC(5,IO3IAL,NR,FX,FX,XO
      WRITE(6,1C3) NL,NR,FX,FX,XC
103  FCRPAT(IX ,Z(14,IX,3E15.7)
      N1=1.45E1C
      C=1.6E-19
      VT=C259
      EPSC=8.66E-14
      KSI=11.7
      KSI2=3.9
      CC=(NSIC2*EFSC/XC)*1.E12
      CI=(1.)/(KSI*EFSC)
      F=1.66
      CMEGA=3.14*F*Z.
      WRITE(6,557)C,N1,VT,EPSC,KSI,KSI02,CMEGA,CI,CC
597  FCRPAT(11 ,***CCNSTANTS***,/,9(11 ,1PE2C.7,/, ,***)
      NY1=5C
      NY2=60
      CC 12C 1=1,25
      VAC(1)=(C.,C.)
120  CCNTINUE
      CC 11 1=1,NL
      VAC(1)=(.,CI,C.)/VT
      VIRET(1)=(C.,C.)
11  CCNTINUE
      WRITE(6,555)
999  FCRPAT(11 ,*ENTERING VAC2C*1)
      CALL VAC2C(NY1,NY2,VIRET)
      WRITE(6,95E)

```

```

SUBROUTINE VACZC(NY1,NY2,VIRET)
CCPFLEX*16 V1,E1Y,JPY,JNY,PI,N1
CCPFLEX*16 VAC,DVL,CVR,VIRACK
CCPFLEX*16 JPYE,JNYB,E1YE,VIB,PIB,NIB
REAL*8 VC
REAL*4 ECX,ECY,PC,NC
REAL*4 TN,TP,MLP,MLN,NDOP
REAL*4 G,NI,VT,EPSC,KSI,KSIC2,ANG,CMEGA,CI,HY,FX,XC
CCPPCN V1(25,7C),E1Y(25,7C),JPY(25,7C)
CCPPCN JAY(25,7C),PI(25,7C),N1(25,7C)
CCPPCN VAC(25),DVL,CVR,VIRACK(25,7C)
CCPPCN JPYB(25),JNYB(25),E1YB(25),VIB(25),PIB(25),NYB(25)
CCPPCN VC(25,6C)
CCPPCN ECX(2,25),ECY(2,25),PC(2,25),NC(2,25)
CCPPCN TN,TP,MLP,MLN,NDOP
CCPPCN G,NI,VT,EPSC,KSI,KSIC2,ANG,CMEGA,CI,HY,FX,XC
C
C
CCPFLEX*16 VIRET(25)
CCPFLEX*16 B(65)
EFS=.8
CC J I=1,25
VIB(I)=(C.,C.)
E1YE(I)=(C.,C.)
JFYE(I)=(C.,C.)
JAYE(I)=(C.,C.)
NIB(I)=(C.,0.)
PIB(I)=(C.,C.)
CC J K=1,7C
VI(I,K)=(C.,C.)
E1Y(I,K)=(C.,0.)
JFY(I,K)=(C.,C.)

```

```

998  FCRPAT(1P, 'RETURNING FROM VAC2D')
      JIMAG=(C,1,1)
      JTCT=(C,C,1)
      CC 12 I=1,25
      T1=VIRET(1)
      T2=AIMAG(VIRET(1))
      WRITE(6,996)I,T1,T2
      CCNTINUE
12   FCRPAT(1P, 'VIRET(',12,1',1PE20.7,','',1PE20.7)
      CRFICT=C.
      CC 25 I=1,NL
      ECISF=- (VAC(I)*VT-VIRET(I))/(XC/10.)
      JTCT=-K$IC2*EFSC*ECISP*JIMAG
      CRF=AIMAG(JTCT)/(VAC(I)*VT)*1.E12/CC
      G=(JTCT/(VAC(I)*VT))*OMEGA
      CRFICT=CRFICT+CRF
      WRITE(6,11C)CRF,G
      CCNTINUE
25   CC 26 I=NR,25
      ECISF=- (VAC(I)*VT-VIRET(I))/(XC/10.)
      JTCT=-K$IC2*EFSC*ECISP*JIMAG
      T1=JTCT
      T2=AIMAG(JTCT)
      WRITE(6,111)I,T1,T2
111  FCRPAT(1P,C,'JTCT(',14,')='',1P2E12.5)
26   CCNTINUE

      WRITE(6,112)CRFICT
112  FCRPAT(1P,C, 'CRFICT='',1PE12.5)
11C  FCRPAT(1P,C,'CRF='',E12.5,5X,'G='',E12.5)
      RETURN
      ENC

```

```

JNY(I,K)=(C.,C.)
PY(I,K)=(C.,C.)
NY(I,K)=(C.,C.)
CCNTINUE
CC 2 I=1,22
EY(I+1,I)=(I.,C.)
JFY(I+1,I+23)=(I.,C.)
JNY(I+1,I+46)=(I.,C.)
CCNTINUE
REAL*8 R1,R2,R3,R4
COMPLEX*16 REAL,IMAGI
REAL=(1.,CCC,C.CCCC)
IPAGI=(0.,CCCC,I.DCC)
REAL(5,IC1)R1,R2
REAL(5,IC1)R3,R4
JFY(1,7C)=(R1*REAL1+R2*IMAGI)
JFY(25,7C)=(R3*REAL1+R4*IPAGI)
REAL(5,IC1)R1,R2
REAL(5,IC1)R3,R4
JAY(1,7C)=(R1*REAL1+R2*IMAGI)
JAY(25,7C)=(R3*REAL1+R4*IPAGI)
REAL(5,IC1)R1,R2
REAL(5,IC1)R3,R4
PI(1,7C)=(R1*REAL1+R2*IMAGI)*C
P(25,7C)=(R3*REAL1+R4*IPAGI)*C
REAL(5,IC1)R1,R2
REAL(5,IC1)R3,R4
N1(1,7C)=(R1*REAL1+R2*IMAGI)*Q
N1(25,7C)=(R3*REAL1+R4*IPAGI)*Q
REAL(5,IC1)R1,R2
REAL(5,IC1)R3,R4
EY(1,70)=(R1*REAL1+R2*IMAGI)
EY(25,7C)=(R3*REAL1+R4*IPAGI)
REAL(5,IC1)R1,R2
REAL(5,IC1)R3,R4
V1(1,7C)=(R1*REAL1+R2*IMAGI)/VT

```

1

3

```

1C1
V1(25,70)=(R3*REAL1+R4*IPAG1)/VT
FCRPA1(IX,IP2C21.14)
NSTART=1
J=NSTART
ECX(1,1)=- (VC(2,J)-VO(1,J))/MX
PLA=65.+(2565./(1.+(ABS(NCCP)/8.5E16)**.72))
PLF=47.7+(1447.3/(1.+(ABS(NDCP)/6.3E16)**.76))
TF=8.E-6
TA=8.E-6
CC 5 I=1,25
FC(1,1)=NI*DEXP(-VC(1,J)/VT)*Q
NC(1,1)=NI*DEXP(VC(1,J)/VT)*Q
ECY(1,1)=- (VC(1,J+1)-VC(1,J))/HY
IF(1.EC.1) GC TC 5
IF(1.EC.25) GC TC 5
ECX(1,1)=- (VC(1+1,J)- VO(I-1,J))/(2.*MX)
CONTINUE
ECX(1,25)=- (VC(25,J)-VC(11,J))/MX
CC 2 J=1,45
ECX(2,1)=- (VC(2,J+1)-VC(1,J+1))/FX
CC 7 I=1,25
FC(2,1)=NI*DEXP(-VC(1,J+1)/VT)*Q
NC(2,1)=NI*DEXP(VC(1,J+1)/VT)*Q
ECY(2,1)=- (VC(1,J+1)-VC(1,J))/(FY)
IF(J.EC.45) GC TC 1C
ECY(2,1)=(ECY(2,1)-(VC(1,J+2)-VC(1,J+1))/(HY))/2.
CONTINUE
IF(1.EC.25) GC TC 7
IF(1.EC.1) GC TC 7
ECX(2,1)=- (VC(1+1,J+1)-VC(I-1,J+1))/(2.*MX)

```

5

1C

```

7   CONTINUE
   ECX(2,25)=- (VC(25,J+1)-VC(11,J+1))/FX
   CALL STEP2(J)
   CC 2 I=1,25
   ECX(1,I)=ECX(2,I)
   ECY(1,I)=ECY(2,I)
   PC(1,I)=PC(2,I)
   NC(1,I)=NC(2,I)
2   CONTINUE
   CALL STEP3
   CC 4 J=51,55
   CALL STEP4
4   CONTINUE
   CALL CALCE(P)
   CC 8 I=1,25
   VIRET(I)=(C.,C.)
   CC 6 K=1,65
   VIRET(I)=VIRET(I)+B(K)*VIBACK(I,K)*VT
6   CONTINUE
   VIRET(I)=VIRET(I)+VIBACK(I,7C)*VT
8   CONTINUE
   RETURN
   END

```

```

SLROUTINE STEP2(J)
CCMPLEX*16 V1,E1Y,JPY,JNY,P1,N1
CCMPLEX*16 VAC,CVL,CVR,VIBACK
CCMPLEX*16 JPYE,JNY8,E1Y8,V1B,P1B,N1B
REAL*8 VC
REAL*4 ECX,ECY,PC,NC
REAL*4 TA,TP,MLP,MUN,NCOP
REAL*4 Q,N1,VT,EPSC,KSI,KSIC2,ANG,CMEGA,C1,HY,HX,XO
CCMPCN V1(25,7C),E1Y(25,7C),JPY(25,7C)
CCMPCN JNY(25,7C),P1(25,7C),N1(25,7C)
CCMPCN VAC(25),CVL,CVR,VIBACK(25,7C)
CCMPCN JPY8(25),JNY8(25),E1Y8(25),V1B(25),P1B(25),N1B(25)
CCMPCN VC(25,6C)
CCMPCN ECX(2,25),ECY(2,25),PC(2,25),NC(2,25)
CCMPCN TA,TP,MLP,MUN,NCOP
CCMPCN Q,N1,VT,EPSC,KSI,KSIC2,ANG,CMEGA,C1,HY,HX,XO

C
C
CCMPLEX*16 CH,CJPX8,CJNX8,CE1XB,CTEMP,OJA(25),CJPX(25),CE1X(
CCMPLEX*16 JFYTEM,JNYTEM,E1YTEM,VITEM,PITEM,ALTEMP
REAL*4 RP(2,25),RN(2,25),TEMP,ZERC

C
C
ZERC=C.
CH=(CPLX(ZERC,CMEGA)
CC 1 I=1,25
TEMP=(NC(1,I)+(NI*C))*TP
TEMP=TEMP+(PC(1,I)+(NI*Q))*TN
TEMP=1./TEMP
RP(1,I)=TEPP*NC(1,I)
RN(1,I)=TEPP*PC(1,I)
TEMP=(NO(2,I)+(NI*C))*TP

```

```

TEMP=TEMP+(PC(2,I)+(NI*Q))*TA
TEMP=1./TEMP
RP(2,I)=TEMP*NC(2,I)
RN(2,I)=TEMP*PC(2,I)
CCONTINUE
CC 2 K=1,7C
CC 3 I=2,24
CEIX(I)=- (V1(I+1,K)+V1(I-1,K)-2.*V1(I,K))*VT/HX**2
CJAX(I)=- (N1(I,K)*(VC(I+1,J)+VC(I-1,J))-2.*VO(I,J))/(HX**2)*V
CTEPP=(ECX(I,I))*(N1(I+1,K)-N1(I-1,K)))/(HX**2.*VT)
CJAX(I)=CJAX(I)+CTEMP
CTEPP=-NC(I,I)*(V1(I+1,K)+V1(I-1,K)-2.*V1(I,K))/(HX**2)
CJAX(I)=CJAX(I)+CTEMP
CTEPP=- (V1(I+1,K)-V1(I-1,K))/(HX**2.)
CTEPP=CTEPP*(NC(I,I+1)-NC(I,I-1))/(HX**2.)
CJAX(I)=CJAX(I)+CTEMP
CTEPP=(N1(I+1,K)+N1(I-1,K)-2.*N1(I,K))/(HX**2)
CJAX(I)=(CJAX(I)+CTEMP)*PLN*VT
CJFX(I)=(F1(I,K)*(VC(I+1,J)+VC(I-1,J))-2.*VC(I,J))/(HX**2)*VT
CTEPP=- (ECX(I,I))*(P1(I+1,K)-P1(I-1,K)))/(HX**2.*VT)
CJFX(I)=CJFX(I)+CTEMP
CTEPP=FO(I,I)*(V1(I+1,K)+V1(I-1,K)-2.*V1(I,K))/(HX**2)
CJFX(I)=CJFX(I)+CTEMP
CTEPP=(V1(I+1,K)-V1(I-1,K))/(HX**2.)
CTEPP=CTEPP*(PC(I,I+1)-PC(I,I-1))/(HX**2.)
CJFX(I)=CJFX(I)+CTEMP
CTEPP=(P1(I+1,K)+P1(I-1,K)-2.*P1(I,K))/(HX**2)
CJFX(I)=- (CJFX(I)+CTEMP)*MLP*VT
JFYE(I)=(C*+RP(I,I))*P1(I,K)+RN(I,I)*N1(I,K)+CJFX(V)
JFYE(I)=-JFYE(I)+JPY(I,K)
JAYE(I)=(C*+RN(I,I))*N1(I,K)+RP(I,I)*P1(I,K)-CJAX(V)
JAYE(I)=JAYE(I)+Y+JNY(I,K)
E1YE(I)=+Y*(C1*(P1(I,K)-N1(I,K))-CEIX(I))+E1Y(I,K)
V1E(I)=+Y+E1Y(I,K)/VI+V1(I,K)
F1E(I)=-JFY(I,K)/(MUP*VT)+P1(I,K)*ECY(I,I)/VT
F1E(I)=(P1E(I)+PC(I,I))*E1Y(I,K)/VT*HY+P1(I,K)
N1E(I)=JAY(I,K)/(PLN*VT)-N1(I,K)*ECY(I,I)/VT
N1E(I)=(N1E(I)-NC(I,I))*E1Y(I,K)/VI*HY+N1(I,K)
CCONTINUE

```

1

3

```

REAL*8 R1,R2,R3,R4
COMPLEX*16 REAL1,IPAG1
REAL1=(1.[CC,0.CCCC)
IPAG1=(0.CECC,I.CCC)
IF(K.LT.7C) GC TC 11
REAC(5,IC1)R1,R2
REAC(5,IC1)R3,R4
JFYE(1)=(R1*REAL1+R2*IMAG1)
JPYE(25)=(R3*REAL1+R4*IMAG1)
REAC(5,IC1)R1,R2
REAC(5,IC1)R3,R4
JAYE(1)=(R1*REAL1+R2*IMAG1)
JAYE(25)=(R3*REAL1+R4*IMAG1)
REAC(5,IC1)R1,R2
REAC(5,IC1)R3,R4
PIB(1)=(R1*REAL1+R2*IMAG1)*C
PIB(25)=(R3*REAL1+R4*IMAG1)*C
REAC(5,IC1)R1,R2
REAC(5,IC1)R3,R4
N1B(1)=(R1*REAL1+R2*IPAG1)*C
N1B(25)=(R3*REAL1+R4*IMAG1)*C
REAC(5,IC1)R1,R2
REAC(5,IC1)R3,R4
E1YE(1)=(R1*REAL1+R2*IMAG1)
E1YE(25)=(R3*REAL1+R4*IMAG1)
REAC(5,IC1)R1,R2
REAC(5,IC1)R3,R4
V1B(1)=(R1*REAL1+R2*IPAG1)/VT
V1B(25)=(R3*REAL1+R4*IMAG1)/VT
FCRPA(IX,IP2C21.14)
1C1
11 CCNTINUE

```

```

CC 5 I=2,24
CE1XB=-(VIE(I+1)+VIB(I-1)-2.*VIB(I))*VT/(H**2)
CJAXB=-(VC(I+1,J+1)+VC(I-1,J+1)-2.*VC(I,J+1))/((H**2)*VT)
CJAXB=NIE(I)*CJAXB
CTEMP=(ECX(2,I)*(NIB(I+1)-NIB(I-1)))/(H**2.*VT)
CJAXB=CJAXB+CTEMP
CTEMP=-NC(2,I)*(VIE(I+1)+VIB(I-1)-2.*VIB(I))/(H**2)
CJAXB=CJAXB+CTEMP
CTEMP=-(VIE(I+1)-VIB(I-1))/(H**2.)
CTEMP=CTEMP*(NC(2,I+1)-NC(2,I-1))/(H**2.)
CJAXB=CJAXB+CTEMP
CTEMP=(NIE(I+1)+NIB(I-1)-2.*NIB(I))/(H**2)
CJAXB=(CJAXB+CTEMP)*MLA*VT
CJPXB=(VC(I+1,J+1)+VC(I-1,J+1)-2.*VC(I,J+1))/((H**2)*VT)
CJPXB=PIE(I)*CJPXB
CTEMP=-(ECX(2,I)*(PIB(I+1)-PIB(I-1)))/(H**2.*VT)
CJPXB=CJPXB+CTEMP
CTEMP=PO(2,I)*(VIE(I+1)+VIB(I-1)-2.*VIB(I))/(H**2)
CJPXB=CJPXB+CTEMP
CTEMP=(VIE(I+1)-VIB(I-1))/(H**2.)
CTEMP=CTEMP*(PC(2,I+1)-PC(2,I-1))/(H**2.)
CJPXB=CJPXB+CTEMP
CTEMP=(PIE(I+1)+PIB(I-1)-2.*PIB(I))/(H**2)
CJPXB=-(CJPXB+CTEMP)*MLP*VT

```

```

CTEMP=(C4+RF(2,I))*PIB(I)+RN(2,I)*NIB(I)
CTEMP=(CTEMP+(C4+RP(1,I))*PI(1,K)+RN(1,I)*NI(1,K))
CTEMP=(CTEMP+CJXR+CJXP(I))/2.
JPYTEP=-CTEMP+PY+JPY(1,K)
CTEMP=(C4+RN(2,I))*NIB(I)+RP(2,I)*PIB(I)
CTEMP=(CTEMP+(C4+RN(1,I))*NI(1,K)+RP(1,I)*PI(1,K))
CTEMP=(CTEMP-CJXR-CJXP(I))/2.
JYTEP=CTEMP+PY+JNY(I,K)
CTEMP=PIB(I)+PI(1,K)-NIB(1)-NI(1,K)
CTEMP=CTEMP+CI-CEIX(I)-DEIXE
EYTEP=PY+(CTEMP/2.)*EY(I,K)
VITEMP=-PY*((EYB(I)+EY(1,K))/2.)/VT+V1(I,K)
CTEMP=-((JFYB(I)/MLPI)+(JPY(I,K)/MLPI))
CTEMP=CTEMP+(PIB(I)*ECY(2,I)+PI(I,K)*ECY(1,I))
CTEMP=CTEMP+(PC(2,I)*EYB(I)+PC(1,I)*EY(1,K))
FITEMP=(PY*CTEMP)/(2.*VT)+PI(I,K)
CTEMP=-((JNYB(I)/MLN)+(JNY(I,K)/MLN))
CTEMP=CTEMP+(NIB(I)*ECY(2,I)+NI(1,K)*ECY(1,I))
CTEMP=CTEMP+(NC(2,I)*EYB(I)+NC(1,I)*EY(1,K))
NITEMP=(-PY*CTEMP)/(2.*VT)+NI(1,K)
JPY(I,K)=JPYTEP
JNY(I,K)=JNYTEP
EY(I,K)=EYTEP
V1(I,K)=VITEMP
PI(I,K)=FITEMP

```

```

5      NI(I,K)=NITEMP
      CCNTINUE
      IF(K.LT.70) GC TC 25
      VI(1,70)=VIB(1)
      EIY(1,70)=EIYE(1)
      JFY(1,70)=JPYE(1)
      JNY(1,70)=JNYE(1)
      FI(1,70)=FIB(1)
      NI(1,70)=NIE(1)
      VI(25,70)=VIB(25)
      EIY(25,70)=EIYE(25)
      JFY(25,70)=JPYE(25)
      JNY(25,70)=JNYE(25)
      FI(25,70)=FIB(25)
      NI(25,70)=NIE(25)
25     CCNTINUE
      CC 4 I=1,25
      VIB(I)=(C.,C.)
      EIYE(I)=(C.,C.)
      JPYE(I)=(C.,C.)
      JNYE(I)=(C.,C.)
      NIE(I)=(C.,0.)
      FIB(I)=(C.,C.)
4      CCNTINUE
2      CCNTIALE
      RETURN
      END

```

```

SLEROUTINE STEF3
CCPFLEX*16 VI,EIY,JPY,JNY,PI,N1
CCPFLEX*16 VAC,CVL,DVR,VIBACK
CCPFLEX*16 JPYE,JNYB,EIYB,VIB,P1B,N1B
REAL*8 VC
REAL*4 ECX,ECY,PC,NC
REAL*4 TN,TP,MLP,MUN,NDOP
REAL*4 Q,N1,VT,EPSC,KSI,KSIC2,ANG,CMEGA,C1,MY,FX,XC
CCMPCN V1(25,7C),EIY(25,7C),JPY(25,7C)
CCMPCN JAY(25,7C),PI(25,7C),N1(25,7C)
CCMPCN VAC(25),CVL,DVR,VIBACK(25,7C)
CCMPCN JPYE(25),JNYB(25),EIYB(25),VIB(25),P1B(25),N1B(25)
CCMPCN VC(25,6C)
CCMPCN ECX(2,25),ECY(2,25),PC(2,25),NC(2,25)
CCMPCN TN,TP,MLP,MUN,NDOP
CCMPCN Q,N1,VT,EPSC,KSI,KSIC2,ANG,CMEGA,C1,MY,FX,XC
CC I K=1,7C
CC I I=2,24
VI(I,K)=V1(I,K)-EIY(I,K)*(KSI/KSIC2)*(XC/10.)/VT
EIY(I,K)=(KSI/KSIC2)*EIY(I,K)
CONTINUE
CVL=(VAC(I)-V1(I,7C))/10.
DVR=(VAC(25)-V1(25,7C))/1C.
V1(I,7C)=V1(I,7C)+CVL
V1(25,7C)=V1(25,7C)+DVR
RETURN
EAC
SLEROUTINE STEF4
CCPFLEX*16 VI,EIY,JPY,JNY,PI,N1
CCPFLEX*16 VAC,CVL,DVR,VIBACK
CCPFLEX*16 JPYE,JNYB,EIYB,VIB,P1B,N1B
REAL*8 VC
REAL*4 ECX,ECY,PC,NC
REAL*4 TN,TP,MLP,MUN,NDOP
REAL*4 Q,N1,VT,EPSC,KSI,KSIC2,ANG,CMEGA,C1,MY,FX,XC
CCMPCN V1(25,7C),EIY(25,7C),JPY(25,7C)
CCMPCN JNY(25,7C),PI(25,7C),N1(25,7C)
CCMPCN VAC(25),CVL,DVR,VIBACK(25,7C)

```

C

1

```

CCMPCN JFYB(25),JAYB(25),E1YB(25),V1B(25),P1B(25),N1B(25)
CCMPCN VC(25,6C)
CCMPCN ECA(2,25),ECY(2,25),PC(2,25),NC(2,25)
CCMPCN TA,TP,MLP,MLN,NDOP
CCMPCN G,NI,VT,EPSC,KSI,KSIK2,ANG,CMEGA,C1,HY,HX,XC
CCMPLEX=16 CH,CJAXB,CJAXB,CE1XB,CE1XB(25),DJPX(25),CE1X(
CC 2 K=1,7C
CC 5 I=1,25
V1B(1,K)=V1(I,K)
CCNTINLE
CC 1 I=2,24
CE1(I)=-(V1(I+1,K)+V1(I-1,K))-2.*V1(I,K))*VT/PI**2
E1Y(I)=(XC/IC.)*(-CE1X(I))+E1Y(I,K)
V1B(I)=-(XC/IC.)*E1Y(I,K)/VT+V1(I,K)
CCNTINLE
IF(K.LT.7C)GC TC 6
V1B(1)=V1(1,7C)+CVL
V1B(25)=V1(25,7C)+CVR
CCNTINLE
CC 3 I=2,24
CE1XB=-(V1E(I+1)+V1B(I-1))-2.*V1B(I))*VT/PI**2
V1(I,K)=-(XC/2C.)*(E1YB(I)+E1Y(I,K))/VT+V1(I,K)
E1Y(I,K)=(XC/2C.)*(-CE1XP-CE1X(I))+E1Y(I,K)
CCNTINLE
IF(K.LT.7C)GC TC 7
V1(1,7C)=V1B(1)
V1(25,70)=V1B(25)
CCNTINLE
CC 4 I=1,25
V1B(I)=(C.,0.)
CCNTINLE
CCNTINLE
RETURN
END

```

5

1

6

3

7

4

2

```

SUBROUTINE CALCE(E)
CCPFLEX*16 VI,EIY,JPY,JNY,PI,A1
CCPFLEX*16 VAC,CVL,CVR,VIBACK
CCPFLEX*16 JPYE,JNYB,EIYE,VIB,PIB,A1B
REAL*8 VC
REAL*4 ECX,ECY,PC,NC
REAL*4 TA,TP,MLP,MUN,NCOP
REAL*4 G,A1,VT,EPSC,KSI,KSIC2,ANG,CMEGA,C1,MY,FX,XC
CCMPCN VI(25,7C),EIY(25,7C),JPY(25,7C)
CCMPCN JAY(25,7C),PI(25,7C),NI(25,7C)
CCMPCN VAC(25),CVL,CVR,VIBACK(25,7C)
CCMPCN JPYE(25),JNYB(25),EIYB(25),VIB(25),PIB(25),A1B(25)
CCMPCN VC(25,6C)
CCMPCN EOX(2,25),EOY(2,25),PC(2,25),NC(2,25)
CCMPCN TA,TP,MLP,MUN,NCOP
CCMPCN G,A1,VT,EPSC,KSI,KSIC2,ANG,CMEGA,C1,MY,FX,XC
CCPFLEX*16 UTEPP(69),R(69),A(69,69),AA(69,69),TEMP
REAL *8 I1,I2
CC 22 I=1,23
CC 22 K=1,69
A(I,K)=VI(I+1,K)*VT
A(I+23,K)=JPY(I+1,K)
A(I+46,K)=JNY(I+1,K)
CCNTINLE
CC I I=1,23
R(I)=VAC(I+1)
R(I)=(R(I)-VI(I+1,7C))*VT
R(I+23)=-JPY(I+1,7C)
R(I+46)=-JAY(I+1,7C)
CCNTINLE
INTEGER*2 IC(69)
NA=69

```

22

1

```

I=IC(N)
IC(N)=IC(JJ)
IC(JJ)=I

CC 250 J=N,NN
TEMP=A(N,J)
A(N,J)=A(I,I,J)
A(I,I,J)=TEMP
250 CONTINUE

TEMP=B(N)
B(N)=B(I,I)
B(I,I)=TEMP
E(N)=E(N)/A(N,N)
IF(A-NN)200,500,200
200 CC 450 J=N2,NN
T1=A(N,J)
T2=A(N,J)*(C.,-).0000)
IF(T1.NE.C.)GC TC 310
IF(T2.EC.C.)GC TC 350
310 CONTINUE
A(N,J)=A(N,J)/A(N,N)
CC 300 I=N2,NN
300 A(I,J)=A(I,J)-A(I,N)*A(N,J)
350 B(J)=B(J)-A(J,N)*B(N)
450 CONTINUE
475 CONTINUE
500 N2=N
N=N-1
IF(N)700,700,550
550 CC 600 J=N2,NN
600 B(N)=B(N)-A(N,J)*B(J)
CC TC 500
700 CONTINUE
CC 550 N=1,NN
CC 900 I=N,NN

```

```

      CC 50 N=1,NN
      IC(N)=N
50    CCNTINUE
      CC 51 I=1,NN
      T1=E(I)
      T2=E(I)*(C.,-1.CCCC)
      WRITE(6,999)I,T1,T2
      CC 51 J=1,NN
      AA(I,J)=A(I,J)
51    CCNTINUE

      CC 475 N=1,NN
      N2=N+1
      C=C.
      CC 100 I=N,NN
      CC 100 J=N,NN
      T1=A(I,J)
      T2=A(I,J)*(C.,-1.CCCC)
      IF(CABS(T1)**2+T2**2)-C)100,90,90
90    C=CABS(T1**2+T2**2)
      II=I
      JJ=J
100   CCNTINUE

      CC 110 I=1,NN
      TEMP=A(I,N)
      A(I,N)=A(I,JJ)
      A(I,JJ)=TEMP
110   CCNTINUE

```

```

750      IF(IC(I)-N)500,750,500
        TEMP=B(N)
        B(N)=B(I)
        E(I)=TEMP
        GO TO 550
900      CONTINUE
950      IC(I)=IC(N)

        DO 10 I=1,NN
          T1=E(I)
          T2=B(I)*(C.,-1.CCCC)
          WRITE(6,999)I,T1,T2
999      FORMAT(1P,'I=',12,2X,'B=(',1PE12.2,',',1PE12.2,')')
10       CONTINUE
        DO 25 I=1,NN
          LTEMP(I)=(C.,C.)
          DO 13 J=1,NN
            LTEMP(I)=LTEMP(I)+AA(I,J)*B(J)
13        CONTINUE
          T1=LTEMP(I)
          T2=LTEMP(I)*(C.,-1.CCCC)
          WRITE(6,998)I,T1,T2
998      FORMAT(1P,'I=',12,2X,'U=(',1PE12.2,',',1PE12.2,')')
25        CONTINUE
          RETURN
        END
//GC.SYSLCT DD CLPPY
//GC.SYSTA CC *
/*

```

REFERENCES

1. R. Camisa, Ph. D. Thesis, CUNY, 1975.
2. J. S. Nadan, "Experimental Capacitance-Voltage Characteristics of Three Terminal Digital MOS Varactors", I.E.E.E. Proc., Vol.61, pp.1512-1513, Oct. 1973.
3. H. K. Gummel, "A Self-Consistent Iterative Scheme for One-Dimensional Steady State Transistor Calculations", I.E.E.E. Trans, on Electron Devices, Vol. ED-11, pp. 455-465, Oct. 1964.
4. A. H. Agajanian, "A Bibliography on Semiconductor Device Modeling", Solid State Electronics, Vol. 18, pp. 917-929, 1975.
5. T. Collins, Ph. D. Thesis, University of California, Davis, 1973.
6. M. Reiser, "A Two-Dimensional Numerical Model for DC, AC, and Large-Signal Analysis", I.E.E.E. Trans. on Electron Devices, Vol. ED-20, pp.35-45, Jan, 1973.
7. A. K. Jonscher, "Transport of Hot Injected Plasmas in Semiconductors", Proc. of the Phys. Soc., Vol.84, pp. 767-779, 1964.
8. J. P. McKelvey, Solid State and Semiconductor Physics, Chap.9, Harper and Row, N.Y.,1966.
9. W. van Roosbreck, "Theory of the Flow of Electrons and Holes in Germanium and Other Semiconductors", Bell Syst. Tech. J., Vol. 29, pp.560-607, Oct. 1950.
10. D. M. Caughey and R. E. Thomas, "Carrier Mobilities in Silicon Empirically Related to Doping and Field", Proc. of the I.E.E.E., pp.2192-2193, Dec. 1967.
11. C. R. Chester, Techniques in Partial Differential Equations, McGraw-Hill, N.Y., 1971.

12. H. F. Wolf, Semiconductors, Chap. 5, Wiley-Inter-Science, N.Y. 1971.
13. G. E. Forsythe and W. Wasow, Finite-Difference Methods for Partial Differential Equations, Wiley, N.Y., 1960.
14. W. F. Ames, Nonlinear Partial Differential Equations in Engineering, Mathematics in Science and Engineering Series, Vol. 18, Academic Press, N.Y., 1965.
15. S. D. Conte and C. deBoor, Elementary Numerical Analysis, International Series in Pure and Applied Mathematics, Mc Graw-Hill, N.Y., 1971.
16. J. M. Ortega and W. C. Rheinboldt, Iterative Solution of Nonlinear Equations in Several Variables, Chap. 12, Academic Press, N.Y., 1970.
17. Ibid.
18. Ibid.
19. P. M. Morse and H. Feshbach, Methods of Theoretical Physics, McGraw-Hill, N.Y. 1953.
20. G. E. Forsythe and W. Wasow, op, cit.
21. M. Reiser, "Computing Methods in Semiconductor Problems", Computing Methods in Applied Sciences and Engineering, Part 1, Lecture Notes in Computer Science, No. 10, Springer-Verlag, N.Y., 1973.
22. J. W. Slotboom, "Computer-Aided Two Dimensional Analysis of Bipolar Transistors", I.E.E. Trans. on Electron Devices, Vol. Ed.-20, pp.669-679, Aug. 1973.
23. D. Greenspan, Lectures on the Numerical Solution of Linear, Singular and Non-linear Differential Equations, Prentice Hall, 1968.

24. J. M. Ortega and W. C. Reinboldt, op.cit., Chap. 10.
25. Ibid.
26. G. E. Forsythe and W. Wasow, op. cit.
27. J. M. Ortega and W. C. Reinboldt, op.cit., Chap.12.
28. D. M. Young, Iterative Solution of Large Linear Systems, Academic Press, N.Y., 1971.
29. D. Greenspan, op. cit.
30. S. M. Sze, Physics of Semiconductor Devices, Wiley-Interscience, N.Y., 1969.
31. T. E. Stern, Theory of Nonlinear Networks and Systems, Chap. 2, Addisnon-Wesley, Reading, Mass., 1975.
32. A. S. Grove, Physics and Technology of Semiconductor Devices, Wiley, N.Y., 1967.
33. R. Camisa and J. S. Nadan, "MOS M-ary Varactors and Their Microwave Application", I.E.E.E. Second Annual Conference on MOS Devices and Integrated Circuits, N.Y., N.Y., Apr. 1972.
34. D. M Brown, W. E. Engeler, J.J. Teimann, "High Frequency MOS Digital Capacitor", Int. Electron Devices Meeting, Dec. 1974, Conf. Dig. pp523-526.
35. E. Wasserstrom and J. McKenna, "The Potential Due to a Charged Metallic Strip on a Semiconductor Surface", Bell Sys. Tech. J., pp.856-877, May-June 1970.
36. S. M. Sze, op. cit. Chap. 9.
37. H. F. Wolf, op. cit., Chap. 5.

38. S. M. Roberts and J. Shipman, Two Point Boundary Problems: Shooting Methods, Modern Analytical and Computational Methods in Science and Mathematics, No. 31, American Elsevier, N.Y., 1972.
39. Ibid., Chap. 4.
40. S. D. Conte, "The Numerical Solution of Linear Boundary Value Problems", SIAM Rev., (3) No. 8, pp. 309-321, Jul. 1966.
41. R. W. Hamming, Numerical Methods for Scientists and Engineers, Chap. 24, International Series in Pure and Applied Mathematics, McGraw-Hill, N.Y. 1973.
42. G. E. Forsythe and W. Wasow, op. cit.
43. W. G. Bickley and J. McNamee, "Matrix and Other Direct Methods for the Solution of Systems of Linear Difference Equations", Phil. Trans, Royal Soc. of London, Series A, 252, pp. 69-131, 1960.
44. L. Fox, The Numerical Solution of Two Point Boundary Problems in Ordinary Differential Equations, Chap. 5, Oxford University Press, London, 1957.
45. S. M. Roberts and J. Shipman, op. cit., Chap. 4.
46. F. W. Door, "The Direct Solution of the Discrete Poisson Equation on a Rectangle", SIAM Rev. Vol. 12, No. 2, Apr. 1970, pp. 248-263.
47. D. R. Edwards and K. F. Hansen, "The Stabilized March Technique Applied to the Diffusion Equation", Nuclear Sci. Eng., No. 25, 1966, pp. 58-65.
48. P. M. DeRusso, R. J. Roy and C. M. Close, State Variables for Engineers, Chap. 4, Wiley, N.Y. 1965.
49. S. M. Roberts and J. Shipman, op. cit. Chap. 4.

50. E. Brenner and M. Javid, Analysis of Electric Circuits, Chap. 14, McGraw-Hill, N.Y., 1959.
51. J. P. McKelvey, op.cit., Chap. 9.
52. A. S. Grove, op. cit., Chap. 9.
53. A. Goetzberger, "Ideal MOS Curves for Silicon" Bell Sys. Tech. J., Vol. 45, 1966, pp. 1097-1122.
54. A. S. Grove, op. cit., Chap. 9.
55. M. Hsue, R. B. Palmer, M. L. Shopbell, and C. C. Mai, "Characteristics of P Channel MOS Field Effect Transistor With Ion Implanted Channels", Solid State Electronics, Vol. 15, 1972, pp.1237-1243.
56. A. S. Grove, op. cit., Chap. 9.
57. Ibid.
58. B. V. Gokhale and J. Ziedenbergs, "MOS Capacitance Under Punchthrough Conditions", I.E.E.E. Int. Elect. Dev. Meet., 1974, Dig. pp. 529-532.
59. W. Shockley, "The Theory of p-n Junctions in Semiconductors and p-n Junction Transistors", Bell Sys. Tech. J., pp.435-489, 1949.
60. R. Froelich, "On Stable Methods of Matrix Fabrication for Block-Tri-Diagonal Matrices, Part I: General Methods and Theorems", Report GA-7164(I), Gen. Atomics, San Diego, Cal., 1966.
61. G. E. Forsythe and W. Wasow, op. cit., p. 92.
62. W. Shockley and W. T. Read, "Statistics of the Recombination of Holes and Electrons", Phys. Rev. No. 87, 1952.

63. R. N. Hall, "Electron-Hole Recombination in Germanium", Phys. Rev., No. 87, 1952.
64. T. E. Stern, op. cit., Chap. 2.
65. A. S. Housholder, Principles of Numerical Analysis, McGraw-Hill, N.Y., 1953.
66. Forsythe and Wasow, op. cit.
67. C. T. Sah, A. B. Toole and R. F. Dierret, Solid State Electronics, No. 12, 1969.
68. H. F. Wolf, op. cit., Chap. 7.
69. S. M. Sze, op. cit., Chap. 9.
70. H. F. Wolf, op. cit., Chap. 5.
71. S. M. Sze, op. cit., Chap. 9, Fig. 12.
72. Ibid.

AUTOBIOGRAPHICAL STATEMENT

Andres G. Fortino was born in Rosario, Argentina on September 29, 1947, and has been a resident of the United States since January, 1961. He became a naturalized U. S. Citizen in 1966.

Mr. Fortino attended the City College of the City University of New York where he majored in Electrical Engineering. Upon receiving the Bachelor's degree in June, 1970, Mr. Fortino entered the U. S. Army as a Second Lieutenant in the Signal Corps. After an honorable discharge in 1971, he returned as a full time student in the Ph. D. program at the City University receiving a Master's degree in Electrical Engineering in 1973.

From 1971 to 1974, Mr. Fortino was a member of the instructional staff in the Electrical Engineering Department and Bachelor of Technology Division of the School of Engineering of the City College of the City University of New York.

Presently he is a Senior Associate Engineer employed by International Business Machines Corporation in Essex Junction, Vermont. Mr. Fortino is a member of Tau Beta Pi and the Institute of Electrical and Electronic Engineering.

Mr. Fortino resides in Essex Junction, Vermont with his wife Kathleen.